Terms and Conditions of Use of Digitised Theses from Trinity College Library Dublin

Copyright statement

All material supplied by Trinity College Library is protected by copyright (under the Copyright and Related Rights Act, 2000 as amended) and other relevant Intellectual Property Rights. By accessing and using a Digitised Thesis from Trinity College Library you acknowledge that all Intellectual Property Rights in any Works supplied are the sole and exclusive property of the copyright and/or other IPR holder. Specific copyright holders may not be explicitly identified. Use of materials from other sources within a thesis should not be construed as a claim over them.

A non-exclusive, non-transferable licence is hereby granted to those using or reproducing, in whole or in part, the material for valid purposes, providing the copyright owners are acknowledged using the normal conventions. Where specific permission to use material is required, this is identified and such permission must be sought from the copyright holder or agency cited.

Liability statement

By using a Digitised Thesis, I accept that Trinity College Dublin bears no legal responsibility for the accuracy, legality or comprehensiveness of materials contained within the thesis, and that Trinity College Dublin accepts no liability for indirect, consequential, or incidental, damages or losses arising from use of the thesis for whatever reason. Information located in a thesis may be subject to specific use constraints, details of which may not be explicitly described. It is the responsibility of potential and actual users to be aware of such constraints and to abide by them. By making use of material from a digitised thesis, you accept these copyright and disclaimer provisions. Where it is brought to the attention of Trinity College Library that there may be a breach of copyright or other restraint, it is the policy to withdraw or take down access to a thesis while the issue is being resolved.

Access Agreement

By using a Digitised Thesis from Trinity College Library you are bound by the following Terms & Conditions. Please read them carefully.

I have read and I understand the following statement: All material supplied via a Digitised Thesis from Trinity College Library is protected by copyright and other intellectual property rights, and duplication or sale of all or part of any of a thesis is not permitted, except that material may be duplicated by you for your research use or for educational purposes in electronic or print form providing the copyright owners are acknowledged using the normal conventions. You must obtain permission for any other use. Electronic or print copies may not be offered, whether for sale or otherwise to anyone. This copy has been supplied on the understanding that it is copyright material and that no quotation from the thesis may be published without proper acknowledgement.

Multiuser Communications for Next Generation Wireless Networks

Trinity College Dublin
Coláiste na Tríonóide, Baile Átha Cliath
The University of Dublin

Arman Farhang

School of Engineering

The University of Dublin
Trinity College

This dissertation is submitted for the degree of
Doctor of Philosophy

PhD.

Trinity College Dublin

October 2015

School of Engineering

I would like to dedicate this thesis to my loving family and the ones who motivated me through preparing it.

Declaration

I declare that this thesis has not been submitted as an exercise for a degree at this or any other university and is entirely my own work.

I agree to deposit this thesis in the University's open access institutional repository or allow the Library to do so on my behalf, subject to Irish Copyright Legislation and Trinity College Library conditions of use and acknowledgement.

Arman Farhang
October 2015

Summary

Orthogonal frequency division multiplexing (OFDM) has been the technology of choice for years in wired and wireless systems. However, it has some drawbacks that limit its use in the fifth generation of wireless communication systems (5G). Apart from interference implications, the large out-of-band emissions of OFDM reduces the potential for utilization of non-contiguous spectrum chunks known as spectrum aggregation. OFDM also has a very high sensitivity to carrier frequency offset (CFO), which can hamper communication in multiuser scenarios such as uplink communications. Accordingly, stringent synchronization is required which imposes a large amount of overhead on the network and can cause some latency issues. These issues are in particular challenging when considering machine-to-machine (M2M) traffic. Bearing in mind that M2M and the Internet-of-Things are of increasing significance in the context of 5G communication systems, these shortcomings are significant.

To address these shortcomings this thesis takes two different approaches. In the first instance the thesis looks at techniques that target the CFO issues associated with OFDM waveforms. In the second instance the thesis adopts the approach that alternative waveforms may offer a better way forward. The underlying philosophy of the thesis whether dealing with OFDM or alternative waveforms is to pursue solutions that exhibit some or all of the following traits: (1) low computational complexity, (2) the ability to serve a large number of users, (3) low latency, (4) relaxed synchronization requirements and (5) localized signals in time and/or frequency domains.

The key contribution of the the section of the thesis that focuses on the uplink of OFDM-based systems lies in the design of CFO compensation algorithms with a substantially reduced complexity, especially in presence of a large number of users, compared with the existing solutions known to have the lowest complexity. To reduce the complexity while maintaining the optimal performance, the proposed CFO correction techniques in this thesis either take advantage of the natural structure of the CFO matrix, known as *interference matrix*, or manipulate the matrix to become sparse. Additionally, the developed techniques in this thesis cover all the subcarrier allocation schemes and thus make dynamic resource allocation possible in the uplink.

The alternative waveforms to OFDM that are considered in the thesis are filter bank multiple access (FBMC) and generalized frequency division multiplexing

(GFDM), known as a generalized version of OFDM. The reason for focusing on these waveforms is that they have emerged as serious candidates for inclusion in 5G standards. This is because they are claimed to have laxer synchronization requirements than OFDM which makes them attractive to the 5G scenarios where a large number of users need to be served simultaneously. Research in new waveforms is in its early stages and hence the waveforms warrant deeper investigation, if they are to be included in 5G standards. Another key technology that is proposed for inclusion in 5G systems utilizes a large number of antennas at the base station to increase the capacity of multiuser networks. This technology that is called massive multiple input multiple output (MIMO) exploits OFDM as a multicarrier modulation technique. However, in this thesis, OFDM is replaced by FBMC in the context of massive MIMO to investigate the impact of these two forerunner technologies proposed for 5G systems on each other. Due to their long prototype filter, FBMC signals are known to have a long transient period which can be a bottleneck in bursty communications. One of the major contributions of this thesis is to reveal an interesting property of FBMC in massive MIMO channels that we call *self-equalization*. This property allows us to widen the subcarrier bands, increase the symbol rate and substantially reduce the signal transients and hence the latency/delay that is caused by the synthesis and analysis filter banks. Self-equalization property leads to a number of by-product benefits; namely, (1) reduced complexity; (2) reduced sensitivity to CFO; (3) reduced peak-to-average power ratio (PAPR); (4) increased bandwidth efficiency. Another contribution of the thesis in FBMC-based massive MIMO systems is the development of a blind channel tracking algorithm that solves the pilot contamination problem in multi-cellular massive MIMO networks.

Inspired by the research that is conducted in this thesis in the realm of CFO compensation for OFDM, a transceiver structure is designed for GFDM which can substantially reduce the implementation complexity compared with the existing GFDM transceiver structures known to have the lowest complexity. The proposed transmitter is based on modulation matrix sparsification through application of fast Fourier transform (FFT) while the proposed receiver techniques benefit from the block circulant property of the matrices involved in the demodulation stage. GFDM is known to be a non-orthogonal waveform which leads to a bit error rate performance penalty. To tackle this problem, a simple modification to GFDM leading to an orthogonalized version of it, known as circular FBMC (C-FBMC), has been recently introduced. In our study, we present a thorough comparison of these two waveform candidates for 5G. The proposed transceiver structures for GFDM are directly applicable to C-FBMC.

Acknowledgements

Firstly, I would like to express my deepest gratitude to my supervisor Prof. Linda Doyle and my co-supervisor Dr. Nicola Marchetti for their guidance, patience, encouragement, enthusiasm and support. Their insights, feedback and and their way of conducting research greatly impacted my work and improved my research skills during the last four years. I believe, this will deeply affect my future career.

Secondly, thanks to everyone in CTVR who made my time towards completing this thesis enjoyable. I learned a lot from discussions and lectures given by the current or former CTVRians and enjoyed working in the same group with them; namely, Paul Sutton, Keith Nolan, Tim Forde, Irene Macaluso, Jasmina McMenamy, Ahmed Selim, Seamas McGettrick, João Paulo Miranda, Colman O'Sullivan, Ismael Gomez, Hamed Ahmadi, Johann M. Marquez Barja, Emanuele Di Pascale, Pedro Alvarez, Elma Avdic, Danny Finn, Paolo Di Francesco, Francisco Paisana, Jonathan Van De Belt, Carlo Galiotto, Justin Tallon, Jacek Kibilda and Ioannis Nellas. I also enjoyed social activities in CTVR such as playing foosball, football and table tennis which makes CTVR a perfect place to work at.

Thirdly, I would like to thank Prof. Behrouz Farhang-Boroujeny for the great discussions and talks from which I benefit a lot towards deepening my knowledge in signal processing aspects of wireless communications. I am also pleased to collaborate with Behrouz's group which mainly formed during my visit to the University of Utah in 2013. I would like to give special thanks to Amir Aminjavaheri, Ahmad Rezazadehreyhani and Arslan Javid Majid for their dedication and hard work as I enjoyed working with them.

Last, but by no means least, I wish to express heartfelt thanks to my family, first and foremost, my parents Ardeshir and Nahid for their insurmountable support, and my dear brothers Armin and Amir for being not only brothers but close friends. This thesis is dedicated to you!

Table of contents

List of figures

List of tables

Notations and Abbreviations

Throughout the thesis, matrices, vectors and scalar quantities are denoted by boldface uppercase, boldface lowercase and normal letters, respectively.

Notations

π	$\simeq 3.14\ldots$
j	Unit imaginary number $\sqrt{-1}$
$[\mathbf{A}]_{m,n}$	The element in the m^{th} row and n^{th} column of matrix $\mathbf{A}$
$\mathbf{A}^{-1}$	The inverse of matrix $\mathbf{A}$
$\mathbf{I}_M$	The identity matrix of size $M \times M$
$\mathbf{0}_{m\times n}$	The zero matrix of size $m \times n$
Rank($\mathbf{A}$)	Rank of the matrix $\mathbf{A}$
Range($\mathbf{A}$)	Range of the matrix $\mathbf{A}$
Null($\mathbf{A}$)	Nullspace of the matrix $\mathbf{A}$
Dim($\mathbf{A}$)	Dimension of the matrix $\mathbf{A}$
$(\cdot)^{\mathrm{T}}$	Transpose of a matrix
$(\cdot)^{\mathrm{H}}$	Conjugate transpose of a matrix
$(\cdot)^*$	Conjugate
diag($\mathbf{x}$)	A diagonal matrix with diagonal elements of the vector $\mathbf{x}$
circ($\mathbf{x}$)	A circulant matrix with the first column $\mathbf{x}$
$*$	Linear convolution operator

$\textcircled{M}$	M-point circular convolution operator
$\delta(\cdot)$	The Dirac delta function
$\cdot \bmod N$	Modulo-N operator
$\lfloor \cdot \rfloor$	Round down operator
$\lceil \cdot \rceil$	Round up operator
$\lvert \cdot \rvert$	Absolute value operator
$\lvert\lvert \cdot \rvert\rvert$	Norm operator
$\odot$	Element-wise matrix multiplication

Acronyms / Abbreviations

4G	Fourth generation of wireless communication systems
5G	Fifth generation of wireless communication systems
ADSL	Asymmetric Digital Subscriber Line
AWGN	Additive White Gaussian Noise
B-CAS	Block Carrier Assignment Scheme
BER	Bit Error Rate
BI-CAS	Block Interleaved Carrier Assignment Scheme
BS	Base Station
CDMA	Code Division Multiple Access
C-FBMC	Circular Filter Bank MultiCarrier
CFO	Carrier Frequency Offset
CG	Conjugate Gradient
CM	Complex Multiplication
CMT	Cosine modulated MultiTone

CP	Cyclic Prefix
CS	Cyclic Suffix
CSI	Channel State Information
DAB	Digital Audio Broadcasting
DFT	Discrete Fourier Transform
DMT	Discrete Multi-Tone
DSL	Digital Subscriber Line
DVB-T	Terrestrial Digital Video Broadcasting
ESPRIT	Estimation of Signal Parameters via the Rotational Invariance Technique
FBMC	Filter Bank MultiCarrier
FDMA	Frequency Division Multiple Access
FDM	Frequency Division Multiplexing
FFT	Fast Fourier Transform
FMT	Filtered MultiTone
FS-FBMC	Frequency Spreading Filter Bank MultiCarrier
FS	Frequency Spreading
FSE	Frequency Spreading Equalization
G-CAS	Generalized Carrier Assignment Scheme
GFDM	Generalized Frequency Division Multiplexing
I-CAS	Interleaved Carrier Assignment Scheme
ICI	Inter Carrier Interference
IDFT	Inverse Discrete Fourier Transform
IFFT	Inverse Fast Fourier Transform

i.i.d	independent and identically distributed
IoT	Internet-of-Things
ISI	Inter-Symbol-Interference
LMS	Least Mean Squares
LS	Least Squares
LTE	Long Term Evolution
M2M	Machine to Machine
MAI	Multiple Access Interference
MF	Matched Filter
MIMO	Multiple Input Multiple Output
ML	Maximum Likelihood
MMSE	Minimum Mean Square Error
MT	Mobile Terminal
MUI	MultiUser Interference
MUSIC	MUltiple SIgnal Classification
OFDMA	Orthogonal Frequency Division Multiple Access
OFDM	Orthogonal Frequency Division Multiplexing
OQAM	Offset Quadrature Amplitude Modulation
PAM	Pulse Amplitude Modulation
PAPR	Peak to Average Power Ratio
PDF	Probability Distribution Function
PUSC	Partially Used SubChanneling
QAM	Quadrature Amplitude Modulation

QPSK	Quadrature Phase Shift Keying
RRC	Root Raised Cosine
SDMA	Space Division Multiple Access
SIC	Successive Interference Cancellation
SINR	Signal to Interference plus Noise Ratio
SIR	Signal to Interference Ratio
CMT	Staggered MultiTone
SNR	Signal to Noise Ratio
SUD	Single User Detection
SVD	Singular Value Decomposition
TDD	Time Division Duplex
TDMA	Time Division Multiple Access
UFMC	Universal Filtered MultiCarrier
VDSL	Very high bit-rate Digital Subscriber Line
VSB	Vestigial Side Band
ZF	Zero Forcing

Chapter 1

Introduction

Wireless communication systems have become an essential part of everyday life. The widespread popularity of smart phones and the emergence of new applications such as the Internet of Things (IoT) and machine to machine communications (M2M) necessitate the need for massive connectivity and higher data rates. The advent of the fifth generation of wireless communication systems (5G) and the associated focus on a wide range of applications from those involving bursty M2M traffic to media-rich high bandwidth applications has led to the requirement for low latency and temporally and spectrally efficient signaling techniques with relaxed synchronization needs.

As opposed to the previous generations of wireless communication systems, 5G is not only about higher data rates but it is also about more and more connected devices. This leads to a number of challenges in such systems. The presence of many connected devices in the network results in multiuser interference (MUI) due to the lack of synchronization among the users. In the current multiuser scenarios such as uplink communication, a negligible drift in synchronization causes a large amount of MUI which can hamper communication. The MUI escalates as the number of users to be simultaneously served increases. A way of dealing with this problem is to synchronize the users before uplink transmission, i.e., during downlink communication and bring their synchronization errors in a very tight range. This in turn demands transmission of a large amount of training signals which imposes a large overhead and hence latency to the network.

Therefore, the challenge in multiuser systems is to (1) lower the latency, (2) relax the synchronization needs, (3) serve a large number of users and (4) serve the users while having a reasonable computational complexity.

The aforementioned requirements and challenges for future wireless communication systems motivate the need for substantial technological improvements that need to be started from the physical layer. To that end, this thesis is focused on the physical layer aspects of the current and future multiuser wireless communication systems. Hence, it provides solutions to the shortcomings of the current multiuser systems and looks into alternative approaches that can greatly improve the capacity and address the requirements of the future multiuser systems. Accordingly, the purpose of the thesis is to look at different waveforms and new technologies being proposed for 5G systems, enhance them and test their applicability to multiuser scenarios where many users are present in the network.

1.1 Current multiuser systems

There exist four main categories of multiple access techniques; namely, frequency division multiple access (FDMA), time division multiple access (TDMA), code division multiple access (CDMA) and space-division multiple access (SDMA). In FDMA, the available bandwidth is divided into different frequency bands or channels with large enough guard bands in between and they are assigned to different users to transmit their signals without interfering each other. The frequency bands are assigned to the users based on their demand and only one user can occupy a channel during each transmission time. Similar to FDMA, in TDMA, the available time frame is divided into several time slots that are assigned to different users. In CDMA, the spectrum of the signal is spread beyond its required bandwidth using a spreading code and hence CDMA is not efficient for single user scenarios. However, in multiuser scenarios, it becomes bandwidth efficient as the available bandwidth is reused by all the users. All the multiple access methods that are mentioned above can utilize another dimension which is space to increase the network capacity. This technique, which is known as SDMA, leverages the non-homogeneous spatial distribution of the users and takes advantage of multiple input multiple output (MIMO) antenna systems.

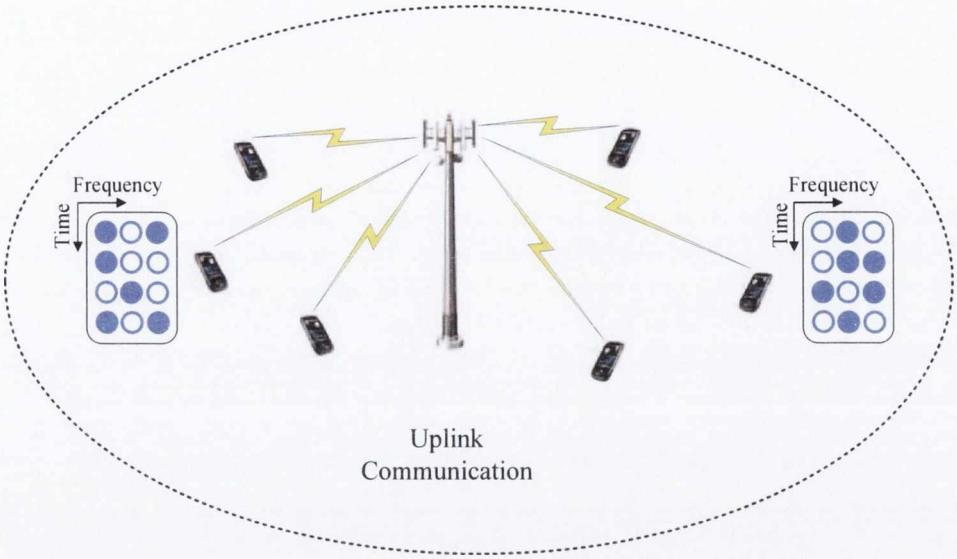

Fig. 1.1 Uplink communication.

The physical layer of 4G systems is based on OFDMA which is a combination of orthogonal frequency division multiplexing (OFDM) and FDMA. OFDM is a multi-carrier technology where the transmit data is modulated with a number of orthogonal tones. The popularity of OFDM systems is due to their simple implementation as well as their robustness against multipath channels. In OFDMA, mutually exclusive sets of subcarriers are assigned to different users based on some carrier assignment scheme[1]. In the uplink of an OFDMA system, the resources in time and frequency are allocated to different users spread in different locations and they transmit their signals to the base station (BS), Fig. 1.1. The inevitable imperfect synchronization between the users and the BS breaks the orthogonality between the subcarriers and causes multiple access interference (MAI) as well as self-user interference [1]. Synchronization errors due to the timing misalignment of the users' signals can be eliminated by a choice of long enough cyclic prefix (CP), to obtain a set of quasi-synchronous OFDM signals. The residual timing mismatch between different users will be reflected as a part of their respective channel impulse responses and hence, can be compensated for at the equalization stage, [2].

Due to the fact that the received signal at the BS is a superposition of all the users' signals, multiple CFOs appear in the received signal. This breaks the orthogonality and results in inter-carrier interference (ICI) and hence MUI. To remove MUI,

[1]Different carrier assignment schemes are discussed in detail in Chapter 2.

a two-step process is applied. First, an appropriate signal processing method is used to estimate different users' CFOs. A CFO compensation method is then employed to remove MUI effects. Several algorithms have been proposed in the literature for the former [2–4]. However, the focus of this thesis in the area of OFDMA uplink is on the latter, i.e., improving on the MUI removal methods. In the study that is conducted in this thesis, it is noticed that the existing CFO correction techniques in the literature suffer from a very large computational complexity specially as the number of users increases. To avoid this large complexity, current wireless standards such as WiMAX and 3GPP Long Term Evolution (LTE) have a very stringent synchronization requirements among the users which does not allow CFOs higher than 2 to 4 percent of subcarrier spacing. This indeed imposes a large amount of overhead to the network and is very costly. Another way of attacking the CFO problem in the uplink is to accept some performance loss and bring the complexity in a reasonable range. Accordingly, all the aforementioned remedies come at a cost which is not negligible. Therefore, the research question that is raised here is the following.

Question 1

- ***Is it possible to serve a large number of users with OFDMA having a reasonable computational burden while providing the optimal performance catering all carrier assignment schemes?***

1.2 Future multiuser systems

To avoid the interference issues of 4G systems and address the challenges of 5G, alternative technologies with relaxed synchronization requirements, capability to serve a large number of users, low latency and complexity have recently emerged. Two major hot research areas to watch out for in the realm of 5G systems are massive multiple input multiple output (MIMO) and new waveforms promising the aforementioned challenges of 5G.

Massive MIMO

In recent years, massive MIMO has stirred a great amount of interest among researchers as a potential candidate to increase the capacity of multiuser networks.

Massive MIMO is a CDMA like multiuser technique where the spreading gains for each user are determined by the channel gains between the respective mobile terminal (MT) antenna and multiple antennas at the BS. As it is shown in [5], by increasing the number of antennas at the BS, the effects of noise and multiuser interference start to vanish until they will be completely removed as the number of BS antennas tends to infinity. Hence, the network capacity can be increased without a bound by increasing the number of antennas at the BS, [5].

The only limiting factor of the network capacity in the single-cell scenario is the number of MTs that has to be proportionally much smaller than the coherence time of the channel to facilitate accurate channel estimation, [5]. In addition to the aforementioned limitation, non-cooperative multi-cellular time-division duplex (TDD) networks suffer from the so called *pilot contamination* problem first reported by Jose et al., [6]. This is known as a major factor in limiting the capacity of such networks, [7]. A number of solutions have been proposed in the literature to attack the pilot contamination problem, [8–10]. However, such solutions are very complex or have certain requirements that may not be easy to satisfy, e.g., the need for eigenvalue analysis of the covariance matrix of the received signal or cooperation among cells.

New waveforms

OFDM has been adopted in many wired and wireless standards. However, it suffers from a number of shortcomings that limit its application to 5G networks. The limitations of OFDM are well documented. OFDM suffers from a large amount of out-of-band emissions that not only lead to interference issues but also limit its application to spectrum aggregation systems. In addition, OFDM is very sensitive to CFO which necessitates strict synchronization requirements. This, in turn, substantially increases the network overhead and thus latency. The situation gets worse in applications like M2M where a large number of devices need seamless connectivity and low latency. As noted earlier, the presence of multiple CFOs in such networks leads to an increased receiver complexity and one of the main advantages of OFDM which is its low complexity is lost. The challenge therefore, is to find waveforms with more relaxed synchronization needs, low latency and more localized signals in both time and frequency domains without the penalty of a more complex transceiver compared with that of OFDM. There are many candidate waveforms on the table that need to be put under the microscope for investigation, [11–15].

Filter bank multicarrier (FBMC) is a method that was initially proposed about 50 years ago, [16, 17], and is recently being considered as a candidate waveform for 5G systems, [11]. All the proposed signaling techniques for 5G are filter bank multicarrier (FBMC) systems that can be categorized into two groups; the ones with linear pulse shaping, [15, 18], and the ones with circular pulse shaping, [12–14]. The idea of FBMC systems with circular pulse shaping was first developed by Fettweis et al., [12], with the goal of removing the ramp-up and ramp-down of the conventional FBMC signals. The outcome from this work was a non-orthogonal waveform that is called generalized frequency division multiplexing (GFDM). In a more recent work, [14], Lin and Siohan applied a modification to GFDM which makes it orthogonal and thus removes the drawbacks of GFDM due to its non-orthogonality. While FBMC systems with linear pulse shaping was proposed long time ago, FBMC systems with circular pulse shaping has emerged only in 2009, [12]. Thus, the research on the latter is not matured and some of the main parts of the puzzle including computationally efficient transceiver structures providing the optimal performance are missing.

Since FBMC systems with circular pulse shaping are known to be a generalized version of OFDM, [19], they have the same properties as OFDM in massive MIMO channels. However, the impact of FBMC waveforms with linear pulse shaping and massive MIMO on each other is not clear. Accordingly, the following research questions are important to be addressed.

Question 2

- ***Given that massive MIMO and FBMC are suitable for serving a large number of users, what is the impact of these two forerunner technologies on each other?***

Question 3

- ***FBMC systems with circular pulse shaping have relaxed synchronization requirements which makes them suitable for applications like M2M. However, the existing transceiver structures for such systems are based on successive interference cancellation techniques which have the drawback of error propagation. Is it possible to design low complexity transceiver structures for such systems while providing the optimal performance?***

1.3 Contributions

For both contemporary and future multiuser systems, in this thesis, the aim is to serve a larger number of users and relax the synchronization requirements among the users in the network and in doing make significant advances over the performance of current systems. In answering the research questions that are raised in Sections 1.1 and 1.2, the following contributions have been made:

1. Contemporary multiuser systems (OFDMA-based uplink)

   - Low complexity MMSE and zero forcing (ZF) CFO correction techniques for interleaved and block interleaved carrier allocation schemes are developed. These techniques provide a complexity reduction over an order of magnitude compared with the solution in the literature known to have the lowest complexity. Additionally, the proposed solutions have a reasonable complexity for large numbers of users in the network.
   - A new class of low complexity CFO compensation techniques for the generalized carrier allocation scheme is developed. The complexity reduction in the proposed solutions is substantial when compared to the existing ones in the literature. Our solutions provide over two orders of magnitude complexity reduction compared to the solution in the literature known to have the lowest complexity. Furthermore, through application of these solutions, a large number of users can be served simultaneously with a low computational load.

2. Future multiuser systems

   - FBMC is applied to massive MIMO channels and it is shown that in such channels, FBMC can gain from the channel flattening effect and reduce the latency of the system due to the ramp-up and ramp-down period of its signals through widening the subcarriers in frequency domain and increasing the symbol rate. As the byproduct of this, we have more relaxed synchronization requirements, a lower peak to average power ratio (PAPR), a higher bandwidth efficiency and a more flexible carrier aggregation.
   - The frequency spreading equalization approach in massive MIMO is also investigated and it has shown that through this type of equalization, further subcarrier widening compared with the polyphase-based FBMC systems is possible.
   - Pilot contamination problem in multi-cellular TDD massive MIMO channels is addressed through development of a blind tracking method. Starting from the corrupted channel estimates, through running a number of iterations, this technique is capable of reaching an SINR performance the same as that of the MMSE solution. In the MMSE solution, it is assumed that the BS in each cell has the perfect knowledge about the channel state information of all the users in its own cell and the ones in the other cells.
   - A low complexity transceiver structure for GFDM is developed which provides a substantial complexity reduction compared with the existing structures that are known to have the lowest complexity.
   - A modified version of GFDM which makes the subcarriers orthogonal is compared with GFDM.
   - Sensitivity of 5G candidate waveforms to timing and frequency misalignment in uplink scenario is analyzed.

1.4 Structure of the thesis

The thesis is laid out as follows. Chapter 2 provides the basics of the building block technologies that are studied in the thesis as well as related literature reviews of each technology. Chapter 3 focuses on the first research question raised in Section 1.1 and therefore is concerned with contemporary multiuser systems and OFDMA. More specifically, it describes and analyses the CFO correction techniques developed for

the interleaved, block-interleaved and generalized carrier allocation schemes. Chapter 4 moves on to future multiuser systems and looks at the application of FMBC to massive MIMO channels to address the second research question raised in Section 1.2. In Chapter 4, the polyphase-based and frequency spreading FBMC systems are investigated and a pilot decontamination technique is designed. Chapter 5 focuses on the third research question of Section 1.2 and as a result, a low complexity transceiver structure is proposed for GFDM. Another waveform that is an orthogonal version of GFDM is analyzed and compared with GFDM. In addition, sensitivity of different contender waveforms proposed for 5G to synchronization errors is analyzed. Finally, Chapter 6 includes the concluding remarks based on the research questions that are asked in this thesis and their corresponding answers. It also provides a number of research directions that can be pursued in future studies.

1.5 Publications record and patents

The following publications relate directly to this thesis:

- **A. Farhang**, N. Marchetti, and L. Doyle, "Low complexity LS and MMSE based CFO compensation techniques for the uplink of OFDMA systems," in *Proc. of the IEEE ICC'13,* June 2013. [20]

- **A. Farhang**, A. Javid Majid, N. Marchetti, L. Doyle, and B. Farhang-Boroujeny, "Interference localization for uplink OFDMA systems in presence of CFOs," in *Proc. of the IEEE WCNC'14,* April 2013. [21]

- **A. Farhang**, N. Marchetti, L. Doyle, and B. Farhang-Boroujeny, "Filter bank multicarrier for massive MIMO," in *Proc. of the IEEE VTC-Fall,* September 2014. [22]

- **A. Farhang**, A. Aminjavaheri, N. Marchetti, L. Doyle, and B. Farhang-Boroujeny, "Pilot decontamination in CMT-based massive MIMO networks," in *Proc. of the ISWCS,* August 2014. [23]

- **A. Farhang**, N. Marchetti, F. Figueiredo, JP. Miranda, "Massive MIMO and waveform design for 5th generation wireless communication systems," in *Proc. of the 1st International Conference on 5G for Ubiquitous Connectivity,* November 2014. [24]

- **A. Farhang**, N. Marchetti, and L. Doyle, "Low complexity GFDM receiver design: A new approach," in *Proc. of the IEEE ICC'15,* June 2015. [25]

- A. Aminjavaheri, **A. Farhang**, N. Marchetti, L. Doyle, and B. Farhang-Boroujeny, "Frequency spreading equalization in multicarrier massive MIMO," in *Proc. of the IEEE ICC'15 Workshop on 5G and Beyond,* June 2015. [26]

- **A. Farhang**, N. Marchetti, L. Doyle, and B. Farhang-Boroujeny, "Low complexity CFO compensation in uplink OFDMA systems with receiver windowing," in IEEE Transactions on Signal Processing, 2015. [27]

- **A. Farhang**, N. Marchetti, and L. Doyle, "Low complexity transceiver design for GFDM," Submitted to IEEE Transactions on Signal Processing, 2015.

- A. Rezazadeh, **A. Farhang**, and B. Farhang-Boroujeny, "Circularly pulse-shaped waveforms for 5G: Options and comparisons," Accepted for presentation in IEEE Globecom 2015.

- A. Aminjavaheri, **A. Farhang**, A. Rezazadeh, and B. Farhang-Boroujeny, "Impact of Timing and Frequency Offsets on Multicarrier Waveform Candidates for 5G," in *Proc. of the IEEE Signal Processing and SP Education Workshop 2015 (SPW'15),* August 2015.

The following book chapter is prepared based on a part of research that is presented in this thesis:

- **A. Farhang**, N. Marchetti, and B. Farhang-Boroujeny, "Filter bank multicarrier for massive MIMO," appearing in book Signal Processing for 5G: Algorithms and Implementations, ***John Wiley and Sons***, 2015.

The following papers are outcome of collaboration with other researchers in other areas than the areas of interest to this thesis:

- A. Selim, **A. Farhang**, and L. Doyle, "Towards easier compliance with out-of-band emissions regulations," in *Proc. of the ICNC'14,* Feb 2014. [28]

- Z. Sharifian, M. J. Omidi, **A. Farhang** and H. Saeedi-Sourck, "Polynomial based compressing and iterative expanding for PAPR reduction in GFDM," in *Proc. of the ICEE'15,* May 2015. [29]

- H. Ahmadi, **A. Farhang**, N. Marchetti, and A. B. MacKenzie, "A game theoretical approach for pilot contamination avoidance in massive MIMO," Accepted for publication in IEEE Wireless Communication letters, 2015.

The following patent applications are filed as a result of the research that is conducted in this thesis:

- **A. Farhang**, "A method and system for compensating for interference due to carrier frequency offset in an OFDM communication system," United States patent application No. 14/484,845, September 2014.
- **A. Farhang**, "A generalized frequency division multiplexing transceiver," UK patent application No. 1417277.9, September 2014.

Chapter 2

Background

Due to the presence of multipath channels in wireless communication systems, the received signal at the receiver of single carrier systems experiences inter-symbol-interference (ISI), [30, 31]. Therefore, to compensate the effect of the wireless channel, efficient channel equalization techniques need to be utilized, [30]. Apart from their high computational complexity, single carrier channel equalizers may suffer from a great amount of noise enhancement. This is linked with the small channel gains over some portions of the frequency band as their inversion, in the equalization process, results in noise amplification for the whole data packet.

Hence, to tackle the multipath effects in a more efficient way than single carrier communications and simplify channel equalization, multicarrier modulation techniques can be utilized. The basic idea behind multicarrier modulation is to transmit N number of low-rate data streams over N frequency channels that are called *subcarriers*. In other words, a high-rate data stream is multiplexed into N low-rate substreams. This obviously simplifies equalization compared to the single carrier case, and delivers an N times faster symbol rate. To put it differently, the higher the symbol rate, the more vulnerability to the multipath effects. Accordingly, multicarrier modulation has resiliency to the multipath channel effects. In order to demultiplex and retrieve the transmitted data, the received signal is down-sampled using each subcarrier frequency and passed through the receiver filter. Fig. 2.1 depicts multicarrier modulation and demodulation. In Fig. 2.1, $s[n]$ is the high-rate data stream to be transmitted, the commutators on the left and right perform multiplexing and demultiplexing operations, respectively, the parameter L can be chosen equal to N or greater than N and f_i's for $i = 1, \ldots, N$ are the subcarrier center frequencies. $P_{\mathrm{T}}[n]$ and $P_{\mathrm{R}}[n]$ are the transmit and receive filters, respectively. The transmit and

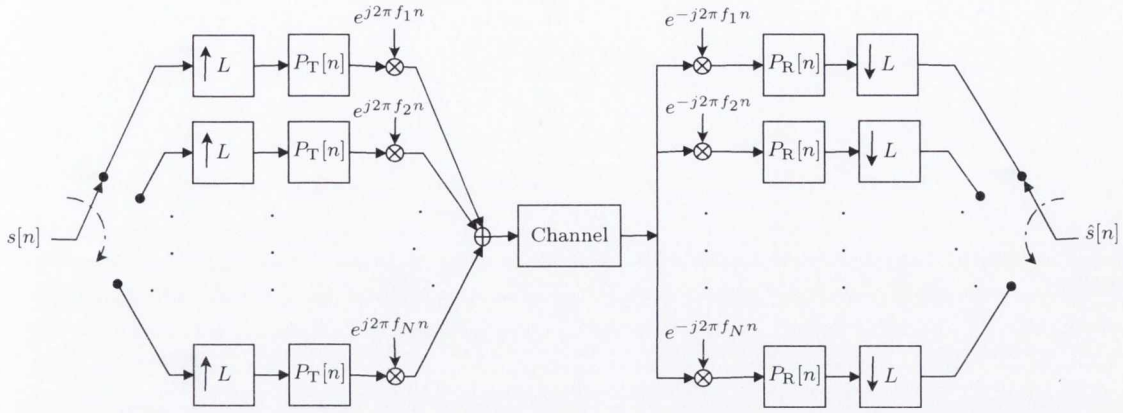

Fig. 2.1 Multicarrier communication transceiver block diagram.

receive filters can be designed in a way to have non-overlapping or overlapping subcarriers. The early frequency division multiplexing (FDM) systems spaced f_i's in a way to avoid any overlap among different subcarriers while using transmit and receive filters with sufficiently large stop band attenuation. However, these techniques are inefficient in utilization of the available spectrum. Hence, bandwidth efficiency can be improved by allowing some level of overlap among different subcarriers given the perfect timing and frequency synchronization of the transmit and receive signals.

A brief history of multicarrier modulation

The idea of multicarrier transmission dates back to around 1950s. In early multicarrier systems, the available bandwidth was divided into several non-overlapping frequency bands. A distinct data stream from the same source was transmitted over each frequency band. While no frequency overlapping between the bands reduces the amount of inter-channel-interference, those systems suffer from a great amount of bandwidth efficiency loss. The orthogonal multicarrier transmission was first introduced in the pioneering works of Chang in 1966, [16],[32] where he suggested the utilization of a bank of overlapping filters to transmit a set of pulse amplitude modulated (PAM) symbol sequences. In the late 1960s, some multicarrier modems for military applications were developed, [33], [34]. However, these modems had a very high hardware complexity as they were implemented based on using a bank of oscillators that were tuned on their corresponding subcarrier frequencies. Therefore, a great amount of research in those days was concentrated on digital multicarrier communications. Orthogonal frequency division multiplexing (OFDM) was introduced by Weinstein and Ebert in 1971, [35], where they proposed base band modulation

and demodulation through inverse discrete Fourier transform (IDFT) and discrete Fourier transform (DFT). To tackle the ISI problem due to the multipath channel, they introduced the concept of using a guard interval in the time domain. The idea of adding a cyclic extension to the OFDM signal was proposed in [36] which completed the missing part of the puzzle in OFDM systems to completely remove the ISI. Even though a substantial complexity reduction had been achieved in OFDM systems compared to other multicarrier techniques, hardware limitations made practical implementation of OFDM impossible and hence these systems were not taken seriously. The progress in hardware technology during 1990s made implementation of fast fourier transform (FFT) and consequently OFDM practically feasible. Since then, a great amount of research has been focused on OFDM systems and they were adopted in many wired and wireless systems; namely, asymmetric digital subscriber loop (ADSL), [37], power line communication systems [38], digital audio broadcasting (DAB), [39], terrestrial digital video broadcasting (DVB-T), [40], Wireless LAN, [41], WiMAX, [42], and 3GPP long term evolution (LTE) systems, [43]. To apply OFDM to multiuser systems, orthogonal frequency division multiple access (OFDMA) which combines frequency division multiple access (FDMA) with OFDM was proposed in [44]. The advancements that OFDM and OFDMA systems have made is due to their low complexity, simple implementation, simple applicability to multiple imput multiple output systems (MIMO) and high flexibility in resource management and dynamic channel assignment.

Another class of multicarrier systems is called filter bank multicarrier (FBMC) which was initially proposed by Chang in [32] and interestingly, it was proposed even before the first paper on OFDM. Bellanger showed that a great amount of complexity reduction in the digital implementation of FBMC through his proposed polyphase transceiver structure can be achieved, [45]. However, due to their high computational complexity, these systems were not as successful as the widely used OFDM systems in being adopted by the standards. They are currently adopted in the power line communication standard IEEE1901, [38] and TIA radio transmission standard, [46]. As it has been noticed in several publications, [2, 20, 21, 47], OFDMA has to deal with many challenges in more complex scenarios than point to point communications such as uplink and some emerging applications like *machine to machine* (M2M) communications and *Internet of Things* (IoT). As a case in point, OFDMA in the uplink of multiuser networks needs full synchronization among the users' signals that are received at the base station (BS). Otherwise, the low complexity benefit of OFDM will be lost and the receiver complexity will be substantially increased (by orders

of magnitude). In contrast, FBMC systems are shown to have a lower complexity than their OFDMA conterpart in the uplink scenario, [48]. Accordingly, multicarrier waveforms with a higher robustness against synchronization errors compared with OFDM have to be sought for the physical layer of the fifth generation of wireless communication systems (5G), [11, 49]. FBMC, as a candidate, has been recently in the center of attention and several implementations of these systems with interesting properties are proposed, [11, 50–54]. Another type of multicarrier modulation which can be thought as an FBMC system with circular pulse shaping rather than linear pulse shaping has recently stirred a great deal of attention among researchers. This idea was first initiated with the proposal of generalized frequency division multiplexing (GFDM), i.e., a non-orthogonal waveform, by Fettweis et al in 2009, [55]. Recently, Lin and Siohan have modified GFDM to preserve the orthogonality and hence avoid the performance loss that happens due to the non-orthogonality of the subcarriers [14, 56]. Another type of FBMC modulation with circular pulse shaping with non-overlapping subcarriers has also been recently introduced by Tonello in [57].

In the rest of this chapter, the merits and demerits of several technologies that are suitable for multiuser applications will be discussed. The mathematical foundation of each technology along with their corresponding system model will be presented. The structure of this chapter is organized as follows. In order to start, Section 2.1 is concentrated on the fundamentals of OFDM and OFDMA modulation schemes. In Section 2.2, OFDMA systems in the uplink are discussed. Since, in this thesis, FBMC is studied in the context of massive MIMO, i.e., a multiuser technique proposed for 5G, Sections 2.3 and 2.4 are dedicated to FBMC and massive MIMO, respectively. Finally, the basics of GFDM are presented in Section 2.4.

2.1 Fundamentals of OFDM/OFDMA modulation

OFDM is a multicarrier signaling technique that is based on orthogonal transmission of a number of data streams over N subcarriers. In OFDM, a high-rate data stream is divided into N low-rate substreams and each substream is up-converted to its corresponding subcarrier frequency. This operation can be performed by using an N-point IDFT operation to form the base band OFDM signal $\mathbf{x}[n]$.

$$\mathbf{x}[n] = \mathbf{F}_N^{\mathrm{H}}\mathbf{d}[n], \tag{2.1}$$

where $\mathbf{F}_N^{\mathrm{H}}$ is the N-point normalized IDFT matrix with the elements $[\mathbf{F}_N^{\mathrm{H}}]_{ik} = \frac{1}{\sqrt{N}} e^{\frac{j2\pi ik}{N}}$ for $i,k = 0,\ldots,N-1$, $\mathbf{d}[n] = [d_0[n],\ldots,d_{N-1}[n]]^{\mathrm{T}}$ are the complex data symbols and n is the OFDM symbol index. From (2.1), it can be understood that the OFDM signal is formed by summation of a number of tones that are modulated by data symbols, $d_i[n]$'s. This is due to the fact that $d_i[n]$'s each scale the i^{th} column of $\mathbf{F}_N^{\mathrm{H}}$ which contains the samples of the complex carrier frequency $\frac{2\pi i}{N}$. Finally, the resulting vectors will be added to each other to form the base band signal $\mathbf{x}[n]$. The subcarrier spacing in an OFDM system with N subcarriers is $\frac{2\pi}{N}$. If the $MN \times 1$ signal vector $\mathbf{x}$ which is comprised of M concatenated OFDM symbols is passed through the wireless channel with the base band impulse response $\mathbf{h}$ which is an $N_{\mathrm{ch}} \times 1$ vector, the resulting signal can be obtained as

$$\mathbf{y} = \mathbf{x} * \mathbf{h} + \boldsymbol{\nu}, \tag{2.2}$$

where $*$ is the linear convolution, $\boldsymbol{\nu}$ is the complex additive white Gaussian noise (AWGN) with the variance of ${\sigma_\nu}^2$ and the signal vector $\mathbf{y}$ has the length $MN + N_{\mathrm{ch}} - 1$. It is known that the resulting signal from convolution of $\mathbf{x}[n]$ and $\mathbf{h}$ has the length $N + N_{\mathrm{ch}} - 1$ and the extra $N_{\mathrm{ch}} - 1$ samples are due to the transient of the channel or the channel delay spread, [58]. Therefore, $N_{\mathrm{ch}} - 1$ samples from each OFDM symbol overlap with the adjacent symbols and $\mathbf{y}$ suffers from a great amount of ISI. In order to compensate this ISI, adaptive channel equalization techniques are needed. However, these techniques suffer from a high computational complexity. As mentioned earlier, a cyclic extension that is called cyclic prefix (CP) is added to the beginning of each OFDM symbol which absorbs the channel transient and converts the linear convolution in (2.2) to a circular one, [31]. This makes it possible to completely remove the channel imposed ISI in OFDM signals with a very low computational complexity. This property of OFDM has made it a very popular technique. It is worth mentioning that the CP length N_{CP} needs to be equal or larger than the channel transient, i.e., $N_{\mathrm{CP}} \geq N_{\mathrm{ch}} - 1$, to avoid ISI. CP addition at the transmitter can be mathematically shown as

$$\mathbf{x}_{\mathrm{CP}}[n] = \mathbf{T}_{CP}\mathbf{x}[n], \tag{2.3}$$

where $\mathbf{x}_{\mathrm{CP}}[n]$ is the cyclic prefixed OFDM symbol with the length $N_T = N + N_{\mathrm{CP}}$, $\mathbf{T}_{CP} = [\mathbf{G}_{CP}^{\mathrm{T}}, \mathbf{I}_N^{\mathrm{T}}]^{\mathrm{T}}$ is the CP addition matrix and $\mathbf{G}_{CP}$ is an $N_{\mathrm{CP}} \times N$ matrix containing the last N_{CP} rows of the identity matrix of size $N \times N$, $\mathbf{I}_N$. After passing a number

of concatenated OFDM symbols with CP through the channel $\mathbf{h} = [h_0, \ldots, h_{N_{\text{ch}}-1}]^{\text{T}}$, given perfect synchronization the received base band signal at symbol n, i.e., $\mathbf{r}_{\text{CP}}[n]$, can be written as

$$\mathbf{r}_{\text{CP}}[n] = \mathbf{H}_1\mathbf{x}_{\text{CP}}[n] + \mathbf{H}_2\mathbf{x}_{\text{CP}}[n-1] + \boldsymbol{\nu}, \tag{2.4}$$

where $\mathbf{H}_1$ and $\mathbf{H}_2$ are Toeplitz matrices of the size $N_T \times N_T$.

$$\mathbf{H}_1 = \begin{pmatrix} h_0 & 0 & 0 & \cdots & 0 \\ h_1 & h_0 & 0 & \cdots & 0 \\ \vdots & \vdots & \vdots & \ddots & \vdots \\ h_{N_{\text{ch}}-1} & h_{N_{\text{ch}}-2} & h_{N_{\text{ch}}-3} & \cdots & 0 \\ 0 & h_{N_{\text{ch}}-1} & h_{N_{\text{ch}}-2} & \cdots & 0 \\ \vdots & \vdots & \vdots & \ddots & \vdots \\ 0 & 0 & 0 & \cdots & h_0 \end{pmatrix}, \quad \mathbf{H}_2 = \begin{pmatrix} 0 & \cdots & h_1 & h_2 & \cdots & h_{N_{\text{ch}}-1} \\ 0 & \cdots & 0 & h_1 & \cdots & h_{N_{\text{ch}}-2} \\ \vdots & \ddots & \vdots & \vdots & \ddots & \vdots \\ 0 & \cdots & \cdots & \cdots & \cdots & h_1 \\ 0 & \cdots & \cdots & \cdots & \cdots & 0 \\ \vdots & \vdots & \vdots & \vdots & \ddots & \vdots \\ 0 & \cdots & \cdots & \cdots & \cdots & 0 \end{pmatrix}.$$

The term $\mathbf{H}_2\mathbf{x}_{\text{CP}}[n-1]$ in (2.4) causes the ISI between consecutive OFDM blocks which is added to the CP and will be eliminated after CP removal. CP removal operation can be performed by multiplication of the matrix $\mathbf{R}_{\text{CP}} = [\mathbf{0}_{N\times N_{\text{CP}}}, \mathbf{I}_N]$ to $\mathbf{r}_{\text{CP}}[n]$ where $\mathbf{0}_{N\times N_{\text{CP}}}$ is a zero matrix of the size $N \times N_{\text{CP}}$. Noting that $\mathbf{R}_{\text{CP}}\mathbf{H}_2 = \mathbf{0}_{N\times N_T}$, we have

$$\mathbf{r}[n] = \mathbf{R}_{\text{CP}}\mathbf{r}_{\text{CP}}[n] = \mathbf{R}_{\text{CP}}\mathbf{H}_1\mathbf{x}_{\text{CP}}[n] + \tilde{\boldsymbol{\nu}}, \tag{2.5}$$

where $\tilde{\boldsymbol{\nu}} = \mathbf{R}_{\text{CP}}\boldsymbol{\nu}$. Feeding the resulting signal from (2.5) into the DFT block, based on the results of equations (2.1) to (2.5) we have

$$\bar{\mathbf{r}}[n] = \mathbf{F}_N\{\mathbf{R}_{\text{CP}}\mathbf{H}_1\mathbf{T}_{\text{CP}}\}\mathbf{F}_N^{\text{H}}\mathbf{d}[n] + \mathbf{F}_N\tilde{\boldsymbol{\nu}} = \mathbf{F}_N\mathbf{H}\mathbf{F}_N^{\text{H}}\mathbf{d}[n] + \mathbf{F}_N\tilde{\boldsymbol{\nu}}, \tag{2.6}$$

where the matrix $\mathbf{H} = \mathbf{R}_{\text{CP}}\mathbf{H}_1\mathbf{T}_{\text{CP}}$ is circulant and hence the matrix $\boldsymbol{\mathcal{H}} = \mathbf{F}_N\mathbf{H}\mathbf{F}_N^{\text{H}}$ is diagonal with the diagonal elements $\sqrt{N}\mathbf{F}_N\tilde{\mathbf{h}}$ and $\tilde{\mathbf{h}} = [\mathbf{h}^{\text{T}}, \mathbf{0}_{1\times(N-N_{\text{ch}})}]^{\text{T}}$ is the first column of $\mathbf{H}$. Therefore, channel equalization can be performed by inverting the elements of the main diagonal of $\boldsymbol{\mathcal{H}}$ and the transmitted symbols can be estimated as

$$\hat{\mathbf{d}}[n] = \boldsymbol{\mathcal{H}}^{-1}\bar{\mathbf{r}}[n]. \tag{2.7}$$

As mentioned earlier, OFDMA is a multiple access technique that is a combination of OFDM and FDMA. In OFDMA, disjoint groups of subcarriers are allocated to different users based on different subcarrier allocation schemes that are going to be discussed in Section 2.1.1. The difference between OFDMA and OFDM lies in the

fact that each OFDMA symbol simultaneously carries information for different users while in OFDM, each super symbol contains the information of one specific user. From the physical layer viewpoint, OFDMA in the downlink is similar to point-to-point communication as the received signal at each mobile terminal is only affected by a single timing as well as frequency offset. Hence, we end up with the same situation as in OFDM where each user only extracts its corresponding subcarriers. In contrast, in OFDMA uplink transmission, different users' signals interfere with each other and create a great amount of multiple access interference (MAI). More detail on the uplink of OFDMA systems will be given in Section 2.2.

2.1.1 Subcarrier allocation in OFDMA systems

Considering an OFDMA system with the total number of N subcarriers with K users, we assume that the available spectrum is evenly assigned to all the users where each user gets $L = N/K$ subcarriers. The available subcarriers can be allocated to the users in different ways; namely, block carrier allocation scheme (B-CAS), interleaved carrier allocation scheme (I-CAS), block interleaved carrier allocation scheme (BI-CAS) and generalized carrier allocation scheme (G-CAS), [2]. Fig. 2.2 depicts these subcarrier allocation schemes for the case of $K = 4$ users. In Fig. 2.2 (a), a continuous fraction of the available spectrum is assigned to each user. However, this technique does not benefit from the multipath channel diversity as a deep fade can adversely affect a large number of the subcarriers belonging to a specific user. In contrast, in I-CAS where the allocated subcarriers to each user are equally spaced with the spacing of K, full channel diversity gain can be achieved. Fig. 2.2 (b) shows this scheme. Although this scheme can achieve full channel diversity gain, it becomes more sensitive to carrier frequency offset (CFO) in the uplink. Therefore, another carrier allocation scheme can be utilized where, as shown in Fig. 2.2 (c), different blocks of subcarriers belonging to different users can be interleaved. This technique is somewhere in between B-CAS and I-CAS and it is more robust to CFOs than I-CAS while still taking advantage of multipath diversity gain [59]. Due to the fact that in all the above techniques, different users' subcarriers need to be assigned based on a certain order, carrier assignment has some limitations and is not fully flexible. In order to enable dynamic resource allocation, the G-CAS technique can be utilized which does not assign the subcarriers based on any specific order (Fig. 2.2 (d)). Instead, the subcarriers can be allocated to the users based on their channel quality and thereby improve the overall performance of the network.

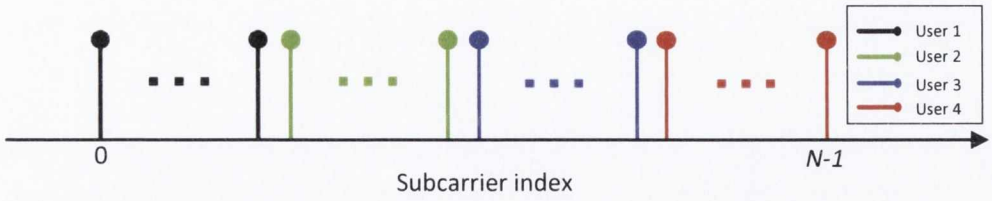

(a) Block subcarrier allocation.

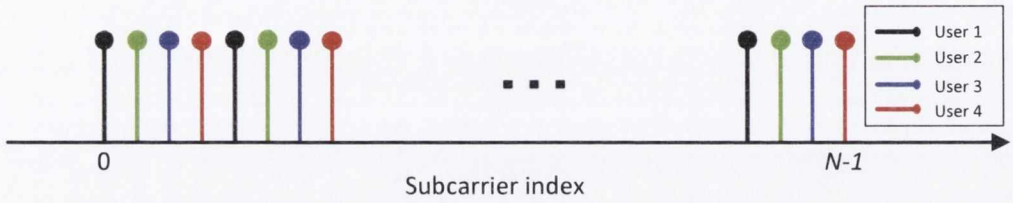

(b) Interleaved subcarrier allocation.

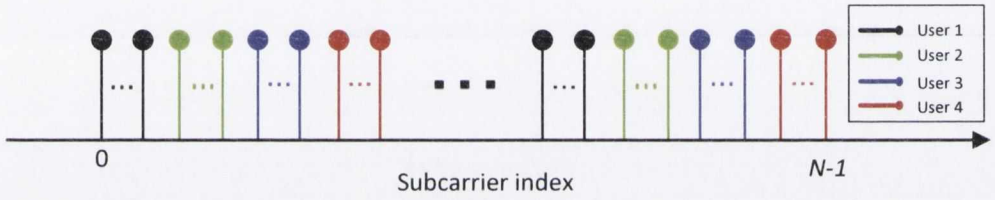

(c) Block interleaved subcarrier allocation.

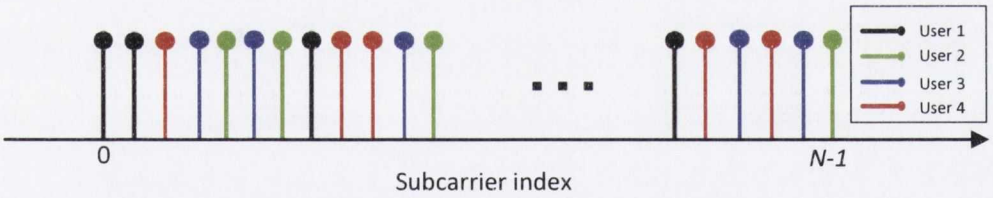

(d) Generalized subcarrier allocation.

Fig. 2.2 Different subcarrier allocation schemes in OFDMA systems.

2.2 OFDMA uplink

Consider the uplink of an OFDMA system where K users are communicating with the base station. The total number of subcarriers in each OFDMA symbol is assumed to be N which translates to $L = N/K$ subcarriers per user. The users are communicating with the base station through K statistically independent multipath wireless channels. To cover all the subcarrier assignment schemes, in this chapter, we consider G-CAS where the base station selects the best subcarriers for each user (i.e., the ones

with the best SNRs). The $L \times 1$ vector $\mathbf{d}^{(i)}[n]$ contains the data symbols of the i^{th} user. It is worth mentioning that the subcarriers of distinct users should be mapped onto mutually exclusive subsets of the available subcarriers. Hence, if the subcarriers allocated to the i^{th} and j^{th} users belong to the sets Ψ_i and Ψ_j, respectively, then $\Psi_i \cap \Psi_j = \emptyset, i \neq j$ and $\bigcup_{m=1}^{K} \Psi_m = \{0, \ldots, N-1\}$. In the OFDMA transmitter, the first step is subcarrier allocation. Thus, the i^{th} user signal vector after subcarrier mapping is

$$\mathbf{x}_{\mathrm{f}}^{(i)}[n] = \mathbf{\Gamma}_i \mathbf{d}^{(i)}[n], \tag{2.8}$$

where the subscript 'f' in $\mathbf{x}_{\mathrm{f}}^{(i)}[n]$ stresses that the data is in the frequency domain and $\mathbf{\Gamma}_i$ is the $N \times L$ subcarrier allocation matrix of user i. $\mathbf{\Gamma}_i$ is comprised of the columns of an $N \times N$ identity matrix whose indices belong to the set Ψ_i. Recalling (2.3), the OFDM modulator output for the n^{th} symbol of user i is given by

$$\mathbf{x}_{\mathrm{CP}}^{(i)}[n] = \mathbf{T}_{\mathrm{CP}} \mathbf{F}_N^{\mathrm{H}} \mathbf{x}_{\mathrm{f}}^{(i)}[n]. \tag{2.9}$$

In order to avoid self and multi-user interference due to the timing offsets of the users, the CP needs to be longer than both the maximum channel delay spread and the two way propagation delay. The residual timing errors between users will be incorporated in their channel impulse responses; thereby, ISI between the users' signals will be avoided [2].

The wireless channels for different users are assumed to be statistically independent with respect to each other and time invariant during one OFDMA symbol. If the channel impulse response of the users has the maximum length equal to N_{ch} samples, for user i, it can be denoted by the vector $\mathbf{h}^{(i)} = [h_0^{(i)}, \ldots, h_{N_{\mathrm{ch}}-1}^{(i)}]^{\mathrm{T}}$ whose elements are assumed to be statistically independent complex Gaussian random variables. Considering the impact of CFOs from different users, the n^{th} OFDMA symbol that is received at the base station can be written as

$$\tilde{\mathbf{r}}[n] = \sum_{i=1}^{K} e^{\frac{j2\pi\epsilon_i n N_{\mathrm{T}}}{N}} \mathbf{\Phi}(\epsilon_i)(\mathbf{h}^{(i)} * \mathbf{x}_{\mathrm{CP}}^{(i)}[n]) + \boldsymbol{\nu}, \tag{2.10}$$

where $\mathbf{\Phi}(\epsilon_i)$ is the $N_{\mathrm{r}} \times N_{\mathrm{r}}$ diagonal CFO matrix whose diagonal elements are equal to $\{1, e^{\frac{j2\pi\epsilon_i}{N}}, \ldots, e^{\frac{j2\pi\epsilon_i(N_{\mathrm{r}}-1)}{N}}\}$, $N_{\mathrm{r}} = N_T + N_{\mathrm{ch}} - 1$ and ϵ_i is the i^{th} user's CFO normalized by subcarrier spacing. Finally, $\boldsymbol{\nu}$ is the complex additive white Gaussian noise (AWGN) vector, i.e., $\boldsymbol{\nu} \sim \mathcal{CN}(0, {\sigma_\nu}^2 \mathbf{I}_{N_{\mathrm{r}}})$ and ${\sigma_\nu}^2$ is the noise variance.

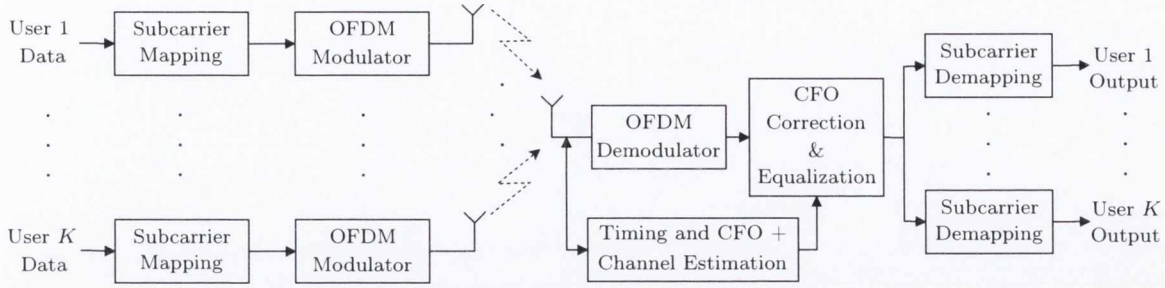

Fig. 2.3 OFDMA uplink communication.

Once the base station receives the signal $\tilde{\mathbf{r}}[n]$, the CFOs of different users as well as their channel responses need to be estimated first. Then the CP samples are discarded and the resulting signal is passed through the DFT block. The next steps are correction of multiple CFOs, channel equalization and finally, different users' subcarriers are demapped and the estimation of the users' transmitted symbols is obtained. This procedure is depicted in Fig. 2.3. In the following Subsections, different CFO estimation and correction techniques will be briefly discussed. Since, one of the main areas of focus in this thesis is multiple CFO correction or in other words MAI removal, more attention is dedicated to this area.

2.2.1 Timing and carrier frequency offset estimation

Synchronization in the uplink of multiuser systems is a complicated procedure and is completely different from the downlink scenario where the received signal is affected only by a single timing and frequency offset. The received uplink signal at the base station is a mixture of multiple users' signals and is characterized by multiple timing and frequency offsets that need to be estimated by the base station. The CFOs cannot surpass $\pm 50\%$ of the normalized subcarrier spacing and thus they need to be brought into a reasonable range before transmission. Therefore, the first step of the uplink synchronization starts from uplink transmission as each user needs to precompensate its own CFO. It is worth mentioning that different techniques are needed for different subcarrier allocation schemes.

B-CAS simplifies synchronization to a large extent as the subbands that are allocated to different users can be separated by utilization of a bank of filters and then single user detection (SUD) methods like the ones that are proposed for the downlink can be used, [2]. Some SUD methods exploit the correlation that is induced by CP to estimate different users' timing and frequency offsets, [60, 61]. Some other methods work based on balancing the energy of the null subcarriers for CFO estimation, [62].

In contrast to B-CAS, in I-CAS, filtering the signals of different users is not possible any more as the level of overlap between different users subcarriers due to the CFOs is large. However, due to the fact that in I-CAS, subcarriers of each user are uniformly spread over the whole band, some periodicity is present in the uplink signal which can be exploited for CFO estimation. From such techniques, we can name [63, 64] which take a similar approach to the MUltiple SIgnal Classification (MUSIC) algorithm, [65], and [66] where the authors used estimation of signal parameters via the rotational invariance technique (ESPRIT) algorithm, [67], to estimate the CFOs. It is worth mentioning that the CFO estimation techniques for I-CAS are blind and do not need transmission of any training signal.

The situation becomes even worse in G-CAS as the placement of the users' subcarriers is not based on any particular structure. One of the early CFO estimation techniques for G-CAS is a maximum likelihood (ML) technique that would sequentially estimate the CFOs of the users at the time of their arrival to the network, [68]. The problem of this techniqe is that whenever a user enters the uplink communication, the CFOs of all the other users need to be estimated and their subcarriers need to be aligned. This requirement sounds infeasible in practice. Thus, alternative ML techniques are proposed in [69] and [70] which enable simultaneous estimation of the channel responses as well as CFOs. A minimum mean square error (MMSE) technique with a much lower complexity than the previously proposed techniques was developed in [3] and it was further modified in [4] to find the channel as well as CFO estimates. In order to improve the bandwidth efficiency, in more recent works, [71–73], some authors have proposed CFO estimation techniques that use scattered pilots rather than the need for transmission of full training signals where all the subcarriers are used for training.

2.2.2 Carrier frequency offset correction

The MAI and self-interference due to the timing misalignment of the users' signals in the uplink can be counteracted by the choice of an adequately long CP resulting in a quasi-synchronous system[1] where the residual timing error of each user will appear in its channel impulse response as a phase factor which will be compensated for in the equalization stage [2]. Thus, we only focus on self-interference and MAI removal due to the CFOs for the rest of this section.

[1] In a quasi-synchronous system, all the received users' signals at the base station are aligned in time within the CP.

After the CFOs are estimated, orthogonality among all the subcarriers need to be recovered. CFO correction in the uplink is not as simple as it is in downlink. In the downlink, the orthogonality of the subcarriers can be restored simply by circular counter rotation of the subcarriers with the value $\frac{2\pi\epsilon}{N}$ where ϵ is the normalized CFO with respect to the subcarrier spacing. This operation is done by multiplication of an exponential signal with the angular frequency of $\frac{2\pi\epsilon}{N}$ to the time domain signal. However, in the uplink case, correction of one user's CFO, in the same way as in downlink, leads to further misalignment of different users' signals. This is due to the fact that the received signal in the uplink not only suffers from self-user interference but it also suffers from a large amount of MAI. Accordingly, other methods than those used in the downlink are needed for the uplink CFO correction. Different CFO correction techniques have been proposed in the literature for various carrier assignment schemes.

As mentioned earlier, the main feature of B-CAS is that the signals of different users can be separated through a bank of filters and therefore, the CFOs of the users can be compensated separately. However, this technique which can be categorized as an SUD technique, has some problems. First of all, complete separation of the users' signals is not possible and some MAI remains in the filtered signal. This is based on the fact that a large amount of leakage remains in the subcarriers that are located at the edges of each subcarrier block even after filtering. Secondly, one large DFT block of size N per user is needed which is not desirable. To reduce the complexity of this approach, some researchers have introduced a method which uses only one DFT block of size N along with frequency domain filtering to separate the users subcarriers and CFO correction through circular convolution, [74]. This procedure can be mathematically written as

$$\bar{\mathbf{r}}_i[n] = \mathbf{\Pi}_i \mathbf{C}(-\epsilon_i)\mathbf{\Pi}_i \bar{\mathbf{r}}[n], \quad \text{for } i = 1, \ldots, K, \tag{2.11}$$

where $\bar{\mathbf{r}}[n] = \mathbf{F}_N \mathbf{R}_{\text{CP}} \tilde{\mathbf{r}}[n]$, $\mathbf{\Pi}_i = \mathbf{\Gamma}_i \mathbf{\Gamma}_i^{\text{H}}$ is an $N \times N$ diagonal matrix with non-zero diagonal elements located at the positions of the corresponding subcarriers to user i and $\mathbf{C}(-\epsilon_i)$ is a circulant matrix whose first column includes the output of N-point DFT of the sequence $\{1, e^{-\frac{j2\pi\epsilon_i}{N}}, \ldots, e^{-\frac{j2\pi\epsilon_i(N-1)}{N}}\}$. Multiplication of the matrix $\mathbf{\Pi}_i$ to the output of the DFT block after CP removal can be thought as filtering operation in the frequency domain which separates the signal of each user from the others. $\bar{\mathbf{r}}_i[n]$ is the estimated signal of the i^{th} user that is scaled by the user's channel and the complex phase of $e^{\frac{j2\pi\epsilon_i n N_{\text{T}}}{N}}$. However, this solution suffers from MAI that

results in performance degradation. In addition, performance degradation due to the MAI becomes even more severe in subcarrier allocation schemes other than B-CAS. Therefore, other CFO correction schemes were developed which can be categorized into interference cancellation and linear multiuser detection techniques. It is worth mentioning that our main focus in this thesis is on the latter, which is discussed in Section 2.2.2.2.

2.2.2.1 Interference cancellation techniques

The idea of interference cancellation techniques is to generate the MAI and to subtract it from the received signal based on the tentatively detected signals of the users in an iterative manner. For instance, in [75], the authors apply the interference cancellation concept to the solution that was proposed in [74]. They use (2.11) to initialize their algorithm. Then, in each iteration, they use $\bar{\mathbf{r}}_i^{(j-1)}[n]$'s, i.e., the results from the previous iteration, to generate the interference to a given user from all the other ones and subtract the result from $\bar{\mathbf{r}}[n]$. This process can be mathematically shown as

$$\breve{\mathbf{r}}_i^{(j)}[n] = \bar{\mathbf{r}}[n] - \sum_{\substack{m=1 \\ m \neq i}}^{K} \mathbf{C}(\epsilon_i)\bar{\mathbf{r}}_m^{(j-1)}[n], \quad \text{for } i = 1, \ldots, K. \tag{2.12}$$

Then, the CFOs can be compensated using (2.11),

$$\bar{\mathbf{r}}_i^{(j)}[n] = \mathbf{\Pi}_i \mathbf{C}(-\epsilon_i)\mathbf{\Pi}_i \breve{\mathbf{r}}_i^{(j)}[n], \quad \text{for } i = 1, \ldots, K. \tag{2.13}$$

This technique was discussed in B-CAS and I-CAS scenarios in [75] and based on the results that are presented there, it leads to a great amount of performance improvement compared with [74]. This study is extended by Chen et al in [76] where they suggest a joint minimum mean square error frequency domain equalization (MMSE-FDE) and CFO compensation technique with interference cancellation.

In [77], the authors propose an interference cancellation method that is applicable to B-CAS. They formulate the self-user interference in terms of a linear system of equations for the block of subcarriers with the highest interference power and then generate the MAI that is caused by that block to the rest of the subcarriers and successively remove it from them. In the second step, the block with the second largest interference power is chosen, its self-user interference is compensated in the same fashion as the previous step and then the MAI from that block to the rest of the subcarriers is generated and removed. This process continues successively until

all the subcarrier blocks are processed. Ahmed and Zhang, [78], suggest a method of preconditioning the received signal vector, before applying the DFT, in order to limit the interfering subcarriers to a few adjacent ones. This preconditioning reduces the complexity of successive interference cancellation. This method was originally introduced by Schniter, [79], in the context of single user OFDM systems with time varying channels.

In [80] and [81], the authors propose time domain MAI cancellation techniques applicable to B-CAS and I-CAS. These techniques require a separate OFDM demodulator per user. The idea behind using one OFDM demodulator per user is to counter rotate the samples of each user in time domain with the angular frequency of $\frac{2\pi\epsilon_i}{N}$ where ϵ_i is the normalized CFO of the corresponding user with respect to subcarrier spacing and remove the self-user interference. Then, the resulting signal is passed through the OFDM demodulator, the subcarriers of the corresponding user are decoded and used to generate the time domain signal of user i for subtraction from the received signal in the input of the other OFDM demodulators. Another time domain MAI compensation technique is proposed in [82] where the CFOs are compensated based on the same approach as in [80] and [81] before the DFT block, then a multistage parallel interference cancellation is performed in the frequency domain with weighted MAIs where the weights are optimized in a way to maximize the output signal-to-interference ratio (SIR). The need for multiple OFDM demodulators obviously is a disadvantage to these techniques since, their complexity substantially grows as the number of users increases. In addition, as the normalized CFOs with respect to subcarrier spacing exceed 0.25%, they suffer from a severe performance degradation.

Accordingly, a drawback of the interference cancellation solutions is that their performance degrades as CFOs increase [75–78, 80–82]. Besides their high computational complexity, such methods may suffer from the error propagation problem, since wrong decisions may be fed back for cancellation. Finally, these solutions are limited to particular carrier allocation schemes while the general trend in CFO compensation is towards proposal of techniques that are applicable to the generalized carrier allocation scheme.

2.2.2.2 Zero forcing and minimum mean square error CFO correction

Another class of CFO correction techniques that are of more interest to this thesis are based on linear multiuser detection. In these techniques, the effect of the CFOs

is translated into a linear system of equations with a coefficient matrix that is called *interference matrix*. It is worth mentioning that a single OFDM demodulator is needed in this class of CFO compensators. The output of the DFT block at the base station is modeled as the multiplication of the interference matrix to a composite data vector that contains the data of all the users, affected by their wireless channels. Solving this system of equations eliminates the MAI as well as self-user interference completely. However, it needs the inversion of an interference matrix, i.e., a square matrix of size equal to the total number of subcarriers which can be as large as a few thousands in practical systems. Obviously, this makes the solution prohibitively complex. Thus, low complexity solutions have to be sought. To this end, a number of solutions have been proposed by several researchers that will be discussed in the following paragraphs.

In [83], Cao et al formulated the received uplink signal at the output of the OFDM demodulator as

$$\begin{aligned}\bar{\mathbf{r}}[n] &= \mathbf{F}_N\mathbf{R}_{\mathrm{CP}}\tilde{\mathbf{r}}[n] = \sum_{i=1}^{K}\mathbf{F}_N\tilde{\mathbf{\Phi}}(\epsilon_i)\mathbf{F}_N^{\mathrm{H}}\mathbf{H}_{\mathrm{f}}^{(i)}\mathbf{x}_{\mathrm{f}}^{(i)}[n] + \mathbf{F}_N\mathbf{R}_{\mathrm{CP}}\boldsymbol{\nu} \\ &= \mathbf{\Lambda}\mathbf{z}[n] + \mathbf{F}_N\mathbf{R}_{\mathrm{CP}}\boldsymbol{\nu}, \end{aligned} \tag{2.14}$$

where

$$\mathbf{z}[n] = \sum_{i=1}^{K}\mathbf{H}_{\mathrm{f}}^{(i)}\mathbf{x}_{\mathrm{f}}^{(i)}[n] = \bar{\mathbf{H}}_{\mathrm{f}}\mathbf{d}[n], \tag{2.15}$$

and

$$\mathbf{\Lambda} = \sum_{i=1}^{K}\mathbf{F}_N\tilde{\mathbf{\Phi}}(\epsilon_i)\mathbf{F}_N^{\mathrm{H}}\mathbf{\Pi}_i, \tag{2.16}$$

is the $N\times N$ interference matrix. The $N\times N$ diagonal matrix $\bar{\mathbf{H}}_{\mathrm{f}}$ contains the composite channel frequency responses of all the users in its diagonal elements. It is worth noting that the phase rotations that are caused by the CFOs in different symbols, $e^{\frac{j2\pi\epsilon_i nN_{\mathrm{T}}}{N}}$, are absorbed to the corresponding users' channel gains. The composite data vector $\mathbf{d}[n]$ includes the information symbols of all the users at their corresponding subcarrier positions as if there has been no interference. $\tilde{\mathbf{\Phi}}(\epsilon_i)$ is the $N\times N$ diagonal CFO matrix whose diagonal elements are $\{1, e^{\frac{j2\pi\epsilon_i}{N}}, \ldots, e^{\frac{j2\pi\epsilon_i(N-1)}{N}}\}$ where ϵ_i is the i^{th} user's CFO normalized by subcarrier spacing and $|\epsilon_i| < 0.5$. Therefore, the matrix $\mathbf{F}_N\tilde{\mathbf{\Phi}}(\epsilon_i)\mathbf{F}_N^{\mathrm{H}}$ is circulant with the first column $[f_N(\epsilon_i), f_N(\epsilon_i-1), \ldots, f_N(\epsilon_i-N+1)]^{\mathrm{T}}$ where $f_N(x) = \frac{\sin(\pi x)}{N\sin(\frac{\pi x}{N})}e^{j\pi x(1-\frac{1}{N})}$. The matrix $\mathbf{\Pi}_i$ chooses the columns of $\mathbf{F}_N\tilde{\mathbf{\Phi}}(\epsilon_i)\mathbf{F}_N^{\mathrm{H}}$ that are associated with the subcarrier indices of the user i. This is due to the fact

that $\mathbf{\Pi}_i$ is a diagonal matrix with only non-zero elements at the positions belonging to the subcarrier set of the i^{th} user, Ψ_i.

Based on the system model in (2.14), the assumption of having perfect knowledge of all the users' CFOs at the base station and due to the fact that the interference matrix is full rank, [83], both the self-user interference and MAI can be completely removed by direct inversion and multiplication of the interference matrix to the received signal samples at the DFT output. This solution is called zero forcing (ZF) solution and can be written as

$$\hat{\mathbf{z}}_{\text{ZF}}[n] = \mathbf{\Lambda}^{-1}\bar{\mathbf{r}}[n] = \mathbf{z}[n] + \mathbf{\Lambda}^{-1}\mathbf{F}_N\mathbf{R}_{\text{CP}}\boldsymbol{\nu}. \tag{2.17}$$

Although this solution completely eliminates both the inter-carrier-interference (ICI) and MAI, multiplication of $\mathbf{\Lambda}^{-1}$ to the noise vector may result in some noise amplification which can be taken care of by application of the MMSE solution for CFO compensation, i.e.,

$$\hat{\mathbf{z}}_{\text{MMSE}}[n] = (\mathbf{\Lambda}^{\text{H}}\mathbf{\Lambda} + {\sigma_\nu}^2\mathbf{I}_N)^{-1}\mathbf{\Lambda}^{\text{H}}\bar{\mathbf{r}}[n], \tag{2.18}$$

where $\mathbf{I}_N$ is the identity matrix of size $N \times N$. However, direct inversion of $N \times N$ matrices in (2.17) and (2.18) demands a very high amount of computations when N becomes very large which is the case in most of the current wireless standards. As a case in point, in the WiMAX standard IEEE 802.16e and 3GPP LTE standard N can be as large as 2048, [42, 43]. Hence, the necessity for development of low complexity ZF and MMSE techniques was stressed by Cao et al in [83]. To this end, they approximated the interference matrix by a banded matrix, simply by assuming that the elements of the matrix outside a bandwidth D (a design parameter) are equal to zero. It is then noted that this approximation of the interference matrix can be used to find the desired solution with a low computational complexity that is in the order of ND^2. Even though this technique has a low complexity and is applicable to G-CAS, approximation of the interference matrix with a banded one results in a significant performance loss, hence, may not be a viable solution in practice.

In [84], Huang et al have proposed an iterative CFO correction technique based on the Neumann power series expansion. However, it has been noted that this method has certain limitations in terms of carrier allocation. A low complexity ZF technique that is only applicable to I-CAS was proposed by Hsu and Wu in [85], where they use Newton's method to solve the matrix inversion problem in an iterative manner. In

this solution, the authors take advantage of the special structure of the interference matrix in I-CAS case to reduce the computational burden of the matrix inversion by using FFT algorithm. In a more recent work, [86], Lee et al introduced an MMSE compensation technique using conjugate gradient (CG) algorithm. This method has a much lower complexity compared to its predecessors and is also applicable to the systems that use the generalized carrier allocation scheme, while maintaining the optimal performance. It is worth mentioning that CG algorithm is a fast implementation of MMSE solution and provides the same result as the direct MMSE solution [86]. In [47], the same authors extended their previous work by proposing a preconditioned CG algorithm.

Summary of contributions

The contribution of this thesis in the area of uplink CFO correction is the development of several low complexity algorithms that address the drawbacks of the previously proposed algorithms in terms of limitations on the range of CFOs, limitation to particular carrier allocations and computational complexity with respect to the number of subcarriers and/or the number of users. Therefore, the challenge in this thesis is to propose CFO correction techniques that:

1. ***Are applicable to a wide range of CFOs.***
2. ***Have a lower computational complexity compared to the existing solutions in the literature.***
3. ***Are applicable to all the carrier allocation schemes.***

My contributions in this area are presented in Chapter 3.

While OFDM has served us well, its high sensitivity to synchronization errors and its high out of band emissions brings some limitations to its application to multiuser scenarios. Thus, the need for more robust waveforms to synchronization errors having a better spectral containment than OFDM has been recently emphasized, [11]. In applications like M2M communications, a large number of users need to be served while the available time-frequency resources may not be sufficient. In conventional multiuser networks, each subset of subcarriers can be allocated only to one user. To

increase the capacity of multiuser networks and serve a large number of users, a new multiuser technique that is called massive MIMO is proposed. In the current literature on massive MIMO, OFDM is used. Accordingly, to remove the limitations of OFDM and at the same time serve a large number of users in a wide range of applications those from bursty M2M communications to media-rich bandwidth thirsty systems, in this thesis, we study FBMC in the context of massive MIMO systems. Therefore, FBMC and massive MIMO systems are discussed in Sections 2.3 and 2.4.

2.3 Filter bank multicarrier

FBMC is a multicarrier modulation technique that was proposed about 50 years ago [16, 17], and is recently being considered as a candidate waveform for 5G networks, [11, 49]. Based on the requirements of 5G systems, waveforms with better spectral properties than OFDM are required in order to remove the tight synchronization constraints of OFDM and also enable some new applications like M2M communication and IoT. FBMC can naturally achieve these requirements thanks to its very well shaped subcarriers in the frequency domain.

Three types of FBMC systems with linear filtering exist; namely, OFDM-OQAM with OQAM standing for offset quadrature amplitude modulation that is due to the fact that the quadrature and in-phase components of the QAM symbol have a time offset with respect to each other, cosine modulated multitone (CMT) and filtered multitone (FMT). In some literature, the term staggered multitone (SMT) is used to refer to OFDM-OQAM where the word 'staggered' reflects the fact that the quadrature and in-phase parts of the QAM symbol are time staggered. From now on, we refer to OFDM-OQAM by the name SMT.

Fig. 2.4 shows the magnitude response of the pulse-shaping filters at different subcarrier positions for various types of FBMC systems. As one may realize, SMT and CMT are more bandwidth efficient than the FMT system as their subcarriers are allowed to overlap. The idea of FMT is based on the conventional FDM systems. In these systems, ICI is avoided through using filters with a very large stop-band attenuation. ISI is taken care of by using square-root Nyquist filters at both transmitter and receiver in the same way as in single-carrier modulation, [31]. In this thesis, we are more interested in the FBMC systems with the highest bandwidth efficiency and thus, we do not look into FMT systems.

Based on the results of [87], it can be proven that SMT and CMT are the same systems in essence. Therefore, as the derivations and explanations in the context

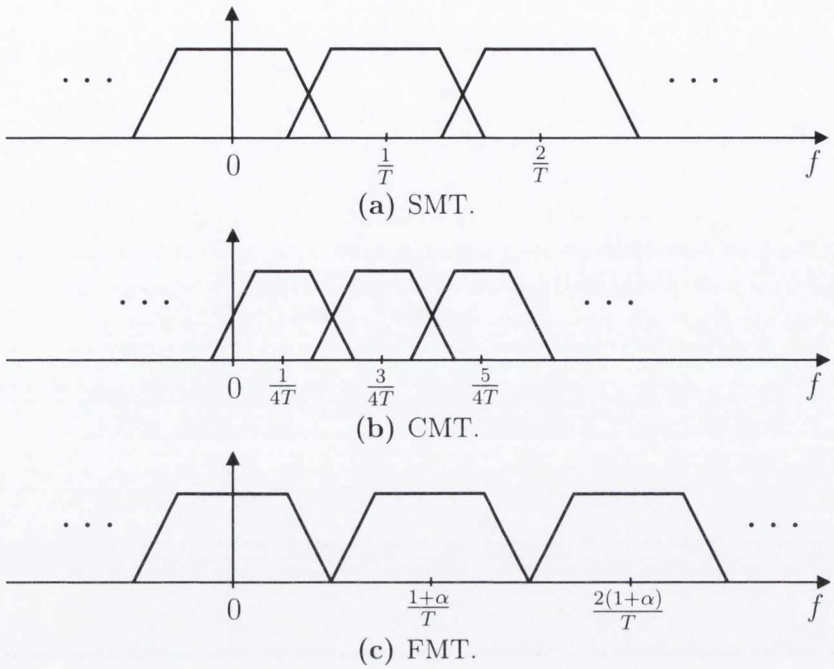

(a) SMT.

(b) CMT.

(c) FMT.

Fig. 2.4 Magnitude response of FBMC pulse-shaping filters at different subcarriers.

of CMT are easier to follow, we only focus on these systems. In CMT, the data symbols, that are chosen from a pulse amplitude modulation (PAM) constellation, are distributed in the time-frequency plane with the density of two symbols per unit time-frequency area that is equivalent to a complex data symbol. From Fig. 2.4 (b), it can be understood that in CMT, only adjacent subcarriers overlap. In order to allow separation of the data symbols (free of ISI and ICI), at the receiver, the carrier phase among adjacent subcarriers is toggled between 0 and $\pi/2$. The aforementioned concepts are visualized in Fig. 2.5 where the carrier phases are color mapped with red for $\pi/2$ and green for 0. After application of the relevant carrier phases to the PAM data symbols, they are modulated through vestigial side-band (VSB) modulation with the subcarrier spacing of $1/2T$ where T is the FBMC symbol duration and placed at different subcarrier positions in the frequency domain. Fig. 2.6 represents the VSB modulation and up-conversion of the PAM data streams to their corresponding subcarrier frequencies. The pulse-shaping and matched filters that are used at the transmitter and the receiver, respectively, are square-root Nyquist filters and their convolution leads to a Nyquist pulse with zero-crossings that are located at multiples of $2T$ in time domain. In addition, the pulse-shaping filter is designed to be an even and real-valued function of time. All the above conditions on the data symbols and

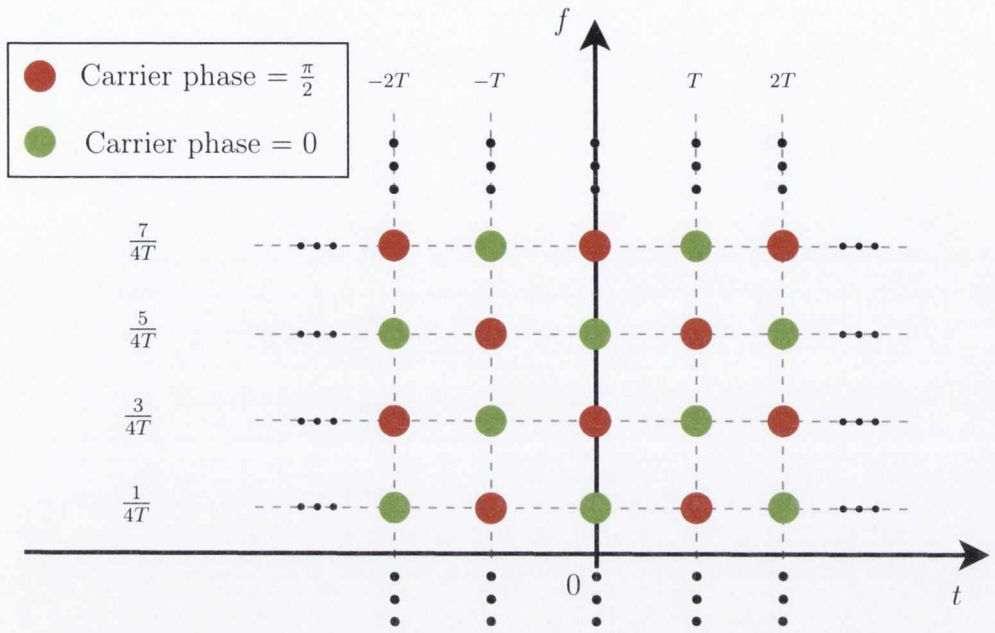

Fig. 2.5 Time-frequency phase-space lattice representation of CMT symbols.

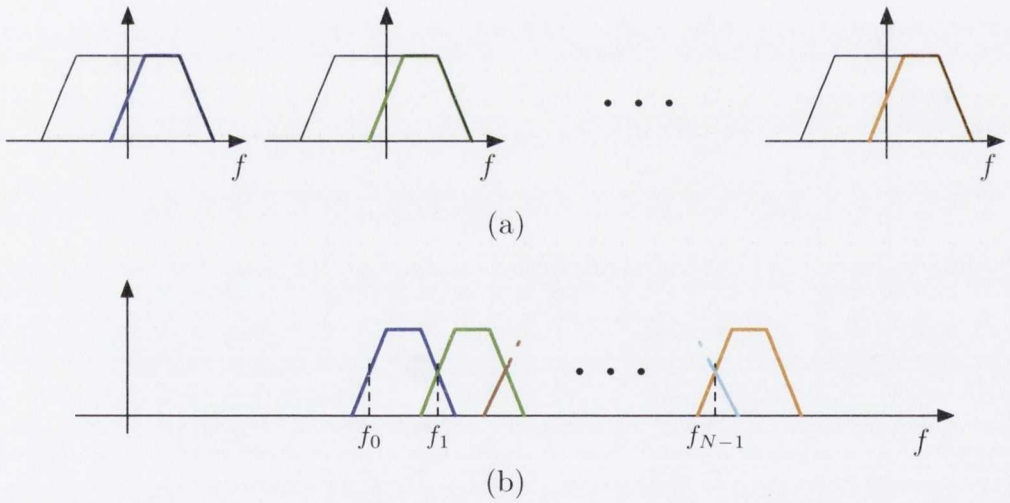

Fig. 2.6 CMT modulation. (a) Spectra of baseband data streams (black) and VSB portion of each (other colors). (b) CMT spectrum consisting of modulated versions of the VSB spectra of the baseband data streams. VSB signals are modulated to the subcarrier frequencies $f_0, f_1, \cdots, f_{N-1}$.

filters are necessary to guarantee the ISI and ICI free communication based on CMT. More details on these conditions can be found in [16, 31, 87].

Demodulation of each subcarrier in CMT is a four step procedure.

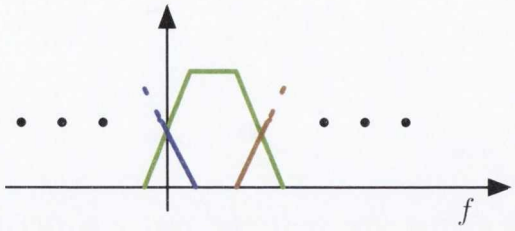

Fig. 2.7 Spectrum of a subcarrier in a CMT system after demodulation to baseband, but before matched filtering. Note that interference from the remaining subcarriers is present. Most of such interference will be removed after matched filtering, but still some residual interference from adjacent subcarriers (those at the corners of the transmission band, i.e., the blue and brown parts) will remain.

1. For each subcarrier, say, the k^{th} one, the received signal is down-converted to the baseband using f_k as the carrier frequency. This results in a spectrum similar to the one presented in Fig. 2.7.

2. The demodulated signal is passed through a matched filter that extracts the desired VSB signal at the baseband. The matched filter removes most of the signal spectra from other subcarriers. However, as may be understood from Fig. 2.7, some residuals of adjacent subcarriers remain.

3. The channel effect is removed from the demodulated signal using a complex-valued single tap equalizer. This is based on the assumption that each subcarrier band is sufficiently narrow such that it can be approximated by a flat gain. A multi-tap equalizer may be adopted if this approximation is not valid.

4. After equalization, the real part of VSB signal contains the desired PAM symbol only. Its imaginary part consists of a mix of ISI components and ICI components from the two adjacent bands. Accordingly, taking the real part of the equalized VSB signal delivers the desired data signal/symbol, free of ISI and ICI.

The CMT signal can be mathematically constructed based on

$$x(t) = \sum_n \sum_i e^{j(i-n)\frac{\pi}{2}} s_i[n] \mathcal{P}_{n,i}(t), \tag{2.19}$$

where $s_i[n]$ is the data symbol to be mapped to the position of the n^{th} symbol and i^{th} subcarrier in the time-frequency lattice, $e^{j(i-n)\frac{\pi}{2}}$ realizes the phase toggle to each of the points on the lattice and $\mathcal{P}_{n,i}(t) = \mathcal{P}(t - nT)e^{j\frac{(2i+1)\pi}{2T}t}$ in which $\mathcal{P}(t)$ is the

pulse-shaping or prototype filter. Fig. 2.8 shows the CMT transceiver system where the data symbols,

$$s_i(t) = \sum_{n=-\infty}^{+\infty} s_i[n]\delta(t - nT), \qquad i = 0, \ldots, N-1, \tag{2.20}$$

are first passed through the synthesis filter bank (transmitter filter bank) to construct the CMT transmit signal and then it is up-converted to the RF frequency and passed through the wireless channel. At the receiver, the signal is first down-converted to the base band and analyzed through the receiver filter bank. In order to combat the channel distortions, equalization needs to be performed. As it was shown in Section 2.1, the presence of the CP in OFDM that is larger than the length of the channel converts the frequency selective channel to subcarrier channels with a completely flat gain over each subcarrier band. However, as there is no CP in FBMC systems to absorb the transient of the channel, the channel response over the band of each subcarrier can only be approximated by a flat gain and this approximation is improved as the bandwidth of the subcarriers becomes narrower. When the assumption of having a flat channel over each subcarrier band is precise enough, as in the case of OFDM, one-tap equalizer per subcarrier can be utilized to equalize the channel. Otherwise, a multi-tap equalization per subcarrier is required. In Fig. 2.8, the flat complex gains of h_i, for $i = 0, \ldots, N-1$ over the subcarriers are considered and therefore, the channel effect can be compensated by multiplication of the gains $w_i = 1/h_i$, for $i = 0, \ldots, N-1$ to the outputs of the analysis filter bank before taking the real part. Finally, the estimation of the transmit symbols can be found by sampling the real part of the equalized signals at the intervals nT.

For implementation of FBMC, digital filters are usually used. By taking advantage of multirate signal processing techniques, computational complexity of these systems can be reduced. Therefore, synthesis and analysis filter banks can be implemented using polyphase structures. such structures were first introduced by Bellanger in [45]. In a more recent work, [51], the same author proposed a new structure for implementation of FBMC systems based on an approach that is called frequency spreading (FS). These structures are presented in the following subsections.

2.3.1 Polyphase implementation

In order to efficiently implement the continuous time FBMC system of Fig. 2.8, polyphase implementation can be utilized. Based on the derivations that are avail-

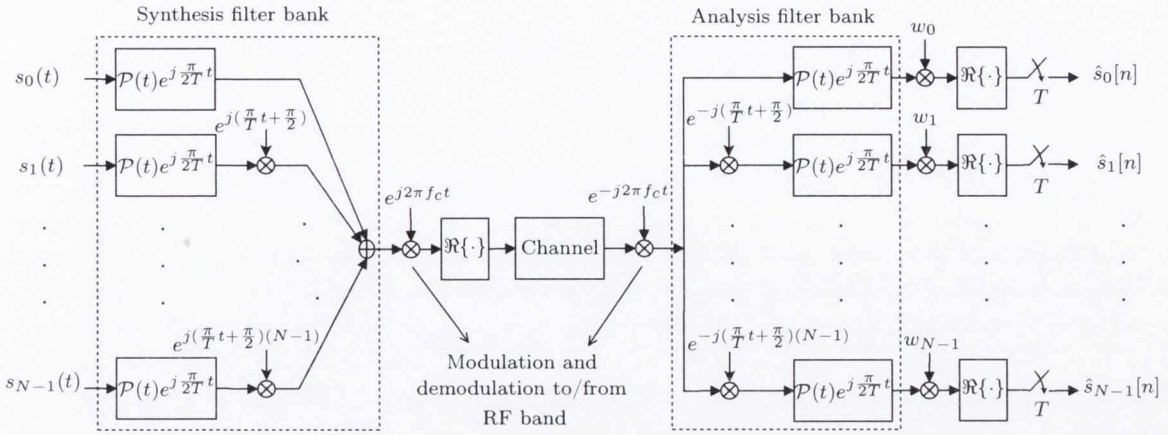

Fig. 2.8 CMT transceiver.

able in the literature, e.g., [31], given $W_{2L} = e^{-j2\pi/2L}$ and $E_\ell(z)$ be the ℓ^{th} polyphase component of the discrete time equivalent of the prototype filter $\mathcal{P}[n]$ in z-domain,

$$E_\ell(z) = \ldots + \mathcal{P}[\ell - 2L]z + \mathcal{P}[\ell] + \mathcal{P}[\ell + 2L]z^{-1} + \ldots, \tag{2.21}$$

the discrete time equivalent of equation (2.19) can be reformulated in z-domain as

$$\begin{aligned} X(z) \;=\; & \overbrace{[S_0(z^L), jS_1(z^L), \ldots, j^{N-1}S_{N-1}(z^L), 0, \ldots, 0]}^{1\times 2L}\,\mathbf{F}_{2L}^{\mathrm{H}} \\ & \cdot \begin{bmatrix} E_0(-z^{2L}) & 0 & \cdots & 0 \\ 0 & E_1(-z^{2L}) & \cdots & 0 \\ \vdots & \vdots & \ddots & \vdots \\ 0 & 0 & \cdots & E_{2L-1}(-z^{2L}) \end{bmatrix} \\ & \cdot \begin{bmatrix} 1 \\ W_{2L}^{-\frac{1}{2}} z^{-1} \\ \vdots \\ W_{2L}^{-\frac{2L-1}{2}} z^{2L-1} \end{bmatrix}, \end{aligned} \tag{2.22}$$

where $S_i(z^L)$ is the up-sampled version of $s_i[n]$ with the up-sampling factor L in z-domain. From (2.22) and using some concepts in multirate signal processing, one can obtain the synthesis filter bank structure as what is shown in Fig 2.9.

Following the same line of derivations as for the transmitter, the transmitted symbols $s_i[n]$'s , withought considering the effect of the channel, can be reconstructed

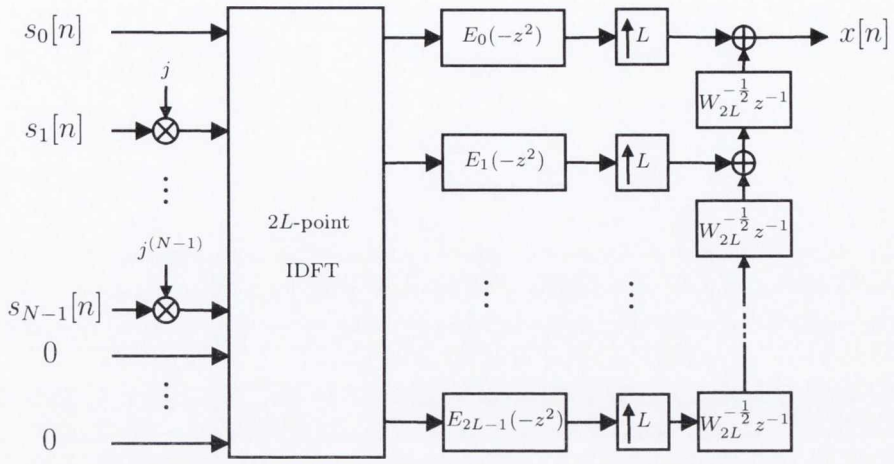

Fig. 2.9 Polyphase implementation of CMT transmitter.

from $x[n]$ as follows, [31],

$$\begin{bmatrix} \hat{S}_0(z) \\ j\hat{S}_1(z) \\ \vdots \\ j^{N-1}\hat{S}_{N-1}(z) \\ \times \\ \vdots \\ \times \end{bmatrix} = \mathbf{F}_{2L}^{\mathrm{H}} \begin{bmatrix} E_0(-z^{2L}) & 0 & \cdots & 0 \\ 0 & E_1(-z^{2L}) & \cdots & 0 \\ \vdots & \vdots & \ddots & \vdots \\ 0 & 0 & \cdots & E_{2L-1}(-z^{2L}) \end{bmatrix} \cdot \begin{bmatrix} 1 \\ W_{2L}^{-\frac{1}{2}}z^{-1} \\ \vdots \\ W_{2L}^{-\frac{2L-1}{2}}z^{2L-1} \end{bmatrix} X(z), \tag{2.23}$$

In the case of a multipath channel, based on the assumption of having a flat gain over each subcarrier band, channel equalization needs to be done before the real part operator. This procedure is included in Fig 2.10. Obviously, for an ideal channel, all the equalizer taps are equal to one. One point that needs special attention in equalizer design for CMT is to find the equalizer coefficients based on the channel samples at the right positions, i.e., the center of each subcarrier band, in frequency domain. This is due to the fact that the subcarriers in CMT are shifted by $1/4T$ in the frequency domain (Fig. 2.4 (b)).

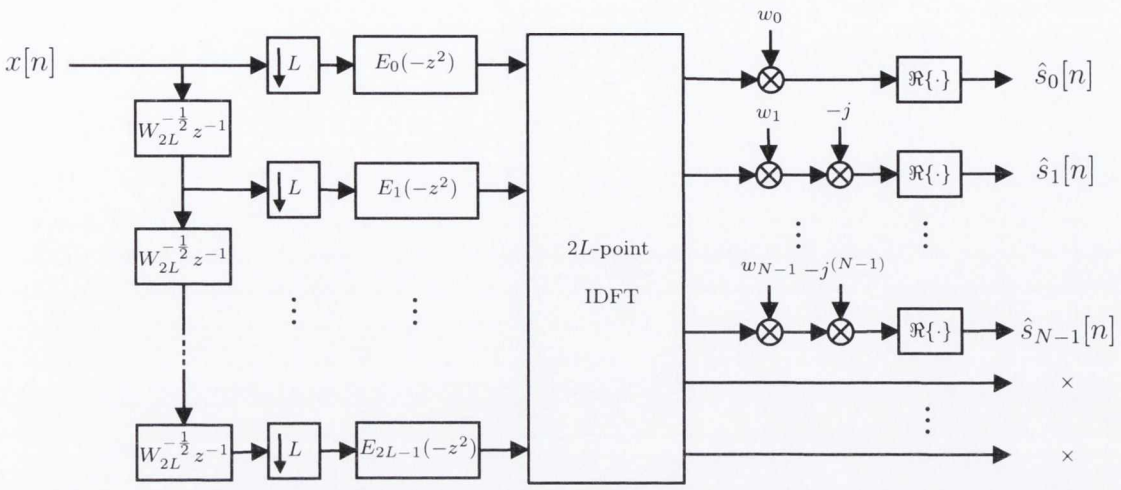

Fig. 2.10 Polyphase implementation of CMT receiver.

2.3.2 Frequency spreading implementation

A few recent publications have introduced an alternative to the traditional polyphase-based implementation of the FBMC systems that is termed as frequency spreading FBMC (FS-FBMC), [51–54]. This technique offers a number of advantages that put FBMC in a strong position as a candidate for the future wireless standards. FS-FBMC was explained for the first time in a document that came out of the PHYDYAS project, [51]. Further details on FS-FBMC are presented in [52] by the same author. The sensitivity of FS-FBMC to the timing offset is studied in [53] where the robustness of the frequency domain equalizer of the FS-FBMC to the timing errors compared with its counterpart with a polyphase-based receiver structure was reported. Berg et al., [54], have explored utilization of FS-FBMC to access the TV white spaces. All these works have used the filter that is designed by Matrin [88] and Mirabbasi and Martin [89] for the implementation of FS-FBMC system.

Martin has proposed a filter design technique for square-root Nyquist filters in [88] with the impulse response

$$\mathcal{P}[n] = \begin{cases} c_0 + 2\sum_{k=1}^{M-1} c_k \cos(\frac{2\pi kn}{K}), & 0 < n < K-1, \\ 0, & \text{otherwise}, \end{cases} \tag{2.24}$$

where $K = 2ML$ is the length of the prototype filter, $\mathcal{P}[n]$, and M is the overlapping factor. The spacing between zero-crossings of the Nyquist pulse $P[n] = \mathcal{P}[-n] * \mathcal{P}[n]$

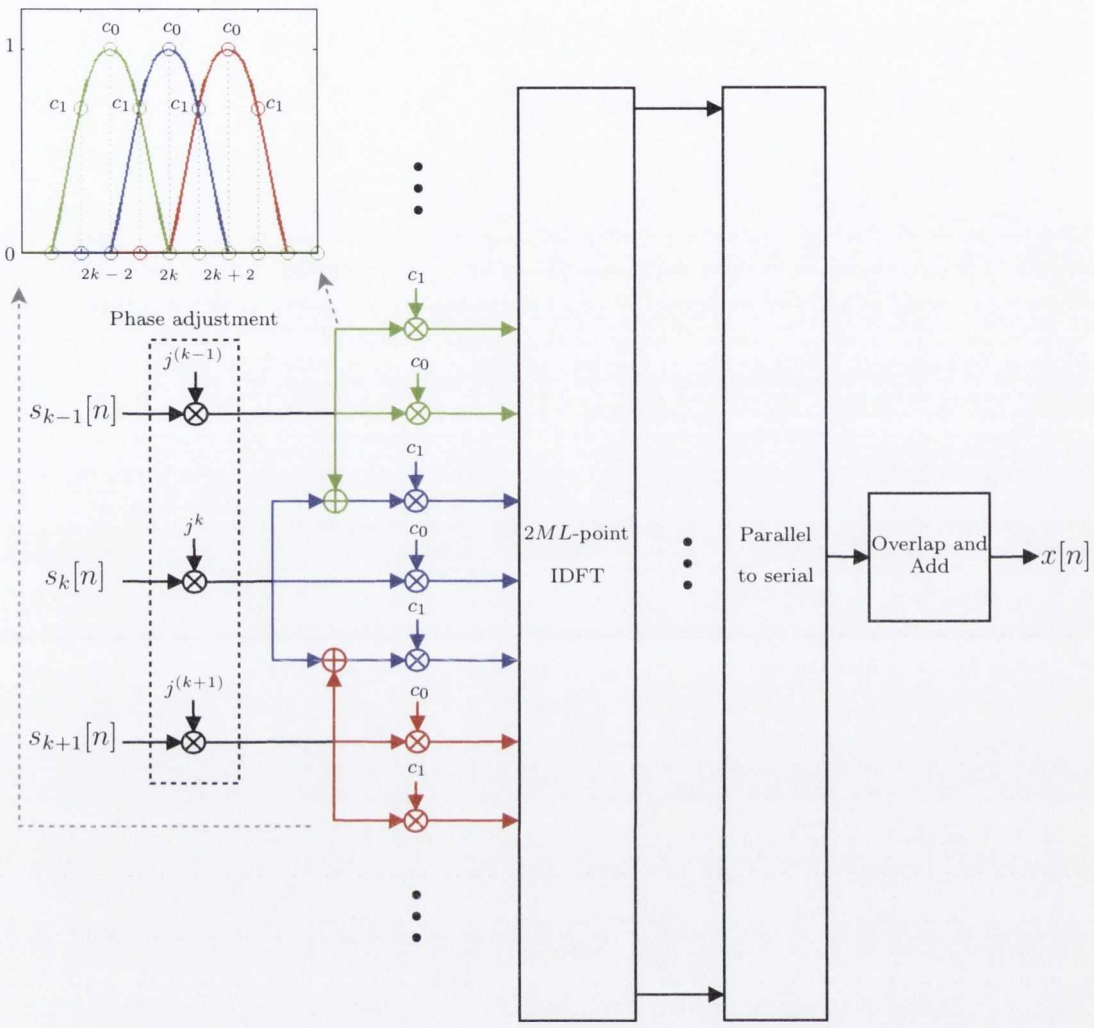

Fig. 2.11 Frequency spreading implementation of CMT transmitter for $M = 2$.

is $2L$ samples. One may note that equation (2.24) can be reformulated as

$$\mathcal{P}[n] = \sum_{k=-M+1}^{M-1} \tilde{c}_k e^{j\frac{2\pi kn}{K}}, \tag{2.25}$$

where

$$\tilde{c}_k = \begin{cases} c_k, & 0 < k < M-1, \\ c_{-k}, & -M+1 < k < -1. \end{cases} \tag{2.26}$$

From (2.25), one may realize that the square-root Nyquist filtering can be performed in the frequency domain by scaling the data symbols at different subcarrier

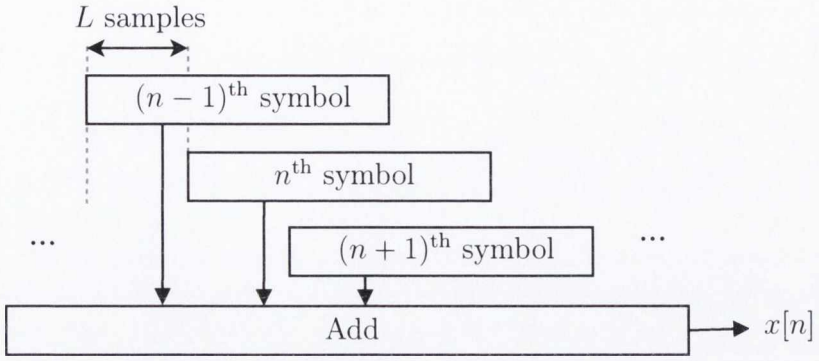

Fig. 2.12 Overlap and add operation.

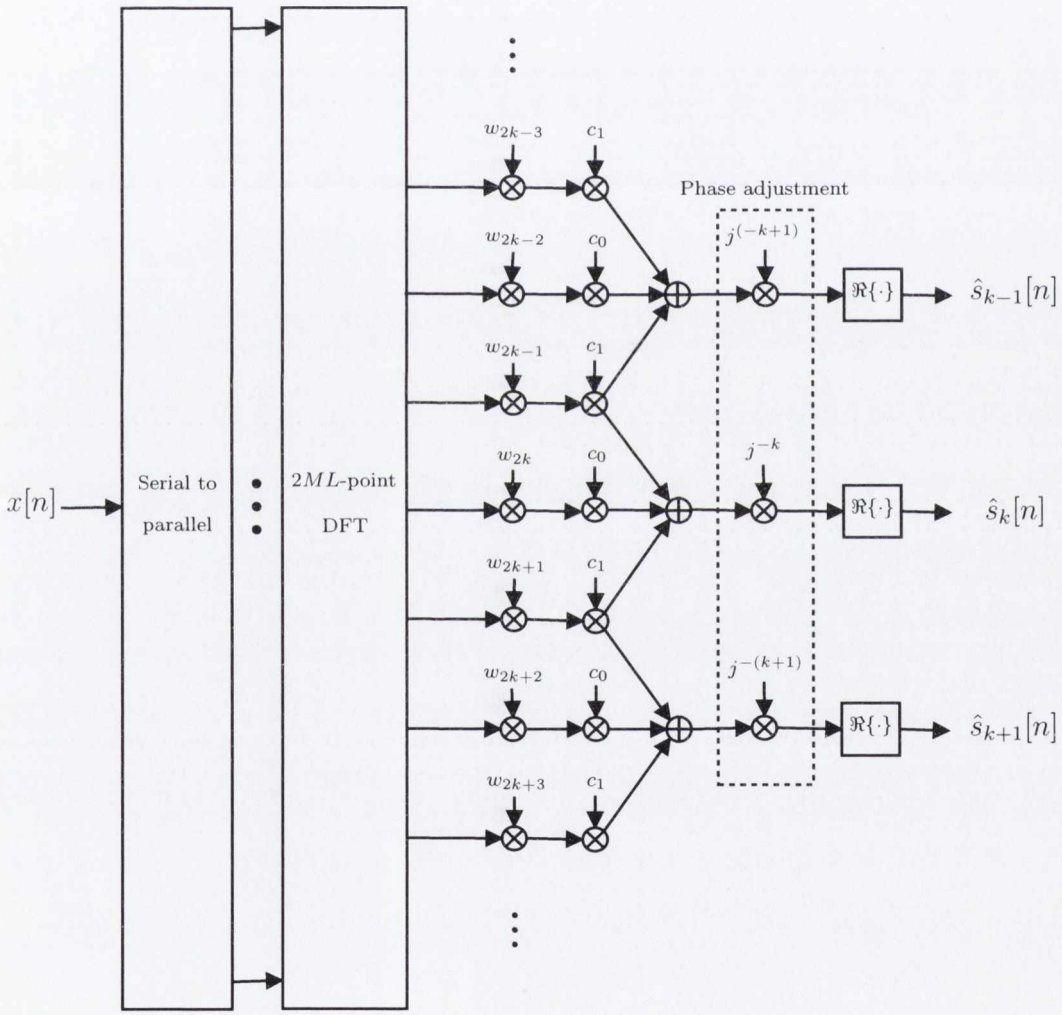

Fig. 2.13 Frequency spreading implementation of CMT receiver for $M = 2$.

positions with the gains c_k's. As it is shown in [52], this concept can be extended to the implementation of FBMC systems. Therefore, the CMT signal can be constructed by first scaling the phase toggled data symbols at different subcarrier positions with the corresponding gains c_k's and then applying an IDFT to the resulting frequency domain signal to generate the time domain signals that are pulse-shaped with square-root Nyquist filtering. The next step is to convert the parallel output of the IDFT block to serial. Since, the symbol spacing in CMT is equal to L samples, the consecutive IDFT outputs should be overlapped and added to each other after every L samples. This process is shown in Fig 2.11, where the overlapping factor $M = 2$ is chosen. The overlap and add procedure is also depicted in Fig 2.12. Fig 2.11 represents the frequency spreading realization of the synthesis filter bank that was shown in Fig 2.8. Equivalently, Fig 2.13 illustrates the frequency spreading implementation of the analysis filter bank including channel equalization for the overlapping factor of $M = 2$. It is worth mentioning that perfect time and frequency synchronization between the transmitter and receiver is considered here.

From Fig 2.13, one realizes that frequency domain channel equalization in these systems needs $2M - 1$ taps per subcarrier. For instance, the equalizer taps $w_{Mk-\frac{M}{2}}$ to $w_{MK+\frac{M}{2}}$ that are equal to the reciprocal of the channel response on the frequency bins from $MK - \frac{M}{2}$ to $MK + \frac{M}{2}$ are used to compensate the channel effect on the k^{th} subcarrier.

2.4 Massive MIMO

In recent past, massive MIMO has gained significant momentum as a potential candidate to increase the capacity of multiuser networks. Based on the recent discussions on 5G, massive MIMO can play a pivotal role in these networks, [49]. In essence, massive MIMO is a multiuser technique (somewhat similar to code division multiple access - CDMA) where the spreading gains for each user are determined by the channel gains between the respective mobile terminal (MT) antenna and the multiple antennas at base station. The number of base station antennas in these systems are assumed to be around an order of magnitude larger than the current wireless systems, [7]. Accordingly, by increasing the number of antennas at the base station, the processing gain can be increased to become arbitrarily large. As discussed in the pioneering work of Marzetta [5], in the limit, as the number of base station antennas tends to infinity, the processing gain of the system tends to infinity and, as a result, the effects of both noise and multiuser interference are completely removed. There-

fore, the network capacity (in theory) can be increased unboundedly by increasing the number of antennas at the base station, [5].

Motivated by Marzetta's observations, [5], multiple research groups in recent years have studied a variety of implementation issues related to massive MIMO systems, e.g., [90–94]. Also, different groups have started development of testbeds to confirm the theoretical observation of [5], in practice. An assumption made by Marzetta [5] and followed by other researchers is that OFDM may be used to convert the frequency selective channels between each MT and the multiple antennas at the base station to a set of flat fading channels. Accordingly, the flat gains associated with the set of channels within each subcarrier constitute the spreading gain vector that is used for despreading of the respective data stream.

2.4.1 Basics of massive MIMO systems

Consider a multiuser MIMO setup similar to the one that is discussed in [5]. There are K MTs and a BS in a cell. Each MT is equipped with a single transmit and receive antenna, communicating with the base station at its cell in a *time division duplexing* (TDD) manner (Fig. 2.14). The base station is equipped with $N \gg K$ transmit/receive antennas that are used to communicate with the K MTs in the cell *simultaneously*. Similar to [5], assume that OFDM is used.

Each MT is distinguished by the base station using the respective subcarrier gains between its antenna and the base station antennas. Ignoring the time and subcarrier indices in our formulation, for simplicity of equations, a transmit symbol $s(\ell)$ from the ℓ^{th} MT arrives at the base station as a vector

$$\mathbf{x}_\ell = s(\ell)\mathbf{h}_\ell, \tag{2.27}$$

where $\mathbf{h}_\ell = [h_\ell(0), \ldots, h_\ell(N-1)]^{\mathrm{T}}$ is the channel gain vector whose elements are the gains between the ℓ^{th} MT and different antennas at the base station. The vector $\mathbf{x}_\ell$ and similar contributions from other MTs, as well as the channel noise vector $\mathbf{v}$, add up and form the base station received signal vector

$$\mathbf{x} = \sum_{\ell=0}^{K-1} \mathbf{x}_\ell + \boldsymbol{\nu}, \tag{2.28}$$

where $\boldsymbol{\nu}$ is the AWGN vector, i.e., $\boldsymbol{\nu} \sim \mathcal{CN}(0, {\sigma_\nu}^2 \mathbf{I}_N)$ and ${\sigma_\nu}^2$ is the noise variance. The base station uses a set of linear estimators that all take $\mathbf{x}$ as their input and

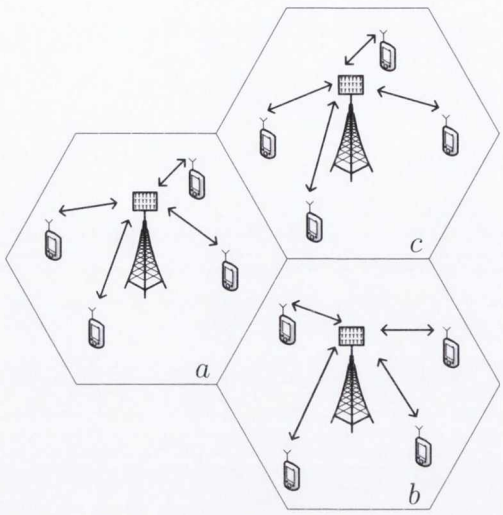

Fig. 2.14 Massive MIMO network.

provide the estimates of the users' data symbols $s(0)$, $s(1)$, $\cdots$, $s(K-1)$ at the output. To cast this process in a mathematical formulation and allow introduction of various choices of estimators, we reformulate equation (2.28) as

$$\mathbf{x} = \mathbf{H}\mathbf{s} + \boldsymbol{\nu}, \tag{2.29}$$

where $\mathbf{H} = [\mathbf{h}_0, \ldots, \mathbf{h}_{K-1}]$ is an $N \times K$ matrix that includes the channel vectors of different users on its columns and the $K \times 1$ vector $\mathbf{s} = [s(0), \ldots, s(K-1)]^{\mathrm{T}}$. Equation (2.29) has the familiar form that appears in CDMA literature, e.g., see [95, 96]. Hence, a variety of solutions that have been given for CDMA systems can be immediately applied to the present problem as well. For instance, the matched filter (MF) detector obtains an estimate of the vector $\mathbf{s}$, according to the equation

$$\hat{\mathbf{s}}_{\mathrm{MF}} = \mathbf{D}^{-1}\mathbf{H}^{\mathrm{H}}\mathbf{x}, \tag{2.30}$$

where $\mathbf{D} = \mathrm{diag}\{\|\mathbf{h}_0\|^2, \ldots, \|\mathbf{h}_{K-1}\|^2\}$ and $\hat{\mathbf{s}}_{\mathrm{MF}} = [\hat{s}_{\mathrm{MF}}(0), \ldots, \hat{s}_{\mathrm{MF}}(K-1)]^{\mathrm{T}}$ whose ℓ^{th} element, $\hat{s}_{\mathrm{MF}}(\ell)$, is the estimated data symbol of user ℓ. This leads to a receiver structure similar to that of [5], where it is shown that when the number of antennas, N, increases to infinity, the multiuser interference and noise effects vanish. Hence, $\hat{\mathbf{s}}_{\mathrm{MF}} = \mathbf{s}$, where the vector $\hat{\mathbf{s}}_{\mathrm{MF}}$ is an estimate of $\mathbf{s}$, and the receiver will be optimum. In the context of CDMA literature, this has the explanation that as N tends to infinity,

the processing gain also goes to infinity and accordingly multiuser interference and noise effects fade away.

In realistic situations when N is finite, the MF estimator is not optimal. Hence, a superior estimator, i.e., the MMSE estimator

$$\hat{\mathbf{s}}_{\text{MMSE}} = (\mathbf{H}^{\text{H}}\mathbf{H} + \sigma_{\nu}^{2}\mathbf{I}_{K})^{-1}\mathbf{H}^{\text{H}}\mathbf{x}, \tag{2.31}$$

can be utilized. Other aspects of massive MIMO systems such as their propagation and information theoretic properties can be found in [5, 7, 90–94].

2.4.2 Pilot contamination problem

The only limiting factor of the network capacity in the single-cell scenario is the coherence time of the channel which limits the number of MTs to be served simultaneously in a cell in order to guarantee accurate channel estimation and allow for data transmission, [5]. However, non-cooperative multi-cellular TDD networks suffer from a *pilot contamination* problem which was first reported by Jose et al, [6]. This is a major factor in limiting the capacity of those networks. Due to the channel reciprocity, in TDD systems, the channel state information (CSI) is obtained at the BS during the uplink transmission. Since the channel coherence time is usually not long enough to allow utilization of orthogonal pilot sequences in different cells, non-orthogonal pilots of neighboring cells will contaminate the pilots of each other [6]. Thus, the channel estimates at each BS will contain the channel information of the MTs located in the other cells as well as its own users. As a result, when the BS linearly combines the received signal in order to decode the transmitted symbols of its MTs, it also combines the data symbols of the users of other cells which results in inter-cell interference. The corresponding inter-cell interference does not vanish even when the number of BS antenna elements tends to infinity [5].

To tackle the pilot contamination problem, a number of solutions have been proposed in the literature [8–10]. The authors of [8] use eigenvalue decomposition of the covariance matrix of the received signal samples for channel estimation and show that the channel can be estimated with a higher accuracy compared with linear estimation techniques. In [9], the authors propose a cooperative Bayesian channel estimation technique where they find that the pilot contamination effect can be removed completely if the channel covariance matrices satisfy certain conditions. In a more recent work, Müller et al, [10], propose a blind technique based on a subspace projection method to mitigate the pilot contamination problem which needs singular

value decomposition (SVD) of the received signal matrix. However, the existing solutions for pilot contamination problem are either highly complex or need cooperation among different cells. Hence, low complexity solutions without the need for any type of cooperation has to be found. In Chapter 4, such a solution will be proposed.

Summary of contributions

As a multicarrier modulation, OFDM is suggested for massive MIMO systems in the literature, [5]. However, It suffers from large out-of-band emissions which not only have interference issues but it also can reduce the potential for exploiting non-contiguous spectrum chunks, i.e., carrier aggregation. Thus, one of the contributions of this thesis in the realm of massive MIMO systems is to replace OFDM with FBMC as a means of increasing the bandwidth efficiency and also an enabler for carrier aggregation. Pilot contamination problem that is discussed above is a limiting factor in multi-cellular massive MIMO networks that cannot be tackled by increasing the number of base station antennas, [7]. The existing solutions to this problem in the literature are either highly complex or need cooperation between the cells. Hence, another contribution of the thesis in massive MIMO systems that will be explained in Chapter 4 is to address this problem by extending the blind equalization property of FBMC from single antenna to massive MIMO systems which has a low complexity and does not need any cooperation between the cells. To summarize, FBMC has the following advantages over OFDM in massive MIMO systems.

- ***More flexible carrier aggregation.***
- ***Lower sensitivity to CFO.***
- ***Lower peak-to-average power ratio.***
- ***Higher bandwidth efficiency.***
- ***Blind equalization.***

2.5 Generalized frequency division multiplexing

Due to the demands of some emerging applications like M2M communications and IoT in 5G, new signaling techniques with a better time and frequency containment than that of the widely used OFDM waveform have to be sought. OFDM has been the technology of choice in many wired and wireless systems for many years [97–99]. However, it has some limitations; namely, large out-of-band emission which limits the utilization of non-contiguous spectrum known as *carrier aggregation* and high sensitivity to synchronization errors, especially CFO. As a case in point, in multiuser uplink scenarios where OFDMA is utilized, in order to avoid the large amount of interference caused by multiple CFOs as well as timing offsets, stringent synchronization is required which in turn imposes a great amount of overhead to the network. Presence of multiple Doppler shifts and propagation delays in the received uplink signal at the base station, as discussed in Section 2.2, results in some residual synchronization errors and hence multiple access interference [2]. In order to tackle this type of interference, some solutions are proposed [20, 21, 47] which lead to an increased receiver computational complexity. Thus, one of the main advantages of OFDM, i.e., its low complexity, will be lost. Therefore, more relaxed synchronization and more localized spectral properties are among the main physical (PHY) layer requirements of the future wireless networks.

The aforementioned requirements of 5G systems have stirred a great amount of interest among researchers and led to the advent of a number of new waveforms [12–14, 22, 50, 57]. All those signaling methods can be considered as filter bank multicarrier systems, some with circular pulse shaping [12–14, 57] and some with linear pulse shaping [22, 50]. As discussed in Section 2.3, FBMC signals with linear pulse shaping have attractive spectral properties [15]. In addition, those systems are resilient to the timing as well as frequency errors. However, the ramp-up and ramp-down of their signal which are due to the transient interval of the prototype filter result in additional latency issues. In contrast, FBMC systems with circular pulse shaping will remove the prototype filter transients thanks to their so called tail biting property [12]. Among all the emerging signaling methods for the PHY layer of 5G systems, GFDM is of interest to this section.

GFDM is considered as a candidate waveform for 5G cellular systems, due to its attractive properties, and has recently received a great deal of attention. GFDM is a generalized form of OFDM which preserves advantageous properties of OFDM while addressing its limitations. As Datta and Fettweis have pointed out in [100], GFDM

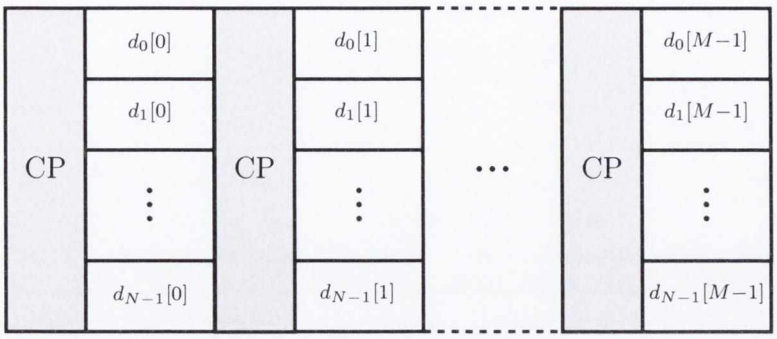

(a) OFDM data packet.

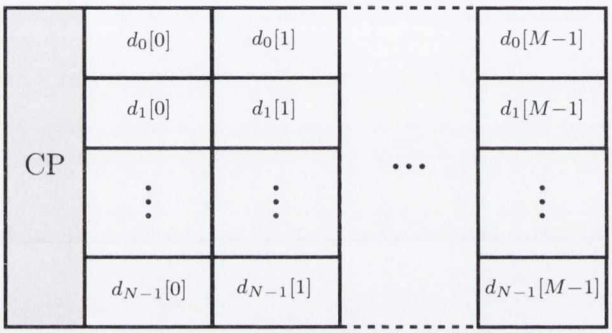

(b) GFDM data packet.

Fig. 2.15 GFDM vs. OFDM packet structure.

can provide a very low out-of-band radiation which removes the limitations of OFDM for carrier aggregation. Since GFDM uses only one CP for a group of symbols rather than a CP per symbol which is the case in OFDM, it is more bandwidth efficient than OFDM. To clarify this, Fig. 2.15 compares the packet structure of GFDM with that of OFDM. Through tail biting, GFDM removes the prototype filter transient intervals and hence the latency. Additionally, its special block structure makes it an attractive choice for the low latency applications like IoT and M2M communications, [101]. Filtering the subcarriers using a well designed prototype filter will limit the ICI only to the adjacent subcarriers which reduces the amount of leakage between subcarriers and increases the resiliency of the system to CFO as well as narrow band interference. In other words, GFDM has robustness to synchronization errors. As Michailow et al report in [101], GFDM is also a good match for MIMO systems.

The advantages of GFDM come at the expense of an increased bit error rate (BER) compared with OFDM. This degradation is due to the fact that GFDM is a non-orthogonal waveform. Consequently, non-orthogonality of the neighboring subcarriers and time slots results in self-interference. To tackle this self-interference, ZF and

MMSE receivers can be derived [102]. Due to their noise enhancement problem, ZF receivers incur some BER performance loss. Thus, the MMSE approach can be used to reduce the noise enhancement effect. As ZF and MMSE receivers involve large matrix inversion operations, they demand a high computational complexity that makes them inefficient in practice. As an alternative solution, Datta et al, [103], take a time domain successive interference cancellation approach. This solution can completely remove the effect of the self-interference. However, that solution is a computationally exhaustive procedure. In a more recent work from the same research group, Gaspar et al, [104], take advantage of the sparsity of the pulse shaping filter in frequency domain to perform the interference cancellation in the frequency domain and hence reduce the computational complexity of the receiver. Even though the solutions that are based on successive interference cancellation, [103, 104], can remove the self-interference, they can incur error propagation problem. Recently, Matthé et al, [105], have proposed a fast algorithm to calculate the ZF and MMSE receiver filters. Their approach is based on the Gabor transform structure of GFDM. Although matrix inversion is circumvented, multiplication of the ZF and MMSE matrices to the received signal is a bottle-neck to this approach as the matrix to vector multiplication is a computationally expensive operation.

2.5.1 GFDM modulation

We consider a GFDM system with the total number of N subcarriers that includes M symbols in each block. In a GFDM block, M symbols overlap in time. Therefore, we call M, *overlapping factor* of the GFDM system. The $MN \times 1$ vector $\mathbf{d} = [\mathbf{d}_0^{\mathrm{T}}, \ldots, \mathbf{d}_{N-1}^{\mathrm{T}}]^{\mathrm{T}}$ contains the complex data symbols of the GFDM block where the $M \times 1$ data vector $\mathbf{d}_i = [d_i[0], \ldots, d_i[M-1]]^{\mathrm{T}}$ contains the data symbols to be transmitted on the i^{th} subcarrier. The data symbols are taken from a zero mean independent and identically distributed (i.i.d.) process with the variance of unity. In GFDM modulation, the data symbols to be transmitted on the i^{th} subcarrier are first up-sampled by the factor of N to form an impulse train

$$s_i[n] = \sum_{k=0}^{M-1} d_i[k]\delta[n - kN], \quad n = 0, \ldots, NM - 1. \tag{2.32}$$

Then, $\mathbf{s}_i = [s_i[0], \ldots, s_i[MN-1]]^{\mathrm{T}}$ is circularly convolved with the prototype filter and up-converted to its corresponding subcarrier frequency. After performing the same procedure for all the subcarriers, the resulting signals are summed up to form

the GFDM signal $x[n]$, [102].

$$x[n] = \sum_{i=0}^{N-1} \sum_{m=0}^{M-1} d_i[m] g_{\{(n-mN) \bmod MN\}} e^{j\frac{2\pi in}{N}}, \tag{2.33}$$

where g_ℓ is the ℓ^{th} prototype filter coefficient.

Putting together all the transmitter output samples in an $MN \times 1$ vector $\mathbf{x} = [x[0], \ldots, x[MN-1]]^{\mathrm{T}}$, the GFDM signal can be represented as multiplication of a modulation matrix $\mathbf{A}$ of size $MN \times MN$ to the data vector $\mathbf{d}$, [102].

$$\mathbf{x} = \mathbf{A}\mathbf{d}. \tag{2.34}$$

Modulation matrix $\mathbf{A}$ encompasses all signal processing steps involved in modulation. Let $\mathbf{g} = [g_0, \ldots, g_{MN-1}]^{\mathrm{T}}$ hold all the coefficients of the pulse shaping/prototype filter, the elements of $\mathbf{A}$ can be represented as,

$$[\mathbf{A}]_{nm} = g_{\{(n-mN) \bmod MN\}} e^{j\frac{2\pi n}{N}\lfloor \frac{m}{M} \rfloor}, \tag{2.35}$$

where $\lfloor \cdot \rfloor$ and 'mod' are the round down and modulo operators, respectively. Based on the equations (2.33) to (2.35), the matrix $\mathbf{A}$ can be written as

$$\mathbf{A} = \left[\boldsymbol{\mathcal{G}} \quad \boldsymbol{\mathcal{E}}_1 \boldsymbol{\mathcal{G}} \quad \ldots \quad \boldsymbol{\mathcal{E}}_{N-1} \boldsymbol{\mathcal{G}} \right], \tag{2.36}$$

where $\boldsymbol{\mathcal{G}}$ is an $MN \times M$ matrix whose first column contains the samples of the prototype filter $\mathbf{g}$ and its consecutive columns are copies of their previous column that are circularly shifted by N samples. $\boldsymbol{\mathcal{E}}_i = \mathrm{diag}\{[\mathbf{e}_i^{\mathrm{T}}, \ldots, \mathbf{e}_i^{\mathrm{T}}]^{\mathrm{T}}\}$ is an $MN \times MN$ diagonal matrix whose diagonal elements are comprised of M concatenated copies of the vector $\mathbf{e}_i = [1, e^{j\frac{2\pi i}{N}}, \ldots, e^{j\frac{2\pi i}{N}(N-1)}]^{\mathrm{T}}$.

GFDM systems use frequency domain equalization to tackle the wireless channel impairments and reduce the channel equalization complexity. In those systems, a CP which is longer than the channel delay spread is added to the beginning of the GFDM block to accommodate the channel transient period. If N_{CP} is the CP length, the last N_{CP} elements of the vector $\mathbf{x}$ are appended to its beginning in order to form the transmitted signal vector $\bar{\mathbf{x}}$ whose length is $MN + N_{\mathrm{CP}}$. Let $\mathbf{h} = [h_0, \ldots, h_{N_{\mathrm{ch}}-1}]^{\mathrm{T}}$ be the channel impulse response. Thus, the CP length N_{CP} needs to be longer than the channel length N_{ch}. The received signal which has gone through the channel, after

CP removal can be shown as

$$\mathbf{r} = \mathbf{H}\mathbf{x} + \boldsymbol{\nu}, \tag{2.37}$$

where $\boldsymbol{\nu}$ is the AWGN vector, i.e, $\boldsymbol{\nu} \sim \mathcal{CN}(0, {\sigma_\nu}^2 \mathbf{I}_{MN})$, ${\sigma_\nu}^2$ is the noise variance, $\mathbf{H} = \text{circ}\{\tilde{\mathbf{h}}\}$ and $\tilde{\mathbf{h}}$ is the zero padded version of $\mathbf{h}$ which has the same size as $\mathbf{x}$. Due to the fact that $\mathbf{H}$ is a circulant matrix and because of the same reasons that were presented in Section 2.1, an FDE procedure can be performed to compensate for the multipath channel impairments. With the assumption of having perfect synchronization and channel estimates, the equalized signal can be obtained as

$$\mathbf{y} = \mathbf{F}_{MN}^{\text{H}} \boldsymbol{\mathcal{H}}^{-1} \mathbf{F}_{MN} \mathbf{r}, \tag{2.38}$$

where $\mathbf{F}_{MN}$ is MN-point normalized DFT matrix and $\boldsymbol{\mathcal{H}}^{-1}$ is a diagonal matrix whose diagonal elements are reciprocals of the elements of the vector obtained from taking MN-point DFT of the zero padded version of $\mathbf{h}$, viz., $\tilde{\mathbf{h}}$. The vector $\mathbf{y} = [y_0, \ldots, y_{MN-1}]^{\text{T}}$ is the output of the FDE block.

In order to remove or suppress ICI due to non-orthogonality of the subcarriers and estimate the transmitted data vector $\mathbf{d}$ from the equalized signal vector, three linear GFDM receivers; namely, MF, ZF and MMSE detectors can be considered.

The simplest way of retrieving the transmitted GFDM signal at the receiver is through application of MF detector to each individual subcarrier, [102],

$$\hat{\mathbf{d}}_{\text{MF}} = \mathbf{A}^{\text{H}} \mathbf{y}. \tag{2.39}$$

However, MF receiver cannot completely remove ICI and thus suffers from some performance loss due to the residual ICI. Instead, ZF receiver can be utilized to completely remove ICI effects. The ZF estimate of the transmitted data vector can be found as

$$\hat{\mathbf{d}}_{\text{ZF}} = (\mathbf{A}^{\text{H}} \mathbf{A})^{-1} \mathbf{A}^{\text{H}} \mathbf{y}. \tag{2.40}$$

Although ZF solution completely eliminates the ICI caused by non-orthogonality of the subcarriers, since $(\mathbf{A}^{\text{H}} \mathbf{A})^{-1} \mathbf{A}^{\text{H}}$ can have large values, its multiplication to $\mathbf{y}$ can result in noise enhancement. This noise amplification problem can be taken care of by utilizing an MMSE receiver

$$\hat{\mathbf{d}}_{\text{MMSE}} = (\mathbf{A}^{\text{H}} \mathbf{A} + {\sigma_\nu}^2 \mathbf{I}_{MN})^{-1} \mathbf{A}^{\text{H}} \mathbf{y}. \tag{2.41}$$

Direct matrix multiplications and inversions in (2.34), (2.40) and (2.41) for modulation and demodulation demand high computational complexity as all the matrices are of the size $MN \times MN$ which may not be affordable for practical systems. Therefore, the authors of [106] and [104] have proposed low complexity transmitter and receiver implementations which take advantage of the sparse properties of the prototype filter in frequency domain to reduce the computational load of both transmitter and receiver. However, as will be shown in Chapter 5, their transmitter is still complex and there is still some space for more complexity reduction. Moreover, the low complexity receiver that is proposed in [104] is based on the successive interference cancellation (SIC) and is not only prone to the error propagation problem but it also is around an order of magnitude more complex than OFDM receiver. Thus, receiver structures with lower complexity than what is proposed in [104] have to be found.

Summary of contributions

As mentioned above, the available GFDM transceiver structures in the literature are highly complex compared with their OFDM counterparts and structures with low computational load have to be sought. Hence, one of the contributions of this thesis is to propose a low complexity transmitter and a unified structure for the MF, ZF and MMSE based GFDM receivers. As will be discussed in Chapter 5, the proposed solutions bring a substantial computational complexity reduction compared to the available ones in the literature while maintaining the optimal performance.

Due to the non-orthogonality of the subcarriers, GFDM suffers from some BER performance loss compared with OFDM. Therefore, a modified version of GFDM has been recently proposed in the literature, [14]. However, a thorough comparison of GFDM with its modified counterpart is missing in the literature. Hence, another contribution of the thesis is to compare GFDM with its modified version. This comparison that reveals the limitations of GFDM is presented in Chapter 5.

Chapter 3

Carrier frequency offset correction in the uplink of OFDMA

Orthogonal frequency division multiple access (OFDMA) is a multiuser technology that is a combination of frequency division multiple access (FDMA) protocol and OFDM. As mentioned in the previous chapter, popularity of OFDMA is due to the fact that it is highly spectral efficient and resilient against multipath fading channels. In OFDMA technology, subcarriers are grouped into distinct sets that are assigned to different users. Despite all the advantages, OFDMA systems especially in the uplink are highly sensitive to synchronization errors.

Inaccurate synchronization destroys the orthogonality between subcarriers and causes multiple access interference (MAI) as well as self-interference, [1]. The MAI and self-interference due to the timing misalignment of the users' signals in the uplink can be omitted by the choice of adequately long cyclic prefix (CP) to have a quasi-synchronous system where the residual timing error of each user will appear in its channel impulse response as a phase factor which will be compensated for in the equalization stage, [2]. On the other hand, distinct local oscillator misalignments, sampling clock frequency offsets and Doppler frequency shifts of the users have detrimental ramifications on the received signal at the base station (BS). Since the received signal at the BS is a mixture of all the users' signals, multiple carrier frequency offsets (CFOs) appear in the received signal and cause intercarrier interference (ICI) and hence MAI. To mitigate the effect of the ICI and MAI induced by the CFOs in the uplink of OFDMA based systems, several approaches have been proposed in the literature, e.g., [2, 85, 86]. The literature on MAI compensation was discussed in detail in Chapter 2. In this chapter, CFO correction techniques that are based on

the linear zero forcing and minumum mean square error criteria are considered as an answer to the first research question that was raised in Chapter 1.

Question 1

- ***Is it possible to serve a large number of users with OFDMA having a reasonable computational burden while providing the optimal performance catering all carrier assignment schemes?***

As it was emphasized in Chapter 2, the available CFO correction techniques in the literature are still complex and as the number of users increases, the computational burden of such techniques substantially increases. Hence, solutions with a reasonable computational complexity for practical systems where a couple of thousands of subcarriers and tens of users are present, have to be sought. Accordingly, in this chapter, low complexity CFO correction techniques that we have developed for a wide range of subcarrier allocation schemes are presented.

The rest of this chapter is laid out as follows. Section 3.1 is focused on linear CFO correction techniques applicable to interleaved and block-interleaved carrier assignment schemes (I-CAS and BI-CAS); namely, zero forcing (ZF) and minimum mean square error (MMSE). The computational costs of the proposed techniques are analyzed and compared with other existing solutions from literature that are known to have the lowest complexity. Section 3.2 is dedicated to CFO correction techniques that are applicable to the generalized carrier assignment scheme (G-CAS). Detailed computational complexity analysis of our proposed solutions with the existing ones in the literature with the lowest complexity is also presented. Finally, the chapter is concluded in section 3.3.

3.1 CFO correction in interleaved and block-interleaved CAS

We consider the uplink of an OFDMA system where K users are communicating with the base station through independent multipath wireless channels. The total number of subcarriers in each OFDMA symbol is assumed to be N which translates into $M = N/K$ subcarriers per user. The OFDMA system adopts the BI-CAS with Q subcarriers in each subcarrier block. Therefore, the number of subcarrier

blocks per user is $L = M/Q$. Obviously, when $Q = 1$, the BI-CAS reduces to I-CAS. The $M \times 1$ vector $\mathbf{d}^{(i)}[n]$ contains information symbols of the i^{th} user in the n^{th} symbol. The information symbols of all the users are assumed as zero mean, independent and identically distributed (i.i.d) processes with the variance of unity. It is worth mentioning that the subcarriers of distinct users are mapped onto mutually disjoint subsets of the available subcarriers. In other words, if the sets Ψ_i and Ψ_j contain the subcarrier indices allocated to the i^{th} and j^{th} users, respectively, then $\Psi_i \cap \Psi_j = \emptyset, i \neq j$. Recalling from Chapter 2, the i^{th} user signal vector after subcarrier mapping is $\mathbf{x}_{\text{f}}^{(i)}[n] = \mathbf{\Gamma}_i \mathbf{d}^{(i)}[n]$ where $\mathbf{\Gamma}_i$ is the $N \times M$ subcarrier allocation matrix of user i whose elements for the general case of BI-CAS are

$$[\mathbf{\Gamma}_i]_{m,p} = \begin{cases} 1, & m = iQ + \ell KQ + q, \\ 0, & \text{otherwise}, \end{cases} \tag{3.1}$$

where $i = 0, \ldots, K-1$, $\ell = 0, \ldots, L-1$, $q = 0, \ldots, Q-1$ and $p = q + \ell Q$. The OFDM modulator output for the n^{th} symbol of user i is given by $\mathbf{x}_{\text{CP}}^{(i)}[n] = \mathbf{T}_{\text{CP}} \mathbf{F}_N^{\text{H}} \mathbf{x}_{\text{f}}^{(i)}[n]$ where $\mathbf{T}_{\text{CP}}$ is the CP addition matrix and $\mathbf{F}_N$ is the N-point DFT matrix with the elements $[\mathbf{F}_N]_{n,k} = \frac{1}{\sqrt{N}} e^{\frac{-j2\pi nk}{N}}$.

From derivations of Chapter 2, the output of OFDM receiver at the base station can be written as

$$\begin{aligned} \bar{\mathbf{r}}[n] &= \mathbf{F}_N \mathbf{R}_{\text{CP}} \tilde{\mathbf{r}}[n] = \sum_{i=1}^{K} \mathbf{F}_N \tilde{\mathbf{\Phi}}(\epsilon_i) \mathbf{F}_N^{\text{H}} \mathbf{H}_{\text{f}}^{(i)} \mathbf{x}_{\text{f}}^{(i)}[n] + \mathbf{F}_N \mathbf{R}_{\text{CP}} \boldsymbol{\nu} \\ &= \mathbf{\Lambda} \mathbf{z}[n] + \mathbf{F}_N \mathbf{R}_{\text{CP}} \boldsymbol{\nu}, \end{aligned} \tag{3.2}$$

where

$$\mathbf{z}[n] = \sum_{i=1}^{K} \mathbf{H}_{\text{f}}^{(i)} \mathbf{x}_{\text{f}}^{(i)}[n] = \bar{\mathbf{H}}_{\text{f}} \mathbf{d}[n], \tag{3.3}$$

and

$$\mathbf{\Lambda} = \sum_{i=1}^{K} \mathbf{F}_N \tilde{\mathbf{\Phi}}(\epsilon_i) \mathbf{F}_N^{\text{H}} \mathbf{\Pi}_i, \tag{3.4}$$

is the $N \times N$ interference matrix. $\tilde{\mathbf{r}}[n]$ is the received signal at BS, $\mathbf{R}_{\text{CP}}$ is the CP removal matrix, $\tilde{\mathbf{\Phi}}(\epsilon_i) = \text{diag}\{1, e^{\frac{j2\pi\epsilon_i}{N}}, \ldots, e^{\frac{j2\pi\epsilon_i(N-1)}{N}}\}$ and ϵ_i[1] is the CFO of user i where $-0.5 < \epsilon_i \leq 0.5$. Finally, the $N \times N$ diagonal matrix $\mathbf{H}_{\text{f}}^{(i)}$ includes the channel frequency response of user i, $\bar{\mathbf{H}}_{\text{f}}$ contains the composite channel frequency responses

[1] In order to make our study independent of subcarrier spacing, normalized CFOs with respect to subcarrier spacing are considered.

of all the users in its diagonal elements and $\mathbf{\Pi}_i = \mathbf{\Gamma}_i \mathbf{\Gamma}_i^{\mathrm{H}}$. It is worth noting that we assume an independent time invariant channel over one OFDMA symbol for each user.

Given the perfect knowledge of the users' CFOs at the base station and using equation (3.2), ZF estimates of $\mathbf{z}[n]$ can be obtained as

$$\hat{\mathbf{z}}_{\mathrm{ZF}}[n] = \mathbf{\Lambda}^{-1}\bar{\mathbf{r}}[n] = \mathbf{z}[n] + \mathbf{\Lambda}^{-1}\mathbf{F}_N\mathbf{R}_{\mathrm{CP}}\boldsymbol{\nu}. \tag{3.5}$$

However, CFO correction based on ZF criterion may lead to noise amplification problem. This problem can be addressed by using the MMSE solution.

$$\hat{\mathbf{z}}_{\mathrm{MMSE}}[n] = (\mathbf{\Lambda}^{\mathrm{H}}\mathbf{\Lambda} + {\sigma_\nu}^2\mathbf{I}_N)^{-1}\mathbf{\Lambda}^{\mathrm{H}}\bar{\mathbf{r}}[n], \tag{3.6}$$

where $\mathbf{I}_N$ is the identity matrix of size $N \times N$. As it was noted in Chapter 2, direct solution of equations (3.5) and (3.6) is prohibitively complex in practical scenarios where a large number of subcarriers in the order of thousands is being used. As a case in point, in the WiMAX standard IEEE 802.16e and 3GPP LTE standard N can be as large as 2048.

In the remainder of this section, ZF and MMSE-based techniques will be proposed that can significantly reduce the computational cost of the CFO compensation in the uplink of OFDMA-based systems. The proposed solutions take advantage of the special structure of the interference matrix $\mathbf{\Lambda}$.

3.1.1 Characteristics of the interference matrix

In this section, we discuss the characteristics of the interference matrix $\mathbf{\Lambda}$ and present some closed forms as well as matrix factorization techniques which enable us to calculate the ZF and MMSE estimates of $\mathbf{z}[n]$ with a very low computational cost.

Before going into the special mathematical properties of the interference matrix, it is of paramount importance to have a deep understanding of the elements of the matrix first. The interference on the m^{th} subcarrier belonging to user i caused by the signal on the p^{th} subcarrier belonging to user j can be mathematically shown as

$$[\mathbf{x}_{\mathrm{f}}^{(j)}[n]]_p[\mathbf{H}_{\mathrm{f}}^{(i)}]_{p,p}[\mathbf{\Lambda}]_{m,p}. \tag{3.7}$$

Assuming the channel coefficients and data symbols of different users to be zero mean Gaussian processes with unit variance, the normalized interference power between the

aforementioned subcarriers will be

$$|[\mathbf{\Lambda}]_{m,p}|^2 = \frac{\sin^2(\pi\epsilon_j)}{N^2\sin^2(\frac{\pi}{N}(p-m+\epsilon_j))}. \tag{3.8}$$

Each column of the matrix $\mathbf{\Lambda}$ is associated with the CFO of the corresponding user and includes the interference contribution of that specific subcarrier to other subcarriers. Based on the equation (3.8), the interference power of each subcarrier to the other subcarriers only depends on the distance, $|p-m| \in [0, N-1]$. As we move further the interference decreases up to the distance $|p-m| = \frac{N}{2}$ and after that it starts to increase again.

Considering the BI-CAS with Q subcarriers per block, in order to exploit the symmetrical structure of $\mathbf{\Lambda}$, we can break the matrix into smaller $KQ \times KQ$ submatrices. If $p \in \Psi_j$ and $m \in \Psi_i$, then $[\mathbf{\Lambda}]_{m,p} = f_N(\epsilon_j + p - m)$ where $f_N(x) = \frac{\sin(\pi x)}{N\sin(\frac{\pi x}{N})}e^{j\pi x(1-\frac{1}{N})}$. Hence, it can be inferred that the first KQ columns of $\mathbf{\Lambda}$ are determined by the CFOs of the users 1 to K and the rest are circularly shifted copies of the $KQ \times KQ$ block matrices, $\mathbf{\Lambda}_\ell$s for $\ell = 0, \ldots, L-1$.

$$\mathbf{\Lambda} = \begin{pmatrix} \mathbf{\Lambda}_0 & \mathbf{\Lambda}_{L-1} & \cdots & \mathbf{\Lambda}_1 \\ \mathbf{\Lambda}_1 & \mathbf{\Lambda}_0 & \cdots & \mathbf{\Lambda}_2 \\ \vdots & \vdots & \ddots & \vdots \\ \mathbf{\Lambda}_{L-1} & \mathbf{\Lambda}_{L-2} & \cdots & \mathbf{\Lambda}_0 \end{pmatrix}. \tag{3.9}$$

From (3.9), one realizes that the interference matrix can be considered as a block circulant matrix and according to the results of [107], it can be block diagonalized using block-DFT and block-IDFT matrices.

3.1.2 Zero forcing CFO correction

From (3.5), ZF estimation of $\mathbf{z}[n]$ requires inversion and multiplication of $\mathbf{\Lambda}$ to $\bar{\mathbf{r}}[n]$. To this end, $\mathbf{\Lambda}$ can be expanded as

$$\mathbf{\Lambda} = \mathbf{A}^{\mathrm{H}}\mathbf{D}\mathbf{A} \tag{3.10}$$

where $\mathbf{A}$ is the $N \times N$ block-DFT matrix comprised of smaller $KQ \times KQ$ submatrices $\mathbf{\Theta}_{m,p} = \frac{1}{\sqrt{L}}e^{(\frac{-j2\pi mp}{L})}\mathbf{I}_{KQ}$ and $m, p = 0, \ldots, L-1$. On the other hand, the matrix $\mathbf{A}^H$ is the block-IDFT matrix and $\mathbf{D}$ is an $N \times N$ block diagonal matrix, $\mathbf{D} = \mathrm{Diag}\{\mathbf{D}_0, \ldots, \mathbf{D}_{L-1}\}$ where $\mathbf{D}_\ell$s are $KQ \times KQ$ matrices. From (3.10) and the

fact that $\mathbf{A}\mathbf{A}^{\mathrm{H}} = \mathbf{I}_N$, $\mathbf{D}$ can be obtained as $\mathbf{A}\mathbf{\Lambda}\mathbf{A}^{\mathrm{H}}$. Therefore, all the elements of $\mathbf{D}_\ell$s can be found by applying L-point DFTs to the equidistant elements in each of the first KQ columns of $\mathbf{\Lambda}$ with the spacing of KQ. This can be deduced from the fact that the equidistant elements in the rows and columns of $\mathbf{\Lambda}$, i.e., KQ apart (equation (3.9)), can be considered as circulant matrices whose eigenvalues can be calculated using L-point DFTs of their first columns. From the Nyquist sampling theorem, it can be recalled that reducing the sampling rate of a sequence in time is equivalent to aliasing in the frequency domain and vice versa. From (2.16), it is easy to show that the p^{th} column of the interference matrix ($p \in \Psi_j$, $j = 0, \ldots, K-1$) is the DFT of the sequence $\varphi_j(p) = \{e^{\frac{j2\pi\epsilon_j p}{N}},\ p = 0, \ldots, N-1\}$, circularly shifted by p samples and scaled by the factor $\frac{1}{\sqrt{N}}$. Due to the fact that applying the DFT to the sequence $\varphi_j(p)$ twice results in the same but circularly folded time domain sequence $\varphi_j((-p))_N$ and using the concept of aliasing, the elements of $\mathbf{D}_\ell$s are obtained as

$$[\mathbf{D}_\ell]_{m,p} = e^{\frac{j2\pi(\epsilon_j+p-m)}{N}((-\ell))_L} f_{KQ}(\epsilon_j + p - m) \tag{3.11}$$

for $\ell = 0, \ldots, L-1$ and $m, p = 0, \ldots, KQ-1$. As can be deduced from (3.11), the same elements of different $\mathbf{D}_\ell$s, all have the same amplitude and they are only different in phase. Consequently, $\mathbf{D}_\ell$s can be represented as the Hadamard product of $KQ \times KQ$ phase shift matrices, $\mathbf{E}_\ell$s, and the first block matrix $\mathbf{D}_0$. Hence, we have

$$\mathbf{D}_\ell = \mathbf{E}_\ell \odot \mathbf{D}_0 \tag{3.12}$$

and

$$[\mathbf{E}_\ell]_{m,p} = e^{\frac{j2\pi(\epsilon_j+p-m)}{N}(L-\ell)} \tag{3.13}$$

for $\ell = 1, \ldots, L-1$ and $m, p = 0, \ldots, KQ-1$. Furthermore, the basis matrix, $\mathbf{D}_0$ can be directly calculated from (3.11). According to (3.5), $\mathbf{\Lambda}^{-1}$ is needed for the CFO compensation using the LS solution. Using (3.10), $\mathbf{\Lambda}^{-1}$ can be shown as

$$\mathbf{\Lambda}^{-1} = \mathbf{A}^{\mathrm{H}}\mathbf{D}^{-1}\mathbf{A} \tag{3.14}$$

where $\mathbf{D}^{-1} = \mathrm{diag}\{\mathbf{D}_0^{-1}, \ldots, \mathbf{D}_{L-1}^{-1}\}$. Given the result in (3.12), $\mathbf{D}_\ell^{-1}$ matrices can be obtained as

$$\mathbf{D}_\ell^{-1} = \mathbf{E}_\ell^{\mathrm{H}} \odot \mathbf{D}_0^{-1}. \tag{3.15}$$

Accordingly, finding $\mathbf{\Lambda}^{-1}$ needs only a $KQ \times KQ$ matrix inversion together with some other mathematical manipulations. A naive ZF solution based on (3.5) can be

obtained by finding $\mathbf{\Lambda}^{-1}$ from (3.14) and its direct multiplication to $\bar{\mathbf{r}}[n]$. Nevertheless, matrix to vector multiplication has a high complexity. This vector by matrix multiplication can be performed efficiently by substituting (3.14) into (3.5). Thus, we have

$$\hat{\mathbf{z}}_{\mathrm{ZF}}[n] = \mathbf{A}^{\mathrm{H}}\mathbf{D}^{-1}\mathbf{A}\bar{\mathbf{r}}[n]. \tag{3.16}$$

Recalling that $\mathbf{A}$ is the block-DFT matrix, $\mathbf{A}\bar{\mathbf{r}}$ can be efficiently implemented using L-point fast Fourier transforms (FFTs). Thus, N^2 complex multiplications needed for the matrix by vector multiplications reduces to $\frac{N}{2}\log_2 L$ complex multiplications. Moreover, $\mathbf{D}^{-1}$ is a block diagonal matrix and its multiplication to the result of $\mathbf{A}\bar{\mathbf{r}}$ which is an $N \times 1$ vector needs a few computations. Finally, $\hat{\mathbf{z}}_{\mathrm{ZF}}[n]$ can be effectively obtained by applying the inverse FFTs (IFFTs).

3.1.3 Minimum mean square error CFO correction

Similar to Section 3.1.2, since $\mathbf{\Lambda}$ and $\mathbf{\Lambda}^{\mathrm{H}}$ are block circulant matrices, it can be easily verified that the resulting matrix from their multiplication keeps the block circulant property. If $m{\in}\Psi_i$, $p{\in}\Psi_j$ for $i, j = 0, \ldots, K-1$, the elements in the matrix $\mathbf{\Lambda}^{\mathrm{H}}\mathbf{\Lambda}$ are

$$\left[\mathbf{\Lambda}^{\mathrm{H}}\mathbf{\Lambda}\right]_{m,p} = \begin{cases} 1, & \epsilon_i = \epsilon_j,\ m = p \\ 0, & \epsilon_i = \epsilon_j,\ m{\neq}p \\ f_N(\xi_{pm}), & \epsilon_i{\neq}\epsilon_j \end{cases} \tag{3.17}$$

where $\xi_{pm} = \epsilon_j - \epsilon_i + p - m$. Considering the MMSE solution in (2.18), the inverse of the matrix $(\mathbf{\Lambda}^{\mathrm{H}}\mathbf{\Lambda} + {\sigma_\nu}^2\mathbf{I}_N)$ is needed and since this matrix is block circulant, the same as in (3.10) it can be factorized into the form of $\mathbf{A}^{\mathrm{H}}\bar{\mathbf{D}}\mathbf{A}$ where $\bar{\mathbf{D}}$ is an $N{\times}N$ block diagonal matrix of the form $\bar{\mathbf{D}} = \mathrm{diag}\{\bar{\mathbf{D}}_0, \ldots, \bar{\mathbf{D}}_{L-1}\}$. Obviously, this matrix is hermitian and correspondingly the block matrices $\bar{\mathbf{D}}_\ell$s are hermitian as well. Similar to (3.11), the closed form for the elements of $\bar{\mathbf{D}}_\ell$s will be

$$\left[\bar{\mathbf{D}}_\ell\right]_{m,p} = \begin{cases} 1 + {\sigma_\nu}^2, & \epsilon_i = \epsilon_j,\ m = p \\ 0, & \epsilon_i = \epsilon_j,\ m{\neq}p \\ e^{\frac{j2\pi\xi_{pm}}{N}((-\ell))_L} f_{KQ}(\xi_{pm}), & \epsilon_i{\neq}\epsilon_j \end{cases} \tag{3.18}$$

for $\ell = 0, \ldots, L-1$ and $m, p = 0, \ldots, KQ-1$. Thus, elements in $\bar{\mathbf{D}}_\ell$s all have the same amplitude and are only different in phase and we have

$$\bar{\mathbf{D}}_\ell = \bar{\mathbf{E}}_\ell \odot \bar{\mathbf{D}}_0 \tag{3.19}$$

Table 3.1 Computational Cost of Different CFO Compensation Techniques

Technique	Number of Complex Multiplications
Direct ZF	$\frac{1}{3}N^3 + 2N^2 + \frac{KN}{2}\log_2 N$
Newton-based ZF, [85]	$(2^I - 1)(\frac{(K+1)N}{2}\log_2 N + KN) + \frac{KN}{2}\log_2 N$
Proposed ZF	$\frac{5}{6}(KQ)^3 + (2L + \frac{5}{4})(KQ)^2 - \frac{5}{6}(KQ) + N\log_2 L$
Direct MMSE	$\frac{5}{6}N^3 + \frac{5}{2}N^2 + \frac{KN}{2}\log_2 N$
CG, [86]	$I(KN\log_2 N + 2KN + 5N) + KN\log_2 N + 2KN$
Proposed MMSE	$\frac{1}{2}(KQ)^3 + (\frac{7}{2}L + \frac{15}{8})(KQ)^2 - (\frac{L}{2} + \frac{1}{8})(KQ) + N\log_2 L$

where $[\bar{\mathbf{E}}_\ell]_{m,p} = e^{\frac{j2\pi\xi pm}{N}(L-\ell)}$ for $\ell = 1, \ldots, L-1$ and $m, p = 0, \ldots, KQ-1$. Finally,

$$(\mathbf{\Lambda}^{\mathrm{H}}\mathbf{\Lambda} + {\sigma_\nu}^2\mathbf{I}_N)^{-1} = \mathbf{A}^{\mathrm{H}}\bar{\mathbf{D}}^{-1}\mathbf{A} \tag{3.20}$$

where $\bar{\mathbf{D}}^{-1} = \mathrm{diag}\{\bar{\mathbf{D}}_0^{-1}, \ldots, \bar{\mathbf{D}}_{L-1}^{-1}\}$ and $\bar{\mathbf{D}}_\ell^{-1} = \bar{\mathbf{E}}_\ell^{\mathrm{H}} \odot \bar{\mathbf{D}}_0^{-1}$. Therefore, we only need to find $\bar{\mathbf{D}}_0^{-1}$. Furthermore, it can be easily shown that $\bar{\mathbf{D}}_0 = \mathbf{D}_0^{\mathrm{H}}\mathbf{D}_0 + {\sigma_\nu}^2\mathbf{I}_{KQ}$ and $\bar{\mathbf{D}}_0$ is a hermitian positive definite matrix. Consequently, it can be inverted efficiently using Cholesky decomposition which requires a lower number of computations compared with direct matrix inversion.

Substituting (3.20) and conjugate transpose of (3.10) into (3.6), we have

$$\hat{\mathbf{z}}_{\mathrm{MMSE}}[n] = \mathbf{A}^{\mathrm{H}}\bar{\mathbf{D}}^{-1}\mathbf{D}^{\mathrm{H}}\mathbf{A}\bar{\mathbf{r}}[n]. \tag{3.21}$$

In the same fashion as for $\hat{\mathbf{z}}_{\mathrm{ZF}}[n]$, matrix multiplications may be implemented efficiently using FFTs and IFFTs and the matrices $\mathbf{D}^{\mathrm{H}}$ and $\bar{\mathbf{D}}^{-1}$ can be easily found from the above derivations and those in section 3.1.2. If we start from the right hand side of the equation (3.21), the $N \times 1$ vector $\mathbf{A}\bar{\mathbf{r}}[n]$ can be obtained by the application of several FFTs. Then we need to multiply the block diagonal matrix $\mathbf{D}^{\mathrm{H}}$ to the resulting vector to obtain another $N \times 1$ vector and the rest is the same as for calculation of $\hat{\mathbf{z}}_{\mathrm{ZF}}[n]$.

3.1.4 Computational complexity

Table 3.1 summarizes the computational complexity of the CFO compensation techniques proposed in sections 3.1.2 and 3.1.3 as well as the ones presented in [85] and [86] for the uplink of OFDMA-based systems. It is worth mentioning that the proposed solutions in [85] and [86] are known to have the lowest complexity among

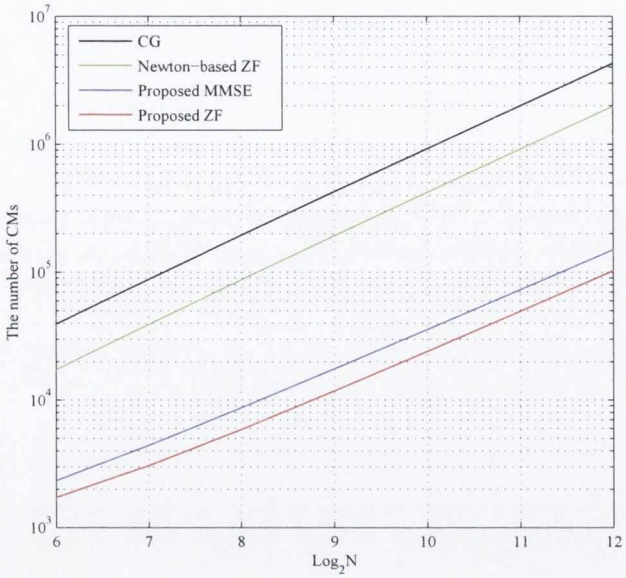

Fig. 3.1 Computational cost of CFO compensation with respect to the number of subcarriers for the case of I-CAS with $K = 8$.

all the available solutions that are applicable to I-CAS and BI-CAS. It is assumed that N subcarriers are allocated to K users based on BI-CAS with Q subcarriers in each block. Therefore, the total number of subcarrier blocks assigned to each user is $L = \frac{N}{KQ}$. As mentioned before, for the case of I-CAS, the parameter Q reduces to 1. Parameter I in the table indicates the number of iterations in the conjugate gradient (CG), [86], and Newton-based ZF, [85], algorithms. Since all the operations include complex numbers, the complexity expressions are presented based on the number of complex multiplications (CMs). Direct ZF and MMSE techniques involve direct computation of the inverse of the interference matrices $\mathbf{\Lambda}$ and $\mathbf{\Lambda}^{\mathrm{H}}\mathbf{\Lambda}$ without exploiting their special properties.

For a fair comparison, the number of iterations for the CG and Newton-based ZF algorithms needs to be chosen to have optimal performance while having the lowest possible computational cost. Based on the results in [86] and [85], to reach the optimal performance in a system with I-CAS, the number of iterations for the CG and Newton-based ZF algorithms needs to be at least equal to K and 3, respectively. A system with BI-CAS and K users where the number of subcarriers in each block are assumed to be Q, can be considered as a system with I-CAS and KQ users where each Q consecutive users experience the same CFOs. Since the Newton-based ZF technique is only applicable to I-CAS [85], in order to be able to use it in BI-CAS

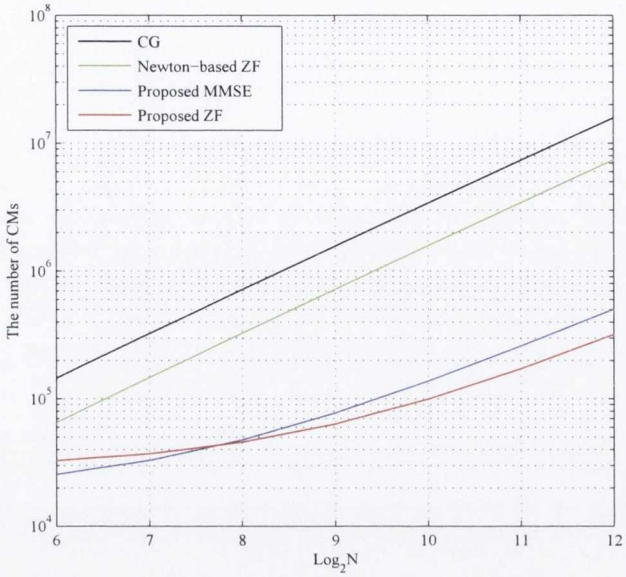

Fig. 3.2 Computational cost of CFO compensation with respect to the number of subcarriers for the case of BI-CAS with $Q = 4$ and $K = 8$.

scenario, we suppose having KQ distinct users with $I = 3$. Based on the results of [86], we consider $I = 32$ for the CG solution when we have 8 users with BI-CAS.

Direct ZF, Newton-based ZF and the proposed ZF solution are all ZF-based compensation techniques. Also, Direct MMSE, CG and the proposed MMSE algorithms all belong to the class of MMSE-based compensation techniques. Therefore, we compare the complexity of each class of compensators separately; due to the fact that they have different performance with respect to each other. Typically, the number of subcarriers in the standards like IEEE 802.16e and 3GPP LTE lies in the range of 128 to 2048. Therefore, the same range is considered here for the complexity analysis. Since the BI-CAS with $Q = 4$ is adopted in the partially used subchanneling (PUSC) mode of IEEE 802.16e [42], the same Q is considered for the complexity analysis in the case of BI-CAS. Since direct ZF and MMSE algorithms need inversion of $N \times N$ matrices and based on the results in [86] and [85], their computational complexity is much higher than that of the Newton-based ZF and CG techniques. Thus, we do not include their complexity in the results of Figs. 3.1, 3.2 and 3.3.

Fig. 3.1 shows the computational costs of the proposed algorithms and other approaches with respect to the number of subcarriers for the case of I-CAS when $K = 8$. For the case of $N = 1024$ and $K = 8$ with I-CAS, complexity of the proposed ZF technique with respect to the Newton-based ZF and direct ZF algorithms is 5.7%

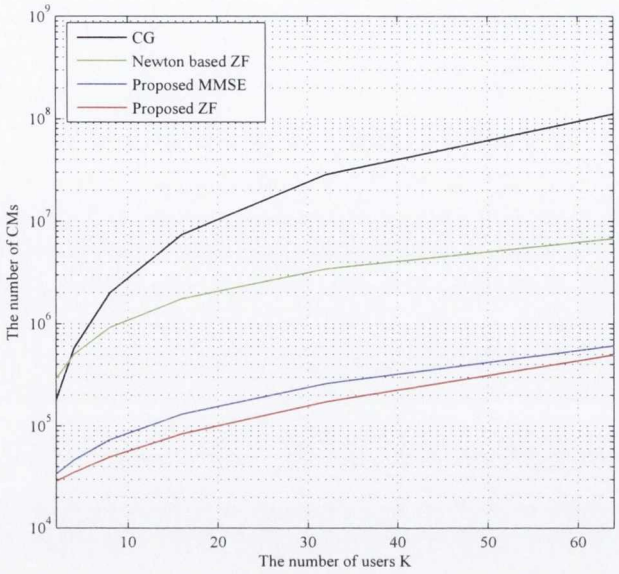

Fig. 3.3 Computational cost of CFO compensation with respect to the number of users for the case of I-CAS with $N = 2048$.

and 0.0067%, respectively, while the complexity of the proposed MMSE solution over CG and direct MMSE algorithms is 3.8% and 0.004%, respectively. As is clear in Fig. 3.2, in the case of BI-CAS, the number of CMs for all the compared algorithms is increased in comparison with I-CAS. However, the difference in the number of CMs between the proposed algorithms and their equivalents is still substantial. Generally, as can be seen in Figs. 3.1 and 3.2 the computational costs of the proposed algorithms are close to each other either in the case of I-CAS or BI-CAS. Fig. 3.3 illustrates the number of CMs according to the number of users for the case of I-CAS when $N = 2048$. Also for different number of users, the proposed solutions offer lower computational load than the existing techniques.

3.2 CFO correction in generalized CAS

In generalized carrier assignment scheme, there is no particular association between the subcarrier placements and users. Hence, G-CAS allows dynamic carrier allocation and higher flexibility than other carrier allocation schemes. Since, there is no certain order in the placement of the users' subcarriers in the uplink of an OFDMA system with G-CAS, as opposed to block carrier allocation scheme (B-CAS), I-CAS and BI-CAS, the interference matrix does not have a fixed structure to be harnessed for

finding ZF or MMSE estimates of the transmitted data symbols with a low complexity. Accordingly, low complexity CFO correction in systems with G-CAS is a challenging task.

Among all the available solutions in the literature, there are a number of solutions that are relevant to this section, [47, 83, 84]. In [83], Cao et al suggest to approximate the interference matrix by a banded matrix, simply by assuming that the elements of the matrix outside a bandwidth D (a design parameter) are equal to zero. It is then noted that this approximation of the interference matrix can be used to find the desired solution with a low computational complexity that is in the order of ND^2, where N is the total number of subcarriers. However, as mentioned in [47], this approximation results in a significant performance loss especially when users with large CFOs are present in the network. Hence, this may not be a viable solution in practice. Huang et al, [84], have proposed an iterative ICI cancellation technique based on the Neumann power series expansion. However, it has been noted that this method has certain limitations in terms of carrier allocation. In [47], Lee et al introduced an MMSE compensation technique using conjugate gradient algorithm. This method has a much lower complexity compared to its predecessors and is also applicable to the systems that use the generalized carrier allocation scheme, while maintaining the optimal performance. It is worth mentioning that CG algorithm is a fast implementation of MMSE solution and provides the same result as the direct MMSE solution [47]. Thus, in the rest of this section, we choose the CG algorithm as a benchmark.

The challenge for this section, therefore, is to design a CFO compensation technique which has the following traits - (1) it is suitable for a wide range of CFOs (2) it has a lower computational complexity than our benchmark (CG algorithm) and (3) it is applicable to G-CAS. To this end, we have investigated several solutions based on the linear ZF and MMSE criteria. For some reasons that will become clear by the end of this chapter, we suggest ZF as the best solution for CFO compensation in the uplink both from implementation and performance viewpoints.

Our solution combines a number of different ideas and concepts. It is based on time domain windowing approaches. It draws on the fact that the quasi-banded property can reduce the CFO compensation complexity in OFDMA systems and hence introduces a means of confining the interference matrix to a quasi-banded one to avail of this. However, it goes much further in the reduction of complexity through the introduction of a ZF technique based on LU-factorization. As it will be shown in the following sections, this results in a technique that can work with all values

of CFOs within the range of $\pm 50\%$ of the subcarrier spacing, is over an order of magnitude lower in complexity than our benchmark CG algorithm, and can be used in G-CAS scenarios. Furthermore, we show even more complexity reduction (two orders of magnitude) still is possible in cases where CFOs are less than 25% of the subcarrier spacing through our proposed ZF technique based on Neumann series.

The significant reduction in complexity that our algorithms provide comes at the expense of some moderate loss in bandwidth efficiency which is due to the need for longer cyclic extensions in OFDM signal required for time domain windowing operations. Hence, there is a tradeoff between computational complexity and bandwidth efficiency. In some scenarios like small cells, the channel transient is small and hence some samples in CP remain unaffected by the channel. Therefore, one can utilize those samples to perform the receiver windowing operation that is proposed in this chapter. In addition, our solution is attractive to some emerging applications like *machine type communications* and *Internet of Things* (IoT) where there is a large number of users in a cell with different CFOs. In these applications, our proposed solutions can provide the optimal performance with an affordable computational complexity and as these systems do not need to have very high bit rates, the bandwidth efficiency loss due to windowing operation may not be critical, [108].

In the following sections, the concept of receiver filtering is first introduced and then ZF and MMSE based CFO correction in an OFDMA uplink receiver with receiver windowing is presented. It is worth mentioning that in the remainder of this chapter, in order to perform time domain receiver windowing, we consider an OFDMA system that uses a cyclic suffix (CS) apart from CP. As a result, the transmit symbol for user i is $\mathbf{x}^{(i)}[n] = \mathbf{T}\mathbf{F}_N^{\mathrm{H}}\mathbf{x}_{\mathrm{f}}^{(i)}[n]$ where $\mathbf{T} = [\mathbf{G}_{\mathrm{CP}}^{\mathrm{T}}, \mathbf{I}_N^{\mathrm{T}}, \mathbf{G}_{\mathrm{CS}}^{\mathrm{T}}]^{\mathrm{T}}$ is the corresponding cyclic extension matrix which is an $N_T \times N$ matrix. N_T is the length of an OFDMA symbol and $N_T = N + N_{\mathrm{CP}} + N_{\mathrm{CS}}$. The rows of $\mathbf{G}_{\mathrm{CP}}$ and $\mathbf{G}_{\mathrm{CS}}$ matrices include the last N_{CP} and the first N_{CS} rows of the identity matrix $\mathbf{I}_N$, respectively.

3.2.1 Receiver filtering for ICI reduction

In conventional OFDMA receivers, after removing the cyclic extensions, DFT is applied to the received signal. This is equivalent to analyzing each received OFDM symbol through a bank of filters that are characterized by a rectangular prototype filter. Due to the fact that the rectangular filter has large side-lobes in its frequency response, such a filter bank system is prone to a significant amount of ICI when different subcarriers are not synchronized in frequency with respect to each other.

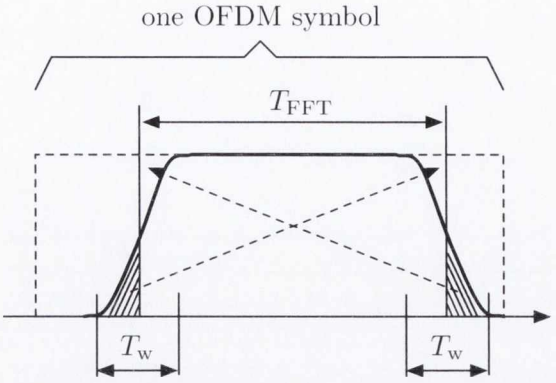

Fig. 3.4 A raised-cosine window and the process of aliasing in time domain. The excess samples beyond the length T_{FFT} on each side are added to the attenuated samples on the other side.

In order to reduce ICI to a limited number of adjacent subcarriers and hence, make the interference matrix quasi-banded[2], we borrow the following idea from the discrete multi-tone (DMT) literature[3]. To mitigate near-end cross-talk and radio frequency interference in very high bit-rate digital subscriber lines (VDSL), the authors of [109] proposed to replace the rectangular prototype filter/window in an OFDM receiver by a window with smooth roll-offs at the sides, e.g., see Fig. 3.4. A raised-cosine window is proposed for this application in [109]. Further study, in [15], indicates that the raised-cosine window is a good compromise choice. On the other hand, it is also noted in [109] that since the number of samples in the time domain are $N + N_{\mathrm{w}}$ and given that we need to analyze the signal samples in the frequency domain at N equally spaced samples, one may conveniently alias the time domain signal, as shown in Fig. 3.4, and then apply an N-point DFT to the result.

An analysis of the raised-cosine window that provides insight to its impact on side-lobe suppression is recently reported in [15]. It is noted that if T_{FFT} denotes the length of DFT and T_{w} the duration of the roll-off at each side, the raised-cosine window can be mathematically expressed as

$$g(t) = \mathrm{rect}\left(\frac{t - T_{\mathrm{FFT}}/2}{T_{\mathrm{FFT}}}\right) * c(t), \tag{3.22}$$

[2]A quasi-banded matrix with bandwidth of $2D + 1$ is a matrix containing nonzero elements in the main diagonal, D bilateral diagonals around the main diagonal and D diagonals at the top-right and bottom-left corners of the matrix and the remaining elements are all zeros.

[3]DMT is the equivalent name for OFDM in the digital subscriber lines (DSL) literature.

where

$$c(t) = \frac{\pi}{2T_{\mathrm{w}}} \sin\left(\frac{\pi t}{T_{\mathrm{w}}}\right) \mathrm{rect}\left(\frac{t - T_{\mathrm{w}}/2}{T_{\mathrm{w}}}\right), \tag{3.23}$$

and $\mathrm{rect}(\cdot)$ is the rectangular function. Accordingly, in the frequency domain,

$$|G(f)| = T_{\mathrm{FFT}} |\mathrm{sinc}(fT_{\mathrm{FFT}})| \times |C(f)|, \tag{3.24}$$

and

$$|C(f)| = \left|\frac{\cos(\pi f T_{\mathrm{w}})}{1 - 4f^2 T_{\mathrm{w}}^2}\right|. \tag{3.25}$$

A point to note here is that $|C(f)|$ has a 'sinc' shape with the main lobe of $3/T_{\mathrm{w}}$ wide. It also drops to below -12 dB beyond the frequency range $(-1.1/T_{\mathrm{w}}, 1.1/T_{\mathrm{w}})$. If this attenuation is taken as sufficient to suppress the subcarrier side-lobes (numerical results presented later in Fig. 3.6 show this is a good compromise choice), one will find that the interference matrix becomes (with a good approximation) quasi-banded with a bandwidth of $2\lfloor 1.1T_{\mathrm{FFT}}/T_{\mathrm{w}} \rfloor + 1$, where $\lfloor \cdot \rfloor$ rounds down the number inside. It is worth nothing that beside raised-cosine window, other window choices have been examined in [15]. The conclusion here is that raised cosine provides a good compromise choice. In the context of the work presented in this chapter, raised cosine window provides a good balance between the reduction of the bandwidth D and suppression of the out of band signals. In our study, we also examined this point by exploring the performance of our system when we used the trapezoidal window as well as other window functions based on Hamming and Hanning functions and the ultimate conclusion was the same as the one in [15].

As mentioned earlier, each OFDMA symbol has N_{CP} and N_{CS} cyclic extension samples at the beginning and the end, respectively. Since, the first N_{GI} samples of the received signal at BS, i.e., $\tilde{\mathbf{r}}[n]$ in (2.10), are affected by the channels of the users, in order to avoid ISI and also leave enough samples for the receiver windowing process, the lengths of the CP and CS need to be $N_{\mathrm{GI}} + \frac{N_{\mathrm{w}}}{2}$ and $\frac{N_{\mathrm{w}}}{2}$, respectively. Discarding the first N_{GI} samples using guard interval removal matrix $\mathbf{R}_{\mathrm{GI}} = [\mathbf{0}_{(N+N_{\mathrm{w}})\times N_{\mathrm{GI}}}, \mathbf{I}_{(N+N_{\mathrm{w}})}]$, we have

$$\mathbf{r}[n] = \sum_{i=1}^{K} e^{\frac{j2\pi\epsilon_i N_{\mathrm{GI}}}{N}} \widetilde{\mathbf{\Phi}}(\epsilon_i) \bar{\mathbf{T}} \mathbf{H}_{\mathrm{t}}^{(i)} \mathbf{x}_{\mathrm{t}}^{(i)}[n] + \mathbf{R}_{\mathrm{GI}} \boldsymbol{\nu}, \tag{3.26}$$

where $\widetilde{\mathbf{\Phi}}(\epsilon_i) = \mathrm{diag}(1, e^{\frac{j2\pi\epsilon_i}{N}}, \ldots, e^{\frac{j2\pi\epsilon_i(N+N_{\mathrm{w}}-1)}{N}})$ and $\bar{\mathbf{T}} = [\mathbf{G}_{\mathrm{W}}^{\mathrm{T}}, \mathbf{I}_N^{\mathrm{T}}, \mathbf{G}_{\mathrm{CS}}^{\mathrm{T}}]^{\mathrm{T}}$. The sub-matrices $\mathbf{G}_{\mathrm{W}}$ and $\mathbf{G}_{\mathrm{CS}}$ are of the size $\frac{N_{\mathrm{w}}}{2} \times N$ and consist of the last and the first $\frac{N_{\mathrm{w}}}{2}$ rows of the identity matrix $\mathbf{I}_N$, respectively. $\mathbf{H}_{\mathrm{t}}^{(i)}$ is the $N \times N$ circulant channel

matrix of user i with the first column $\mathbf{h}^{(i)}$ being zero padded to have the length of N. The windowed and aliased signal can be presented as

$$\mathbf{r}'[n] = \sum_{i=1}^{K} e^{\frac{j2\pi\epsilon_i N_{\mathrm{GI}}}{N}} (\bar{\mathbf{T}}^{\mathrm{T}}\mathbf{W}\widetilde{\mathbf{\Phi}}(\epsilon_i)\bar{\mathbf{T}})\mathbf{H}_{\mathrm{t}}^{(i)}\mathbf{x}_{\mathrm{t}}^{(i)}[n] + \bar{\mathbf{T}}^{\mathrm{T}}\mathbf{W}\mathbf{R}_{\mathrm{GI}}\boldsymbol{\nu}, \tag{3.27}$$

where $\mathbf{W} = \mathrm{diag}(\mathbf{w}_{\mathrm{rc}})$, $\mathbf{w}_{\mathrm{rc}}$ is the raised-cosine window vector and $\bar{\mathbf{T}}^{\mathrm{T}}$ does the aliasing operation. Since, $\mathbf{H}_{\mathrm{t}}^{(i)}$ is a circulant matrix, it can be spectrally factorized as $\mathbf{F}_N^{\mathrm{H}}\mathbf{H}_{\mathrm{f}}^{(i)}\mathbf{F}_N$ where $\mathbf{H}_{\mathrm{f}}^{(i)}$ is the $N\times N$ diagonal matrix whose diagonal elements are the channel frequency response of the user i. Hence, $\mathbf{H}_{\mathrm{t}}^{(i)}\mathbf{x}_{\mathrm{t}}^{(i)}[n]$ can be written as $\mathbf{F}_N^{\mathrm{H}}\mathbf{H}_{\mathrm{f}}^{(i)}\mathbf{x}_{\mathrm{f}}^{(i)}[n]$ and after passing the signal through the DFT block, we have

$$\begin{aligned}
\bar{\mathbf{r}}[n] &= \mathbf{F}_N\mathbf{r}'[n] \\
&= \sum_{i=1}^{K} e^{\frac{j2\pi\epsilon_i N_{\mathrm{GI}}}{N}} (\mathbf{F}_N\bar{\mathbf{T}}^{\mathrm{T}}\mathbf{W}\widetilde{\mathbf{\Phi}}(\epsilon_i)\bar{\mathbf{T}}\mathbf{F}_N^{\mathrm{H}})\mathbf{H}_{\mathrm{f}}^{(i)}\mathbf{x}_{\mathrm{f}}^{(i)}[n] + \tilde{\boldsymbol{\nu}} \\
&= \boldsymbol{\Lambda}\mathbf{z}[n] + \tilde{\boldsymbol{\nu}},
\end{aligned} \tag{3.28}$$

where

$$\mathbf{z}[n] = \sum_{i=1}^{K} e^{\frac{j2\pi\epsilon_i N_{\mathrm{GI}}}{N}} \mathbf{H}_{\mathrm{f}}^{(i)}\mathbf{x}_{\mathrm{f}}^{(i)}[n] = \bar{\mathbf{H}}_{\mathrm{f}}\bar{\mathbf{d}}[\mathbf{n}], \tag{3.29}$$

and

$$\boldsymbol{\Lambda} = \sum_{i=1}^{K} \mathbf{F}_N\bar{\mathbf{T}}^{\mathrm{T}}\mathbf{W}\widetilde{\mathbf{\Phi}}(\epsilon_i)\bar{\mathbf{T}}\mathbf{F}_N^{\mathrm{H}}\mathbf{\Pi}_i, \tag{3.30}$$

is the $N\times N$ interference matrix and $\tilde{\boldsymbol{\nu}} = \mathbf{F}_N\bar{\mathbf{T}}^{\mathrm{T}}\mathbf{W}\mathbf{R}_{\mathrm{GI}}\boldsymbol{\nu}$. $\bar{\mathbf{H}}_{\mathrm{f}}$ is an $N\times N$ diagonal matrix which contains the composite channel frequency responses of all the users in its diagonal elements. It is worth mentioning that the phase factors $e^{\frac{j2\pi\epsilon_i N_{\mathrm{GI}}}{N}}$ are absorbed into the composite channel of the users. The composite data vector $\bar{\mathbf{d}}[n]$ includes the information symbols of all the users corresponding to their allocated subcarriers as if there has been no interference that are transmitted on the n^{th} OFDMA symbol.

As noted before, windowing at the receiver confines the interference generated by each subcarrier only to a number of its neighbouring subcarriers which depends on the roll-off factor of the window. Fig. 3.5, shows a snapshot of the interference power from each subcarrier to the others for both cases of OFDMA system with and without receiver windowing. In Fig. 3.5, we consider an OFDMA system with 32 subcarriers and 4 users with G-CAS. The CFOs are randomly chosen from a uniform distribution in the range $(-0.5, 0.5]$. From Fig. 3.5, one may notice that the interference power

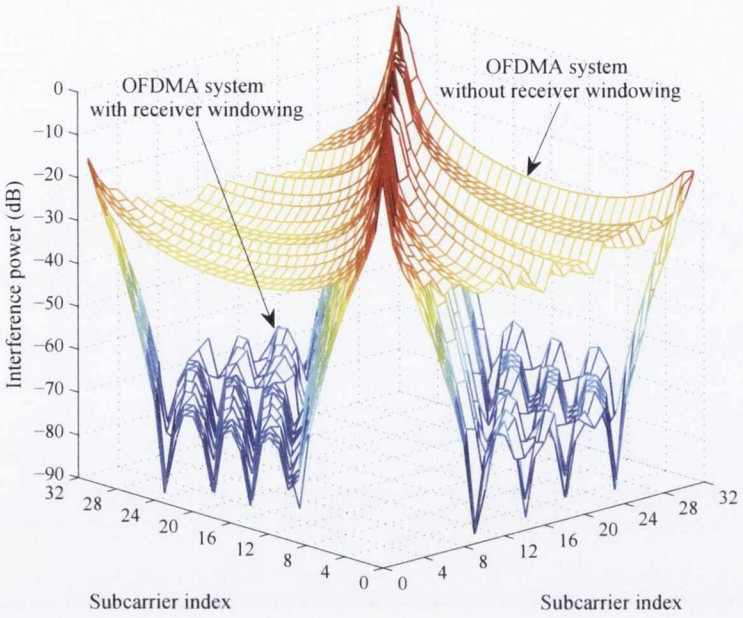

Fig. 3.5 Interference power between different subcarriers for G-CAS case when $N = 32$, $K = 4$, $N_{\mathrm{w}} = 8$, CFOs $= [0.20, -0.35, 0.45, -0.11]$ for the systems with and without receiver filtering.

from each subcarrier to the others in the system with receiver filtering is very small after a certain modulo-N distance and hence may be considered as negligible. Thus, the interference matrix can be approximated with a quasi-banded matrix with very good precision. The simulation results which will be presented in Section 3.2.5 will attest to this fact. It can be inferred from Fig. 3.5 that approximation of the interference matrix, in the system without receiver windowing, with a banded matrix as is proposed in [83] will result in a significant performance loss in presence of large CFOs [47].

Accordingly, we can write the interference matrix as the summation of a quasi-banded matrix, $\mathbf{\Lambda}_{\mathrm{QB}}$, and the matrix $\mathbf{\Lambda}_{\mathrm{I}}$ which contains the negligible elements of $\mathbf{\Lambda}$ outside the certain bandwidth of $2D + 1$.

$$[\mathbf{\Lambda}_{\mathrm{QB}}]_{m,p} = \begin{cases} [\mathbf{\Lambda}]_{m,p}, & |m-p| < D, \\ & \text{and } |m-p| > N-D, \\ 0, & \text{otherwise}, \end{cases} \tag{3.31}$$

where the bandwidth of the matrix $\mathbf{\Lambda}_{\mathrm{QB}}$ is $2D+1$. Also, $\mathbf{\Lambda}_{\mathrm{I}} = \mathbf{\Lambda} - \mathbf{\Lambda}_{\mathrm{QB}}$.

Discussion

As mentioned earlier, the CS samples can be absorbed into CP. The usual value for the CP length in IEEE 802.11 and 802.16 standards is $0.25N$, [31, 41, 42]. This is a relatively long period for CP, and is to serve the largest possible cell sizes. In smaller cells, the channel transient time gets shorter and only a small part of CP is affected by the channel delay spread. Therefore, a large number of CP samples remain intact and can be used for receiver windowing. In this case, the parameters N_{w} and D can be chosen based on the channel delay spread. One may first count the number of samples that are left for receiver windowing, i.e, $N_{\mathrm{w}} = N_{\mathrm{CP}} - N_{\mathrm{ch}}$. Consequently, the parameter D needs to be designed in a way not to neglect the dominant interference terms of the matrix $\mathbf{\Lambda}$. To that end, the maximum CFO, $\epsilon_{\max} = \max |\epsilon_i|$ for $i = 0, \ldots, K-1$, should be considered and the interference terms due to $\epsilon_{\max}$ need to be generated. The interference terms can be obtained by taking N-point DFT from the main diagonal of the matrix

$$\mathbf{\Xi} = \bar{\mathbf{T}}^{\mathrm{T}} \mathbf{W} \widetilde{\mathbf{\Phi}}(\epsilon_{\max}) \bar{\mathbf{T}}, \tag{3.32}$$

where $\widetilde{\mathbf{\Phi}}(\epsilon_{\max}) = \mathrm{diag}(1, e^{\frac{j2\pi\epsilon_{\max}}{N}}, \ldots, e^{\frac{j2\pi\epsilon_{\max}(N+N_{\mathrm{w}}-1)}{N}})$, $\mathbf{\Xi} = \mathrm{diag}(\boldsymbol{\xi})$ and $\boldsymbol{\xi}$ contains the windowed and aliased version of the vector $[1, e^{\frac{j2\pi\epsilon_{\max}}{N}}, \ldots, e^{\frac{j2\pi\epsilon_{\max}(N+N_{\mathrm{w}}-1)}{N}}]^{\mathrm{T}}$. Thus, the interference terms can be found as $\boldsymbol{\chi} = \mathbf{F}_N \boldsymbol{\xi}$. The interference terms in the vector $\boldsymbol{\chi}$ with the power less than -60dB may be neglected and replaced by zero. Accordingly, the number of non-zero elements that remain is equal to $2D+1$. Thereby, the parameter D can be designed.

As a case in point, Fig. 3.6 illustrates the interference terms for different values of N_{w} and the threshold line of -60dB for an uplink scenario where $N = 256$ and $\epsilon_{\max} = 0.4$. As mentioned above, the interference terms below this threshold are negligible and can be replaced by zero. Additionally, Fig. 3.6 depicts the localization of interference power with respect to different values of N_{w}. As can be seen, the system without receiver windowing suffers from a large amount of interference and none of the interference terms falls below -60dB. In contrast, for the system with receiver windowing and $N_{\mathrm{w}} = 10$ a large number of interference terms fall below -60dB and as N_{w} increases to 26 the interference power becomes more localized. As a result, a larger number of interference terms can be neglected and the bandwidth of the interference matrix is further reduced.

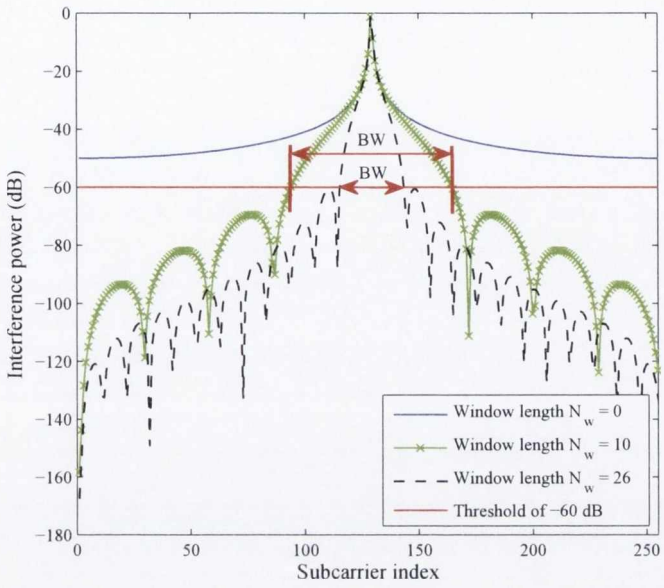

Fig. 3.6 Interference power for different values of N_{w} and the threshold line of -60dB for an uplink scenario where $N = 256$ and $\epsilon_{\max} = 0.4$.

3.2.2 Zero forcing CFO correction

Since, the interference matrix is full rank (see Appendix A, for a proof); given the received signal model in (3.28), the ICI caused by multiple CFOs can be completely removed based on the ZF criterion [83], viz.,

$$\hat{\mathbf{z}}_{\mathrm{ZF}}[n] = \mathbf{\Lambda}^{-1}\bar{\mathbf{r}}[n] = \mathbf{z}[n] + \mathbf{\Lambda}^{-1}\tilde{\boldsymbol{\nu}}. \tag{3.33}$$

However, in practice, where N may be many hundreds, or even thousands, the computational complexity of the matrix inversion in (3.33) may be prohibitively high. Examples are in WiMAX IEEE 802.16e and 3GPP LTE standards, where N can be as large as 2048 [42, 43].

As noted in section 3.2.1, due to the effect of receiver filtering, the interference matrix $\mathbf{\Lambda}$ can be approximated with the quasi-banded matrix $\mathbf{\Lambda}_{\mathrm{QB}}$. This, as shown in the rest of this section, allows one to implement the ZF and MMSE solutions with an affordable complexity.

ZF solution is expressed as

$$\hat{\mathbf{z}}_{\mathrm{ZF}}[n] = \mathbf{\Lambda}_{\mathrm{QB}}^{-1}\bar{\mathbf{r}}[n] = \mathbf{z}[n] + \mathbf{\Lambda}_{\mathrm{QB}}^{-1}\mathbf{\Lambda}_{\mathrm{I}}\mathbf{z}[n] + \mathbf{\Lambda}_{\mathrm{QB}}^{-1}\tilde{\boldsymbol{\nu}}. \tag{3.34}$$

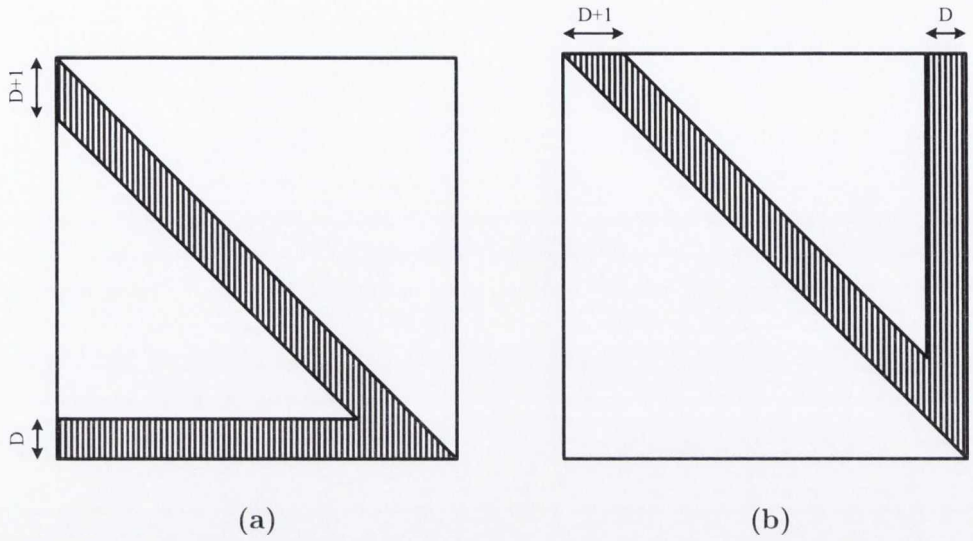

Fig. 3.7 **(a)** and **(b)** depict the structure of $\mathbf{L}$ and $\mathbf{U}$ matrices after LU factorization of a quasi-banded matrix, respectively.

Clearly, the approximation of $\mathbf{\Lambda}$ by the banded matrix $\mathbf{\Lambda}_{\mathrm{QB}}$ results in some residual interference; the second term on the right-hand side of (3.34). However, as will be shown in section 3.2.5, this residual interference is so negligible that does not have any impact on the bit error rate (BER) performance of the system and thus the term $\mathbf{\Lambda}_{\mathrm{QB}}^{-1}\mathbf{\Lambda}_{\mathrm{I}}\mathbf{z}[n]$ can be ignored in (3.34).

Due to the fact that receiver filtering does not bring a great amount of reduction to the subcarrier sidelobes that are close to the main lobe, [15], after receiver filtering, even for small CFO ranges the system with G-CAS suffers from a great amount of MAI which needs to be canceled. To this end, in the following subsections, we propose three CFO compensation techniques based on the ZF criterion. All of our proposed techniques have low computational complexity, thanks to the banded property of $\mathbf{\Lambda}_{\mathrm{QB}}$. Unlike solutions proposed in [85] and [20], our proposed techniques here are not limited to a particular subcarrier assignment. They both are applicable to G-CAS.

3.2.2.1 LU Factorization

Due to the banded form of the matrix $\mathbf{\Lambda}_{\mathrm{QB}}$, it can be efficiently factorized into a pair of lower and upper triangular matrices ($\mathbf{\Lambda}_{\mathrm{QB}} = \mathbf{LU}$). In general, LU factorization of a quasi-banded matrix leads to a pair of upper and lower triangular matrices with a V-shape structure, similar to the one in Fig. 3.7. However, in the case of interest in this section, since the off-diagonal elements of $\mathbf{\Lambda}_{\mathrm{QB}}$ are all less than one in amplitude

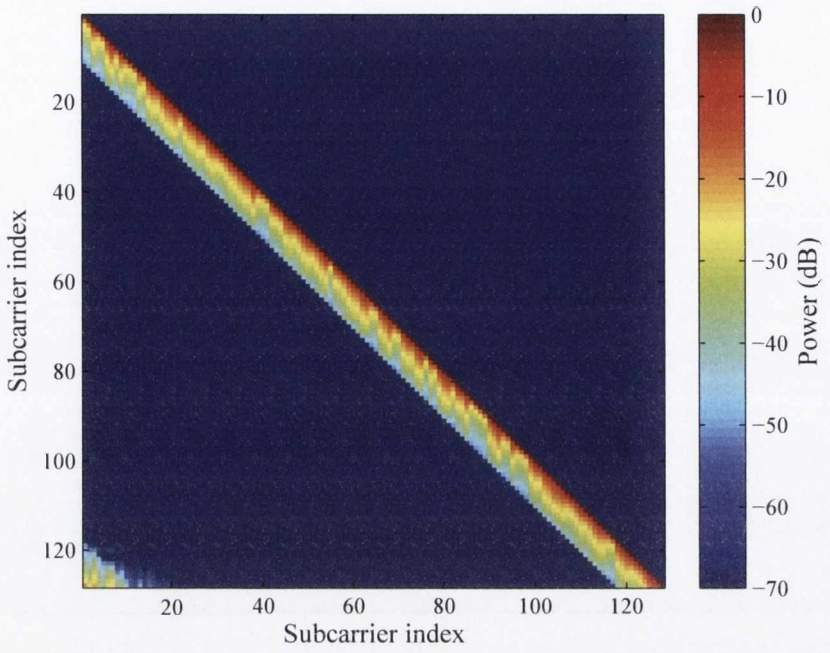

Fig. 3.8 The matrix $\mathbf{L}$ for G-CAS case when $N = 128$, $K = 4$, CFOs $= [0.27, -0.35, -0.43, 0.12]$.

and are decreasing very fast as they move away from the main diagonal, one will find that the elements of $\mathbf{L}$ and $\mathbf{U}$ matrices vanish as they move away from the corners. Fig. 3.8 highlights this fact for a typical example of the lower triangular matrix. Likewise, the upper triangular matrix follows the same structure as that of the matrix $\mathbf{L}^{\mathrm{T}}$. Hence, $\mathbf{L}$ and $\mathbf{U}$ can be approximated with lower and upper quasi-banded matrices, respectively. As a result, the LU factorization can be implemented with a low computational complexity.

Once the LU factorization is performed, the vector $\hat{\mathbf{z}}_{\mathrm{ZF}}[n]$ is calculated, simply, by using the forward and backward substitution method [110]. The large number of zero elements in the lower and upper triangular matrices significantly reduces the complexity of forward and backward substitutions. The numerical results in section 3.2.5 prove the high accuracy of this approximation when compared with the case where the full interference matrix is considered.

3.2.2.2 Truncated Neumann Series

The matrix $\mathbf{\Lambda}_{\mathrm{QB}}^{-1}$ can be approximated using truncated von Neumann series to reduce the computational cost of the ZF solution even more than that of the LU factorization

method. $\mathbf{\Lambda}_{\mathrm{QB}}$ can be written as the summation of its diagonal, $\mathbf{D}$, and its off-diagonal part, $\tilde{\mathbf{\Lambda}}$, and rearrange the result as

$$\begin{aligned}\mathbf{\Lambda}_{\mathrm{QB}} &= \mathbf{D} + \tilde{\mathbf{\Lambda}} \\ &= \mathbf{D}(\mathbf{I}_N + \mathbf{D}^{-1}\tilde{\mathbf{\Lambda}}).\end{aligned} \tag{3.35}$$

Next, we note that ${\mathbf{\Lambda}_{\mathrm{QB}}}^{-1} = (\mathbf{I}_N + \mathbf{D}^{-1}\tilde{\mathbf{\Lambda}})^{-1}\mathbf{D}^{-1}$ and $(\mathbf{I}_N + \mathbf{D}^{-1}\tilde{\mathbf{\Lambda}})^{-1}$ can be approximated using the M^{th} order truncation of the Neumann series

$$(\mathbf{I}_N + \mathbf{D}^{-1}\tilde{\mathbf{\Lambda}})^{-1} = \sum_{i=0}^{M}(-\mathbf{D}^{-1}\tilde{\mathbf{\Lambda}})^i, \tag{3.36}$$

if the spectral radius[4] of the matrix $\mathbf{D}^{-1}\tilde{\mathbf{\Lambda}}$ is smaller than one. A smaller spectral radius allows the adoption of a smaller value of M, and hence a further reduction of complexity in the implementation of (3.36).

Since, in G-CAS case, the interference matrix does not follow any particular structure, it is difficult (if not impossible) to mathematically identify the spectral radius of $\mathbf{D}^{-1}\tilde{\mathbf{\Lambda}}$. Here, we resort to a numerical analysis and find the probability density function (PDF) of the spectral radius of $\mathbf{D}^{-1}\tilde{\mathbf{\Lambda}}$ as CFOs take random values. Fig. 3.9 presents sample examples of such PDF for the cases where $N = 512, 1024$, $K = 4, 32$, and CFOs are chosen randomly from the interval of $[-0.25, 0.25]$. The PDFs are obtained based on 1,000,000 random choices of CFOs. For all the cases, the spectral radius of $\mathbf{D}^{-1}\tilde{\mathbf{\Lambda}}$ is limited by some upper bound that is less than one. In order to study the effect of the increase in the number of users we have considered the case where $N = 512, K = 32$ and compared it with the case where $N = 512, K = 4$. As it can be observed from Fig. 3.9, for the same number of subcarriers, as the number of users increases, the spectral radius becomes more concentrated to values around 0.4 with a higher probability. From comparison of the PDF of the cases where $N = 512, K = 32$ and $N = 1024, K = 32$, one can conclude that increasing the number of subcarriers does not have a dramatic effect on the lower and upper bound of the spectral radius of $\mathbf{D}^{-1}\tilde{\mathbf{\Lambda}}$. Additional tests reveal that the spectral radius of $\mathbf{D}^{-1}\tilde{\mathbf{\Lambda}}$ gets smaller as the range of CFOs reduces, and it gets larger as the range increases. For the broader ranges beyond $[-0.25, 0.25]$, the spectral radius of $\mathbf{D}^{-1}\tilde{\mathbf{\Lambda}}$ approaches one and in that case M has to be increased and this in turn increases the complexity. Moreover, as CFOs spread over a wider range, beyond $[-0.4, 0.4]$, the spectral radius of $\mathbf{D}^{-1}\tilde{\mathbf{\Lambda}}$

[4]The spectral radius of a square matrix $\mathbf{A}$ refers to the amplitude of its largest eigenvalue.

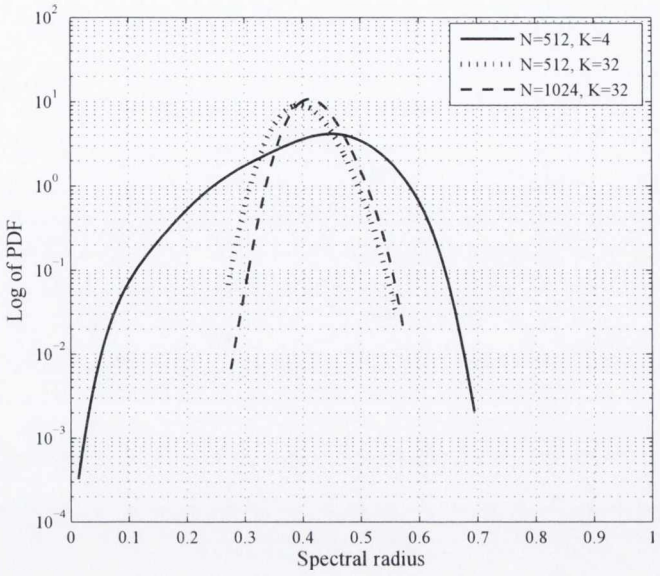

Fig. 3.9 Spectral radius of the matrix $\mathbf{D}^{-1}\tilde{\mathbf{\Lambda}}$ for a system with the CFOs in the range of $[-0.25, 0.25]$.

may exceed one and in that case the Neumann series diverges. Hence, the method described here will not be applicable.

Using (3.35) and (3.36) in (3.34), we obtain

$$\hat{\mathbf{z}}_{\mathrm{ZF}}^{(M)}[n] = \left(\sum_{i=0}^{M}(-\mathbf{D}^{-1}\tilde{\mathbf{\Lambda}})^{i}\right)\mathbf{D}^{-1}\bar{\mathbf{r}}[n]. \tag{3.37}$$

Taking note of the above observations, we propose to use the Neumann series expansion for the case where CFOs fall in a range of $[-0.25, 0.25]$ or smaller, and switch to other methods (e.g., the LU-factorization) when CFOs spread over a wider range. At the same time, it should be noted that the range $[-0.25, 0.25]$ is relatively relaxed and can be easily retained in practice, for example see [75] where the authors have argued that the range $[-0.2, 0.2]$ is a very relaxed one. They have noted that the aforementioned CFO range is much larger than the 2% maximum CFO requirement of IEEE 802.16a standard.

To keep the implementation complexity of equation (3.37) at a minimum level, it may be implemented recursively according to the algorithm listed in the following table (Algorithm 1). Each step of the algorithm involves a matrix by vector multiplication (multiplication of $-\mathbf{D}^{-1}\tilde{\mathbf{\Lambda}}$ by $\hat{\mathbf{z}}_{\mathrm{ZF}}^{(i-1)}[n]$) followed by a vector addition (addition of $\hat{\mathbf{z}}_{\mathrm{ZF}}^{(0)}[n]$). Moreover, noting that $-\mathbf{D}^{-1}\tilde{\mathbf{\Lambda}}$ is a very sparse matrix (most of

Algorithm 1 Interference cancellation algorithm based on truncated Neumann series

1: $\hat{\mathbf{z}}_{\mathrm{ZF}}^{(0)}[n] = \mathbf{D}^{-1}\bar{\mathbf{r}}[n]$ ▷ initialization
2: **for** $i = 1$ to M **do**
3: $\quad \hat{\mathbf{z}}_{\mathrm{ZF}}^{(i)}[n] = (-\mathbf{D}^{-1}\tilde{\mathbf{\Lambda}})\hat{\mathbf{z}}_{\mathrm{ZF}}^{(i-1)}[n] + \hat{\mathbf{z}}_{\mathrm{ZF}}^{(0)}[n]$
4: **end for**

its elements are zero), the complexity of the multiplication $(-\mathbf{D}^{-1}\tilde{\mathbf{\Lambda}})\hat{\mathbf{z}}_{\mathrm{ZF}}^{(i-1)}[n]$ remains relatively small; see Section 3.2.4 for details.

3.2.2.3 Conjugate Gradient Algorithm

The CG algorithm is only applicable to the linear systems of equations with positive definite and Hermitian coefficient matrices [111]. Therefore, in order to be able to estimate the transmitted symbols of different users based on the ZF criterion using the CG algorithm, both sides of (3.28) can be multiplied by $\mathbf{\Lambda}^{\mathrm{H}}$. Therefore, the ZF solution in (3.33) can be reformulated as $\hat{\mathbf{z}}_{\mathrm{ZF}}[n] = (\mathbf{\Lambda}^{\mathrm{H}}\mathbf{\Lambda})^{-1}\mathbf{\Lambda}^{\mathrm{H}}\bar{\mathbf{r}}[n]$. From approximation of $\mathbf{\Lambda}$ with $\mathbf{\Lambda}_{\mathrm{QB}}$, equation (3.34) can be rearranged as

$$\hat{\mathbf{z}}_{\mathrm{ZF}}[n] = \mathbf{P}_{\mathrm{ZF}}^{-1}\mathbf{\Lambda}^{\mathrm{H}}\bar{\mathbf{r}}[n], \tag{3.38}$$

where $\mathbf{P}_{\mathrm{ZF}} = \mathbf{\Lambda}^{\mathrm{H}}\mathbf{\Lambda}$. The Hermitian and positive definite property of $\mathbf{P}_{\mathrm{ZF}}$ allows utilization of the CG algorithm for another low complexity computation of $\hat{\mathbf{z}}_{\mathrm{ZF}}[n]$. This idea was first suggested in [47], where authors used the special structure of the interference matrix $\mathbf{\Lambda}$ to propose a low complexity MMSE solution. Although the same solution (with some minor modifications) is applicable to the case of interest to this section as well, here, the banded nature of $\mathbf{\Lambda}_{\mathrm{QB}}$ and $\mathbf{P}_{\mathrm{ZF}}$ allows a more direct and lower complexity implementation of the CG algorithm. The pseudo code that is presented under Algorithm 2 lists the CG algorithm when applied for computation of $\hat{\mathbf{z}}_{\mathrm{ZF}}[n]$, [111]. The subscript/superscript i indicates the iteration index, δ is the convergence tolerance and $\hat{\mathbf{z}}_{\mathrm{CG}}^{(i)}[n]$ is the estimation of $\hat{\mathbf{z}}_{\mathrm{ZF}}[n]$ at the i^{th} iteration of the CG algorithm. Finally, the vectors $\mathbf{d}_i$ and $\boldsymbol{\xi}_i$ denote the search direction and residual vectors in the i^{th} iteration, respectively. The complexity of this algorithm is dominated by matrix to vector multiplication $\mathbf{P}_{\mathrm{ZF}}\mathbf{d}_i$. In [47], the special form of $\mathbf{\Lambda}$ is taken advantage of and $\mathbf{P}_{\mathrm{ZF}}\mathbf{d}_i$ is implemented using a sequence of FFT/IFFT operations. Here, we note that since $\mathbf{P}_{\mathrm{ZF}}$ is banded (sparse), direct calculation of $\mathbf{P}_{\mathrm{ZF}}\mathbf{d}_i$ results in a lower complexity.

Algorithm 2 The CG algorithm

$\boldsymbol{\xi}_0 = \mathbf{P}_{\mathrm{ZF}}\hat{\mathbf{z}}_{\mathrm{CG}}^{(0)}[n] - \boldsymbol{\Lambda}_{\mathrm{QB}}^{\mathrm{H}}\bar{\mathbf{r}}[n]$
$\mathbf{d}_1 = \boldsymbol{\xi}_0$
$i = 0$
while $\|\boldsymbol{\xi}_i\| \geq \delta\|\boldsymbol{\xi}_0\|$ **do**
  $i = i + 1$
  $\alpha_i = \frac{\boldsymbol{\xi}_{i-1}^{\mathrm{H}}\boldsymbol{\xi}_{i-1}}{\mathbf{d}_i^{\mathrm{H}}\mathbf{P}_{\mathrm{ZF}}\mathbf{d}_i}$
  $\hat{\mathbf{z}}_{\mathrm{CG}}^{(i)}[n] = \hat{\mathbf{z}}_{\mathrm{CG}}^{(i-1)}[n] + \alpha_i\mathbf{d}_i$
  $\boldsymbol{\xi}_i = \boldsymbol{\xi}_{i-1} + \alpha_i\mathbf{P}_{\mathrm{ZF}}\mathbf{d}_i$
  $\gamma_i = \frac{\boldsymbol{\xi}_i^{\mathrm{H}}\boldsymbol{\xi}_i}{\boldsymbol{\xi}_{i-1}^{\mathrm{H}}\boldsymbol{\xi}_{i-1}}$
  $\mathbf{d}_{i+1} = \mathbf{d}_i + \gamma_i\mathbf{d}_i$
end while

The CG algorithm has to run over a number of iterations to converge. The number of iterations depends on the eigenvalue spread of the underlying matrix, $\mathbf{P}_{\mathrm{ZF}}$. In [47] it is noted that the eigenvalue spread of $\mathbf{P}_{\mathrm{ZF}}$ is rather limited and hence the authors have concluded that the CG algorithm will converge within a number of iterations that is much smaller than N. The same conclusion is applicable to our proposed implementation.

3.2.3 Minimum mean square error CFO correction

Even though the ZF solution removes the effect of the CFOs, multiplication of $\boldsymbol{\Lambda}_{\mathrm{QB}}^{-1}$ to the noise in (3.34) may result in noise enhancement. In order to avoid the noise enhancement problem, it is common to use MMSE criterion. This leads to a balance between residual self/multiple user interference and noise enhancement at the detector output. The MMSE solution of (3.28) with quasi-banded approximation of the interference matrix is given by

$$\hat{\mathbf{z}}_{\mathrm{MMSE}}[n] = \mathbf{P}^{-1}\boldsymbol{\Lambda}_{\mathrm{QB}}^{\mathrm{H}}\bar{\mathbf{r}}[n], \tag{3.39}$$

where $\mathbf{P} = \boldsymbol{\Lambda}_{\mathrm{QB}}^{\mathrm{H}}\boldsymbol{\Lambda}_{\mathrm{QB}} + {\sigma_\nu}^2\mathbf{I}_N$, [83]. We refer to (3.39) as MMSE CFO compensator.

Similar to its ZF counterpart, the MMSE CFO compensator can also benefit from the quasi-banded property of the interference matrix which enables the development of a class of low complexity algorithms. In particular, the matrix $\mathbf{P}$ is also banded, however, it has a bandwidth that can be as much as twice the bandwidth of $\boldsymbol{\Lambda}_{\mathrm{QB}}$. Hence, the MMSE CFO compensator algorithms that are presented below, expect-

edly, have a higher complexity than the ZF CFO compensator algorithms that were presented in the previous section.

3.2.3.1 LU Factorization

In the same fashion as in Section 3.2.2.1, the matrix $\mathbf{P}$ can be efficiently factorized into lower and upper triangular matrices and $\hat{\mathbf{z}}_{\text{MMSE}}[n]$ can be estimated using forward and backward substitutions technique. Clearly, the wider bandwidth of $\mathbf{P}$, compared to that of $\mathbf{\Lambda}_{\text{QB}}$, leads to a higher complexity. Complexity details are given in the next section.

3.2.3.2 Truncated Neumann Series

The same as in Section 3.2.2.2, we can write $\mathbf{P}$ as the sum of its main diagonal and off-diagonal elements. Therefore, $\mathbf{P}^{-1}$ can be rearranged as $(\mathbf{I}_N+\mathbf{D}_P^{-1}\tilde{\mathbf{P}})^{-1}\mathbf{D}_P^{-1}$ where $\mathbf{D}_P$ and $\tilde{\mathbf{P}}$ contain the diagonal and off-diagonal elements of $\mathbf{P}$, respectively. If the spectral radius of $\mathbf{D}_P^{-1}\tilde{\mathbf{P}}$ is smaller than one, a similar iterative algorithm to the one presented in Algorithm 1, based on M^{th} order truncation of Neumann series can be developed to estimate $\hat{\mathbf{x}}_{\text{MMSE}}$. Thus, we have

$$\hat{\mathbf{z}}_{\text{MMSE}}^{(M)}[n] = \left(\sum_{i=0}^{M}(-\mathbf{D}_P{}^{-1}\tilde{\mathbf{P}})^i\right)\mathbf{D}_P{}^{-1}\mathbf{\Lambda}_{\text{QB}}^{\text{H}}\bar{\mathbf{r}}[n]. \tag{3.40}$$

Fig. 3.10 depicts PDF of the spectral radius of $\mathbf{D}_P^{-1}\tilde{\mathbf{P}}$ for the cases of having $N = 512, 1024$ subcarriers and $K = 4, 32$ users where the CFOs are in the range of $[-0.25, 0.25]$. The PDFs are derived based on $1,000,000$ random choices of CFOs for the G-CAS case. About the effects of the number of subcarriers and users on the spectral radius of $\mathbf{D}_P^{-1}\tilde{\mathbf{P}}$, we have similar observations as in Section 3.2.2.2. Based on Fig. 3.10, in all the cases, the upper bound for the spectral radius of $\mathbf{D}_P^{-1}\tilde{\mathbf{P}}$ is approximately 0.9 which guarantees convergence of the Neumann series. For the same reasons as in Section 3.2.2.2, we propose this solution for the cases where CFOs fall in the range of $[-0.25, 0.25]$.

Comparing Fig. 3.9 and Fig. 3.10, one may realize that the spectral radius of the matrix $\mathbf{D}_P^{-1}\tilde{\mathbf{P}}$ in MMSE case is larger than the spectral radius of the matrix $\mathbf{D}^{-1}\tilde{\mathbf{\Lambda}}$ in ZF case, for the same CFO range. Thus, our MMSE solution based on Neumann series needs more iterations to converge than its ZF counterpart which translates into a higher complexity.

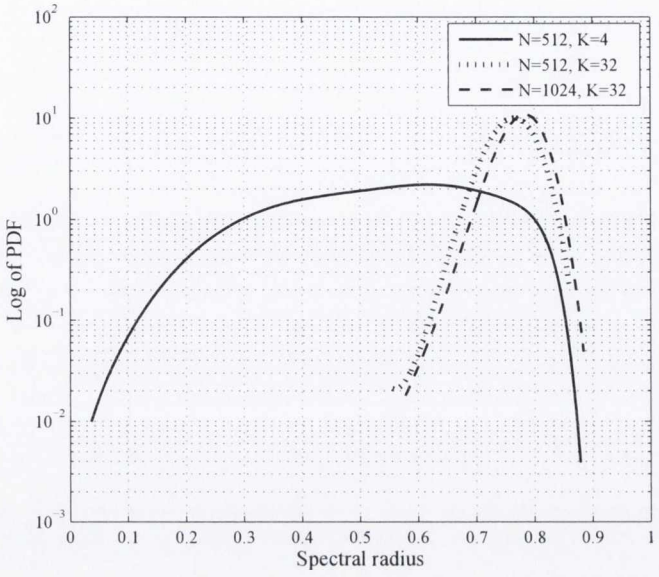

Fig. 3.10 Spectral radius of the matrix $\mathbf{D}_P^{-1}\tilde{\mathbf{P}}$ for a system with the CFOs in the range of $[-0.25, 0.25]$.

3.2.3.3 Conjugate Gradient Algorithm

As the only difference between $\mathbf{P}$ and $\mathbf{P}_{\mathrm{ZF}}$ is their main diagonal, following the same line of derivations as in Section 3.2.2.3, the MMSE estimates of the transmitted signals can be found simply by replacing $\mathbf{P}_{\mathrm{ZF}}$ with $\mathbf{P}$ in Algorithm 2.

3.2.4 Computational complexity

Table 3.2 summarizes the computational complexity of the ZF and MMSE CFO compensation techniques/algorithms that were developed in the previous sections and compares them with the direct solutions[5] and the CG algorithm of [47]. The reader should be reminded that prior to this work, the CG algorithm of [47] was the technique with lowest complexity applicable to G-CAS. We thus use this as a base to evaluate the effectiveness of the methods developed in section 3.2.

Following our earlier notations, the total number of subcarriers and the number of users are denoted by N and K, respectively. The parameters I, D and N_{w} in the table indicate the number of iterations, bandwidth of the interference matrix $\mathbf{\Lambda}_{\mathrm{QB}}$ and roll-off width of the receiver window, respectively. All the operations involve complex numbers. Therefore, we provide the computational complexity expressions

[5]Direct solutions involve direct matrix inversion and multiplication operations.

Table 3.2 Computational Complexity of Different CFO Compensation Techniques

Technique	Number of CMs for ZF-based CFO compensation	Number of CMs for MMSE-based CFO compensation
Direct	$\frac{1}{3}N^3 + 2N^2 + \frac{KN}{2}\log_2 N$	$\frac{5}{6}N^3 + \frac{5}{2}N^2 + \frac{KN}{2}\log_2 N$
Proposed LU factorization	$\frac{1}{3}D^3 + (2N-1)D^2 + (4N - \frac{1}{3})D + \frac{KN}{4}\log_2 N + N_w$	$\frac{9}{8}D^3 + \frac{9}{4}(\frac{17}{6}N - 1)D^2 + (\frac{43}{4}N - \frac{1}{2})D + 2N + \frac{KN}{4}\log_2 N + N_w$
Proposed Truncated series	$I(2ND + N) + N + \frac{KN}{4}\log_2 N + N_w$	$I(3ND + N) + \frac{15}{8}ND^2 + \frac{19}{4}ND + 3N + \frac{KN}{4}\log_2 N + N_w$
Proposed CG	$I(4ND + 7N) + N(2D + 1) + \frac{KN}{4}\log_2 N + N_w$	$I(4ND + 7N) + N(2D + 1) + \frac{KN}{4}\log_2 N + N_w$
CG, [47]	$I(KN\log_2 N + 2KN + 5N) + KN\log_2 N + 2KN$	$I(KN\log_2 N + 2KN + 5N) + KN\log_2 N + 2KN$

based on the number of complex multiplications. Direct ZF and MMSE solutions involve direct inversion of the matrices $\mathbf{\Lambda}$ and $\mathbf{P}$, respectively. Since, we approximate $\mathbf{\Lambda}$ with $\mathbf{\Lambda}_{\mathrm{QB}}$ in our proposed algorithms, there is no need to calculate all the elements of $\mathbf{\Lambda}$. Accordingly, FFT pruning techniques can be utilized to further reduce the computational cost of calculating $\mathbf{\Lambda}_{\mathrm{QB}}^{-1}$, [112], following the CG algorithm of [47].

All the proposed solutions in section 3.2 include time domain windowing that needs N_w CMs. In order to calculate the columns of the matrix $\mathbf{\Lambda}_{\mathrm{QB}}$, as only $2D+1$ elements out of N are needed, FFT pruning techniques can be utilized and hence $\frac{KN}{4}\log_2 N$ CMs need to be performed. In ZF-based LU factorization solution, the number of complex multiplications that are needed for calculation of the lower and upper triangular matrices as well as forward and backward substitutions is equal to $\frac{1}{3}D^3 + (2N-1)D^2 + (4N - \frac{1}{3})D$. In MMSE-based LU factorization, the complexity overhead with respect to the ZF-based solution is mainly laid in multiplication of $\mathbf{\Lambda}_{\mathrm{QB}}^{\mathrm{H}}$ to $\bar{\mathbf{r}}$ and calculation of $\mathbf{\Lambda}_{\mathrm{QB}}^{\mathrm{H}}\mathbf{\Lambda}_{\mathrm{QB}}$. This complexity overhead is $\frac{19}{24}D^3 + \frac{5}{4}(3.5N-1)D^2 + (\frac{27}{4}N - \frac{1}{6})D + 2N$. The ZF technique based on the truncated Neumann series needs N CMs for initialization step and $2ND + N$ CMs per iteration. In the same way as for the MMSE-based LU factorization technique, there exists a complexity overhead with respect to the ZF-based solution which is equal to $\frac{15}{8}ND^2 + \frac{19}{4}ND + 2N$ CMs and ND complex multiplications per iteration. As can be understood from Table 3.2, both CG-based ZF and MMSE techniques that we propose have the same computational complexity which is due to the equations that were discussed in sections 3.2.2 and 3.2.3. Multiplication of $\mathbf{\Lambda}_{\mathrm{QB}}^{\mathrm{H}}$ to $\bar{\mathbf{r}}[n]$ involves $N(2D+1)$ CMs. In addition, $4ND+7N$ number of CMs is needed for each iteration.

The computational cost for CFO compensation in single user systems is low and thus affordable from a practical implementation point of view. It involves N complex multiplications and an N-point FFT operation. In order to provide a good understanding of the level of complexity of the various CFO compensation techniques, we normalize the complexity of all of them to that of a single user receiver and present the results. This allows us to assess the practicality of different solutions.

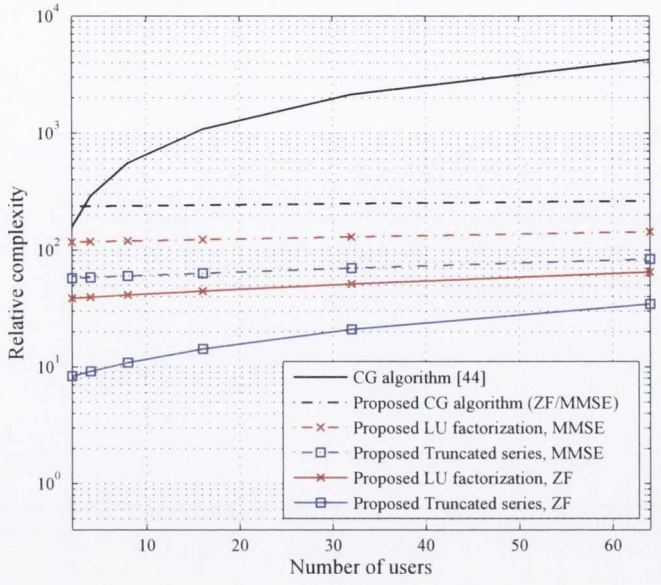

Fig. 3.11 Relative complexity of different CFO compensation techniques with respect to single user case when N = 2048.

The complexity formulas presented in Table 3.2 are evaluated for the case where $N = 2048$ and the results after normalization with respect to that of a single user receiver are presented in Fig. 3.11. Different numbers of iterations are required for convergence of different algorithms. Hence, we consider $I = 2$ and 4 for our proposed Neumann series based ZF and MMSE techniques, respectively and $I = 32$ for the CG-based algorithms (as is prescribed in [47]). The parameters, roll-off width of the receiver window and bandwidth of the interference matrix are set as $N_{\mathrm{w}} = \lfloor 0.1N \rfloor$ and $D = 10$, respectively. These results reveal the following instructive and interesting facts:

- The complexity of CG algorithm of [47] is at least over two orders of magnitude larger than that of a single user receiver. It even grows to over three orders of magnitude as the number of users increases. Although the processing is done at the base station, these complexity numbers are clearly excessively large.
- The ZF solution based on the Neumann series brings down the complexity by two orders of magnitude, hence, leads to a much more affordable implementation.
- Other algorithms/solutions that are proposed in section 3.2 also have complexities that are lower than the complexity of the CG algorithm in [47].

On the other hand, the simulation results that are presented in the next section reveal that the performance difference between the ZF and MMSE solutions is negligible. Hence, given the low complexity advantage of the ZF solutions and particularly of the one based on the Neumann series, there is no reason to adopt an MMSE solution for CFO compensation. ZF solutions work as well and for practical cases of interest, where CFOs remain in the range of $\pm 25\%$ of carrier spacing or lower, the ZF solution based on the Neumann series is the best solution.

3.2.5 Numerical results

In this section, we present the BER performance of our proposed solutions in the uplink of an OFDMA system for different cases. We assume different numbers of subcarriers and users with generalized carrier allocation scheme. The multipath channel SUI-2 proposed by the IEEE802.16 broadband wireless access working group, [113], is considered. The CP is chosen long enough to accommodate both the wireless channel delay spread and the samples needed for the receiver windowing operation, i.e., $N_{\mathrm{CP}} = 0.25N$. Uncoded 4-QAM and 16-QAM modulation schemes are considered in our numerical evaluations and each point in the results is based on $10,000$ simulation runs. In each simulation run, random subcarrier indices based on G-CAS are allocated to the users. The CFOs, ϵ_i's, are independently chosen from a uniform distribution. In this section, different CFO ranges of $\pm 25\%$ and $\pm 50\%$ of subcarrier spacing are considered[6]. A raised-cosine window with the roll-off width of $N_{\mathrm{w}} = \lfloor 0.1N \rfloor$ samples is used. The bandwidth $D = 10$ is chosen for the quasi-banded approximation of the interference matrix.

In Figs. 3.12 and 3.13, the performance of the proposed ZF solutions are investigated and compared with that of the direct solution[7] for the CFO range of $\pm 25\%$ subcarrier spacing for two cases of $N = 512$, $K = 4$ and $N = 1024$, $K = 32$ with 4-QAM and 16-QAM modulations, respectively. We investigate the BER performance of our algorithms for small and large number of users with two constellation sizes to show the efficacy of our proposed algorithms. As Figs. 3.12 and 3.13 depict, in both cases, the LU factorization technique has a BER performance similar to the direct solution with a negligible performance loss at very high signal-to-noise ratios (SNRs). This shows that approximation of $\mathbf{L}$ and $\mathbf{U}$ matrices as quasi-banded ones,

[6] In all cases, normalized CFOs with respect to subcarrier spacing are considered and therefore our results are valid for any arbitrary subcarrier spacing.

[7] Direct solution involves direct inversion and multiplication of the matrix $\mathbf{\Lambda}$ to the received signal, $\bar{\mathbf{r}}[n]$.

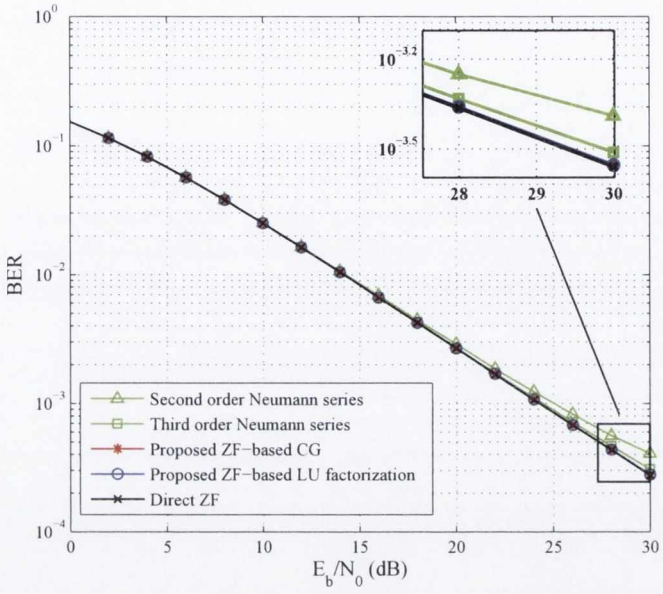

Fig. 3.12 BER performance of our proposed techniques compared with the direct ZF solution for the uplink of OFDMA systems with G-CAS, 4-QAM, $N = 512$ and $K = 4$ when $|\epsilon_i| \leq 0.25$.

as predicted, is accurate enough to guarantee a satisfactory performance. However, the second order truncation of Neumann series incurs a performance loss of around 1 dB and 3 to 4 dB at high SNRs for the cases of Fig. 3.12 and Fig. 3.13, respectively. This performance loss at high SNRs can be avoided by adding one more iteration to the Neumann series. This of course constitutes a small increase in complexity.

As noted in section 3.2.2.2, for large CFOs up to 50% subcarrier spacing, convergence of the Neumann series, unfortunately, is not guaranteed and thus, such method cannot be used. Fig. 3.14, illustrates the performance of our proposed ZF-based LU factorization and CG techniques and compares them with those of the direct ZF solution and the MMSE-based CG algorithm of [47] for $\epsilon_i \in [-0.5, 0.5)$, $N = 512$, $K = 4$ and 4-QAM modulation. In Fig. 3.15, we have investigated the performance of our proposed ZF-based techniques and compared them with that of the direct solution for the case of having a larger number of users and subcarriers; namely: $K = 32$ and $N = 1024$ and larger constellation size of 16-QAM. Figs. 3.14 and 3.15 indicate the robust performance of our proposed ZF-based LU factorization and CG techniques under harsh CFO conditions. In [47], Lee et al have shown that their MMSE-based solution provides the optimal performance. Comparing the performance of the proposed MMSE solution in [47] with our LU factorization technique reveals that in

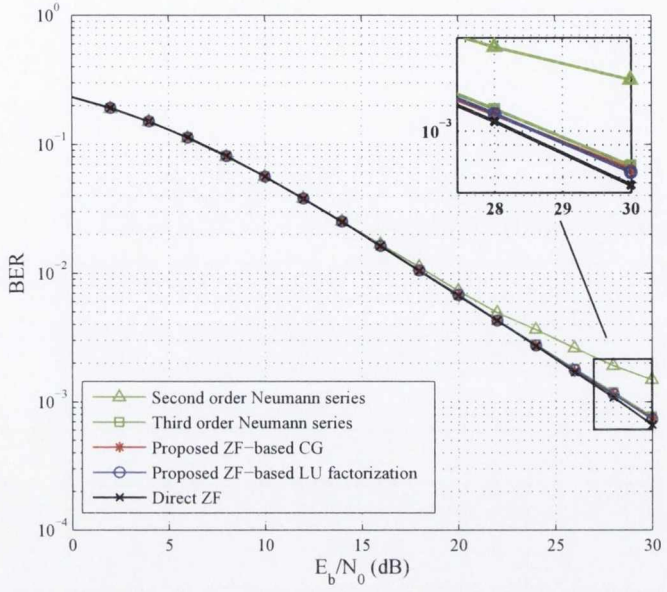

Fig. 3.13 BER performance of our proposed techniques compared with the direct ZF solution for the uplink of OFDMA systems with G-CAS, 16-QAM, $N = 1024$ and $K = 32$ when $|\epsilon_i| \leq 0.25$.

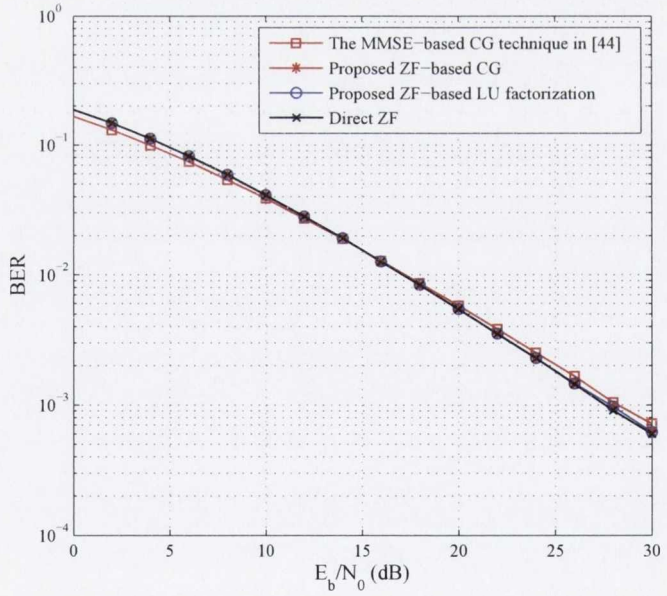

Fig. 3.14 BER performance of our proposed techniques compared with the direct ZF solution and the solution in [47] for the uplink of OFDMA systems with G-CAS, 4-QAM, $N = 512$ and $K = 4$ when $|\epsilon_i| < 0.5$.

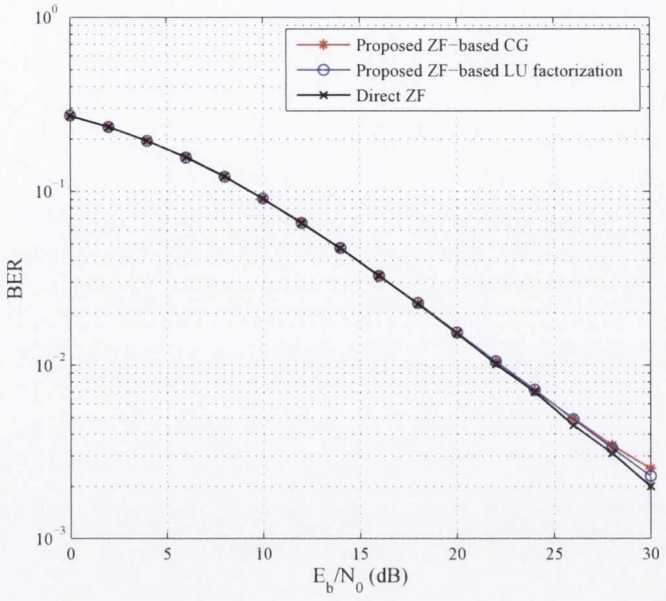

Fig. 3.15 BER performance of our proposed techniques compared with the direct ZF solution for the uplink of OFDMA systems with G-CAS, 16-QAM, $N = 1024$ and $K = 32$ when $|\epsilon_i| < 0.5$.

this particular application, MMSE and ZF solutions provide very close BER curves (Fig. 3.14). As emphasized in section 3.2.4, the proposed ZF solutions have a lower computational complexity compared with that of the MMSE solutions. Accordingly, the ZF techniques are more practical and hence attractive for the uplink of OFDMA systems. As highlighted in section 3.2.4, our ZF solution based on truncated Neumann series which is applicable to the CFO range of $\pm 25\%$ has the lowest complexity. Therefore, only when CFOs may be out of the range $\pm 25\%$ other solutions should be considered and in that case the clear choice (considering the computational complexity) is ZF-based LU factorization.

3.3 Conclusion

In this chapter, we proposed low complexity ZF and MMSE based CFO compensation techniques suitable for the uplink of OFDMA-based systems adopting I-CAS, BI-CAS and G-CAS. The proposed techniques for CFO correction in I-CAS and BI-CAS take advantage of the special structure of the interference matrix to find the ZF and MMSE solutions without making any approximations or having performance loss. It was shown that highly complex matrix multiplications can be effectively implemented

by the application of the FFT and IFFT operations. Finally, computational costs of the developed algorithms were analyzed and compared with other existing algorithms. Significant computational complexity reduction up to over an order of magnitude has been achieved through our approach. Such a substantial reduction in the amount of computations makes the proposed algorithms attractive for hardware implementation of the real time uplink communication systems while having optimal performance.

We also developed a new class of low complexity receivers addressing the same problem in the uplink of OFDMA systems with G-CAS. The developed techniques reduce the complexity through utilization of receiver windowing. Time domain receiver windowing enables reduction of the interference induced by multiple CFOs. This leads to a class of low complexity CFO compensation techniques that can reduce the computational complexity of the receiver up to over two orders of magnitude, when compared to the lowest complexity algorithm in the literature. This great reduction in complexity comes at the expense of a longer cyclic extension, i.e., a compromise in bandwidth efficiency. Both ZF and MMSE compensators were thoroughly studied and for each, a number of solutions were developed. Simulations showed that all solutions lead to the same bit error rate performance and thus the choice between different CFO compensation algorithms is dictated by their computational complexity. While the proposed ZF-based Neumann series compensator was found to be the simplest, it works only when the CFO range is limited to approximately $\pm 25\%$ of carrier spacing. For cases where CFOs fall outside of the range of $\pm 25\%$ of carrier spacing, the proposed ZF-based LU factorization method should be adopted. The complexity analysis presented was in the unit of single user complexity. These techniques led to CFO compensation algorithms whose complexity was only one order of magnitude greater than that of the single user case while keeping very close to the optimal performance. Such a substantial complexity reduction makes our algorithms feasible in practice and therefore, suitable for hardware implementation of real-time uplink OFDMA systems.

In OFDMA, each subcarrier in the system is used by only one user. Due to the ever increasing demand for higher data rates and the number of connected devices, massive MIMO has been recently proposed to increase the capacity of multiuser channels, [5]. This technique allows the users in the network to reuse all the available subcarriers while removing the multiuser interference through utilization of a large number of receive antennas at the base station. OFDM has been proposed as the modulation technique for massive MIMO. However, it suffers from a large amount of out of band emissions and thus limits spectrum aggregation in massive MIMO channels.

To increase the bandwidth efficiency of such channels and more efficiently utilize the spectrum, in the following chapter, we look into another multicarrier modulation technique, i.e., filter bank multicarrier (FBMC). FBMC has better spectral properties than OFDM thanks to its well-localized subcarriers in frequency. Application of FBMC to massive MIMO makes it possible to not only reuse the same spectrum by each user but also use the available bandwidth more efficiently.

Chapter 4

Filter bank multicarrier for massive MIMO

Recent proposal of massive MIMO as a candidate for the fifth generation of wireless communication networks (5G) has sparked a great deal of interest among researchers. This is due to the fact that such technology can greatly increase the capacity of multiuser networks. As it was discussed in Chapter 2, massive MIMO is a multiuser technique whose ideas are somewhat similar to the spread-spectrum systems. The spreading gains of different users come from the corresponding channel gains between each mobile terminal (MT) antenna and the base station (BS) antennas. Therefore, a significant processing gain can be achieved by utilizing a massive number of antenna elements at the BS. In other words, the processing gain can arbitrarily grow by increasing the number of antenna elements at the BS. As the pioneering work of Marzetta points out, given perfect channel state information (CSI), as the number of BS antennas, in limit, tends to infinity, the processing gain of the system tends to infinity and, accordingly, the effects of both noise and multiuser interference (MUI) completely fade away, [5]. Hence, the network capacity, in theory, can be increased without a bound by increasing the number of BS antennas, [5].

As it is suggested in [5], orthogonal frequency division multiplexing (OFDM) can be used to convert the frequency selective channels between each MT and the multiple antennas at the BS to a set of flat fading channels. Accordingly, the flat gains associated with the set of channels within each subcarrier constitute the spreading gain vector that is used for despreading of the respective data stream.

In this chapter, embarking on the above concept, we introduce the application of filter bank multicarrier (FBMC) to the area of massive MIMO communications to answer the following research question that was raised in Chapter 4.

Question 2

- ***Given that massive MIMO and FBMC are suitable for serving a large number of users, what is the impact of these two forerunner technologies on each other?***

FBMC methods have their roots in the pioneering works of Chang [32] and Saltzberg [17], who introduced multicarrier techniques over two decades before introduction and application of OFDM to wireless communication systems. While OFDM relies on cyclic prefix (CP) samples to avoid intersymbol interference (ISI) and to convert the channel to a set of subcarrier channels with flat gains (perfectly, when channel impulse response duration is shorter than CP), FBMC, without using CP, by adopting a sufficiently large number of subcarriers, relies on the fact that when each subcarrier band is narrow, it is characterized by an approximately flat gain, hence, may suffer only from a negligible level of ISI.

A new and interesting finding out of our research in this area is that in the case of massive MIMO systems, linear combining of the signal components from different channels smooths channel distortion. We call this property of FBMC in massive MIMO channels *self-equalization*. Hence, one may relax on the requirement of having approximately flat gain for the subcarriers. This observation, which is confirmed numerically in this chapter, positions FBMC as a strong candidate in the application of massive MIMO. As a result, in a massive MIMO setup, one may significantly reduce the number of subcarriers in an FBMC system. This reduces both system complexity and the latency/delay caused by the synthesis filter bank (at the transmitter) and the analysis filter bank (at the receiver). Also, since linear combining of the signal components equalizes the channel gain across each subcarrier, one may adopt larger constellation sizes, hence, further improve on the system bandwidth efficiency. Moreover, increasing the subcarrier spacing has the obvious benefit of reducing the sensitivity to carrier frequency offset.

An additional benefit of FBMC here is that carrier/spectral aggregation (i.e., using non-contiguous bands of spectrum for transmission) becomes a trivial task, since each

subcarrier band is confined to an assigned range and has a negligible interference to other bands. This is not the case in OFDM, [15].

A major factor in limiting the capacity of non-cooperative multi-cellular massive MIMO networks working in time-division duplex (TDD) mode is *pilot contamination* problem, [7]. Another contribution of this chapter is to address the pilot contamination problem in massive MIMO networks using cosine modulated multitone (CMT) viz., a particular form of FBMC. This type of FBMC has a blind equalization capability, [114]. In this chapter, we extend the blind equalization capability of CMT to massive MIMO application in order to remove the channel estimation errors caused by contaminated pilots. Based on our observations through numerical results, the proposed blind equalization technique is able to remove the pilot contamination effects in multi-cellular massive MIMO networks and converge towards the optimal linear minimum mean square error (MMSE) performance. More details on the proposed pilot decontamination technique will be presented in section 4.4

The rest of this chapter is laid out as follows. Section 4.1 is dedicated to the system model and formulation of FBMC in massive MIMO channels. Self-equalization property of FBMC in massive MIMO channels is discussed in section 4.2. A qualitative comparison of FBMC and OFDM in massive MIMO systems is presented in section 4.3. Section 4.4 addresses pilot contamination problem in a multi-cellular massive MIMO network and finally, the conclusions are drawn in section 4.5.

4.1 System model and FBMC formulation in massive MIMO

Detailed information on different types of FBMC systems were presented in Chapter 2; as noted there, we are more interested in FBMC systems with overlapping subcarriers in frequency domain; namely, staggered multitone (SMT) and CMT. Both CMT and SMT can be adopted for massive MIMO, leading to the same performance. However, it turns out that derivations and explanation of the results in the context of CMT are easier to follow. We thus limit our attention in the rest of this chapter to development of CMT in massive MIMO application. As was discussed in Chapter 2, there are two different implementations for FBMC systems that are based on polyphase networks and the frequency spreading concepts, respectively. In section 4.1.1, we consider polyphase implementation of CMT while its frequency spreading (FS) implementation is considered in section 4.1.2.

In CMT, a set of pulse amplitude modulated (PAM) baseband data streams are vestigial side-band (VSB) modulated and placed at different subcarriers. Fig. 2.6 from Chapter 2 depicts this process. Moreover, to allow separation of the data symbols (free of ISI and ICI), at the receiver, the carrier phase of the VSB signals is toggled between 0 and $\pi/2$ among adjacent subcarriers. The detailed equations explaining why this approach works can be found in [32] and many other publications; a recommended reference is [87]. Reference [31] also provides more details, including the implementation structures and their relevant MATLAB codes.

Demodulation of each subcarrier in CMT is performed in four steps. (1) the received signal is down-converted to base-band using the corresponding carrier frequency to each subcarrier. (2) The demodulated signal is passed through a matched filter that extracts the desired signal at the base-band. Due to the overlap among the adjacent subcarriers, some residuals from adjacent subcarriers remain after matched filtering. (3) A complex-valued single tap equalizer is utilized to equalize the channel effect.[1] (4) As the real part of the equalized signal contains the desired PAM symbol and its imaginary part consists of a mix of ISI components and ICI components from the two adjacent bands, taking the real part of the equalized signal delivers the desired data symbol, free of ISI and ICI.

4.1.1 Polyphase-based CMT in massive MIMO

Consider a multiuser MIMO setup similar to the one discussed in [5]. There are K MTs and a BS in a cell. Each MT is equipped with a single transmit and receive antenna, communicating with the cell BS in TDD manner. The BS is equipped with $N \gg K$ transmit/receive antennas that are used to communicate with the K MTs in the cell *simultaneously*. We also assume, similar to [5], multicarrier modulation is used for data transmissions. However, we replace OFDM modulation by CMT modulation.

Each MT is distinguished by the BS using the respective subcarrier gains between its antenna and the BS antennas. Ignoring the time and subcarrier indices in our formulation, for simplicity of equations, a transmit symbol $s(\ell)$ from the ℓ^{th} MT arrives at the BS as a vector

$$\mathbf{x}_\ell = (s(\ell) + jq(\ell))\mathbf{h}_\ell, \tag{4.1}$$

[1] This is based on the assumption that each subcarrier band is sufficiently narrow such that it can be approximated by a flat gain. A multi-tap equalizer may be adopted if this approximation is not valid.

where $\mathbf{h}_\ell = [h_\ell(0), \ldots, h_\ell(N-1)]^{\mathrm{T}}$ is the channel gain vector whose elements are the gains between the ℓ^{th} MT and different antennas at the BS. $q(\ell)$ is the contribution of ISI and ICI. The vector $\mathbf{x}_\ell$ and similar contributions from other MTs, as well as the channel noise vector $\mathbf{v}$, add up and form the BS received signal vector

$$\mathbf{x} = \sum_{\ell=0}^{K-1} \mathbf{x}_\ell + \mathbf{v}. \tag{4.2}$$

The BS uses a set of linear estimators that all take $\mathbf{x}$ as their input and provide the estimates of the users' data symbols $s(0)$, $s(1)$, $\cdots$, $s(K-1)$ at the output. To cast this process in a mathematical formulation and allow introduction of various choices of estimators, we proceed as follows. We define $\tilde{\mathbf{x}} = [\mathbf{x}_{\mathrm{R}}^{\mathrm{T}}\ \mathbf{x}_{\mathrm{I}}^{\mathrm{T}}]^{\mathrm{T}}$, $\tilde{\mathbf{v}} = [\mathbf{v}_{\mathrm{R}}^{\mathrm{T}}\ \mathbf{v}_{\mathrm{I}}^{\mathrm{T}}]^{\mathrm{T}}$, $\tilde{\mathbf{h}}_\ell = [\mathbf{h}_{\ell,\mathrm{R}}^{\mathrm{T}}\ \mathbf{h}_{\ell,\mathrm{I}}^{\mathrm{T}}]^{\mathrm{T}}$, $\breve{\mathbf{h}}_\ell = [-\mathbf{h}_{\ell,\mathrm{I}}^{\mathrm{T}}\ \mathbf{h}_{\ell,\mathrm{R}}^{\mathrm{T}}]^{\mathrm{T}}$, $\mathbf{s} = [s(0)\ s(1)\ \cdots\ s(K-1)]^{\mathrm{T}}$ and $\mathbf{q} = [q(0)\ q(1)\ \cdots\ q(K-1)]^{\mathrm{T}}$, where the subscripts 'R' and 'I' denote the real and imaginary parts, respectively. Using these definitions, (4.2) may be rearranged as

$$\tilde{\mathbf{x}} = \mathbf{A} \begin{bmatrix} \mathbf{s} \\ \\ \mathbf{q} \end{bmatrix} + \tilde{\mathbf{v}}, \tag{4.3}$$

where $\mathbf{A} = [\tilde{\mathbf{H}}\ \breve{\mathbf{H}}]$, and $\tilde{\mathbf{H}}$ and $\breve{\mathbf{H}}$ are $2N \times K$ matrices with columns of $\{\tilde{\mathbf{h}}_\ell,\ \ell = 0, 1, \cdots, K-1\}$ and $\{\breve{\mathbf{h}}_\ell,\ \ell = 0, 1, \cdots, K-1\}$, respectively. Equation (4.3) has the familiar form that appears in CDMA literature, e.g., see [95, 96]. Hence, a variety of solutions that have been given for CDMA systems can be immediately applied to the present problem as well. For instance, the matched filter (MF) detector obtains an estimate of the vector $\mathbf{s}$, according to the equation

$$\hat{\mathbf{s}}_{\mathrm{MF}} = \mathbf{D}^{-1}\mathbf{\Gamma}\mathbf{A}^{\mathrm{T}}\tilde{\mathbf{x}}, \tag{4.4}$$

where $\mathbf{D} = \mathrm{diag}\{\|\tilde{\mathbf{h}}_0\|^2, \ldots, \|\tilde{\mathbf{h}}_{K-1}\|^2\}$, the matrix $\mathbf{\Gamma}$ consists of the first K rows of the identity matrix $\mathbf{I}_{2K}$ of size $2K \times 2K$ and $\hat{\mathbf{s}}_{\mathrm{MF}} = [\hat{s}_{\mathrm{MF}}(0), \ldots, \hat{s}_{\mathrm{MF}}(K-1)]^{\mathrm{T}}$ whose ℓ^{th} element, $\hat{s}_{\mathrm{MF}}(\ell)$, is the estimated data symbol of user ℓ. Using (4.4), each element of $\hat{\mathbf{s}}_{\mathrm{MF}}$ can be expanded as

$$\hat{s}_{\mathrm{MF}}(\ell) = s(\ell) + \sum_{\substack{i=0 \\ i\neq\ell}}^{K-1} \frac{\tilde{\mathbf{h}}_\ell^{\mathrm{T}}}{\|\tilde{\mathbf{h}}_\ell\|^2}(\tilde{\mathbf{h}}_i s(i) + \breve{\mathbf{h}}_i q(i)) + \frac{\tilde{\mathbf{h}}_\ell^{\mathrm{T}}}{\|\tilde{\mathbf{h}}_\ell\|^2}\tilde{\mathbf{v}}. \tag{4.5}$$

This leads to a receiver structure similar to that of [5], where it is shown that when the number of antennas, N, increases to infinity, the multiuser interference and noise effects vanish to zero. Hence, $\hat{\mathbf{s}} = \mathbf{s}$, where the vector $\hat{\mathbf{s}}$ is an estimate of $\mathbf{s}$, and the receiver will be optimum. In the context of CDMA literature, this has the explanation that as N tends to infinity, the processing gain also goes to infinity and accordingly multiuser interference and noise effects vanish.

In realistic situations when N is finite, the MF estimator is not optimal. A superior estimator is the MMSE estimator

$$\hat{\mathbf{s}} = \mathbf{W}^{\mathrm{T}} \tilde{\mathbf{x}}, \tag{4.6}$$

where the coefficient matrix $\mathbf{W}$ is chosen to minimize the cost function

$$\zeta = \mathbb{E}[\|\mathbf{s} - \mathbf{W}^{\mathrm{T}} \tilde{\mathbf{x}}\|^2]. \tag{4.7}$$

This solution is optimal in the sense that it maximizes the signal-to-interference-plus-noise ratio (SINR), [96].

Following the standard derivations, the optimal choice of $\mathbf{W}$ is obtained as

$$\mathbf{W}_{\mathrm{o}} = \mathbf{A} \left(\mathbf{A}^{\mathrm{T}} \mathbf{A} + \sigma_v^2 \mathbf{I}_{2K} \right)^{-1} \mathbf{\Gamma}^{\mathrm{T}}. \tag{4.8}$$

Here, it is assumed that the elements of the noise vector $\tilde{\mathbf{v}}$ are independent and identically distributed Gaussian random variables with variances of σ_v^2, hence, $\mathbb{E}\left[\tilde{\mathbf{v}}\tilde{\mathbf{v}}^{\mathrm{T}}\right] = \sigma_v^2 \mathbf{I}$. The columns of $\mathbf{W}_{\mathrm{o}}$ contain the optimal filter tap weights for different users.

Substitution of (4.8) into (4.6) leads to the MMSE solution

$$\begin{aligned} \hat{s}_{\mathrm{MMSE}}(\ell) &= \mathbf{w}_{\mathrm{o},\ell}^{\mathrm{T}} \tilde{\mathbf{h}}_\ell s(\ell) + \sum_{\substack{i=0 \\ i \neq \ell}}^{K-1} \mathbf{w}_{\mathrm{o},\ell}^{\mathrm{T}} \tilde{\mathbf{h}}_i s(i) \\ &\quad + \sum_{i=0}^{K-1} \mathbf{w}_{\mathrm{o},\ell}^{\mathrm{T}} \breve{\mathbf{h}}_i q(i) + \mathbf{w}_{\mathrm{o},\ell}^{\mathrm{T}} \tilde{\mathbf{v}}, \end{aligned} \tag{4.9}$$

where $\mathbf{w}_{\mathrm{o},\ell}$ is the ℓ^{th} column of $\mathbf{W}_{\mathrm{o}}$. Ignoring the off-diagonal elements of $\left(\mathbf{A}^{\mathrm{T}} \mathbf{A} + \sigma_v^2 \mathbf{I}_{2K}\right)$ and also removing the term $\sigma_v^2 \mathbf{I}_{2K}$ from (4.8), one will realize that (4.9) boils down to the MF tap weights (4.5).

The first terms on the right hand side of equations (4.5) and (4.9) are the desired signal and the rest are the interference plus noise terms. We consider $s(\ell)$ and $q(\ell)$ as independent variables with variance of unity. With the assumption of having a

flat channel impulse response in each subcarrier band, SINR at the output of the MF and MMSE detectors for user ℓ in a certain subcarrier can be derived, respectively, as

$$\mathrm{SINR}_{\mathrm{MF}}(\ell) = \frac{\|\tilde{\mathbf{h}}_\ell\|^4}{\sum\limits_{\substack{i=0 \\ i\neq\ell}}^{K-1} \left(|\tilde{\mathbf{h}}_\ell^{\mathrm{T}}\tilde{\mathbf{h}}_i|^2 + |\tilde{\mathbf{h}}_\ell^{\mathrm{T}}\breve{\mathbf{h}}_i|^2\right) + \sigma_v^2\|\tilde{\mathbf{h}}_\ell\|^2}, \tag{4.10}$$

and

$$\mathrm{SINR}_{\mathrm{MMSE}}(\ell) = \frac{|\mathbf{w}_{\mathrm{o},\ell}^{\mathrm{T}}\tilde{\mathbf{h}}_\ell|^2}{\sum\limits_{\substack{i=0 \\ i\neq\ell}}^{K-1} |\mathbf{w}_{\mathrm{o},\ell}^{\mathrm{T}}\tilde{\mathbf{h}}_i|^2 + \sum\limits_{i=0}^{K-1} |\mathbf{w}_{\mathrm{o},\ell}^{\mathrm{T}}\breve{\mathbf{h}}_i|^2 + \sigma_v^2\|\mathbf{w}_{\mathrm{o},\ell}\|^2}. \tag{4.11}$$

4.1.2 FS-based CMT in massive MIMO

An interesting property of FS-FBMC structure is its high-performance equalization capability. This frequency spreading equalization (FSE) can be utilized in the context of massive MIMO as will be discussed in the following. In the rest of this section, and for our later reference, we review the frequency spreading structure when applied to CMT, which we hereafter call *FS-CMT*.

The basic idea of the frequency spreading method is that a discrete-time square-root Nyquist filter, $p(n)$, of size $P = ML$, can be synthesized in the frequency domain using a set of $2M-1$ distinct tones, as

$$p(n) = \sum_{k=-M+1}^{M-1} c_k e^{j\frac{2\pi kn}{P}}. \tag{4.12}$$

Here, c_k is a real-valued coefficient that indicates the frequency response of $p(n)$ at the frequency $\omega_k = \frac{2\pi k}{P}$, M is the overlapping factor, i.e., it signifies the number of symbols that overlap in the time domain and L is the sample spacing of the zero-crossings of the Nyquist filter $q(n) = p(n) \star p^*(-n)$.

When the above idea is extended to the multicarrier case, the symbols at each subcarrier should be pulse-shaped in the frequency domain using the set of c_k's. An inverse discrete Fourier transform (IDFT) block of size P can then be used to calculate the time domain samples from their frequency domain counterparts. Casting the above discussion into the mathematical form, the FS-CMT symbol can be obtained

as

$$\mathbf{x}(n) = \mathbf{F}_P^{\mathrm{H}} \mathbf{A} \mathbf{\Phi} \mathbf{s}(n). \tag{4.13}$$

Here, $\mathbf{s}(n) = \begin{bmatrix} s_0(n) & s_1(n) & \cdots & s_{L-1}(n) \end{bmatrix}^{\mathrm{T}}$, where $s_k(n)$ indicates the data symbol at the k^{th} subcarrier and n^{th} symbol time, $\mathbf{\Phi}$ indicates the phase-adjustment matrix which is an $L \times L$ diagonal matrix with the diagonal elements $\{1, e^{j\frac{\pi}{2}}, \ldots e^{j\frac{\pi}{2}(L-1)}\}$, $\mathbf{A}$ is the spreading matrix of size $P \times L$ whose k^{th} column contains the coefficients c_ℓ's that are centered at the center frequency of the k^{th} subcarrier, $\mathbf{F}_P^{\mathrm{H}}$ indicates the IDFT matrix of the size $P \times P$ and $\mathbf{x}(n)$ is an $P \times 1$ vector indicating the n^{th} FS-CMT symbol in time domain.

Noting that the size of each FS-CMT symbol is P and the symbol spacing is equal to $L/2$, the transmit signal can be constructed by performing the overlap-and-add operations on the symbol vectors as illustrated in Fig. 2.12 of Chapter 2. Assuming an ideal channel and having a perfect synchronization between transmitter and receiver, the P samples that correspond to the n^{th} symbol are collected in the vector $\hat{\mathbf{r}}(n)$, at the receiver side, and the data symbols are recovered according to

$$\hat{\mathbf{s}}(n) = \Re\left\{\mathbf{\Phi}^{-1} \mathbf{A}^{\mathrm{T}} \mathbf{F}_P \hat{\mathbf{r}}(n)\right\}. \tag{4.14}$$

Since we assumed an ideal channel, equalization was not considered here. In the presence of the channel, the equalization can be embedded after obtaining the discrete Fourier transform (DFT) output samples, [52]. In the following, we extend the equalization scheme that was originally proposed for single antenna systems in [52] to the context of massive MIMO.

Based on the structure of the CMT receiver, the output at the i^{th} bin of the DFT block from the ℓ^{th} user at all the receive antennas can be stacked into an $N \times 1$ vector $\tilde{\mathbf{r}}_i^\ell = r_i^\ell \mathbf{h}_i(\ell)$ where $\mathbf{h}_i(\ell)$ is the channel gain vector whose elements are the gains between the ℓ^{th} MT antenna and the BS antennas at the i^{th} frequency bin. The coefficient r_i^ℓ is the received signal at the i^{th} bin of the output of the DFT block at the receiver from user ℓ in an ideal channel. The vectors $\tilde{\mathbf{r}}_i^\ell$ are the received signals from different users that contribute to form the received signal at the BS. Accordingly, the received signal vector can be written as

$$\tilde{\mathbf{r}}_i = \sum_{\ell=0}^{K-1} \tilde{\mathbf{r}}_i^\ell + \mathbf{v}_i = \mathbf{H}_i \mathbf{r}_i + \mathbf{v}_i, \tag{4.15}$$

where $\mathbf{H}_i = [\mathbf{h}_i(0), \ldots, \mathbf{h}_i(K-1)]$, $\mathbf{r}_i = [r_i^0, \ldots, r_i^{K-1}]^{\mathrm{T}}$ and $\mathbf{v}_i$ is an $N \times 1$ vector that contains the FFT samples of the additive white Gaussian noise (AWGN) at the i^{th} bin of the output of the FFT blocks at different receive antennas.

In order to estimate different users' transmitted symbols, a number of equalization techniques can be utilized; namely, MF and MMSE. However, as it was noted before, in realistic situations when the number of BS antennas is finite, MF equalization incurs some performance degradation due to the residual multiuser interference. In this section, our discussion will be limited to the MMSE-FSE which is known to be a superior technique.

In MMSE-FSE for massive MIMO systems, similar to single antenna FS-FBMC systems, equalization needs to be performed before despreading the output of the FFT blocks. Therefore, the MMSE linear combining aims at estimating the vector $\mathbf{r}_i$ that contains the equalized samples of different users at the output of their FFT blocks. The MMSE solution of (4.15) is optimal as it maximizes the SINR,[96]. Following the same line of derivations as in section 4.1.1, the MMSE estimates of $\mathbf{r}_i$'s can be obtained as

$$\hat{\mathbf{r}}_i = \mathbf{W}_i^{\mathrm{H}} \tilde{\mathbf{r}}_i, \tag{4.16}$$

where the coefficient matrix $\mathbf{W}_i = \mathbf{H}_i(\mathbf{H}_i^{\mathrm{H}}\mathbf{H}_i + \sigma_v^2 \mathbf{I}_K)^{-1}$ contains the optimal MMSE filter tap weights for different users in its columns. It is worth mentioning that the elements of the noise vector $\mathbf{v}_i$ are assumed independent and identically distributed Gaussian random variables with variances of σ_v^2 and $\mathbb{E}\left[\mathbf{v}_i \mathbf{v}_i^{\mathrm{H}}\right] = \sigma_v^2 \mathbf{I}_P$. After the MMSE estimation of the vectors $\hat{\mathbf{r}}_i$ for $i = 0, \ldots, P-1$, frequency despreading can be separately applied for each user. To this end, let $\hat{\mathbf{R}} = [\hat{\mathbf{r}}_0, \ldots, \hat{\mathbf{r}}_{P-1}]^{\mathrm{T}}$. Consequently, the MMSE estimates of the transmitted data symbols of different users, i.e., $\mathbf{s}_\ell$ for $\ell = 0, \ldots, K-1$ can be obtained through frequency despreading

$$\hat{\mathbf{S}} = \Re\{\mathbf{\Phi}^{-1}\mathbf{A}^{\mathrm{T}}\hat{\mathbf{R}}\}, \tag{4.17}$$

where the $L \times K$ matrix $\hat{\mathbf{S}}$ contains the MMSE estimation of different users transmitted data symbols, i.e., $\hat{\mathbf{s}}_\ell$'s, on its columns.

Based on equations (4.15) to (4.17) and the assumption of having a flat fading channel gain over each frequency bin of DFT, the output SINR of the CMT receiver with MMSE channel equalization for the ℓ^{th} user at subcarrier i can be calculated as follows.

$$\mathrm{SINR}_{\mathrm{MMSE}}^{(\ell,i)} = \frac{P_{\mathrm{s}}^{(\ell,i)}}{P_{\mathrm{I}}^{(\ell,i)}}, \tag{4.18}$$

where $P_{\mathrm{s}}^{(\ell,i)}$ and $P_{\mathrm{I}}^{(\ell,i)}$ are signal and interference-plus-noise powers, respectively. $P_{\mathrm{s}}^{(\ell,i)}$ and $P_{\mathrm{I}}^{(\ell,i)}$ can be obtained as

$$P_{\mathrm{s}}^{(\ell,i)} = \sum_{m=-M+1}^{M-1} c_k^2 |\mathbf{w}_{i+m,\Re}^{\mathrm{T}}(\ell)\mathbf{h}_{i+m,\Re}(\ell) + \mathbf{w}_{i+m,\Im}^{\mathrm{T}}(\ell)\mathbf{h}_{i+m,\Im}(\ell)|^2, \tag{4.19}$$

and

$$\begin{aligned} P_{\mathrm{I}}^{(\ell,i)} = & \sum_{m=-M+1}^{M-1} \sum_{\substack{k=0 \\ k\neq\ell}}^{K-1} c_m^2 |\mathbf{w}_{i+m,\Re}^{\mathrm{T}}(\ell)\mathbf{h}_{i+m,\Re}(k) + \mathbf{w}_{i+m,\Im}^{\mathrm{T}}(\ell)\mathbf{h}_{i+m,\Im}(k)|^2 \\ & + \sum_{m=-M+1}^{M-1} \sum_{k=0}^{K-1} c_m^2 |\mathbf{w}_{i+m,\Re}^{\mathrm{T}}(\ell)\mathbf{h}_{i+m,\Im}(k) - \mathbf{w}_{i+m,\Im}^{\mathrm{T}}(\ell)\mathbf{h}_{i+m,\Re}(k)|^2 \\ & + \sum_{m=-M+1}^{M-1} c_m^2 \sigma_v^2 \|\mathbf{w}_{i+m}(\ell)\|^2, \end{aligned} \tag{4.20}$$

where $\mathbf{w}_{i,\Re}(k)$ and $\mathbf{h}_{i,\Re}(k)$ represent the real parts of the k^{th} column of the matrices $\mathbf{W}_i$ and $\mathbf{H}_i$, respectively. Similarly, the subscript $\Im$ in the equations (4.19) and (4.20) shows the imaginary part of the corresponding vectors. It is worth mentioning that equation (4.18) is used as a benchmark to investigate the channel flatness assumption in section 4.2.2.

4.2 Self-equalization property of FBMC in massive MIMO

In the conventional (single-input single-output) FBMC systems, in order to reduce channel equalization to single tap per subcarrier, it is often assumed that the number of subcarriers is very large. Hence, each subcarrier band may be approximated by a flat gain. This, clearly, has the undesirable effect of reducing the symbol rate (per subcarrier) which along with it brings (i) the need for longer pilot preambles (equivalently, reduces the bandwidth efficiency); (ii) increases latency in the channel; (iii) higher sensitivity to carrier frequency offset (CFO); and (iv) higher peak-to-average power ratio (PAPR) due to the large number of subcarriers which increases the dynamic range of the FBMC signal.

Massive MIMO channels have an interesting property that allows us to resolve the above problems. The MF and MMSE detectors that are used to combine signals

from the receive antennas average distortions from different channels and thus, as the number of BS antennas increases, result in a nearly equalized gain across each subcarrier band. This property of massive MIMO channels, that we call *self-equalization* is confirmed numerically in sections 4.2.1 and 4.2.2.

4.2.1 Numerical study of polyphase-based CMT in a massive MIMO channel

In this section, a broad set of numerical results is presented to confirm the theoretical developments of section 4.1 as well as the earlier claims on self-equalization property. It was noted in the previous sections that massive MIMO, through use of a large number of antennas at the BS, can provide a large processing gain. Hence, noise and MUI effects can be reduced. In addition, when FBMC is used for signal modulation, linear combining of the signals from multiple antennas at the BS has a flattening effect (i.e., the channel will be equalized) over each subcarrier band. This interesting impact of massive MIMO allows reducing the number of subcarriers in FBMC and this, in turn, has the effect of reducing (i) complexity; (ii) the preamble (training) length, hence, increasing bandwidth efficiency; (iii) sensitivity to CFO; (iv) PAPR; and (v) system latency. The first set of results that we present in this section provide evidence of the self-equalization property.

Fig. 4.1 presents a set of results that highlights the effect of increasing the number of antennas at the receiver on the signal-to-interference ratio (SIR) for different number of subcarriers in the single-user case. The results are presented for a noise free channel to explore the impact of the number of subcarriers (equivalently, the width of each subcarrier band) and the number of BS antennas in achieving a flat channel response over each subcarrier band. The results are for a sample set of channel responses generated according to the SUI-4 channel model proposed by the IEEE802.16 broadband wireless access working group, [113]. SIRs are evaluated at all subcarrier channels. Note that in each curve, the number of points along the normalized frequency is equal to the number of subcarrier bands, L. For the channel model used here, the total bandwidth, equivalent to the normalized frequency one, is equal to 2.8 MHz. This, in turn, means the subcarrier spacing in each case is equal to $2800/L$ kHz. As an example, when $L = 32$, subcarrier spacing is equal to 87.5 kHz. This, compared to the subcarrier spacing in OFDM-based standards (e.g., IEEE 802.16 and LTE), is relatively broad; $87.5/15 \approx 6$ times larger. Reducing the number of subcarriers (equivalently, increasing symbol rate in each subcarrier band),

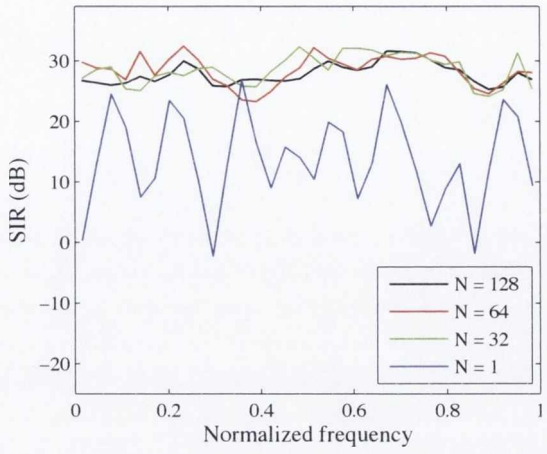

(a) $L = 32$

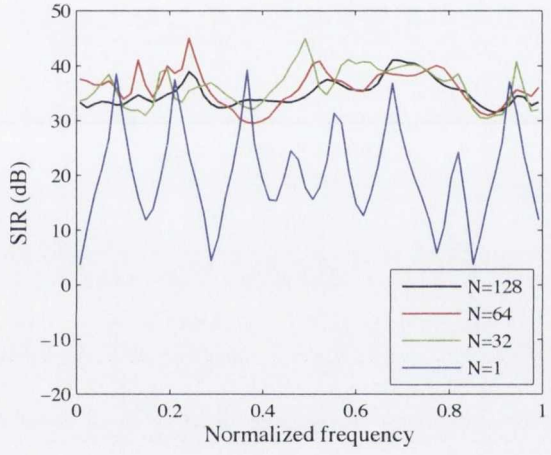

(b) $L = 64$

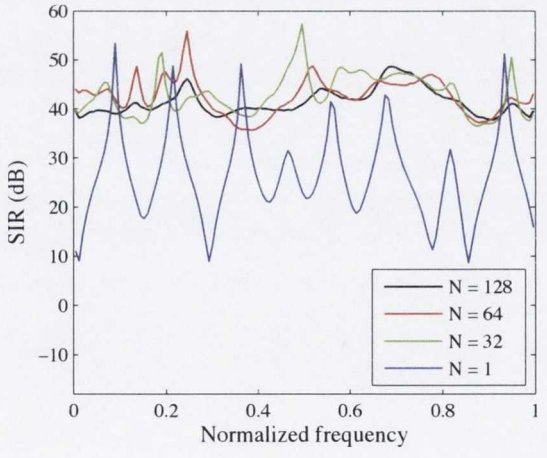

(c) $L = 128$

Fig. 4.1 SIR comparison of the MF linear combining technique for different number of receive antennas, N.

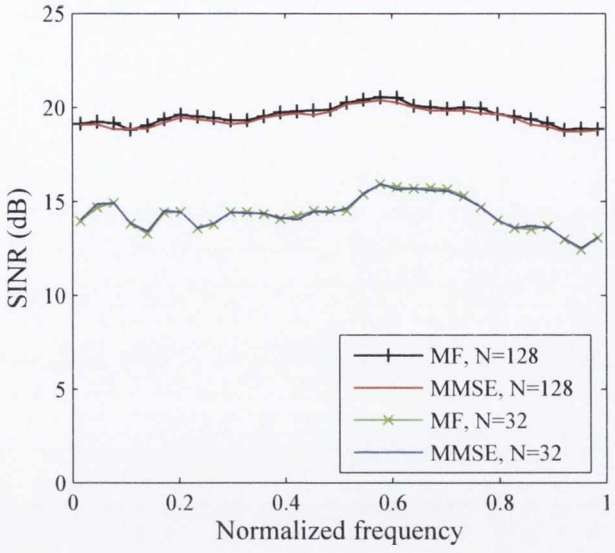

Fig. 4.2 SINR comparison between MMSE and MF linear combining techniques in the single user case with $L = 32$, when the user's SNR at the receiver input is -1 dB for two cases of $N = 128$ and $N = 32$.

as noted earlier, reduces transmission latency, increases bandwidth efficiency, and reduces sensitivity to CFO and PAPR.

Next, the channel noise is added to explore similar results to those in Fig. 4.1. Since a MF/MMSE receiver in the uplink (or a precoding in the downlink) has a processing gain of N, the SINR at the output may be calculated as $\mathrm{SNR}_{\mathrm{in}} + 10\log_{10} N$, where $\mathrm{SNR}_{\mathrm{in}}$ is the signal-to-noise ratio (SNR) at each BS antenna. The results, presented in Fig. 4.2, are for the cases where there are 32 and 128 antennas at the BS, the number of subcarriers is equal to 32 and $\mathrm{SNR}_{\mathrm{in}} = -1$ dB. As seen, here, the SINR curves in both MMSE and MF receivers coincide. The processing gains for $N = 128$ and 32 antennas are respectively 21 and 15 dB, and the expected output SINR values 20 and 14 dB are observed.

The above results were presented for the single user case. The situation changes significantly in the multiuser scenario due to the presence of MUI. As shown in the following results, when multiple MTs simultaneously communicate with a BS, MMSE outperforms MF by a significant margin. This result that is applicable to both FBMC and OFDM-based MIMO systems is indeed a very interesting observation that has also been recently reported in [115].

The analytical SINR relationships derived in section 4.1 are calculated with the assumption of having a flat channel per subcarrier. Therefore, they can be chosen as

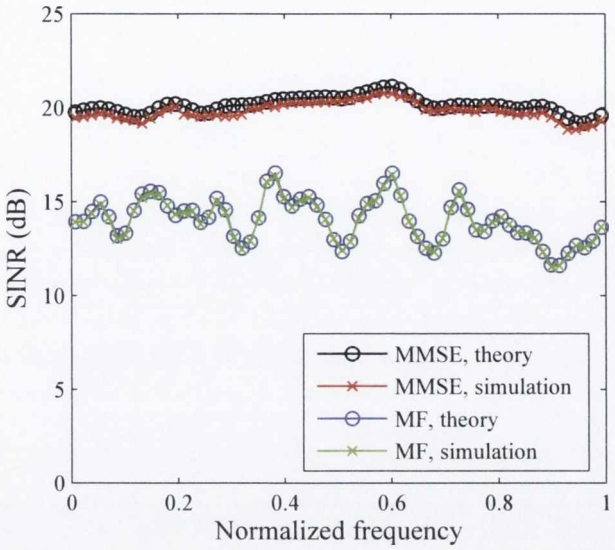

Fig. 4.3 SINR comparison between MMSE and MF linear combining techniques for the case of $K = 6$, $L = 64$ and $N = 128$.

benchmarks to evaluate the channel flatness in the subcarrier bands. Figs. 4.3 and 4.4 present the theoretical and simulations results in a multiuser scenario where $K = 6$, $N = 128$, the target SINR is 20 dB (the SNR at each antenna at the BS is selected as $20 - 10\log_{10} N$ dB) and the cases of $L = 64$ and 32 are examined. As the figures depict, the MMSE combining technique is superior to the MF one and its SINR is about the same for all the subcarriers, i.e., has smaller variance across the subcarriers. When $L = 64$ (Fig. 4.3), for the SINR curves for both MF and MMSE techniques, the simulation results coincide with the theoretical ones almost perfectly, confirming the self-equalization property of linear combining in massive MIMO FBMC systems. When $L = 32$ (wide-band subcarriers with 87.5 kHz width), the SINR curves from simulations for the MF receiver is still the same as the theoretical curve. However, the SINR simulations for the MMSE combining falls 1 dB below the theoretical predictions.

4.2.2 Numerical study of FS-based CMT in a massive MIMO channel

In this section, the theoretical developments of section 4.1.2 are analyzed and corroborated through numerical results. We use the results of section 4.2.1 as the basis in order to evaluate the signal processing power of the FS method in the context of

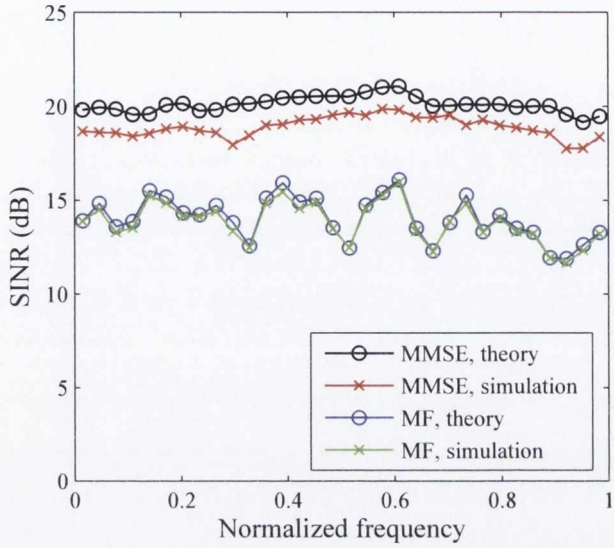

Fig. 4.4 SINR comparison between MMSE and MF linear combining techniques for the case of $K = 6$, $L = 32$ and $N = 128$.

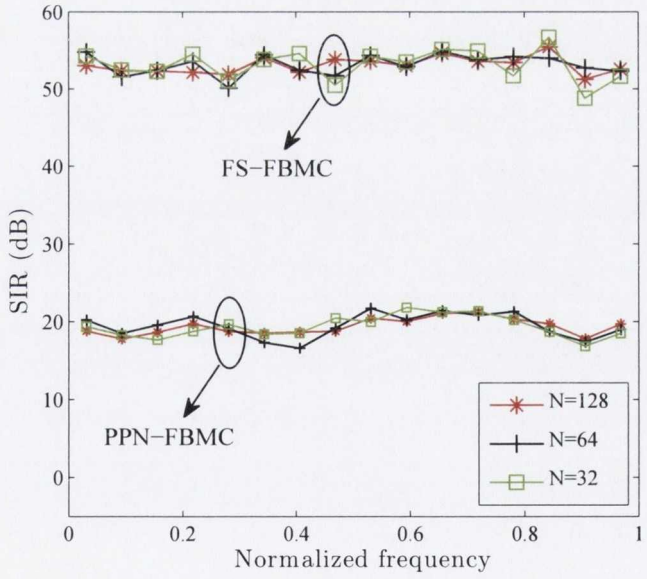

Fig. 4.5 SIR for the case of having $L = 16$, $M = 4$, $K = 1$ and different number of BS antennas.

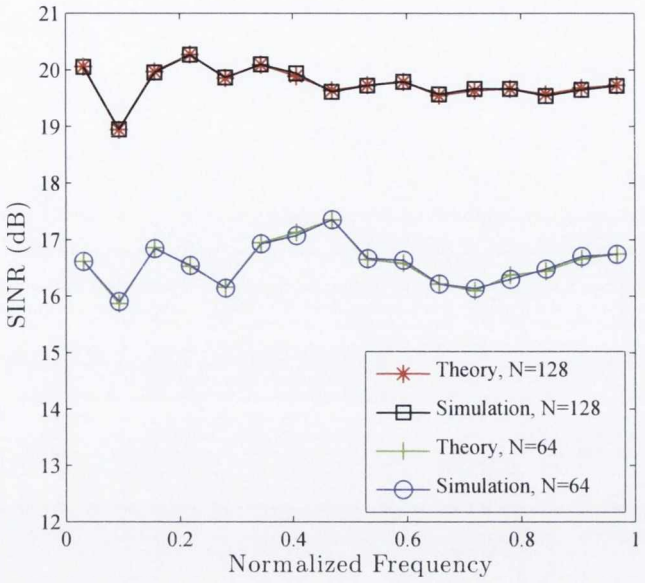

Fig. 4.6 SINR evaluation of the MMSE linear combining for the case of $L = 16$, $M = 4$, and $K = 6$. The SNR at the receiver input is -1 dB.

massive MIMO. It is worth noting that all of our simulations are based on a sample set of channel responses generated according to the SUI-4 channel model proposed by the IEEE802.16 broadband wireless access working group, [113]. Additionally, the channels between different users and different antennas are considered independent with respect to each other.

In the first set of simulations, a noise free single-user scenario is considered in order to investigate the self-equalization property in FS-FBMC systems. Fig. 4.5 compares the signal-to-interference ratio (SIR) performance of the PPN-FBMC with FS-FBMC systems. A single-tap equalizer per subcarrier is used in the PPN-FBMC structure. SIRs are evaluated at all the subcarrier channels. Note that in each curve, the number of points along the normalized frequency is equal to the number of subcarrier bands, L. From Fig. 4.5, it can be understood that an SIR improvement of higher than 30 dB can be achieved through FS-FBMC in comparison with the PPN-FBMC structure. This means that higher order modulation schemes can be utilized in FS-FBMC based massive MIMO systems. The total bandwidth is fixed to 2.8 MHz, the number of subcarriers $L = 16$ and overlapping factor of $M = 4$ are considered. This results in the subcarrier spacing of $2800/16 = 175$ kHz. This subcarrier spacing is relatively wide. In fact, it is $175/15 \approx 12$ times larger than the subcarrier spacing of the OFDM-based systems (e.g. IEEE 802.16 and LTE).

Next, we consider a multiuser scenario with $K = 6$ users, $L = 16$ subcarriers and $M = 4$. The signal-to-noise-ratio (SNR) of -1 dB at the input of BS antennas is considered. The output SINR can be obtained using $\text{SNR}_{\text{in}} + 10\log_{10} N$ in dB, [5]. Fig. 4.6 presents the theoretical (based on (4.18)) and simulation-based SINR values at different subcarriers for two cases of $N = 128$ and $N = 64$. As the figure depicts, the theoretical derivations match perfectly with the simulation results. The subcarrier spacing that achieves the same SINR as that of (4.18) is 4 times larger than what was suggested in section 4.2.1. This can be deduced from comparing Figs. 4.6 and 4.3.

4.3 Comparison with OFDM

In the case of OFDM, the multiuser equation (4.3) simplifies to

$$\mathbf{x} = \mathbf{H}\mathbf{s} + \mathbf{v}. \tag{4.21}$$

Here, $\mathbf{x}$ is the vector of the received signal samples (over a specified subcarrier), $\mathbf{H}$ is the matrix of channel gains, $\mathbf{s}$ is the vector of data symbols from different users, and $\mathbf{v}$ is the channel noise vector. All these quantities are complex-valued.

The following differences pertain if one compares (4.3) and (4.21).

1. While all variables/constants in (4.3) are real-valued, their counterparts in (4.21) are complex-valued.

2. The users' data vector $\mathbf{s}$ in (4.21) has K elements. This means each user receives multiuser interference from $K-1$ other users. In (4.3), on the other hand, each user receives interference from $2(K-1)$ users, from which $K-1$ are actual users and the rest we refer to as virtual users. For instance, if the data user of interest is $s(0)$, it may receive interference from $s(1)$, $s(2)$, $\cdots$, $s(K-1)$ (the actual user symbols) and $q(1)$, $q(2)$, $\cdots$, $q(K-1)$ (the virtual user symbols - contributions from ISI and ICI components).

3. While the processing gain in the OFDM-based systems is N (equal to the number of elements is each column of channel gain matrix $\mathbf{H}$), this number doubles in the CMT-based system.

4. Considering the observations 2) and 3), it is readily concluded that both CMT-based and OFDM-based systems suffer from the same level of multiuser interference.

These observations imply that, in massive MIMO, signal enhancement through linear combining leads to the same results for both OFDM and CMT-based systems. Nevertheless, CMT offers the following advantages over OFDM.

More flexible carrier aggregation: To make a better use of the available spectrum, recent wireless standards put a lot of emphasis on carrier aggregation. Variety of implementations of carrier aggregation has been reported. Apparently, some companies use multiple radios to transmit/receive signals over different portions of the spectrums. Others, e.g., [12], suggest modulation and filtering of the aggregated spectra. These solutions are more expensive and less flexible than carrier aggregation in FBMC. Hence, one compelling reason to adopt FBMC in future standards may be this advantage that it has over OFDM.

Lower sensitivity to CFO: As numerically demonstrated in the previous sections, compared to OFDM, FBMC allows an increase in subcarrier spacing. This, in turn, reduces the sensitivity of FBMC to CFO.

Lower PAPR: Reduced number of subcarriers naturally brings low PAPR property to the FBMC signal.

Higher bandwidth efficiency: Because of the absence of CP in FBMC, it expectedly offers higher bandwidth efficiency than OFDM. One point to be noted here is that FBMC usually requires a longer preamble than OFDM. The possibility of reducing the number of subcarriers in FBMC, that was noted earlier, can significantly reduce the preamble length in FBMC. Hence, it reduces the overhead of the preamble to a negligible amount.

4.4 Blind equalization and pilot decontamination

As discussed in Chapter 2, pilot contamination problem in massive MIMO networks operating in TDD mode can limit their expected capacity to a great extent, [6]. This section addresses this problem in CMT-based massive MIMO networks; taking advantage of their so-called blind equalization property. It is worth mentioning that we consider the polyphase implementation of CMT system here. We extend and apply the blind equalization technique from single antenna case, [114], to multi-cellular massive MIMO systems and show that it can remove the channel estimation errors

(due to pilot contamination effect) without any need for cooperation between different cells or transmission of additional training information. Our numerical results that are presented in section 4.4.1 advocate the efficacy of the proposed blind technique in improving the channel estimation accuracy and removal of the residual channel estimation errors caused by the users of the other cells.

Consider a multi-cellular massive MIMO network consisting of $C > 1$ cells and K MTs in each cell. Each MT is equipped with a single transmit and receive antenna, communicating with the BS in a TDD manner. Each BS is equipped with $N \gg K$ transmit/receive antennas that are used to communicate with the K MTs in the cell *simultaneously*.

Each MT is distinguished by the BS using the respective subcarrier gains between its antenna and the BS antennas. Ignoring the time and subcarrier indices in our formulation, for simplicity of equations, a transmit symbol $s_c(\ell)$ from the ℓ^{th} MT located in the c^{th} cell, arrives at the j^{th} BS as a vector

$$\mathbf{x}_{j\ell} = t_c(\ell)\mathbf{h}_{cj\ell}, \tag{4.22}$$

where $t_c(\ell) = s_c(\ell) + jq_c(\ell)$ and $q_c(\ell)$ is the contribution of ISI and ICI. $\mathbf{h}_{cj\ell} = [h_{cj\ell}(0), \ldots, h_{cj\ell}(N-1)]^{\mathrm{T}}$ indicates the channel gain vector whose elements are the gains between the ℓ^{th} MT located in cell c and different antennas at the j^{th} BS. The received signal vector at the j^{th} BS, $\mathbf{x}_j$, contains contributions from its own MTs and the ones located in its neighboring cells apart from the channel noise vector $\mathbf{v}_j$.

$$\mathbf{x}_j = \sum_{c=0}^{C-1}\sum_{\ell=0}^{K-1} \alpha_{cj\ell}\mathbf{x}_{c\ell} + \mathbf{v}_j, \tag{4.23}$$

where $\alpha_{cj\ell}$'s are the cross-gain factors between the ℓ^{th} user of the c^{th} cell and the BS antennas of the j^{th} cell which can be thought as path loss coefficients. In general, $\alpha_{cj\ell} \in [0, 1]$. Considering perfect power control for the users of each cell implies that $\alpha_{cj\ell} = 1$ for $c = j$. The vector $\mathbf{x}_j$ is fed into a set of linear estimators at the j^{th} BS to estimate the users' data symbols $s_j(0)$, $s_j(1)$, $\cdots$, $s_j(K-1)$. The equation (4.23) can be rearranged as

$$\mathbf{x}_j = \mathbf{H}_{jj}\mathbf{t}_j + \sum_{\substack{c=0 \\ c\neq j}}^{C-1} \mathbf{H}_{cj}\boldsymbol{\alpha}_{cj}\mathbf{t}_c + \mathbf{v}_j, \tag{4.24}$$

where the vector $\mathbf{t}_c = [t_c(0), \ldots, t_c(K-1)]^{\mathrm{T}}$, $\boldsymbol{\alpha}_{cj} = \mathrm{diag}\{\alpha_{cj0}, \ldots, \alpha_{cj(K-1)}\}$ and $\mathbf{H}_{cj}$'s are $N \times K$ fast fading channel matrices with the columns $\mathbf{h}_{cj\ell}$, $\ell = 0, 1, \ldots, K-1$.

With the assumption of having the perfect CSI knowledge, the matched filter tap-weight vector for user ℓ located in the j^{th} cell can be represented as

$$\mathbf{w}_{j\ell} = \frac{\mathbf{h}_{jj\ell}}{\mathbf{h}_{jj\ell}^{\mathrm{H}}\mathbf{h}_{jj\ell}}. \tag{4.25}$$

The estimated users' data symbols at the output of the matched filters of the cell j can be mathematically written as

$$\hat{\mathbf{s}}_j = \Re\{\mathbf{D}^{-1}\mathbf{H}_{jj}^{\mathrm{H}}\mathbf{x}_j\}, \tag{4.26}$$

where $\mathbf{D} = \mathrm{diag}\{\|\mathbf{h}_{jj0}\|^2, \ldots, \|\mathbf{h}_{jj(K-1)}\|^2\}$ and $\hat{\mathbf{s}}_j$ is the estimation of the vector $\mathbf{s}_j = [s_j(0), \ldots, s_j(K-1)]^{\mathrm{T}}$ which contains the users' transmitted data symbols. As discussed in [5], given the perfect CSI knowledge at the BS, when the number of antennas, N, tends to infinity, the antenna array gain goes to infinity and hence the multiuser interference and thermal noise effects vanish. As a result, we have $\hat{\mathbf{s}}_j = \mathbf{s}_j$ and the receiver will be optimum.

The channel gains between the MTs and the BS antennas in each cell are estimated through training pilots transmitted during the uplink phase. The MTs in each cell transmit pilots from a set of mutually orthogonal pilot sequences which allows the BS to distinguish between the channel impulse responces of different users in channel estimation stage. As the authors argued in [6], the channel coherence time does not allow the users of neighboring cells to use orthogonal pilot sequences in the multi-cellular scenario. In TDD multi-cellular massive MIMO networks, C base stations use the same set of pilot sequences as well as frequencies. In addition, synchronous transmissions are assumed. Therefore, the same set of pilot sequences being used in neighboring cells will adversely affect the channel estimates at the BS. This effect is called pilot contamination. After correlating the received training symbols with the set of pilot sequences at the BS j, the estimates of the channel gains between the MTs and massive array antennas of the BS can be given as

$$\hat{\mathbf{H}}_{jj} = \mathbf{H}_{jj} + \sum_{\substack{c=0 \\ c\neq j}}^{C-1} \mathbf{H}_{cj}\boldsymbol{\alpha}_{cj} + \tilde{\mathbf{V}}_j, \tag{4.27}$$

where the $N \times K$ matrix $\tilde{\mathbf{V}}_j = [\tilde{\mathbf{v}}_j(0), \ldots, \tilde{\mathbf{v}}_j(K-1)]$ contains the channel noise vector $\mathbf{v}_j$ correlated with the pilot sequences of the BS j on its columns. As one can realize from (4.27), the channel estimates at the j^{th} cell are corrupted by the

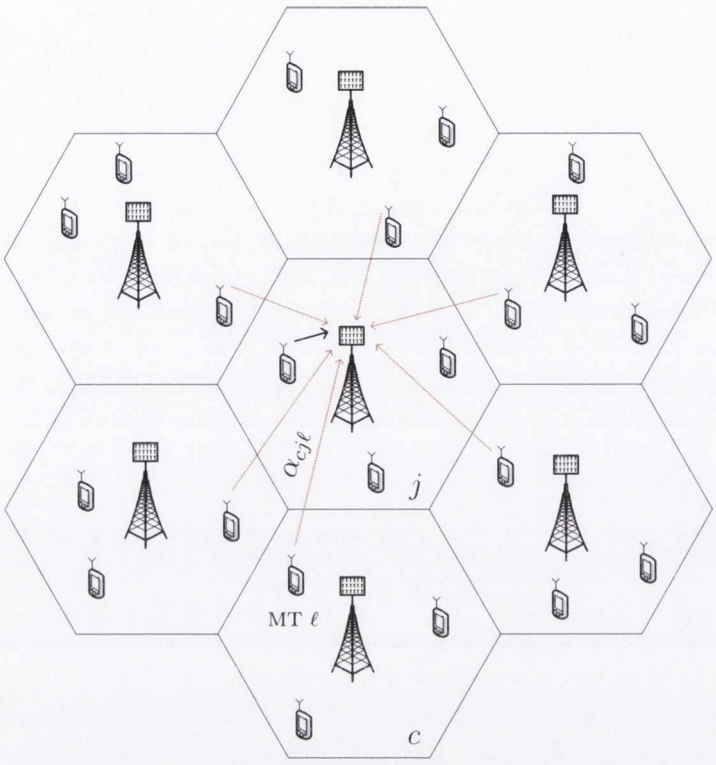

Fig. 4.7 Pilot contamination effect in a multi-cellular massive MIMO network.

channel impulse responses of its adjacent cells. Therefore, even with infinite number of receive antennas at the BS, there will exist some multiuser interference from the users of other cells. Fig. 4.7 shows this problem in a multi-cellular massive MIMO network where the red arrows show the interference from other cells and the black one shows the transmitted signal of the desired user in the training phase, i.e., uplink transmission. Pilot contamination can have detrimental effects on the performance of multi-cellular networks and greatly impair their sum rate [5]. In the next section, we extend the blind equalization property of CMT to massive MIMO systems in order to purify the channel estimates and tackle the pilot contamination problem without any need for cooperation among the cells or additional training information.

As it is noted in [114], the imaginary part of the CMT symbol at each subcarrier, i.e. $q_c(\ell)$ is formed from a linear combination of a large number of symbols from the corresponding and also adjacent subcarriers. Following the central limit theorem, one can come up with three observations here:

1. The favorable real-part of the equalized CMT symbol at each subcarrier is free of ISI and ICI and so its distribution follows that of the respective PAM alphabet.

2. The respective imaginary part suffers from ISI and ICI and is distributed in a Gaussian manner.

3. Both the real and imaginary parts of an unequalized symbol at a subcarrier comprise of ISI and ICI terms and indeed are distributed in a Gaussian manner.

Based on the aforementioned properties, a blind equalization algorithm similar to the Godard blind equalization algorithm [116] was developed in [114] such that the cost function

$$\xi = \mathbb{E}[(|y_k(n)|^p - R)^2], \tag{4.28}$$

is minimized. $y_k(n)$ is the equalizer output (in the case here, the equalizer output of the k^{th} subcarrier channel), p is integer (usually set equal to 1 or 2), n is the iteration index, $R = \mathbb{E}[|s|^{2p}]/\mathbb{E}[|s|^p]$, and s is a random selection from the PAM symbols alphabet.

In the following, we propose to exploit this algorithm in order to adaptively correct the imperfect channel estimates and hence greatly alleviate the performance degradation due to the contaminated pilots. An LMS (least mean squares) like blind-tracking algorithm, which is computationally inexpensive, based on the cost function (4.28) can be adopted. Extension of the proposed blind equalization technique of [114] to massive MIMO application can be straightforwardly derived as

$$\mathbf{w}_{j\ell}(n+1) = \mathbf{w}_{j\ell}(n) - 2\mu \text{sign}(\hat{s}_j^{(n)}(\ell))(|\hat{s}_j^{(n)}(\ell)| - R) \cdot \mathbf{x}_j(n), \tag{4.29}$$

where $\hat{s}_j^{(n)}(\ell) = \mathbf{w}_{j\ell}^{\text{H}}(n)\mathbf{x}_j(n)$, the $N \times 1$ vector $\mathbf{x}_j(n)$ is the n^{th} symbol of the received data packet at the BS antennas, the $N \times 1$ vector $\mathbf{w}_{j\ell}(n)$ contains the combiner tap-weights calculated in the n^{th} iteration and μ is the step-size parameter. We initialize the algorithm through the matched filter tap-weight vector

$$\mathbf{w}_{j\ell}(0) = \frac{\hat{\mathbf{h}}_{jj\ell}}{\hat{\mathbf{h}}_{jj\ell}^{\text{H}}\hat{\mathbf{h}}_{jj\ell}}, \tag{4.30}$$

where $\hat{\mathbf{h}}_{jj\ell}$ is the estimated channel vector between the user ℓ located in the cell j and the j^{th} BS antenna arrays, i.e., the ℓ^{th} column of $\hat{\mathbf{H}}_{jj}$ in (4.27). In the next section, we will show through numerical results that our proposed channel tracking algorithm is able to effectively converge towards the MMSE linear combining with

perfect knowledge of channel responses of all the users in all the considered cells, while starting from matched filter tap-weights with imperfect CSI.

4.4.1 Simulation results

In this section, we will numerically investigate the performance of our proposed pilot decontamination technique based on equation (4.29). This solution extends the blind equalization capability of CMT to massive MIMO networks in order to cope with imperfect channel estimates caused by the pilot contamination effect.

In our simulations, we consider a massive MIMO network which is comprised of seven cells where the pilot signals of the cell of interest, viz. cell j, are interfered by the users of its adjacent cells (Fig. 4.7). We assume one interferer in each neighbouring cell, i.e., 6 interferers in total whose random cross-gains are less than one. Without loss of generality, in order to expedite our simulations, we consider one user in the j^{th} cell using the same pilot sequence as the users in all its neighbouring cells. Thus, its channel estimates at the BS include some residuals from the channel responses of the users of other cells. One transmit antenna is assumed for each user and the number of antennas at the BS are $N = 128$. Uncorrelated channel impulse responses between the users and the BS antennas are assumed. The results are for a sample set of channel responses generated based on the Cost 207 channel model for typical urban area with 6 taps. The cross-gain factors, $\alpha_{cj\ell}$'s, are randomly chosen from the range [0,1]. The total bandwidth for this channel is equal to 5 MHz. We take into account $L = 256$ number of subcarriers in our simulations whose subcarrier spacing is equal to 19.531 kHz. Binary PAM signaling is used in our simulations. This is equivalent to QPSK (quadrature phase shift keying) signaling if OFDM was adopted. The target SINR in our simulations is set equal to 32 decibels (dB).

After the BS estimates the channel responses of its users through their pilot sequences, the equalizer tap-weights are initialized using equation (4.30). Then filter tap-weight adaptation will be performed. Due to the different channel gains, each subcarrier has a different signal level. Therefore, the step-size μ will be normalized with respect to the instantaneous signal energy in each iteration. Accordingly, for the binary PAM signaling, the combiner tap-weights can be updated using

$$\mathbf{w}_{j\ell}(n+1) = \mathbf{w}_{j\ell}(n) - \frac{2\mu}{\mathbf{x}_j^{\mathrm{H}}(n)\mathbf{x}_j(n) + \epsilon} \operatorname{sign}(\hat{s}_j^{(n)}(\ell)) \times (|\hat{s}_j^{(n)}(\ell)| - R) \cdot \mathbf{x}_j(n), \tag{4.31}$$

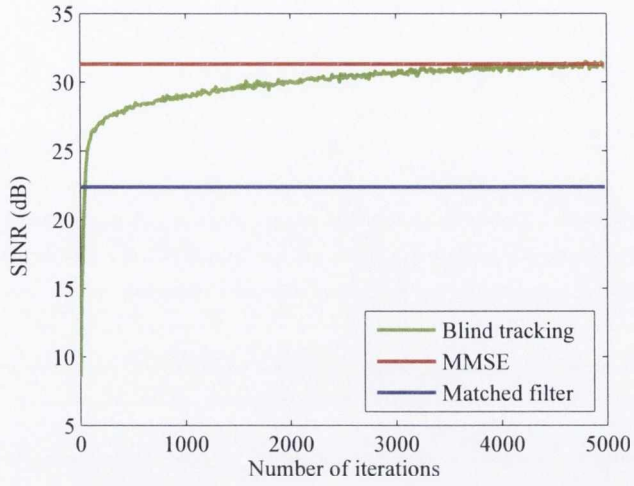

Fig. 4.8 SINR comparison of our proposed blind tracking technique with respect to the MF and MMSE detectors having the perfect CSI knowledge.

where ϵ is a small positive constant which assures numerical stability of the algorithm when the term $\mathbf{x}_j^{\mathrm{H}}(n)\mathbf{x}_j(n)$ has a small value.

Our proposed pilot decontamination technique is evaluated through looking into its SINR performance and comparing it with the SINRs of the MF and MMSE detectors having the perfect CSI knowledge of all the users in all the cells. The SINRs of the MF and MMSE linear combiners are calculated based on equations (4.10) and (4.11), respectively. It is worth mentioning that for the MMSE combining, the j^{th} BS needs to know the perfect channel impulse responses of all the users located in its neighbouring cells having the same pilot sequences as its own user.

Fig. 4.8, shows the SINR performance of the proposed blind tracking technique in dB with respect to the number of iterations. As the figure depicts, there exists an abrupt SINR improvement during the first 50 iterations where the output SINR of the blind combiner reaches that of the MF combiner with the perfect CSI knowledge. Running larger numbers of iterations has shown that the output SINR of our blind channel tracking technique can suppress the pilot contamination effect and converge towards that of the MMSE combiner. Apart from its high computational complexity, the MMSE detector needs perfect knowledge of the channel impulse responses between the interfering users of the other cells and its array antennas. This clearly is an impossible condition. Methods proposed here, on the other hand can approach MMSE performance, simply by running an LMS like algorithm.

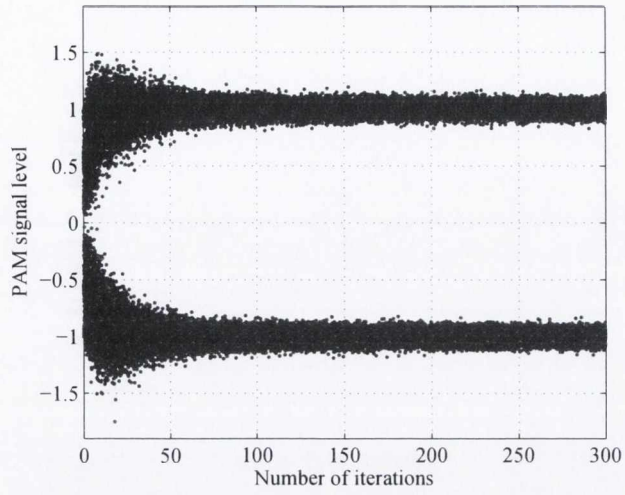

Fig. 4.9 Eye pattern of the combined symbols using the proposed blind tracking technique.

Fig. 4.9 represents the eye pattern of the detected symbols using our proposed blind combiner with respect to the number of iterations. As can be seen, the eye pattern of the detected symbols improves as the number iterations increases.

The existing techniques in the literature which address the pilot contamination problem, [8–10], either need cooperation between the cells or they are computationally intensive. The solutions that are applicable to non-cooperative cellular networks are of interest here, [8, 10]. The solution proposed in [8] needs eigenvalue decomposition of the covariance of the received signal and the one presented in [10] has to calculate the SVD of the received signal matrix. The involved matrices are of size N (128 for the examples given here). However, our solution simply needs to update the combiner tap-weights using (4.31). Hence, it has a low computational complexity. In addition, it is structurally simple which makes it attractive from practical implementation point of view.

From Fig. 4.8, one may realize that a large number of iterations are needed for our algorithm to approach the SINR performance of the MMSE detector. This does not mean that a very long packet of data is needed for this algorithm to converge towards the MMSE detector's performance. The MMSE performance can be achieved through multiple runs of the algorithm over a much shorter packet of data.

4.5 Conclusion

In this chapter, we introduced FBMC as a viable candidate waveform in the application of massive MIMO. Among various FBMC techniques, CMT was identified as the best choice. It was shown that while FBMC offers the same processing gain as OFDM, it offers the advantages of more flexible carrier aggregation, higher bandwidth efficiency (because of the absence of CP), blind channel equalization and larger subcarrier spacing, hence, less sensitivity to CFO and lower PAPR. The self-equalization property of CMT in massive MIMO channels was also elaborated on. The SINR performance for two different linear combining techniques; namely, MF and MMSE linear combiners were investigated. The analytical SINR equations for the aforementioned techniques were derived for both polyphase-based and FS-based implementations of CMT and their accuracy were evaluated through numerical examples. We addressed the pilot contamination problem in a TDD multi-cellular massive MIMO network. The pilot contamination problem can adversely affect the performance of the massive MIMO networks and as a result create a great amount of multi-cell interference in both uplink and downlink transmissions. The blind equalization capability of CMT is extended to massive MIMO networks to mitigate the pilot contamination effect. The performance of our proposed solution is analyzed through computer simulations. It has been shown that starting from corrupted channel estimates, after running a small number of iterations our algorithm performs as well as or better than the matched filter with perfect CSI. We have shown that the output SINR of our algorithm converges towards that of the MMSE solution where the BS should have the perfect knowledge of CSI for all the users located in its neighboring cells.

Opposed to chapter 3, in this chapter, we looked into FBMC as an alternative waveform to the widely used OFDM waveform. Based on the aforementioned points, FBMC is a strong candidate for the physical (PHY) layer of 5G systems. Apart from FBMC, some other waveforms are also being discussed to be used in the PHY layer of 5G wireless network. Due to the advent of some applications in such networks such as Internet of Things (IoT) and machine to machine (M2M) communications, the waveform to be used in 5G needs to meet specific requirements, e.g. the need for a laxer synchronization in multiuser scenarios, lower latency and lower out of band emissions as compared to OFDM. The main trend in waveform design for 5G is to find a waveform that keeps the good properties of OFDM while addressing its shortcomings, [11]. Hence, we look into such potential waveform candidates for 5G in the next chapter.

Chapter 5

Potential waveforms for future multiple access systems

OFDM (orthogonal frequency division multiplexing) has been the technology of choice in wired and wireless systems for years, [97–99]. The advent of the fifth generation of wireless communication systems (5G) and the associated focus on a wide range of applications from those involving bursty machine-to-machine (M2M) like traffic to media-rich high bandwidth applications has led to a requirement for new signaling techniques with better time and frequency containment than that of OFDM. Hence, a plethora of waveforms are coming under the microscope for analysis and investigation.

The limitations of OFDM are well documented. OFDM suffers from large out-of-band emissions which not only have interference implications but it also can reduce the potential for exploiting non-contiguous spectrum chunks through such techniques as carrier aggregation, [117]. For future high bandwidth applications this can be a major drawback. OFDM also has high sensitivity to synchronization errors especially carrier frequency offset (CFO). As a case in point, in multiuser uplink scenarios where OFDMA is utilized, in order to avoid the large amount of interference caused by multiple CFOs as well as timing offsets, stringent synchronization is required which in turn imposes a great amount of overhead to the network. This overhead is not acceptable for lightweight M2M applications for example. As discussed in Chapter 3, the presence of multiple Doppler shifts and propagation delays in the received uplink signal at the base station (BS) results in some residual synchronization errors and hence multiuser interference (MUI), [2]. The MUI problem can be tackled with a range of different solutions, [2, 47], including the ones that were discussed in Chapter 3. However, these lead to an increased receiver computational complexity. Thus, one of

the main advantages of OFDM, i.e., its low complexity, is lost. The challenge therefore is to provide waveforms with more relaxed synchronization requirements and more localized signals in time and frequency to suit future 5G applications, without the penalty of a more complex transceiver.

There are many suggestions on the table as candidate waveforms [12–14, 22, 50]. In general, all of these signaling methods can be considered as filter bank multicarrier (FBMC) systems. They can be broadly broken into two categories, those with linear pulse shaping [22, 50] and those with circular pulse shaping, [12–14]. The former signals with linear pulse shaping have attractive spectral properties, [15]. In addition, these systems are resilient to the timing as well as frequency errors. However, the ramp-up and ramp-down of their signal which are due to the transient interval of the prototype filter result in additional latency issues. As it was highlighted in Chapter 4, ramp-up and ramp-down of the FBMC signal that is formed through linear pulse shaping can be reduced in the context of 5G massive MIMO systems, thanks to the *self-equalization* property of these systems in such channels. In contrast, FBMC systems with circular pulse shaping such as generalized frequency division multiplexing (GFDM) remove the prototype filter transients thanks to their so called tail biting property, [12]. It is worth noting that the waveforms of interest in this chapter are based on FBMC signaling with circular pulse shaping. This chapter strives to respond the following research question raised in Chapter 1.

Question 3

- ***FBMC systems with circular pulse shaping have relaxed synchronization requirements which makes them suitable for applications like M2M. However, the existing transceiver structures for such systems are based on successive interference cancellation techniques which have the drawback of error propagation. Is it possible to design low complexity transceiver structures for such systems while providing the optimal performance?***

The rest of this chapter is organized as follows. Section 5.1 is dedicated to generalized frequency division multiplexing which is a candidate waveform for 5G. Low complexity transmitter and receiver structures are developed in sections 5.1.1 and 5.1.2, respectively. The computational complexity of these structures are analyzed and

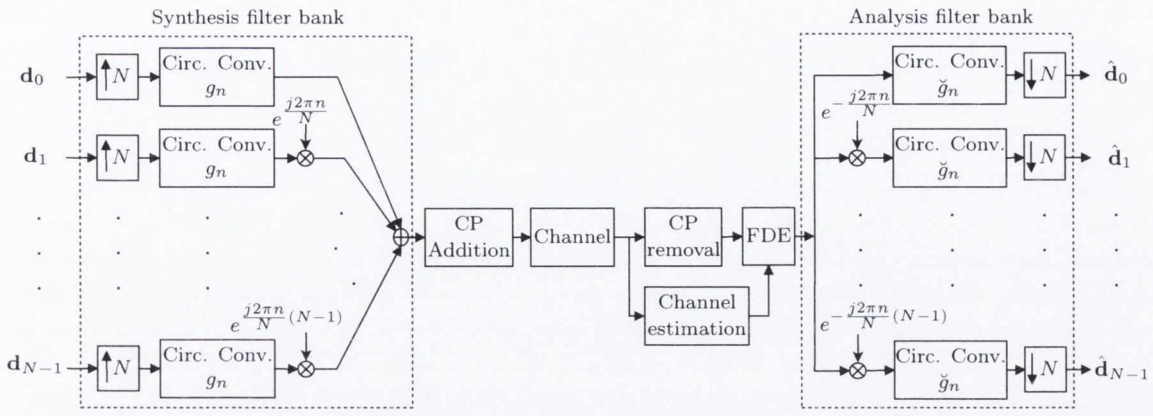

Fig. 5.1 Baseband block diagram of a GFDM transceiver system.

compared with the existing transceiver structures in the literature in section 5.1.3.1. Circular filter bank multicarrier which is another candidare waveform for 5G is explained in section 5.2. Section 5.2.1 compares circular filter bank multicarrier with generalized frequency division multiplexing. Sensitivity of 5G candidate waveforms to timing and frequency misalignment in uplink scenario is analyzed in section 5.3. Finally, the chapter is concluded in section 5.4.

5.1 Generalized frequency division multiplexing

As it was discussed in Chapter 2, generalized frequency division multiplexing (GFDM) is recently being discussed as a candidate waveform for 5G. GFDM can be categorized as a waveform with circular pulse shaping. In addition, it is introduced as a generalized form of the widely used OFDM modulation scheme and since it uses only one cyclic prefix (CP) for a group of symbols rather than a CP per symbol, it is more bandwidth efficient than OFDM.

The mathematical foundation of GFDM was introduced in Chapter 2. Consider a GFDM system with the total number of N subcarriers that includes M symbols in each block. In a GFDM data block, M symbols overlap in time and hence we call M the *overlapping factor* of the system. The $MN \times 1$ vector $\mathbf{d} = [\mathbf{d}_0^{\mathrm{T}}, \ldots, \mathbf{d}_{N-1}^{\mathrm{T}}]^{\mathrm{T}}$ contains the complex data symbols of the GFDM block where the $M \times 1$ data vector $\mathbf{d}_i = [d_i(0), \ldots, d_i(M-1)]^{\mathrm{T}}$ contains the data symbols to be transmitted on the i^{th} subcarrier.

Fig. 5.1, depicts the baseband block diagram of a GFDM transceiver when we have perfect synchronization in time and frequency between the transmitter and receiver. Fig. 5.1 summarizes the modulation and demodulation process that was

discussed in Chapter 2. It is worth mentioning that g_n's for $n = 0, \ldots, MN-1$ are the prototype filter coefficients and $\breve{g}_n$'s are the receiver filter coefficients which can be taken from the coefficients of matched filter (MF), zero forcing (ZF) or minimum mean square error (MMSE) receiver filter. As it was mentioned above, GFDM is a type of filter bank multicarrier system with circular pulse shaping. Therefore, GFDM transmitter and receiver can be thought of as a pair of synthesis and analysis filter banks, respectively. After the GFDM symbol is formed through the synthesis filter bank, a CP that is longer than the delay spread of the channel is added to absorb the transient of the channel and ease equalization at the receiver side. Assuming full time and frequency synchronization between the transmitter and receiver and having perfect estimation of the channel, a frequency domain equalizer (FDE) is utilized to compensate for the channel distortion. Then, the equalized signal is passed through an analysis filter bank to find the estimates of the transmitted data vectors, i.e., $\hat{\mathbf{d}}_i$'s for $i = 0, \ldots, N-1$.

Recalling from Chapter 2, all the signal processing steps that are involved in GFDM modulation can be performed by multiplication of a modulation matrix $\mathbf{A}$ to the data vector $\mathbf{d}$, i.e., $\mathbf{x} = \mathbf{A}\mathbf{d}$. Let $\mathbf{g} = [g_0, \ldots, g_{MN-1}]^{\mathrm{T}}$ hold all the coefficients of the pulse shaping/prototype filter with the length MN, the elements of $\mathbf{A}$ can be represented as,

$$[\mathbf{A}]_{nm} = g_{\{(n-mN) \bmod MN\}} e^{j\frac{2\pi n}{N}\lfloor \frac{m}{M} \rfloor}. \tag{5.1}$$

Based on the GFDM formulation in Chapter 2, the matrix $\mathbf{A}$ can be written as

$$\mathbf{A} = \begin{bmatrix} \boldsymbol{\mathcal{G}} & \boldsymbol{\mathcal{E}}_1\boldsymbol{\mathcal{G}} & \ldots & \boldsymbol{\mathcal{E}}_{N-1}\boldsymbol{\mathcal{G}} \end{bmatrix}, \tag{5.2}$$

where $\boldsymbol{\mathcal{G}}$ is an $MN \times M$ matrix whose first column contains the samples of the prototype filter $\mathbf{g}$ and its consecutive columns are the copies of the previous column that are circularly shifted by N samples. $\boldsymbol{\mathcal{E}}_i = \mathrm{diag}\{[\mathbf{e}_i^{\mathrm{T}}, \ldots, \mathbf{e}_i^{\mathrm{T}}]^{\mathrm{T}}\}$ is an $MN \times MN$ diagonal matrix whose diagonal elements are comprised of M concatenated copies of the vector $\mathbf{e}_i = [1, e^{j\frac{2\pi i}{N}}, \ldots, e^{j\frac{2\pi i}{N}(N-1)}]^{\mathrm{T}}$.

5.1.1 Low complexity transmitter design

This section presents our proposed low complexity GFDM transmitter design and implementation. In the following subsections, we will show how the synthesis filter bank of Fig. 5.1 can be simplified to have a very low computational load.

5.1.1.1 GFDM transmitter design

Starting from (2.34), one can realize that direct multiplication of the matrix $\mathbf{A}$ to the data vector $\mathbf{d}$ is a complex operation which demands $(MN)^2$ complex multiplications. Therefore, complexity will be an issue for practical systems as the number of subcarriers and/or the parameter M increases. Accordingly, a low complexity implementation technique for GFDM transmitter has to be sought. To this end, equation (2.34) can be written as

$$\mathbf{x} = \mathbf{A}\mathbf{d} = \mathbf{A}\boldsymbol{\mathcal{F}}_b^{\mathrm{H}}\boldsymbol{\mathcal{F}}_b\mathbf{d}, \tag{5.3}$$

where $\boldsymbol{\mathcal{F}}_b$ is the $MN \times MN$ normalized block DFT matrix that includes $M \times M$ submatrices $\boldsymbol{\Omega}_{ni} = \frac{1}{\sqrt{N}} e^{-j\frac{2\pi ni}{N}} \mathbf{I}_M$ and $n, i = 0, \ldots, N-1$. Validity of equation (5.3) is based on the fact that $\boldsymbol{\mathcal{F}}_b^{\mathrm{H}}\boldsymbol{\mathcal{F}}_b = \mathbf{I}_{MN}$. As it is derived in Appendix B, the resulting matrix from multiplication of the block DFT matrix $\boldsymbol{\mathcal{F}}_b$ into $\mathbf{A}^{\mathrm{H}}$ is sparse and it is comprised of the prototype filter coefficients scaled by $\sqrt{N}$. From equation (5.3), it can be inferred that $\boldsymbol{\Gamma}^{\mathrm{H}} = \mathbf{A}\boldsymbol{\mathcal{F}}_b^{\mathrm{H}}$ is also sparse since it is the conjugate transpose of $\boldsymbol{\mathcal{F}}_b\mathbf{A}^{\mathrm{H}}$. Hence, our strategy allows us to make the matrix $\mathbf{A}$ sparse and real as the prototype filter is usually chosen to have a real and symmetrical impulse response. Due to (5.3) and the definition of $\boldsymbol{\mathcal{F}}_b$, $\boldsymbol{\mathcal{F}}_b\mathbf{d}$ can be implemented by performing M DFT operations of size N on the data samples, i.e., one per GFDM symbol. Let $\bar{\mathbf{d}} = \boldsymbol{\mathcal{F}}_b\mathbf{d} = [\bar{\mathbf{d}}_0^{\mathrm{T}}, \ldots, \bar{\mathbf{d}}_{N-1}^{\mathrm{T}}]^{\mathrm{T}}$ where the $M \times 1$ vector $\bar{\mathbf{d}}_i = [\bar{d}_i(0), \ldots, \bar{d}_i(M-1)]^{\mathrm{T}}$ contains the i^{th} output of each DFT block, then (5.3) can be rearranged as

$$\mathbf{x} = \boldsymbol{\Gamma}^{\mathrm{H}}\bar{\mathbf{d}} = \sum_{i=0}^{N-1} \boldsymbol{\Gamma}_i^{\mathrm{H}}\bar{\mathbf{d}}_\kappa, \tag{5.4}$$

where $\kappa = (N-i) \bmod N$. As discussed in Appendix C, the $M \times MN$ matrices $\boldsymbol{\Gamma}_i$'s have only M non-zero columns and the sets of those column indices are mutually exclusive with respect to each other. As a result, $\boldsymbol{\Gamma}_i^{\mathrm{H}}\bar{\mathbf{d}}_\kappa$ will be a sparse vector with only M non-zero elements located on the positions $\kappa, \kappa+N, \ldots, \kappa+(M-1)N$. On the basis of the derivations that are presented in Appendix B, the non-zero elements of $\boldsymbol{\Gamma}_i^{\mathrm{H}}\bar{\mathbf{d}}_\kappa$ can be obtained from M-point circular convolution of $\bar{\mathbf{d}}_\kappa$ with the κ^{th} polyphase component of the prototype filter $\mathbf{g}_\kappa$ that is scaled by $\sqrt{N}$. Therefore, defining the non-zero elements of $\boldsymbol{\Gamma}_i^{\mathrm{H}}\bar{\mathbf{d}}_\kappa$ as the vector $\mathbf{x}_\kappa = [x_\kappa, x_{\kappa+N}, \ldots, x_{\kappa+(M-1)N}]^{\mathrm{T}}$, we get

$$\mathbf{x}_\kappa = \bar{\mathbf{g}}_\kappa \textcircled{M} \bar{\mathbf{d}}_\kappa, \tag{5.5}$$

where $\bar{\mathbf{g}}_\kappa = \sqrt{N}\mathbf{g}_\kappa$.

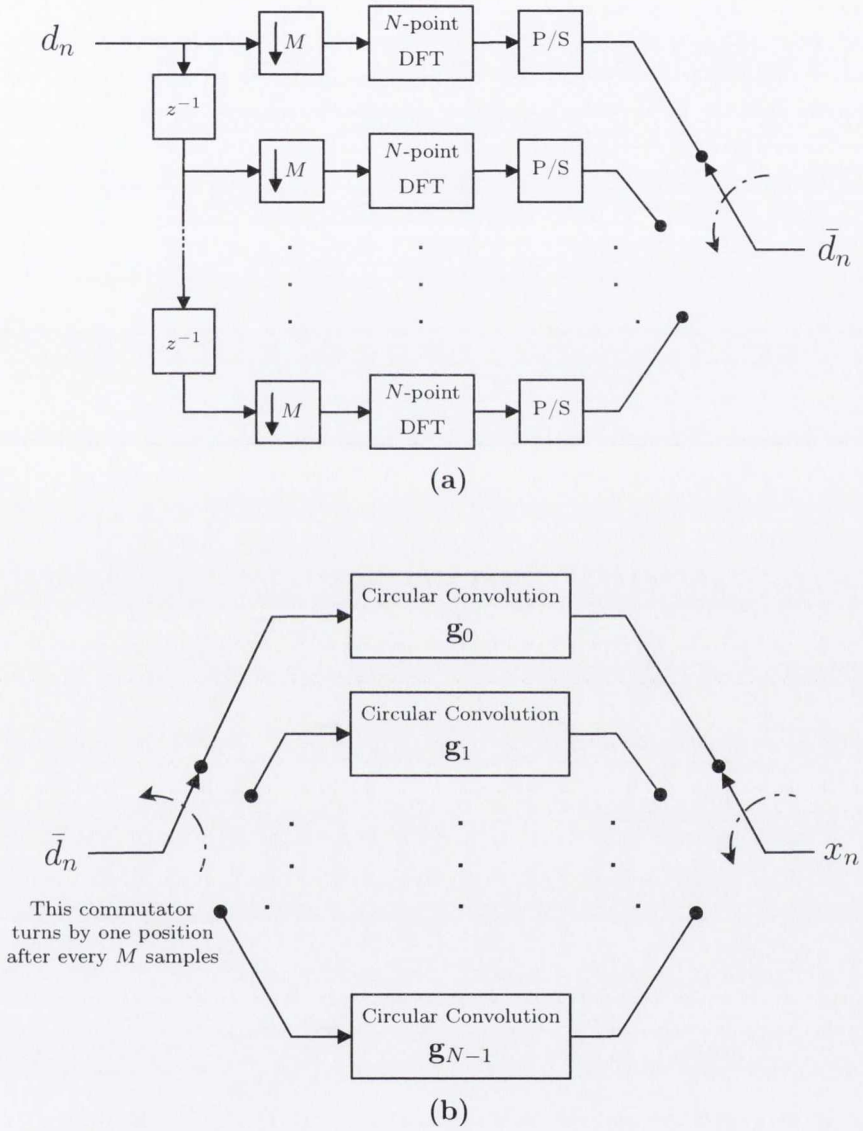

Fig. 5.2 Concatenation of **(a)** and **(b)** show the implementation of the proposed GFDM transmitter.

5.1.1.2 GFDM transmitter implementation

In this subsection, implementation of the designed GFDM transmitter in Section 5.1.1.1 is discussed. From the equations (5.3) to (5.5), GFDM modulation, based on our design, can be summarized into two steps.

1. M number of N-point DFT operations, i.e., application of N-point DFT to each individual GFDM symbol which includes N subcarriers. This can be efficiently implemented by taking advantage of the fast Fourier transform (FFT) algorithm.

2. N number of M-point circular convolution operations.

Therefore, the first and second steps of our GFDM transmitter can be implemented by cascading the block diagrams shown in Fig. 5.2 (a) and (b), respectively. The blocks P/S convert the parallel FFT outputs to serial streams. All the commutators shown in Fig. 5.2 turn counter clockwise. Both commutators located on the right hand side of the Fig. 5.2 (a) and (b) turn after one sample collection. However, the one located on the left hand side of Fig. 5.2 (b) turns by one position after sending M samples to each M-point circular convolution block.

5.1.2 Low complexity receiver design

In this section, we derive low complexity MF, ZF and MMSE receivers for GFDM systems. It is worth mentioning that our solutions are direct and hence lower complexity of these receivers comes for free as they do not result in any performance loss, thanks to the special structure of the matrix $\mathbf{A}^{\mathrm{H}}\mathbf{A}$. The characteristics of $\mathbf{A}^{\mathrm{H}}\mathbf{A}$ will be discussed in the next subsection and then we will derive our proposed receivers on the basis of those traits.

5.1.2.1 Block-diagonalization of the matrix $\mathbf{A}^{\mathrm{H}}\mathbf{A}$

The key idea behind our proposed GFDM receiver techniques is to take advantage of the particular structure of the matrix $\mathbf{A}^{\mathrm{H}}\mathbf{A}$ which is present in both ZF and MMSE receiver formulations. Using (2.36), one can calculate $\mathbf{A}^{\mathrm{H}}\mathbf{A}$ and find out that it has

the following structure

$$\mathbf{A}^{\mathrm{H}}\mathbf{A} = \begin{bmatrix} \boldsymbol{\mathcal{G}}^{\mathrm{H}}\boldsymbol{\mathcal{G}} & \boldsymbol{\mathcal{G}}^{\mathrm{H}}\boldsymbol{\mathcal{E}}_1\boldsymbol{\mathcal{G}} & \cdots & \boldsymbol{\mathcal{G}}^{\mathrm{H}}\boldsymbol{\mathcal{E}}_{N-1}\boldsymbol{\mathcal{G}} \\ \boldsymbol{\mathcal{G}}^{\mathrm{H}}\boldsymbol{\mathcal{E}}_1^{\mathrm{H}}\boldsymbol{\mathcal{G}} & \boldsymbol{\mathcal{G}}^{\mathrm{H}}\boldsymbol{\mathcal{G}} & \cdots & \boldsymbol{\mathcal{G}}^{\mathrm{H}}\boldsymbol{\mathcal{E}}_{N-2}\boldsymbol{\mathcal{G}} \\ \vdots & \vdots & \ddots & \vdots \\ \boldsymbol{\mathcal{G}}^{\mathrm{H}}\boldsymbol{\mathcal{E}}_{N-1}^{\mathrm{H}}\boldsymbol{\mathcal{G}} & \boldsymbol{\mathcal{G}}^{\mathrm{H}}\boldsymbol{\mathcal{E}}_{N-2}^{\mathrm{H}}\boldsymbol{\mathcal{G}} & \cdots & \boldsymbol{\mathcal{G}}^{\mathrm{H}}\boldsymbol{\mathcal{G}} \end{bmatrix}. \tag{5.6}$$

From the definition of vector $\mathbf{e}_i$, it can be straightforwardly perceived that $\mathbf{e}_{N-i}^{\mathrm{H}} = \mathbf{e}_i$ and hence $\boldsymbol{\mathcal{E}}_{N-i}^{H} = \boldsymbol{\mathcal{E}}_i$. Therefore, the columns of $\mathbf{A}^{\mathrm{H}}\mathbf{A}$ as shown in (5.6) are circularly shifted with respect to each other. Accordingly, $\mathbf{A}^{\mathrm{H}}\mathbf{A}$ is a block-circulant matrix with blocks of size $M \times M$. Following a similar line of derivations as in [107] and [20], $\mathbf{A}^{\mathrm{H}}\mathbf{A}$ can be expanded as follows

$$\mathbf{A}^{\mathrm{H}}\mathbf{A} = \boldsymbol{\mathcal{F}}_b^{\mathrm{H}}\boldsymbol{\mathcal{D}}\boldsymbol{\mathcal{F}}_b, \tag{5.7}$$

where $\boldsymbol{\mathcal{D}}$ is an $MN \times MN$ block-diagonal matrix, $\boldsymbol{\mathcal{D}} = \mathrm{diag}\{\boldsymbol{\mathcal{D}}_0, \ldots, \boldsymbol{\mathcal{D}}_{N-1}\}$ and $\boldsymbol{\mathcal{D}}_i$'s are $M \times M$ block matrices. From (5.7), $\boldsymbol{\mathcal{D}}$ can be derived as

$$\boldsymbol{\mathcal{D}} = \boldsymbol{\mathcal{F}}_b(\mathbf{A}^{\mathrm{H}}\mathbf{A})\boldsymbol{\mathcal{F}}_b^{\mathrm{H}}. \tag{5.8}$$

As it is explained in Appendix C, $\boldsymbol{\mathcal{D}}_i$'s can be derived from polyphase components of the prototype filter.

$$\boldsymbol{\mathcal{D}}_i = N\mathrm{circ}\{\mathbf{g}_\kappa \textcircled{M} \tilde{\mathbf{g}}_\kappa\}, \tag{5.9}$$

where $\kappa = (N-i) \bmod N$, the vector $\mathbf{g}_i$ contains the elements of i^{th} polyphase component of $\mathbf{g}$ and $\tilde{\mathbf{g}}_i = [g_i, g_{i+(M-1)N}, \ldots, g_{i+N}]^{\mathrm{T}}$ is its circularly folded version. As (5.9) highlights, $\boldsymbol{\mathcal{D}}_i$'s are all real and circulant matrices.

5.1.2.2 Low complexity MF receiver

Based on equation (2.39) from Chapter 2, direct implementation of MF receiver involves a matrix to vector multiplication which has the computational cost of $(MN)^2$ complex multiplications. This procedure becomes highly complex for large values of N and/or M which may be the case in the future standards. As discussed in Appendix B, multiplication of $\mathbf{A}^{\mathrm{H}}$ by the block DFT matrix results in a sparse matrix. Due to the fact that $\boldsymbol{\mathcal{F}}_b^{\mathrm{H}}\boldsymbol{\mathcal{F}}_b = \mathbf{I}_{MN}$, similar to the transmitter (equation(5.3)), equation (2.39)

can be written as

$$\begin{aligned}\hat{\mathbf{d}}_{\mathrm{MF}} &= \boldsymbol{\mathcal{F}}_b^{\mathrm{H}}\boldsymbol{\mathcal{F}}_b\mathbf{A}^{\mathrm{H}}\mathbf{y} \\ &= \boldsymbol{\mathcal{F}}_b^{\mathrm{H}}\boldsymbol{\Gamma}\mathbf{y},\end{aligned} \tag{5.10}$$

where $\boldsymbol{\Gamma}$ is a sparse matrix with only NM^2 non-zero elements that are the scaled version of the prototype filter coefficients. Closed form of $\boldsymbol{\Gamma} = [\boldsymbol{\Gamma}_0^{\mathrm{T}}, \ldots, \boldsymbol{\Gamma}_{N-1}^{\mathrm{T}}]^{\mathrm{T}}$ is derived in Appendix B and it is shown that the matrix is real valued and comprised of the prototype filter elements. Non-zero columns of the $M \times MN$ block matrices $\boldsymbol{\Gamma}_i$'s are circularly shifted copies of each other. Hence, multiplication of $\boldsymbol{\Gamma}_i$ and $\mathbf{y}$ is equivalent to M-point circular convolution of M equidistant elements of $\mathbf{y}$ starting from the κ^{th} position and circularly folded version of the κ^{th} polyphase component of $\mathbf{g}$ scaled by $\sqrt{N}$, viz., $\sqrt{N}\tilde{\mathbf{g}}_\kappa$. Usually, the prototype filter coefficients are real-valued. Thus, $\boldsymbol{\Gamma}$ is real-valued. Multiplication of $\boldsymbol{\mathcal{F}}_b^{\mathrm{H}}$ to the vector $\boldsymbol{\Gamma}\mathbf{y}$ can be implemented by applying M number of N-point IDFT operations. Let $\bar{\mathbf{y}} = \boldsymbol{\Gamma}\mathbf{y} = [\bar{\mathbf{y}}_0^{\mathrm{T}}, \ldots, \bar{\mathbf{y}}_{N-1}^{\mathrm{T}}]^{\mathrm{T}}$ and $\mathbf{y}_\kappa = [y_\kappa, y_{\kappa+N}, \ldots, y_{\kappa+(M-1)N}]^{\mathrm{T}}$. Therefore, we have

$$\bar{\mathbf{y}}_i = \boldsymbol{\Gamma}_i\mathbf{y} = \mathbf{v}_\kappa \textcircled{\scriptsize M} \mathbf{y}_\kappa, \tag{5.11}$$

where $\mathbf{v}_\kappa = \sqrt{N}\tilde{\mathbf{g}}_\kappa$. Finally, the MF estimates of $\mathbf{d}$ can be obtained as

$$\hat{\mathbf{d}}_{\mathrm{MF}} = \boldsymbol{\mathcal{F}}_b^{\mathrm{H}}\bar{\mathbf{y}}. \tag{5.12}$$

5.1.2.3 Low complexity ZF receiver

Inserting (5.7) into (2.40), we get

$$\hat{\mathbf{d}}_{\mathrm{ZF}} = \boldsymbol{\mathcal{F}}_b^{\mathrm{H}}\boldsymbol{\mathcal{D}}^{-1}\boldsymbol{\mathcal{F}}_b\mathbf{A}^{\mathrm{H}}\mathbf{y}. \tag{5.13}$$

Multiplication of matrix $\mathbf{A}^{\mathrm{H}}$ to the vector $\mathbf{y}$ is the first source of computational burden in ZF receiver which has computational cost of $(MN)^2$. However, this complexity can be reduced by taking advantage of the sparsity of the matrix $\boldsymbol{\Gamma} = \boldsymbol{\mathcal{F}}_b\mathbf{A}^{\mathrm{H}}$ as it was suggested in the previous subsection. Equation (5.11) can be written as $\bar{\mathbf{y}}_i = \boldsymbol{\Gamma}_i\mathbf{y} = \sqrt{N}\mathrm{circ}\{\tilde{\mathbf{g}}_\kappa\}\mathbf{y}_\kappa$. Let $\tilde{\mathbf{y}} = \boldsymbol{\mathcal{D}}^{-1}\bar{\mathbf{y}} = [\tilde{\mathbf{y}}_0^{\mathrm{T}}, \ldots, \tilde{\mathbf{y}}_{N-1}^{\mathrm{T}}]^{\mathrm{T}}$ where

$$\tilde{\mathbf{y}}_i = \sqrt{N}\boldsymbol{\mathcal{D}}_i^{-1}\mathrm{circ}\{\tilde{\mathbf{g}}_\kappa\}\mathbf{y}_\kappa. \tag{5.14}$$

Therefore, from rearranging equation (5.9) as $\boldsymbol{\mathcal{D}}_i = N\text{circ}\{\tilde{\mathbf{g}}_\kappa\}\text{circ}\{\mathbf{g}_\kappa\}$ and inserting it into (5.14), we have

$$\begin{aligned}\tilde{\mathbf{y}}_i &= \frac{1}{\sqrt{N}}(\text{circ}\{\tilde{\mathbf{g}}_\kappa\}\text{circ}\{\mathbf{g}_\kappa\})^{-1}\text{circ}\{\tilde{\mathbf{g}}_\kappa\}\mathbf{y}_\kappa \\ &= \frac{1}{\sqrt{N}}(\text{circ}\{\mathbf{g}_\kappa\})^{-1}\mathbf{y}_\kappa \\ &= \mathbf{q}_\kappa \textcircled{M} \mathbf{y}_\kappa, \end{aligned} \tag{5.15}$$

where $\mathbf{q}_\kappa$ includes the first column of the circulant matrix $(\text{circ}\{\mathbf{g}_\kappa\})^{-1}$ scaled by $\frac{1}{\sqrt{N}}$. Due to the fact that the the coefficients of the prototype filter are known, the vectors $\mathbf{q}_\kappa$'s can be calculated offline. Additionally, since the prototype filter coefficients are real, $\mathbf{q}_\kappa$'s are also real. From (5.15), one may realize that calculation of the vector $\tilde{\mathbf{y}}$ needs N number of M-point circular convolutions. After acquiring $\tilde{\mathbf{y}}$, the ZF estimates of the transmitted symbols can be obtained as

$$\hat{\mathbf{d}}_{\text{ZF}} = \boldsymbol{\mathcal{F}}_b^{\text{H}}\tilde{\mathbf{y}}. \tag{5.16}$$

As can be inferred from (5.16), finding $\hat{\mathbf{d}}_{\text{ZF}}$ from $\tilde{\mathbf{y}}$ requires M number of N-point inverse DFT (IDFT) operations.

5.1.2.4 Low complexity MMSE receiver

Using (5.7) in (2.41), we get

$$\begin{aligned}\hat{\mathbf{d}}_{\text{MMSE}} &= (\boldsymbol{\mathcal{F}}_b^{\text{H}}\boldsymbol{\mathcal{D}}\boldsymbol{\mathcal{F}}_b + {\sigma_\nu}^2\mathbf{I}_{MN})^{-1}\mathbf{A}^{\text{H}}\mathbf{y} \\ &= \boldsymbol{\mathcal{F}}_b^{\text{H}}\bar{\boldsymbol{\mathcal{D}}}^{-1}\boldsymbol{\mathcal{F}}_b\mathbf{A}^{\text{H}}\mathbf{y}, \end{aligned} \tag{5.17}$$

where $\bar{\boldsymbol{\mathcal{D}}} = \boldsymbol{\mathcal{D}} + {\sigma_\nu}^2\mathbf{I}_{MN} = \text{diag}\{\bar{\boldsymbol{\mathcal{D}}}_0, \ldots, \bar{\boldsymbol{\mathcal{D}}}_{N-1}\}$ and $\bar{\boldsymbol{\mathcal{D}}}_i = \boldsymbol{\mathcal{D}}_i + {\sigma_\nu}^2\mathbf{I}_M$. Recalling circulant property of $\boldsymbol{\mathcal{D}}_i$ from (5.9), it can be understood that $\bar{\boldsymbol{\mathcal{D}}}_i$ is also circulant and can be expanded as $\bar{\boldsymbol{\mathcal{D}}}_i = \mathbf{F}_M^{\text{H}}(\boldsymbol{\Phi}_\kappa^*\boldsymbol{\Phi}_\kappa + {\sigma_\nu}^2\mathbf{I}_M)\mathbf{F}_M$ where $\boldsymbol{\Phi}_\kappa = MN\text{diag}\{\mathbf{F}_M\mathbf{g}_\kappa\}$[1]. Let $\breve{\mathbf{y}} = [\breve{\mathbf{y}}_0^{\text{T}}, \ldots, \breve{\mathbf{y}}_{N-1}^{\text{T}}]^{\text{T}} = \bar{\boldsymbol{\mathcal{D}}}^{-1}\boldsymbol{\mathcal{F}}_b\mathbf{A}^{\text{H}}\mathbf{y}$, we can write

$$\begin{aligned}\breve{\mathbf{y}}_i &= \mathbf{F}_M^{\text{H}}(\boldsymbol{\Phi}_\kappa^*\boldsymbol{\Phi}_\kappa + {\sigma_\nu}^2\mathbf{I}_M)^{-1}\boldsymbol{\Phi}_\kappa^*\mathbf{F}_M\mathbf{y}_\kappa \\ &= \mathbf{p}_\kappa \textcircled{M} \mathbf{y}_\kappa, \end{aligned} \tag{5.18}$$

where $\mathbf{p}_\kappa$ includes the first column of the circulant matrix $\mathbf{F}_M^{\text{H}}\{(\boldsymbol{\Phi}_\kappa^*\boldsymbol{\Phi}_\kappa + {\sigma_\nu}^2\mathbf{I}_M)^{-1}\boldsymbol{\Phi}_\kappa^*\}\mathbf{F}_M$. Since, in MMSE receiver, the matrix $\bar{\boldsymbol{\mathcal{D}}}^{-1}$ depends on ${\sigma_\nu}^2$ and the receiver cannot be

[1]Since, $\tilde{\mathbf{g}}_\kappa$ is a real vector and circularly folded version of $\mathbf{g}_\kappa$, $\boldsymbol{\Phi}_\kappa^* = MN\text{diag}\{\mathbf{F}_M\tilde{\mathbf{g}}_\kappa\}$.

simplified as in (5.11) or (5.15), circular convolution of (5.18) needs to be calculated in the frequency domain, known as fast convolution, in order to have the lowest complexity. After obtaining $\breve{\mathbf{y}}$, the MMSE estimates of the transmitted symbols can be found as

$$\hat{\mathbf{d}}_{\text{MMSE}} = \boldsymbol{\mathcal{F}}_b^{\text{H}} \breve{\mathbf{y}}. \tag{5.19}$$

5.1.2.5 Receiver implementation

In this subsection, we present a unified implementation of the MF, ZF and MMSE receivers that we proposed in Sections 5.1.2.2, 5.1.2.3 and 5.1.2.4. As Fig. 5.3 depicts, the proposed GFDM receivers can be implemented by cascading Fig. 5.3 (a) and (b). It is worth mentioning that the commutator on the right hand side of Fig. 5.3 (a) will turn by one position after collecting M samples from the i^{th} branch, i.e., $M \times 1$ vector $\bar{\mathbf{y}}_i/\tilde{\mathbf{y}}_i/\breve{\mathbf{y}}_i$, in the clockwise direction. In the MF and ZF receivers, the vectors $\boldsymbol{\gamma}_i$ are replaced by $\mathbf{v}_i$'s and $\mathbf{q}_i$'s, respectively, and in MMSE receiver, they will be replaced by $\mathbf{p}_i$'s. Due to the fact that in the MF and ZF receivers, the vectors $\mathbf{v}_i$ and $\mathbf{q}_i$ are fixed and only depend on the prototype filter coefficients, they can be calculated offline and hence there is no need for their real-time calculation. However, in MMSE receivers, the vectors $\mathbf{p}_i$ depend on the signal to noise ratio and hence they should be calculated in real-time. As mentioned earlier in Section 5.1.2.4, circular convolutions in our MMSE receiver need to be performed by taking advantage of fast convolution to keep the complexity low.

5.1.3 Computational Complexity

In this section, the computational complexity of our proposed GFDM transmitter and receiver structures are discussed and compared to the existing ones that are known to have the lowest complexity, [104, 106]. In both cases, total number of N subcarriers and overlapping factor of M are considered.

5.1.3.1 Transmitter complexity

Table 5.1 presents the computational complexity of different GFDM transmitter implementations based on the number of complex multiplications (CMs).

As discussed in Section 5.1.1.2, our proposed GFDM transmitter involves two steps. The first step includes M number of N-point FFT operations that requires $\frac{MN}{2}\log_2 N$ CMs. The second step needs N number of M-point circular convolutions. Recalling equation (5.5), since $\mathbf{g}_\kappa$'s are real-valued vectors, one may realize that

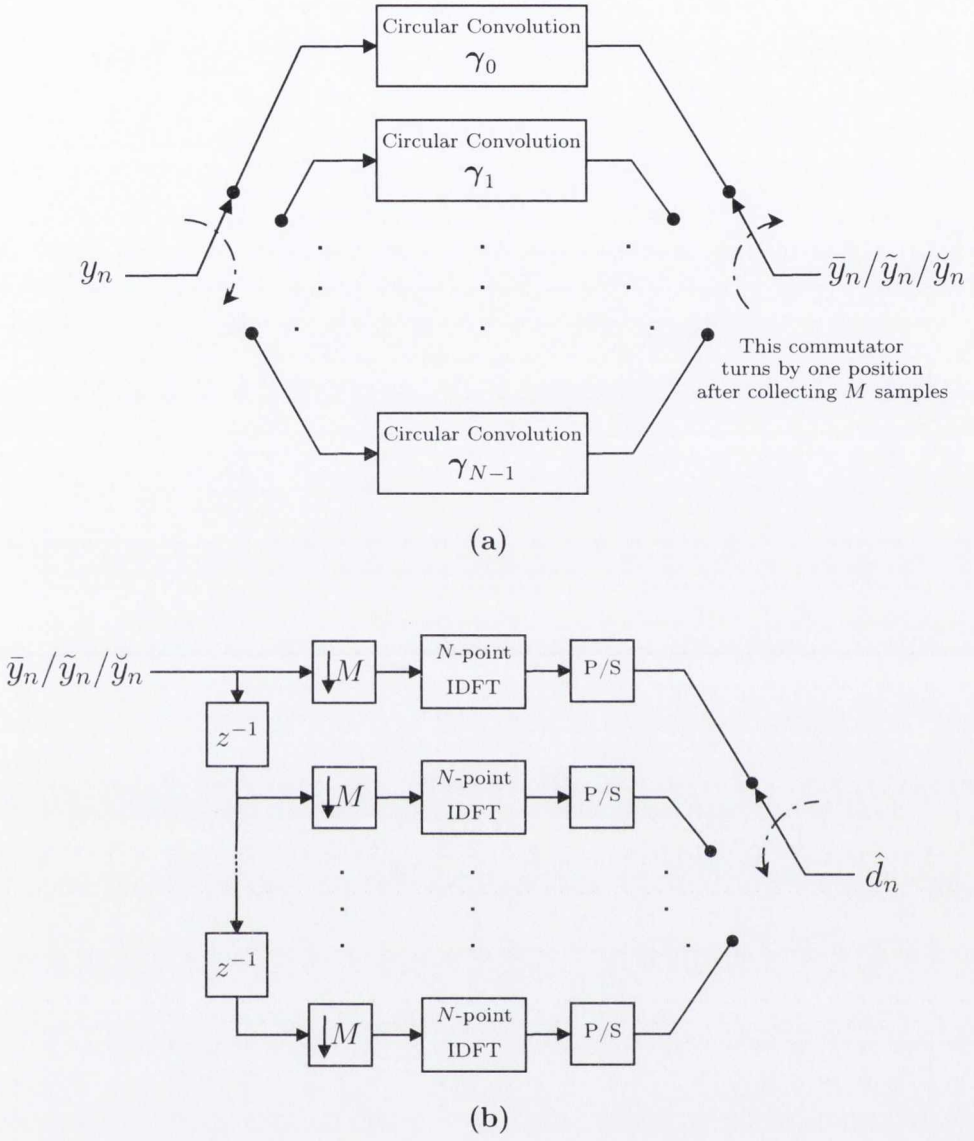

Fig. 5.3 Unified implementation of our proposed MF, ZF and MMSE-based GFDM receivers from cascading the block diagrams **(a)** and **(b)**.

each M-point circular convolution demands $\frac{M^2}{2}$ number of CMs. If M is a power of two, the complexity can be further reduced by performing the circular convolutions in frequency domain. This is due to the fact that circular convolution in time is multiplication in the frequency domain. Thus, to perform each circular convolution, a pair of M-point FFT and IFFT blocks together with M complex multiplications to the filter coefficients in frequency domain are required.

The complexity relationships that are presented in Table 5.1 are calculated and plotted in Fig. 5.4 for $N = 1024$ subcarriers with respect to different values of over-

Table 5.1 Computational Complexity of Different GFDM Transmitter Implementations

Technique	Number of Complex Multiplications
Direct matrix multiplication	$(MN)^2$
Proposed transmitter in [106]	$MN(\log_2 N + 2\log_2 M + L)$
Our proposed transmitter	$\frac{MN}{2}(M + \log_2 N)$

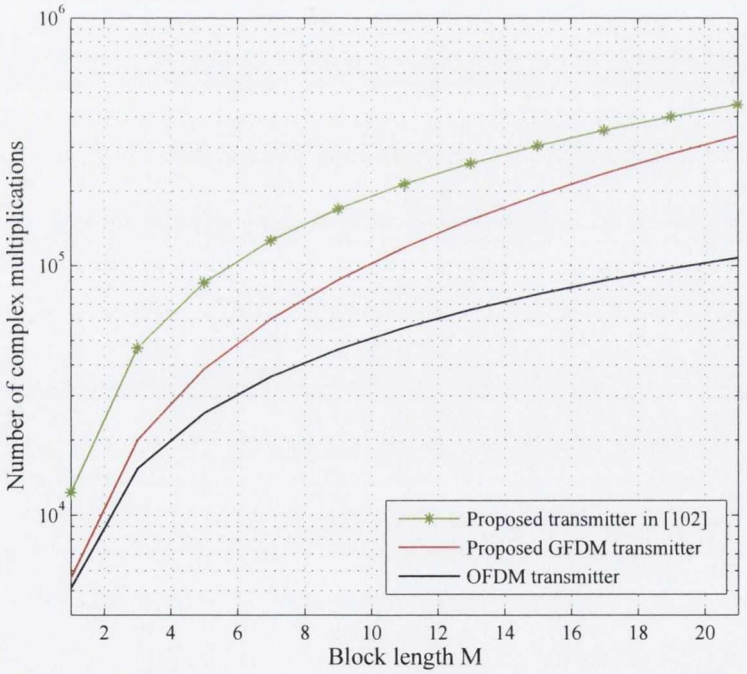

Fig. 5.4 Computational complexity comparison of different GFDM transmitter techniques and the OFDM transmitter technique for $N = 1024$.

lapping factor M. The parameter L indicates the number of overlapping subcarriers with a given subcarrier in the frequency domain. As the authors of [106] suggest, $L = 2$ is chosen[2] for calculating their GFDM transmitter complexity. Due to the fact that direct multiplication of $\mathbf{A}$ to the data vector $\mathbf{d}$ demands a large number of CMs and is impractical, we do not present it in Fig. 5.4. To give a quantitative indication of the complexity reduction that our proposed transmitter provides compared with the direct computation of the equation (2.34), in the same system setting as used for our other comparisons, i.e., $N = 1024$ and $M \in [1, 21]$, complexity reduction of around three orders of magnitude can be achieved. According to Fig. 5.4, for the small values of M our proposed transmitter structure has a complexity very close to that of OFDM. However, as M increases the complexity of our transmitter increases with a higher pace than OFDM. This is due to the overhead of $\frac{NM^2}{2}$ number of CMs compared with OFDM. Compared with the transmitter structure that is proposed in this chapter, for small values of M up to 11, the transmitter proposed in [106] demands about two times higher number of CMs. As M increases, complexity of our technique gets close to that of the one proposed in [106]. GFDM transmitter of [106] is about 3 to 4 times more complex than OFDM.

5.1.3.2 Receiver complexity

Table 5.2 summarizes the computational complexity of different GFDM receivers in terms of the number of complex multiplications. The parameter I is the number of iterations in the algorithm with interference cancellation.

From Fig. 5.3, it can be understood that our proposed receivers involve N and M numbers of M-point circular convolutions and N-point IDFT operations, respectively. IDFT operations can be efficiently implemented using N-point IFFT algorithm which requires $\frac{N}{2}\log_2 N$ CMs. As mentioned earlier, in the proposed MF and ZF receivers, the vectors $\boldsymbol{\gamma}_i$ have fixed values and hence can be calculated and stored offline. Furthermore, $\boldsymbol{\gamma}_i$'s are real-valued vectors. Thus, the number of complex multiplications needed for N number of M-point circular convolutions is $\frac{NM^2}{2}$.

In contrast to the MF and ZF receivers, in the MMSE receiver, the vectors $\boldsymbol{\gamma}_i$'s are not fixed and depend on the signal-to-noise ratio (SNR). Hence, they need to be calculated in real-time. To this end, as highlighted in Section 5.1.2.4, those operations can be performed by using M-point DFT and IDFT operations. Due to the fact that $(\boldsymbol{\Phi}_\kappa^* \boldsymbol{\Phi}_\kappa + {\sigma_\nu}^2 \mathbf{I}_M)$ is a real-valued diagonal matrix, its inversion and multiplication

[2]This is due to the fact that only two adjacent subcarriers overlap in the frequency domain with a given one.

Table 5.2 Computational Complexity of Different GFDM Receiver Techniques

Technique	Number of Complex Multiplications
Direct ZF	$2(MN)^2$
Direct MMSE	$\frac{1}{3}(MN)^3 + 2(MN)^2$
Matched filter + SIC, [104]	$MN(\log_2 MN + \log_2 M + L + I(2\log_2 M + 1))$
Proposed MF/ZF	$\frac{MN}{2}(M + \log_2 N)$
Proposed MMSE	$\frac{MN}{2}(4M + \log_2 N + 3)$

to $\mathbf{\Phi}_\kappa^*$ only needs $\frac{M}{2}$ CMs. The resulting diagonal matrix $(\mathbf{\Phi}_\kappa^*\mathbf{\Phi}_\kappa + {\sigma_\nu}^2\mathbf{I}_M)^{-1}\mathbf{\Phi}_\kappa^*$ is multiplied into an $M \times 1$ vector which needs M CMs. Since, M is not necessarily a power of 2, complexity of M-point DFT and IDFT operations in the implementation of the circular convolutions is considered as M^2. Obviously, if M is a power of 2, a further complexity reduction by taking advantage of FFT and IFFT algorithms is possible. Therefore, the complexity of our proposed MMSE receiver only differs from the MF and ZF ones in the implementation of the circular convolution operations.

Table 5.2 also presents the complexity of the direct MF, ZF and MMSE detection techniques, i.e., direct matrix multiplications and solutions to the equations (2.40) and (2.41), respectively. Those solutions involve direct inversion of an $MN \times MN$ matrix which has the complexity of $\mathcal{O}(M^3N^3)$ and two vector by matrix multiplications with the computational burden of $2(MN)^2$ CMs.

The complexity formulas that are presented in Table 5.2 are evaluated and plotted in Fig. 5.5 for different values of overlapping factor $M \in [1, 21]$, $N = 1024$ and $I = 8$ for the receiver that is proposed in [104]. Based on the results of [104], $I = 8$ and $L = 2$ are considered. Due to the fact that the complexity of MF, ZF and MMSE receivers with direct matrix inversion and multiplications is prohibitively high compared with other techniques (the difference is in the level of orders of magnitude), they are not presented in Fig. 5.5. However, to quantify the amount of complexity reduction that our proposed techniques provide, in the case of $N = 1024$ and $M = 7$, our proposed MF/ZF receiver is three orders of magnitude and the proposed MMSE receiver is six orders of magnitudes simpler than the direct ones, respectively, in terms of the required number of CMs. As Fig. 5.5 depicts, our proposed ZF receiver is around an order of magnitude simpler than the proposed receiver with SIC in [104]. In addition, our proposed MMSE receiver has 2 to 3 times lower complexity than the one with SIC in [104]. Apart from lower computational cost compared with the existing receiver structures, our techniques maintain the optimal ZF and MMSE performance as they

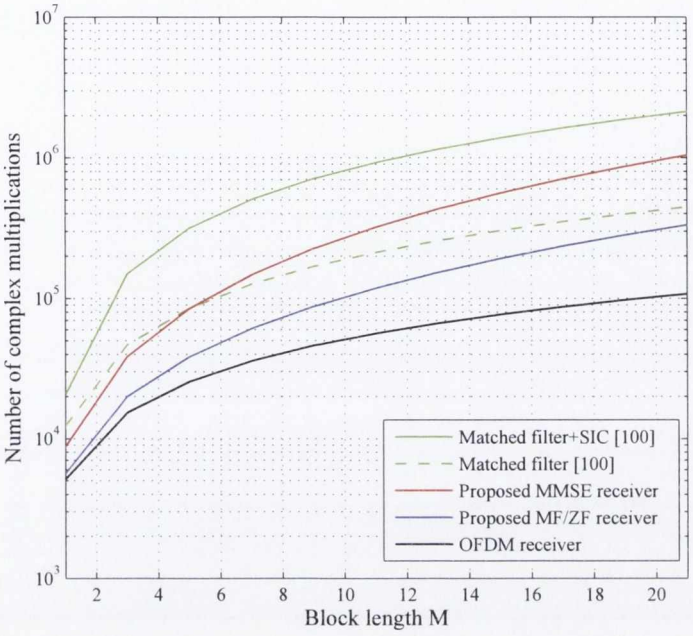

Fig. 5.5 Computational complexity comparison of different GFDM receiver techniques with respect to each other and that of OFDM receiver when $N = 1024$ and $I = 8$ for [104].

are direct. Finally, the ZF and MMSE receivers that we are proposing are closer in complexity to OFDM as compared to the receiver with SIC in [104] which is over an order of magnitude more complex than OFDM.

5.2 Circular filter bank multicarrier

GFDM is a non-orthogonal waveform that is circularly pulse-shaped. Through filtering each subcarrier band with a well-designed prototype filter, GFDM gains resiliency against CFO as only its adjacent subcarriers overlap in frequency domain and hence the leakage among subcarriers is reduced (Fig. 5.6). The price to pay for gaining all the aforementioned advantages is some bit error rate (BER) performance loss compared with OFDM when linear detectors like ZF or MMSE are used, [102]. This performance loss is due to the fact that GFDM is a non-orthogonal waveform and thus suffers from intercarrier interference (ICI). Additionally, GFDM has a limitation in the number of symbols, M, that are present in each packet which needs to have an odd value, [105]. When M is even, the modulation matrix is singular and hence the ZF receiver does not exist. Moreover, the MMSE receiver has a poor performance in

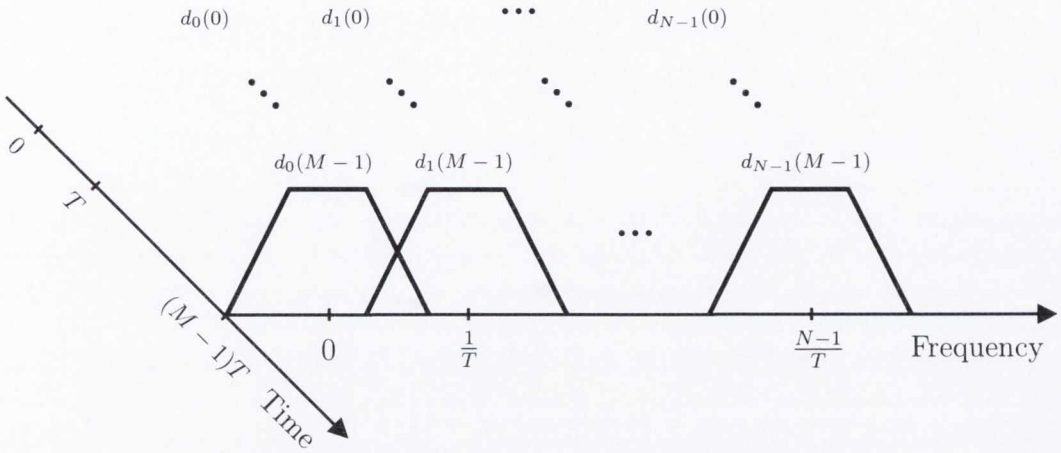

Fig. 5.6 Frequency Overlap.

such cases. In order to avoid this performance degradation and remove the limitation of GFDM on M, interference cancellation techniques have to be utilized which demand a large amount of computational burden compared with the linear detectors, [101].

To tackle the performance degradation of GFDM, some researchers have recently proposed a multicarrier technique that is inspired by GFDM, but is able to preserve the orthogonality among the subcarriers, [14]. In these systems that we call *circular filter bank multicarrier* (C-FBMC), similar to filter bank multicarrier systems with linear pulse shaping, [15], a carrier phase of $\pi/2$ is applied to the adjacent subcarriers containing real data symbols to satisfy the orthogonality in real domain. Hence, simple detectors with a very low complexity such as MF detector lead to the same BER performance as that of OFDM. C-FBMC may be thought of as a modified version of GFDM.

In C-FBMC, the transmission is established through offset QAM (OQAM) modulation, e.g., see [87] and [15]. In OQAM, the real and imaginary parts of each QAM symbol are separated and transmitted with a time offset of $T/2$, as two pulse amplitude modulated (PAM) symbols. In addition, a $\pi/2$ phase shift is added between the adjacent PAM symbols. This setup assures the orthogonality of the modulated PAM symbols, with the orthogonality defined as real orthogonality, e.g., see [87]. The real orthogonality implies that, in the absence of noise, perfect recovery of data symbols is possible after taking the real part of the matched filters outputs.

In C-FBMC, after separating the real and imaginary parts of the data symbols $d_n(m) = d_n^{\Re}(m) + jd_n^{\Im}(m)$ to the respective PAM symbols, we obtain the real-valued

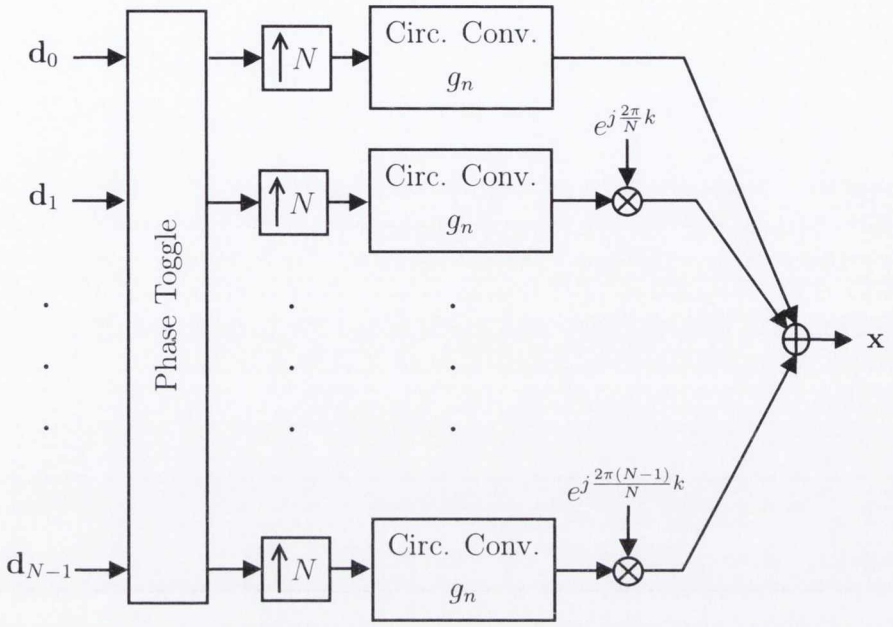

Fig. 5.7 C-FBMC transmitter block diagram.

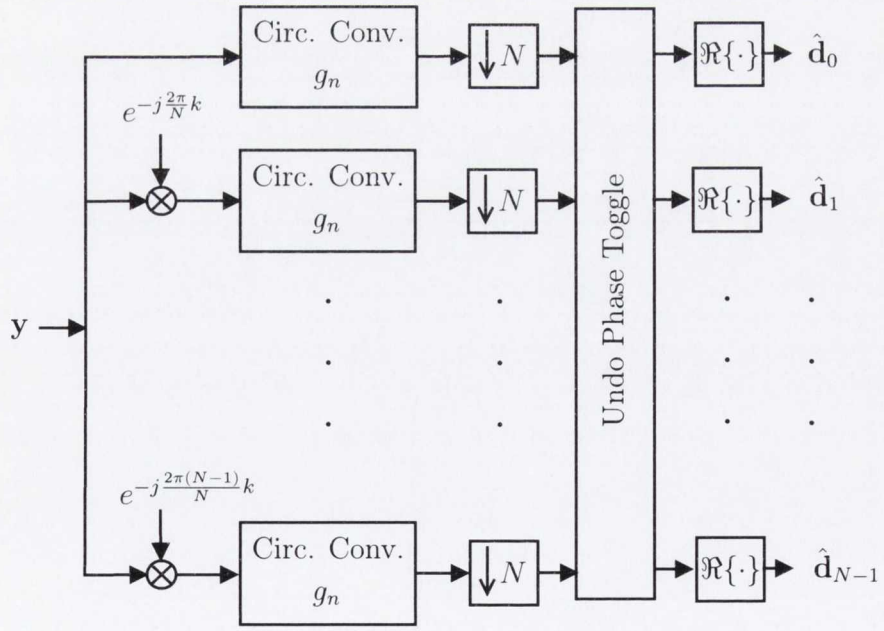

Fig. 5.8 C-FBMC receiver block diagram.

symbol matrix

$$\mathbf{D} = \begin{bmatrix} d_0^{\Re}(0) & d_0^{\Im}(0) & \cdots & d_0^{\Re}(M-1) & d_0^{\Im}(M-1) \\ d_1^{\Re}(0) & d_1^{\Im}(0) & \cdots & d_1^{\Re}(M-1) & d_1^{\Im}(M-1) \\ \vdots & \vdots & \ddots & \vdots & \vdots \\ d_{N-1}^{\Re}(0) & d_{N-1}^{\Im}(0) & \cdots & d_{N-1}^{\Re}(M-1) & d_{N-1}^{\Im}(M-1) \end{bmatrix}. \tag{5.20}$$

The transmitter and receiver structure of C-FBMC are presented in Figs. 5.7 and 5.8, respectively. The input vectors $\mathbf{d}_0$ through $\mathbf{d}_{N-1}$ in Fig. 5.7 are the rows of the matrix $\mathbf{D}$ in (5.20). The phase toggle block at the transmitter adds the required phase changes of $\pi/2$ to the adjacent symbols. The added phase shifts are removed at the receiver output.

5.2.1 Performance comparison of GFDM and C-FBMC

In this section, we evaluate the BER performance of different receivers for GFDM and C-FBMC through numerical simulations. It is worth noting that the BER performance of OFDM is chosen as a reference. Simulated receivers include GFDM matched filter receiver, GFDM matched filter receiver with 1 iteration of successive interference cancellation (GFDM-SIC-1), GFDM matched filter receiver with 3 iteration of successive interference cancellation (GFDM-SIC-3), and C-FBMC matched filter receiver (C-FBMC-MF). Each point of the following BER performance plots is based on simulation of sufficient data which results in at least 1000 error bits.

For C-FBMC modulation, adjacent subbands are real orthogonal. Thus, it is desirable to choose a prototype filter that fully extends up to the center of the adjacent subbands. This choice minimizes stop band response of the prototype filter which is the key factor in decreasing interference from far subbands. We have chosen the prototype filter based on the method presented in [89]. A point to make, here, is that choosing a prototype filter for GFDM with the same frequency span as C-FBMC, causes a very high level of ICI among adjacent subbands. Fig. 5.9 presents BER performance of all receivers for prototype filter of [89] and 16-QAM modulation. Here, one notices that while C-FBMC-MF has the same BER performance as that of OFDM, all GFDM receivers have very high error levels. Based on GFDM-SIC-3 curve where 3 iterations are involved in the SIC procedure, the BER curve of GFDM cannot get even close to that of OFDM. As shown in Figs. 5.11 to 5.14, increasing the constellation

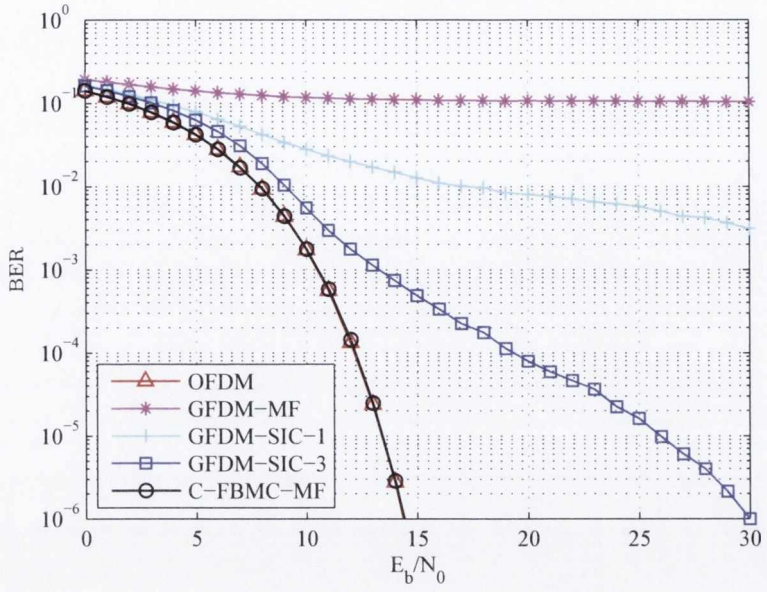

Fig. 5.9 BER performance for [89] prototype filter where $N = 64$, $M = 5$, and 16-QAM.

size makes SIC inefficient and a residual ICI remains. As a result, the BER will be higher. Therefore, the prototype filter for GFDM modulation should be chosen such that each subband has a small overlap with the adjacent subbands. The consequence of this selection is sacrificing good stop band response of the prototype filter. An example is presented in Fig. 5.10.

Fig. 5.11 through Fig. 5.14 present BER performance of all receivers for different constellation sizes. In these simulations, $N = 64$ subcarriers and an overlapping factor of $M = 5$ are considered. A root raised cosine (RRC) prototype filter with the roll-off factor $\alpha = 0.3$ is utilized for GFDM and the prototype filter of [89] is employed for C-FBMC. According to our results here, we conclude that C-FBMC-MF receiver has the same performance as that of OFDM receiver, while GFDM-SIC receivers can approach C-FBMC-MF performance by incorporating a higher number of SIC iterations, i.e., by increasing the complexity of the receiver.

The above conclusion is the case only for odd numbers of overlapping factor M. For M even, BER is higher than OFDM and SIC algorithm is not as effective as for odd value of M. Fig. 5.15 presents the receivers performance for $M = 6$. As seen, here, GFDM-SIC receiver is not able to reach an acceptable BER performance, while C-FBMC-MF keeps the same performance as OFDM. This observation is in line with [102] and [104], where it has been noted that for even values of M, the modulation matrix $\mathbf{A}$ of GFDM is ill-conditioned.

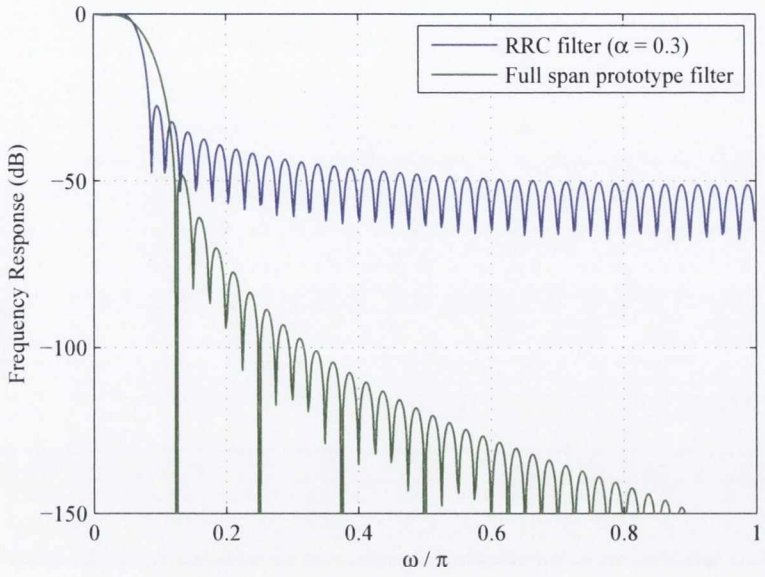

Fig. 5.10 Frequency response comparison of prototype filters.

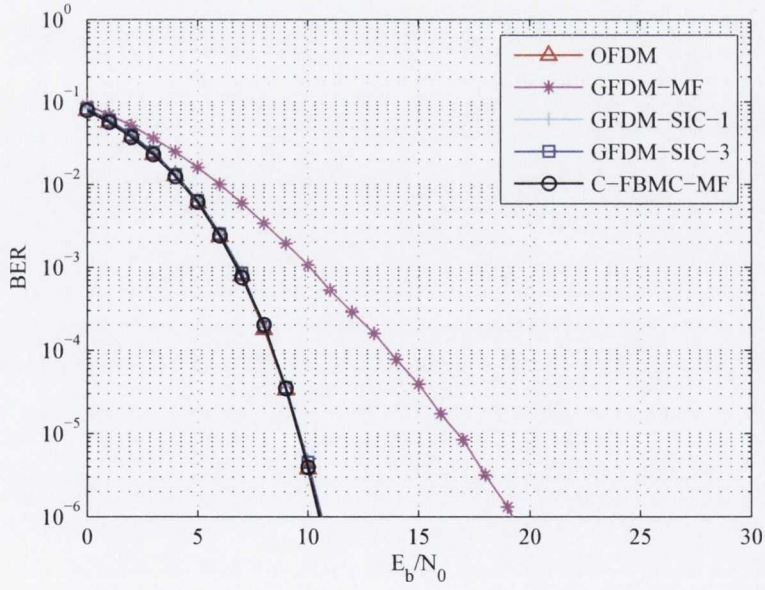

Fig. 5.11 BER performance for $N = 64$, $M = 5$, and 4-QAM Modulation.

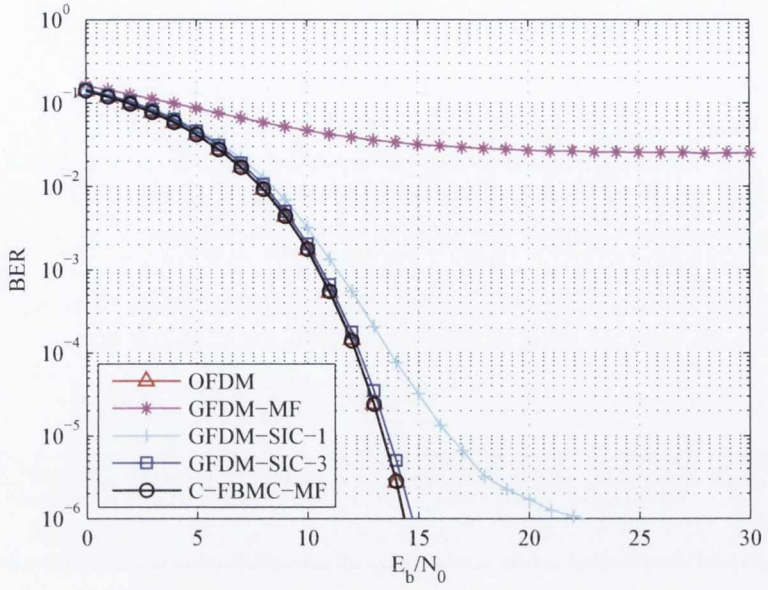

Fig. 5.12 BER performance for $N = 64$, $M = 5$, and 16-QAM Modulation.

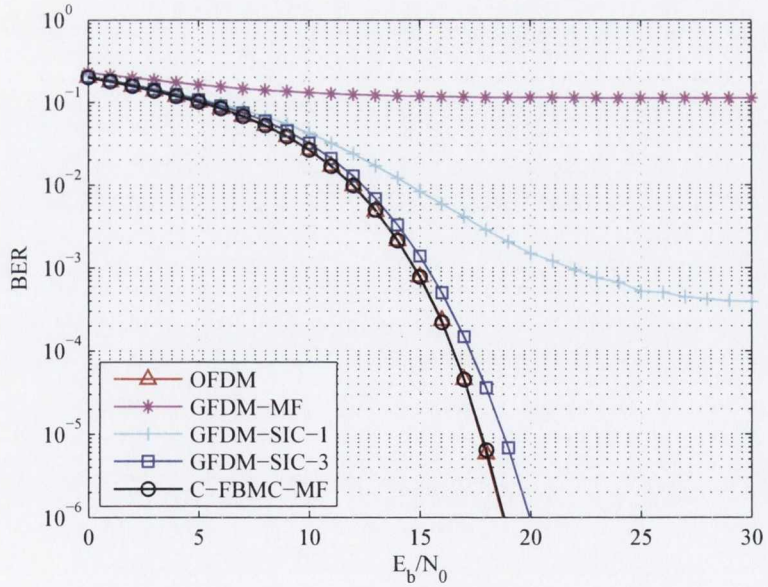

Fig. 5.13 BER performance for $N = 64$, $M = 5$, and 64-QAM Modulation.

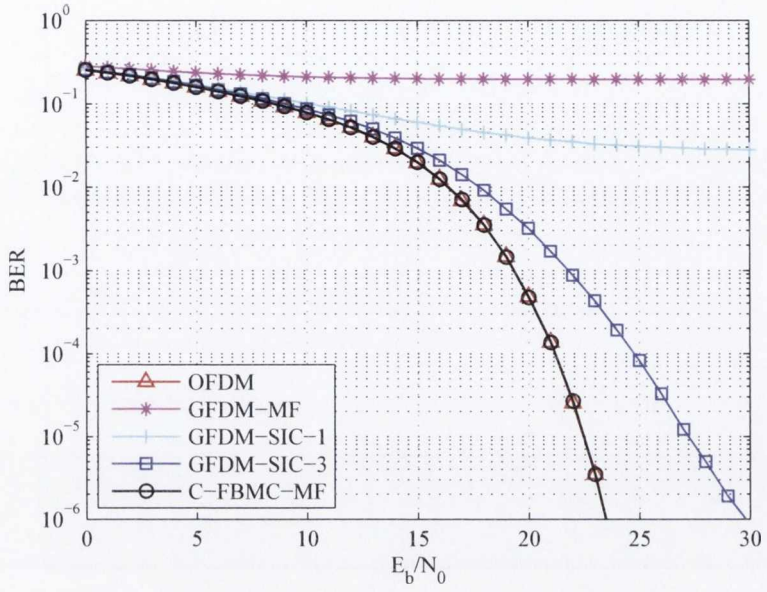

Fig. 5.14 BER performance for $N = 64$, $M = 5$, and 256-QAM Modulation.

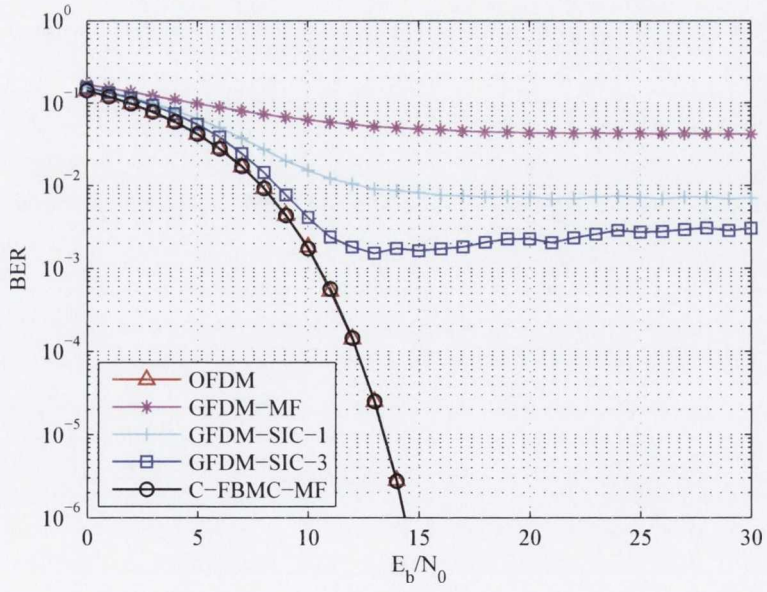

Fig. 5.15 BER performance for $N = 64$, $M = 6$, and 16-QAM Modulation.

5.3 Impact of timing and frequency offsets on waveform candidates for 5G

This section is dedicated to sensitivity analysis of different candidate waveforms in multiuser scenarios such as uplink communications. Apart from GFDM and C-FBMC that are discussed in the previous sections, universal filtered multicarrier (UFMC), [18], is another candidate waveform proposed for 5G. UFMC modifies OFDM by applying a filter on each group of subcarriers, i.e., a physical resource block, in the context of 3GPP long term evolution (LTE) systems. This improves the robustness to synchronization errors by limiting the out of band emissions of the subcarriers.

The impact of multiuser synchronization errors including symbol timing offset (TO) and CFO on the performance of OFDM and FBMC systems has been studied extensively in the past, [1, 118–122]. Moreover, a performance comparison between UFMC and OFDM with respect to TO and CFO has been recently presented in [18, 123]. However, there exists no study in the literature investigating the TO and CFO effects on all the major 5G candidate waveforms. In this section, we scrutinize the performance of all the proposed candidate waveforms for 5G in presence of timing and frequency offsets in an attempt to answer the question ***"Which one of the 5G candidate waveforms has more relaxed synchronization requirements?"***. Accordingly, the aim in this section is to (i) provide a clear-cut explanation on the behavior of the aforementioned 5G contender waveforms with respect to multiuser timing and frequency misalignments; (ii) compare their robustness with each other; and (iii) highlight the fact that the linear FBMC has the least sensitivity to TO and CFO.

5.3.1 Uplink System Model

Any multicarrier scheme can be thought of as a mapping between the message space and the signal space using a basis that spans in both the time and frequency domain [124]. Moreover, one can successfully recover the message at the receiver, if the mapping is one-to-one. Here the scenario that we are considering is the uplink transmission direction of a multicarrier frequency division multiple access (FDMA) system, where the bandwidth is partitioned into the total of N subcarriers and each user accesses a cluster of subcarriers. Thus, for the ℓ^{th} user, the transmit symbol

$X_{mk}^{(\ell)}$ corresponds to the data symbol $D_{mk}^{(\ell)}$ according to

$$X_{mk}^{(\ell)} = \begin{cases} D_{mk}^{(\ell)}, & k \in \mathcal{N}_\ell \\ 0, & k \notin \mathcal{N}_\ell \end{cases} \tag{5.21}$$

where k is the subcarrier index, m is the symbol time index, and $\mathcal{N}_\ell$ denotes the set of subcarrier indices that are devoted to the ℓ^{th} user. Consequently, we can represent the transmit signal of the ℓ^{th} user by

$$x_\ell(t) = \sum_{m=-\infty}^{+\infty} \sum_{k=0}^{N-1} X_{mk}^{(\ell)} g_{mk}(t) \tag{5.22}$$

where $g_{mk}(t)$ is the transmitter basis function corresponding to the (m, k) time-frequency point.

After propagating through the channel, and assuming a TO error of τ_ℓ and a CFO error of ε_ℓ between the ℓ^{th} transmitter and the base station (BS), the received signal at the BS can be expressed as

$$y(t) = \sum_{\ell} y_\ell(t - \tau_\ell) e^{j2\pi\varepsilon_\ell t/T} + n(t) \tag{5.23}$$

where

$$y_\ell(t) = \int_\tau c_\ell(\tau, t) x_\ell(t - \tau) d\tau, \tag{5.24}$$

is the signal of the ℓ^{th} user distorted by the multipath time-varying channel impulse response $c_\ell(\tau, t)$, $n(t)$ is the AWGN, and T denotes the symbol period.

In order to focus on the effects of timing and frequency misalignments of FDMA users, we ignore the fading effect of the channel and assume ideal channel response. Moreover, given the ℓ^{th} user is the user of interest, we assume $\tau_\ell = 0$, and $\varepsilon_\ell = 0$, meaning the BS is synchronized with the signal coming from the user of interest. However, signals of other users are not perfectly aligned with respect to the receiver. Based on this plot, the transmitted data symbols of the user of interest can be recovered according to

$$\hat{X}_{mk}^{(\ell)} = \langle y(t), h_{mk}(t) \rangle \tag{5.25}$$

$$= X_{mk}^{(\ell)} + I_{\text{MAI}} + \eta \tag{5.26}$$

where $h_{mk}(t)$ represents the receiver basis corresponding to the (m, k) time-frequency point. If the underlying modulation scheme is orthogonal, e.g. OFDM, FBMC, etc., $h_{mk}(t) = g_{mk}(t)$. However, for a non-orthogonal waveform, e.g. GFDM, the receiver basis is not the same as the transmitter basis in general. Time and frequency misaligned symbols of other users will cause a multiple access interference (MAI) which we have denoted by I_{MAI}. The noise contribution is also denoted by η.

5.3.2 TO Sensitivity Analysis

This section focuses on the timing offset sensitivity analysis of different candidate waveforms for the physical layer of 5G systems. To pave the way for a better understanding of our analysis in Section 5.3.2.2, some general concepts on timing offset effects are first discussed in Section 5.3.2.1.

5.3.2.1 Spectral Leakage Due to Timing Offset

In any multicarrier waveform, as far as a particular symbol time index is concerned, an observation window with a finite duration is applied to the received signal and the processing is performed on that finite interval. This fact can be realized from (5.25) and it can be noticed that the receive pulse shape (windowing function), $h_{mk}(t)$, has a finite duration in practice. This finite windowing leads to some peculiarities when a symbol timing misalignment exists between the frequency separated users. The objective of this section is to explain this phenomenon, hence, facilitate understanding of the behavior of different waveforms and, accordingly, develop the respective sensitivity in Section 5.3.2.

We use T to denote the symbol period, and T_W for the duration of the window for data detection at the receiver. We also note that it is common to choose $T_W = KT$, where K is an integer. In filter bank literature, K is called the overlapping factor. For OFDM $K = 1$, for UFMC $K = 2$ (including the padded zero for analysis), and for filter bank based waveforms K is a design factor that indicates the number of overlapping symbols in the time domain. Since the processing is limited to the signals with the duration of T_W, Fourier series analysis can be employed in order to explain the behavior of different waveforms with respect to the timing misalignment. Based on the Fourier series analysis, an intuitive approach to understand (5.25) is to think of the windowed signal as a *single period* of a periodic signal. In (5.25), if perfect reconstruction is assumed when the users are fully synchronous, $X_{mk}^{(\ell)}$ can be retrieved free of MAI. However, in presence of timing offset, the periodic extension of

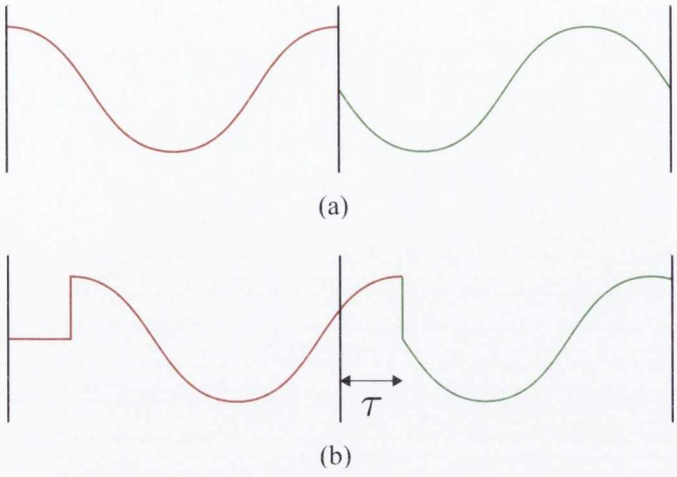

Fig. 5.16 Illustration of signal discontinuities due to TO.

the signals from other users exhibits discontinuities which cause non-zero projections on the frequencies belonging to the user of interest.

To illustrate the above point, consider Fig. 5.16a. This represents two sinusoids that are perfectly time aligned with their corresponding observation window. In this case, the periodic extension of each observation window is also a pure sinusoid and, thus, it exhibits a non-zero projection onto the respective basis function/frequency and results in a zero projection onto the other basis functions/frequencies. Fig. 5.16b, on the other hand, illustrates the case of having a TO error, τ, between the observation window and the received signal. In this case, the periodic extension of each observation window exhibits discontinuities at three different points; two at the boundaries and one at the intersection of two symbols. These discontinuities cause non-zero projections on the entire Fourier series expansion, and thus, *spectral leakage* due to symbol timing misalignment occurs. This spectral leakage is the source of interference between the FDMA users in the uplink of a cellular system that are asynchronous in time.

To decrease the level of discontinuities and hence reduce the impact of spectral leakage, windows with smooth tails should be utilized at both the transmitter and the receiver. When such a window is used at the transmitter, at the receiver, the discontinuities at the symbol intersection points disappear. On the other hand, applying a window at the receiver will remove the discontinuities at the window boundaries.

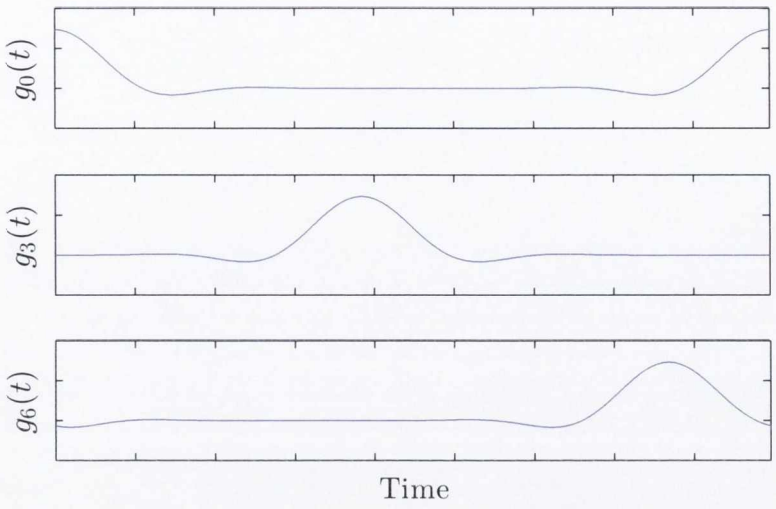

Fig. 5.17 Circular filters in GFDM.

5.3.2.2 Sensitivity of Different Waveforms to Timing Offset

As discussed above, the amount of multiuser spectral leakage due to TO for any multicarrier waveform is closely related to the discontinuities in the observation window at the receiver. Moreover, filtering at both transmitter and receiver sides helps to mitigate the performance loss caused by timing offset. Based on this discussion, it is clear that since UFMC adds a filtering operation to OFDM at the transmitter, it has a better ability to resolve the multi-user TO interference than OFDM. Moreover, FBMC can perform even better, thanks to its smooth filters both at the transmitter and receiver.

In waveforms with linear pulse shaping, such as FBMC and UFMC, the same pulse shape is used for symbols at different time indices, and thus there is a symmetry in the TO performance of different symbols of a packet. Interestingly, this is not the case for circularly pulse shaped waveforms. To better understand this phenomenon, consider Fig. 5.17, where we have depicted typical pulse shapes of the 1^{st}, 4^{th} and 7^{th} symbol indices of a GFDM packet consisting a total of seven symbol periods. Here, although $g_3(t)$, and in general, the central symbols can effectively bring the boundary discontinuities close to zero, the symbols located at the edges of the packet, specially $g_0(t)$, cannot achieve the boundary continuity in presence of timing offset. This results in higher performance degradation in the symbols located at the edges of the data packet as compared to the central ones.

Besides the boundary discontinuities, another discontinuity also occurs inside the receive window, as discussed earlier. Since other pulses than $g_0(t)$ have zero-merging

tails, the magnitude of this discontinuity is closely related to $g_0(t)$, which has large magnitudes at the edges of the packet. Accordingly, the cause of this discontinuity is mainly due to the symbol corresponding to $g_0(t)$ being shifted as a result of the timing misalignment. In this case, at the receiver, the symbol that its main lobe coincides with the position of the discontinuity undergoes a maximum the spectral leakage. Other symbol indices bring that discontinuity close to zero and thus may not experience spectral leakage to that extent. This suggests that to reduce the amount of MAI induced by TO in GFDM and C-FBMC, one remedy could be to turn off the first symbol of the packet. Obviously, this leads to some loss in spectral efficiency. This method has been applied in [125] in the context of reducing out-of-band (OOB) emission. Here, we emphasize that this also has the impact of reducing MAI at the receiver.

Next, we present some numerical results that confirm that above observations and provide more insight to the sensitivity of different waveform to TO. We consider an uplink scenario with two users. The total number of subcarriers for all waveforms is 256. From these a total of 72 subcarriers are used; 36 contiguous subcarriers are allocated to each user. There is null subcarrier between the two users' subcarriers. Perfect power control is assumed for the users. For OFDM, C-FBMC, and GFDM, a CP length of 32 samples is used. Seven symbols are transmitted in each GFDM or C-FBMC packet. In UFMC, a Dolph-Chebyshev filter with the length 33 and stop band attenuation of 40 dB is used. In the both cases of FBMC and C-FBMC the Mirabbasi-Martin filter [89] is used. For GFDM, we have used a root raised-cosine filter with the roll-off factor of $\alpha = 0.4$. We only consider an AWGN channel, hence, channel does not introduce any time spreading and as a result the whole range of CP introduces a time period where OFDM, GFDM, and C-FBMC remain insensitive to TO. As the following numerical results show, this statement is not quite an exact one for GFDM. This is a result of the fact that GFDM is a non-orthogonal waveform and as a result the ZF detector (that we use here) has some peculiar behaviors whose details are beyond the scope of this chapter and remains as a future study.

One of the two users is considered as the user of interest, and it is assumed that the BS is time-aligned with the signal coming from this user. A TO is applied to the second user and the impact of this TO on the MAI seen by the first user is studied. In Fig. 5.18, we have compared the MAI power, $P_{\text{MAI}} = E\{|I_{\text{MAI}}|^2\}$, for different values of TO in OFDM, UFMC, FBMC, C-FBMC, and GFDM waveforms.

Considering the results in Fig. 5.18, the following observations are made. (i) OFDM is the most sensitive waveform to TO. (ii) FBMC has almost no sensitivity to

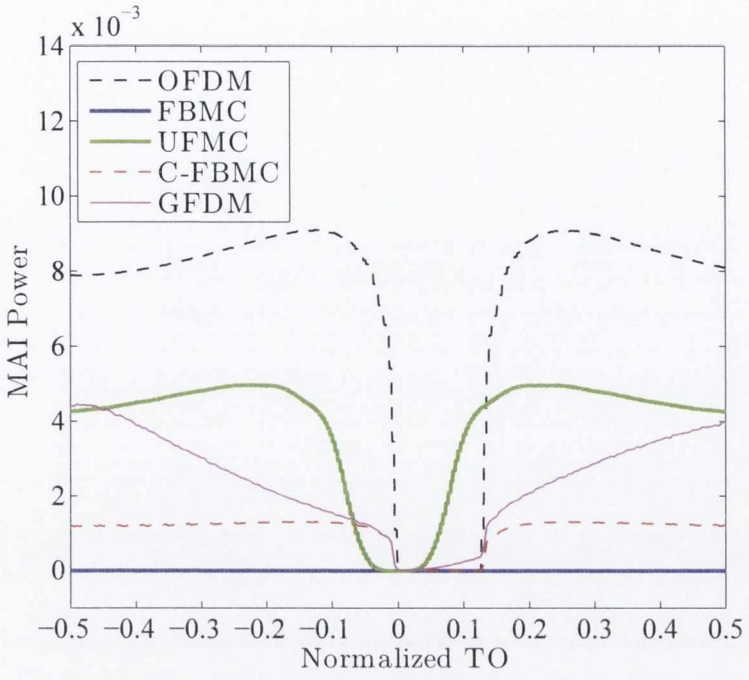

Fig. 5.18 MAI power as a function of TO for different waveforms.

TO, as noted before, thanks to combined filtering at both the transmitter and receiver sides. (iii) The CP interval introduces a time zone that can absorb TO errors. As noted above, when TO is within this range, OFDM, GFDM, and C-FBMC remain insensitive to TO. Presence of time spreading in the channel, clearly, reduces this range, (iv) UFMC also exhibits a TO insensitive range. This corresponds to small tails of the transmitter filter in UFMC.

5.3.3 CFO Sensitivity Analysis

OFDM systems, in uplink, are known to be highly sensitive to CFOs between different users. Therefore, new waveforms proposed for 5G systems have to provide a much lower sensitivity to CFOs compared with OFDM systems. Imperfect frequency domain synchronization among different uplink users leads to MAI caused by ICI. To reduce the CFO induced MAI and hence provide a more relaxed synchronization requirements than OFDM, the candidate waveforms for 5G strive to localize their subcarriers in frequency. This directly impacts the leakage from asynchronous subcarriers to the others.

In this study, we consider block subcarrier allocation scheme where a block of contiguous subcarriers is allocated to each user and one guard subcarrier is considered

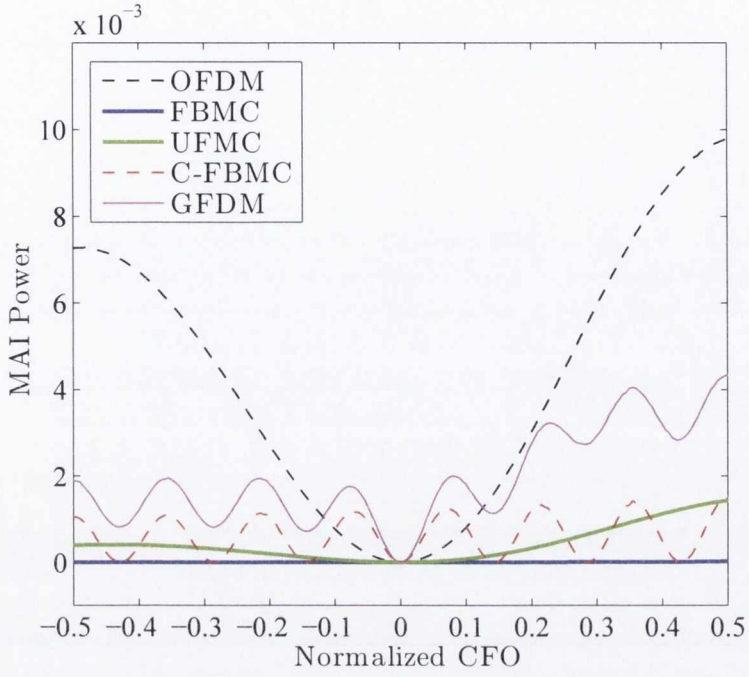

Fig. 5.19 MAI power as a function of CFO for different waveforms.

between different users. Due to the linear pulse shaping, each user's block in FBMC and UFMC is highly localized in the frequency domain, given that a well designed prototype filter is deployed. Thus, the amount of leakage among different users due to the CFOs is negligible. Based on the results of [126], due to the circular pulse shaping, GFDM and C-FBMC signals can be thought as superposition of a number of tones that are scaled by the data symbols as well as frequency response of the prototype filter. More specifically, each data bearing subcarrier in such systems include $2K-1$ frequency samples scaled with prototype filter coefficients in the frequency domain where K is the number of symbols in each data packet. Due to the presence of the rectangular window in such systems, each frequency sample, i.e., a tone, can be represented by a sinc function in frequency domain. It is worth mentioning that all the zero crossings of the sinc functions due to different subcarriers in a fully synchronous system are coinciding. If the subcarrier spacing is Δf, the spacing between different tones in such systems is $\frac{\Delta f}{K}$. Consequently, a normalized CFO of ε circularly rotates the sinc functions by the relative CFO of $M\varepsilon$ in the frequency domain.

Fig. 5.19 compares sensitivity of different waveforms to CFO in the uplink of a multiuser system with two active users. The same as in our TO sensitivity analysis, total number of $N = 256$ subcarriers is considered. Both users occupy the same bandwidth each consisting of 36 subcarriers with a guard band subcarrier in between

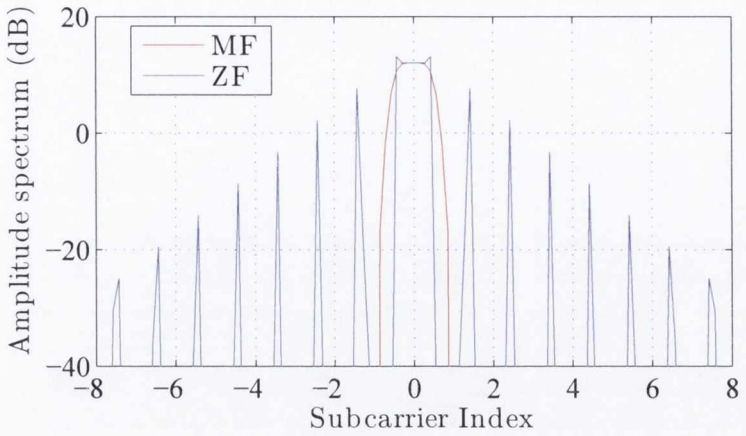

Fig. 5.20 Amplitude spectrum of the receiver matched filter in C-FBMC and zero-forcing detector in GFDM.

the users. Perfect power control is also assumed. It is worth mentioning that the overlapping factors of $K = 4$, 7 and 7 are considered for FBMC, C-FBMC and GFDM, respectively. To analyze the CFO effect, the user of interest is perfectly synchronized while the other user has the normalized CFO of ε that varies in the range $[-0.5, 0.5]$. In our analysis, we compare the MAI power of different waveforms with respect to the normalized CFO. Since all the candidate waveforms for 5G are in the quest for a higher robustness against CFOs than OFDM, in multiuser scenarios like uplink communications, we set the MAI curve of OFDM as a reference.

As can be seen from Fig. 5.19, FBMC and UFMC have a much higher robustness to CFO compared with OFDM. In contrast, GFDM and C-FBMC are more sensitive to CFO than OFDM around the range $\varepsilon \in [-0.1, 0.1]$ and they have a higher robustness to CFOs than OFDM outside that range. One may wonder about the reason for periodic behavior of MAI in C-FBMC and GFDM. As noted earlier, both C-FBMC and GFDM are based on transmission of $2K-1$ tones per subcarrier and overlapping of $K-1$ of them at each side of a given subcarrier. CFO of ε circularly rotates these tones by $K\varepsilon$ and hence there are points where $K\varepsilon$ is an integer, i.e., $\varepsilon \approx \pm 0.143, \pm 0.286, \pm 0.428$ in Fig. 5.19. Due to the real orthogonality in C-FBMC signal and the shape of the matched filter that is shown in Fig. 5.20, when $K\varepsilon$ is an integer, zero crossings of the sinc pulses coincide and therefore as long as the frequency samples of different users do not overlap, no MAI is present. This is the reason for the periodic behavior of MAI in C-FBMC. The same as in C-FBMC, the zero crossings of the sinc pulses in GFDM are coinciding when $K\varepsilon$ is an integer. However, the MAI is not zero in this case which is due to the particular shape of the zero forcing (ZF) filter that

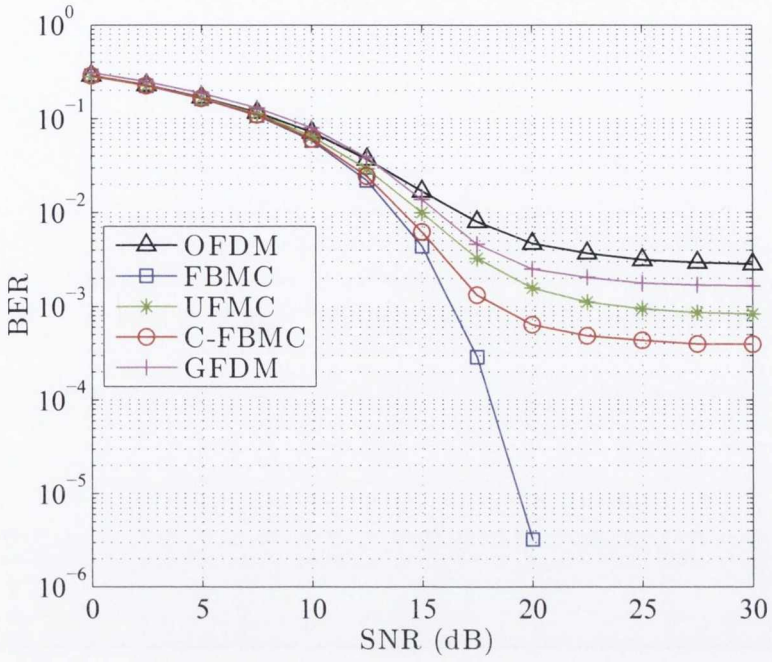

Fig. 5.21 BER performance of different waveforms. The normalized TOs and CFOs are selected randomly between -0.5 and +0.5.

is used at the receiver side. From Fig. 5.20, one may realize that when $K\varepsilon$ is integer, ZF filter takes samples from wrong discrete Fourier transform (DFT) bins outside its main lobe which extends up to 8 subcarriers at each side. This is the source of residual MAI in GFDM for integer values of $K\varepsilon$. Another observation from Fig. 5.19 is that FBMC has the highest CFO robustness compared with other waveforms while GFDM is the most sensitive one after OFDM. UFMC seems to be the second best candidate waveform among the ones analyzed in this chapter from CFO robustness point of view.

5.3.4 Putting All Together

In this section, we evaluate the combined effect of timing and frequency misalignments for different waveforms using computer simulations. Fig. 5.21 presents the uncoded bit error rate (BER) for different waveforms. Here, 5 active users are considered, and the user of interest is assumed to be the middle one in the frequency. The values of normalized TOs and CFOs for other users are selected randomly between -0.5 and $+0.5$, which represents a complete asynchronous scenario. Data symbols are from a 16-QAM constellation. All other simulation parameters are the same as

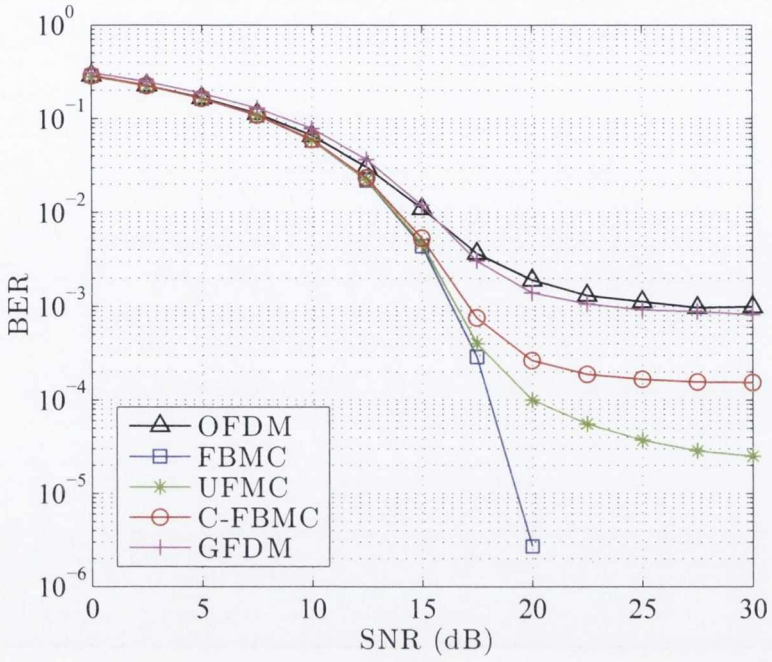

Fig. 5.22 BER performance of different waveforms. The users are quasi-synchronous in time but the CFO errors are selected randomly between -0.5 and +0.5.

before. In Fig. 5.22, we assumed the users are *quasi-synchronized* in time, meaning TOs for CP-based waveforms are in the range of CP, for UFMC are in the range of $[-0.02, +0.02]$, and for FBMC are in the range of $[-0.5, +0.5]$ (i.e., a complete asynchronous scenario). This ensures that the MAI due to timing misalignment is negligible. However, since CFOs are selected randomly between -0.5 and $+0.5$, MAI due to frequency misalignments remains.

5.4 Conclusion

In this chapter, two candidate waveforms for the physical layer of 5G with circular pulse shaping are studied and compared. Beginning with GFDM, our study led to the proposal of a pair of low complexity transceiver structures. The proposed transceiver techniques exploit the special structure of the modulation matrix to reduce the computational cost without incurring any performance loss penalty. In our proposed transmitter, block DFT and IDFT matrices were used to make the modulation matrix sparse and hence reduce the computational burden. We designed low complexity MF, ZF and MMSE receivers by block diagonalization of the matrices involved in demodulation. It was shown that through this block diagonalization, a substantial

amount of complexity reduction in the matrix inversion and multiplication operations can be achieved. A unified receiver structure based on MF, ZF and MMSE criteria was derived. The closed form expressions for the ZF and MMSE receiver filters were also obtained. We also analyzed and compared the computational complexities of our techniques with the existing ones known so far to have the lowest complexity. We have shown that all the proposed techniques in this chapter involve lower computational cost than the existing low complexity techniques [104, 106]. For instance, over an order of magnitude complexity reduction can be achieved through our ZF receiver as compared to the proposed technique in [106]. Such a substantial reduction in the amount of computations that are involved makes our proposed transceiver structures attractive for hardware implementation of the real time GFDM systems.

However, non-orthogonality of the GFDM signal results in a large amount of ICI that needs to be compensated through successive interference cancellation techniques, demanding a great amount of computational burden. In contrast, C-FBMC preserves the orthogonality through a simple modification to GFDM structure. Hence, a simple matched filter receiver leads to a BER performance which is the same as that of OFDM. Our BER performance analysis revealed that GFDM has a serious limitation with respect to the number of symbols in each data block. It does not allow having an even number of symbols in each data block. C-FBMC, on the other hand, does not suffer from this limitation and works for any arbitrary number of symbols in each data block. Moreover, we showed that for large constellation sizes, GFDM suffers from a BER performance loss compared with OFDM while C-FBMC keeps the same performance. C-FBMC may be thought as a modified GFDM, when QAM symbols are replaced by OQAM ones. This replacement leads to an orthogonal modulation and, as a result, resolves the limitations of GFDM which all originate from its non-orthogonal design.

The sources of interference when multicarrier systems are subject to TO and CFO are identified. The studied waveforms are OFDM, GFDM, C-FBMC, UFMC, and linear FBMC. It was noted that to reduce sensitivity to TO and CFO, windows with smooth edges should be applied at both the transmitter and receiver sides. Among the above waveforms only linear FBMC satisfies this condition. Second to linear FBMC is UFMC where a window with smooth edges is used at the transmitter. OFDM, GFDM, and C-FBMC fail our tests as, in their conventional form, they lack windows with smooth transitions at both the transmitter and receiver sides. However, improvements are possible by taking note of the points discussed in this chapter and applying the necessary windows.

Chapter 6

Conclusions and future work

The study that is conducted in this thesis addresses the problems in both current and future multiuser networks from the physical layer perspective. The goal of this thesis has been to provide solutions that allow building low latency multiuser networks with the capability of serving a large number of users. All the techniques that are proposed in this thesis share a common goal that is computational complexity reduction while preserving the optimal performance.

6.1 Summary of contributions and conclusions

In this section, the contributions of the thesis that were previously discussed in detail in chapters 3, 4 and 5 are briefly presented. This paves the way for a better explanation of the possible research directions that can be taken to extend the study that is conducted in this thesis.

6.1.1 Research question 1

- ***Is it possible to serve a large number of users with OFDMA having a reasonable computational burden while providing the optimal performance catering all carrier assignment schemes?***

As discussed in chapter 2, orthogonal frequency division multiple access (OFDMA) systems are highly sensitive to carrier frequency offset (CFO) especially in the uplink. Multiple CFO correction in the uplink of such systems is a challenging task as it imposes a large amount of computational load to the base station when increasing the number of subcarriers or simultaneous users to be served in the network. As noted

in chapters 2, multiple access interference (MAI) due to different users' CFOs has different characteristics in different carrier allocation schemes. Therefore, to reduce the complexity of CFO correction in uplink OFDMA, in chapter 3, we proposed techniques applicable to interleaved, block interleaved and generalized carrier allocation schemes; namely, I-CAS, BI-CAS and G-CAS. Our contributions to this area are summarized as follows.

- **CFO correction in I-CAS and BI-CAS:** In our study, multiple CFOs effect on the received uplink signal is modeled as a linear system of equations with a coefficient matrix that is called interference matrix. We have developed low complexity zero forcing (ZF) and minimum mean square error (MMSE) based CFO correction taking advantage of the special structure of the interference matrix. It is worth noting that our algorithms do not involve any approximation and hence the optimal performance is preserved. Based on our comparisons with the existing solutions known to have the lowest complexity, our solutions can reduce the complexity up to over an order of magnitude. Such a substantial complexity reduction makes our proposed algorithms attractive for hardware implementation.

- **CFO correction in G-CAS:** We have proposed a new class of low complexity ZF and MMSE receivers applying time domain windowing techniques to the received uplink signal. This receiver windowing technique enables reduction of induced interference by multiple CFOs. This leads to a class of low complexity CFO correction techniques that can reduce the computational load of the system up to two orders of magnitude compared with the existing solution that is known to have the lowest complexity. This great reduction in complexity comes at the expense of a longer cyclic extension, i.e., a compromise in bandwidth efficiency. Based on the simulation results presented in chapter 3, the proposed solutions can provide the optimal bit error rate performance.

Concluding remarks

In this thesis, we revisited the CFO correction in the uplink of OFDMA based systems. As mentioned in Chapters 2 and 3, the available solutions in the literature are either highly complex or suffering from performance degradation penalty. Therefore, we developed solutions that are capable of maintaining the optimal performance while having a low computational complexity especially in scenarios where a large number

of users have to be served simultaneously. In the journey towards finding such solutions, we realized that we are tweaking the OFDMA waveform at the receiver to achieve the aforementioned goals. Based on our study, we may conclude that every possible solution for the CFO correction problem in the uplink of OFDMA systems is available in the literature and our solutions, in this area, might have been the only missing pieces of the puzzle. Hence, the motivation for exploring other waveforms than OFDMA that are known to be more robust against synchronization deficiencies, in this thesis, originates from the fact that OFDMA in the uplink faces some serious problems. In addition, each subcarrier in the OFDMA systems can only be allocated to a single user while in an emerging technology that has been recently proposed for increasing the capacity of the future multiuser networks, i.e., known as massive multiple input multiple output (MIMO), all the subcarriers can be reused by all the users. However, OFDM is suggested in the literature as the air interface in massive MIMO networks which suffers from a large amount of out-of-band emissions and has some limitations in spectrum aggregation applications. Consequently, this motivates the investigation of an alternative waveform to OFDM in massive MIMO channels, in this thesis, that not only enables reusing the same spectrum by all the users but it is also using the available spectrum in a highly efficient manner.

6.1.2 Research question 2

- ***Given that massive MIMO and FBMC are suitable for serving a large number of users, what is the impact of these two forerunner technologies on each other?***

Massive MIMO is a new multiuser technique that is recently proposed to increase the capacity of multiuser networks, [7]. Massive MIMO systems were explained in chapter 2. As highlighted in chapter 2, a large number of antennas, i.e., in the order of hundreds, are considered at the base station. The main idea in such systems is that the effects of noise and multiuser interference fade away as the number of base station antennas tends to infinity. The contributions of this thesis in this area are the following.

- **Filter bank multicarrier for massive MIMO:** We introduced filter bank multicarrier (FBMC) to massive MIMO channels. An interesting finding in our research is the self-equalization property of FBMC in massive MIMO channels which allows us to widen the subcarrier bands, increase the symbol rate and

reduce the transients of the signal due to the prototype filter. Compared with OFDM (orthogonal frequency division multiplexing), i.e., the usual multicarrier technique that is used in massive MIMO channels, FBMC offers the advantages of more flexible carrier aggregation, higher bandwidth efficiency (because of the absence of CP) and larger subcarrier spacing, hence, lower sensitivity to CFO and lower PAPR. In addition, we studied and compared both polyphase based and frequency spreading based FBMC structures in massive MIMO channels (details are presented in chapter 4).

- **Pilot decontamination in FBMC-based massive MIMO networks:** Pilot contamination problem that occurs in multicellular massive MIMO networks operating in time-division duplex (TDD) mode is addressed in our study. We extend and apply the blind equalization capability of FBMC to massive MIMO channels in order to tackle this problem. Based on the simulation results that are presented in chapter 4, the channel estimation errors due to the pilot contamination problem can be removed with a low complexity, without any need for cooperation among the cells or transmission of additional training information.

Concluding remarks

Based on the recent discussions on the fifth generation of wireless networks (5G), some candidate waveforms and multiuser solutions have been proposed to address the shortcomings of OFDMA systems, [7, 11–14]. Due to its very low out-of-band emissions, among all the proposed waveforms for 5G, we chose FBMC as an alternative modulation technique to OFDM for massive MIMO systems. The attractive features of FBMC in massive MIMO channels are well articulated in Chapter 4. We started this new line of research in this thesis which can be pursued in different number of directions that will be discussed in Section 6.2.

As it was shown in Chapter 4, due to the self-equalization property of FBMC in massive MIMO channels, we can widen the subcarrier bands in the frequency domain. Widening the bandwidth of each subcarrier is equivalent to shortening the length of the prototype filter. This, in turn, has the impact of increasing the bandwidth efficiency of FBMC, as the ramp-up and ramp-down of the FBMC signal will be shortened. A factor that limits utilization of FBMC systems in some applications like bursty machine to machine communications (M2M) is the long ramp-up and ramp-down of their signals. The approach in this thesis is to reduce the ramp-up and ramp-down of the FBMC signal through widening the subcarriers while achieving a

good equalization performance. An alternative solution to tackle the ramp-up and ramp-down problem of the linearly pulse shaped FBMC signals is to utilize FBMC systems with circular pulse-shaping, [12–14], where the prototype filter transients can be removed through the so called *tail biting property.*

6.1.3 Research question 3

- ***FBMC systems with circular pulse shaping have relaxed synchronization requirements which makes them suitable for applications like M2M. However, the existing transceiver structures for such systems are based on successive interference cancellation techniques which have the drawback of error propagation. Is it possible to design low complexity transceiver structures for such systems while providing the optimal performance?***

As it was highlighted earlier, proposal of new signaling techniques to relax on the tight synchronization requirements of OFDM has been recently one of the main areas of focus in 5G research. Consequently, a number of new waveforms have been proposed, [11]. As it was mentioned in chapter 5, all the candidate waveforms for 5G are based on the idea of FBMC and can be categorized into two groups; the ones with linear pulse-shaping and the ones with circular pulse-shaping. The former has been studied for years while the latter emerged recently. FBMC systems with linear pulse-shaping are studied in this thesis in chapter 4 in the context of massive MIMO systems. Chapter 5 studies FBMC systems with circular pulse-shaping. The contributions of this thesis in this area can be presented as follows.

- **Low complexity transceiver design for generalized frequency division multiplexing (GFDM):** As it is shown in chapter 5, based on the lessons that we learned from CFO correction in the uplink of OFDMA systems (chapter 3), low complexity transceiver structures can be designed. Our designs take advantage of the particular structure of the GFDM modulation matrix to reduce the computational burden of the system. A unified structure for matched filter, ZF and MMSE receivers is developed. Having a unified structure is important from implementation viewpoint as only the filter coefficients need to be changed to have different receivers. Since no approximation is involved in our designs the optimal performance is preserved.

- **Comparison of circularly pulse-shaped waveforms:** Based on the results of [14], a simple modification to GFDM can make the subcarriers orthogonal with respect to each other and hence get rid of the performance penalty of GFDM due to the non-orthogonality of its subcarriers. We put GFDM and its modified version under investigation in chapter 5 and studied these systems from practical feasibility and performance point of view. According to our results in chapter 5, the modified version of GFDM that we call circular FBMC (C-FBMC) is a superior choice to GFDM.

Concluding remarks

As noted earlier, the need for new signaling techniques for the physical layer of 5G networks with more relaxed synchronization requirements than OFDM has led to the proposal of a number of new waveforms. These new waveforms need to go under the microscope and be meticulously investigated. From filter bank viewpoint, the proposed waveforms for 5G can be categorized into the ones with linear pulse shaping and the ones with cuircular pulse shaping. In the realm of the waveforms with circular pulse shaping, we explored GFDM and C-FBMC. GFDM transceiver structures that are available in the literature are known to have a high computational complexity. Hence, we proposed low complexity transceiver structures for such systems in this thesis which leads to a substantial complexity reduction. Moreover, a comparison between the two circularly pulse shaped wavefroms; namely, GFDM and C-FBMC is presented in Chapter 5. Accordingly, C-FBMC was shown to be a stronger candidate than GFDM among the available waveforms with circular pulse shaping.

6.2 Future work and final remarks

The work that is presented in this thesis initiates new research lines that can be pursued in a number of directions. Among these, the following research topics may be named at this time.

- The GFDM transceiver structure that is proposed in chapter 5 can be implemented in practice. The same structure can be modified to also have C-FBMC system implementation. This way, the efficacy of the proposed structure in chapter 5 can be confirmed through practical implementation. Implementing such systems also allows us to investigate them under real world machine to machine (M2M) and Internet of Things (IoT) scenarios. As latency plays an

important role in 5G networks, latency of such systems can be investigated under practical scenarios.

- Literature on synchronization techniques for OFDM based systems is quite saturated. However, the literature on synchronization of the emerging waveforms that are being proposed for 5G is still not mature. Therefore, a thorough study on synchronization of the new waveforms such as GFDM, C-FBMC and universal filtered multicarrier (UFMC), [18], is important. This can reveal the superiority of some waveforms to others from synchronization perspective.

- Preamble design and development of channel estimation techniques in the context of new waveforms for both downlink and uplink is another important research direction that can be pursued.

- Faster than Nyquist signaling, [127], is another interesting research area that can be studied for the non-orthogonal waveforms such as GFDM. Since, in GFDM, the adjacent subcarriers are overlapping with each other, the orthogonality is already lost. Therefore, the subcarriers can be pushed towards each other in the frequency domain to increase the bandwidth efficiency. Intercarrier interference cancellation due to this procedure can be studied or alternatively, design of some filters that reduce the interference due to the signal compression in frequency domain can be investigated.

- Pilot reuse strategies among different cells to suppress the pilot contamination effect in massive MIMO networks along with application of the proposed pilot decontamination technique proposed in chapter 4 can be studied to expedite convergence of the proposed tracking technique.

- The effect of asynchronous users on the performance of massive MIMO systems needs to be investigated. In addition, it would be interesting to compare the effect of synchronization errors on the performance of massive MIMO systems with the emerging waveforms that claim to have relaxed synchronization requirements.

All in all, the aforementioned research directions attest the fact that at least from physical layer perspective a large amount of research needs to be done in the journey towards 5G. This is due to the fact that 5G is not about incremental improvements in data rates and network capacity. Apart from improvements in data rates, massive connectivity among devices is required which is imposed to the network due to some

emerging applications such as M2M and IoT. Accordingly, low latency techniques and relaxed synchronization requirements have to be met in such heavily dense networks.

Appendix A

Proof of Full Rank Property of $\mathbf{\Lambda}$

Using (2.16), the interference matrix $\mathbf{\Lambda}$ can be written as

$$\begin{aligned}\mathbf{\Lambda} &= \mathbf{F}_N \bar{\mathbf{T}}^{\mathrm{T}} \mathbf{W} \sum_{i=1}^{K} \widetilde{\mathbf{\Phi}}(\epsilon_i) \bar{\mathbf{T}} \mathbf{F}_N^{\mathrm{H}} \mathbf{\Pi}^{(i)} \\ &= \mathbf{F}_N \bar{\mathbf{T}}^{\mathrm{T}} \mathbf{W} \mathbf{\Omega}, \end{aligned} \tag{A.1}$$

where

$$\mathbf{\Omega} = \sum_{i=1}^{K} \widetilde{\mathbf{\Phi}}(\epsilon_i) \bar{\mathbf{T}} \mathbf{F}_N^{\mathrm{H}} \mathbf{\Pi}^{(i)} = [\boldsymbol{\omega}_0, \ldots, \boldsymbol{\omega}_{N-1}], \tag{A.2}$$

and $\boldsymbol{\omega}_\ell$s are the column vectors of the matrix $\mathbf{\Omega}$.

Since the DFT matrix, $\mathbf{F}_N$, is full rank, if we show that all the rows of $\bar{\mathbf{T}}^{\mathrm{T}} \mathbf{W} \mathbf{\Omega}$ are linearly independent, we can conclude that the interference matrix is also full rank. The matrix $\mathbf{\Omega}$ is an $(N + N_{\mathrm{w}}) \times N$ matrix with the ℓ^{th} column of

$$\begin{aligned}\boldsymbol{\omega}_\ell &= \Big[e^{-\frac{j2\pi}{N}(\frac{N_{\mathrm{w}}}{2})(\epsilon_j+\ell)}, \ldots, e^{-\frac{j2\pi}{N}(\epsilon_j+\ell)}, \\ &\quad 1, e^{\frac{j2\pi}{N}(\epsilon_j+\ell)}, \ldots, e^{\frac{j2\pi}{N}(N-1)(\epsilon_j+\ell)}, \\ &\quad e^{j2\pi(\epsilon_j+\ell)}, \ldots, e^{\frac{j2\pi}{N}(N+\frac{N_{\mathrm{w}}}{2}-1)(\epsilon_j+\ell)}\Big]^{\mathrm{T}} \times \\ &\quad e^{\frac{j2\pi N_{\mathrm{w}}}{2N}\epsilon_j} \end{aligned} \tag{A.3}$$

where $\ell \in \Psi_j$. From (A.3), one may notice that the elements of the vector in the right hand side are all different powers of $e^{\frac{j2\pi}{N}(\epsilon_j+\ell)}$ scaled by $e^{\frac{j2\pi N_{\mathrm{w}}}{2N}\epsilon_j}$. Hence, in order to make the columns of the matrix $\mathbf{\Omega}$ linearly dependent, there should be two columns ℓ and ℓ' that satisfy the following condition

$$\ell + \epsilon_j = \ell' + \epsilon_k, \tag{A.4}$$

where $\ell \in \Psi_j$ and $\ell' \in \Psi_k$. Therefore, $|\ell - \ell'| = |\epsilon_k - \epsilon_j|$. Due to the fact that ℓ and ℓ' are column indices, they are different integers and $|\ell - \ell'|$ is also an integer while ϵ_k and ϵ_j are residual CFOs in the range of $(-0.5, 0.5]$. Thereby, $|\epsilon_k - \epsilon_j| < 1$ and (A.4) does not hold. Thus, we can conclude that all the columns in $\mathbf{\Omega}$ are linearly independent and therefore the rank of $\mathbf{\Omega}$ is N. The general rule for finding the rank of the product of matrices $\mathbf{A}$ and $\mathbf{B}$ is as follows [110]

$$\text{Rank}(\mathbf{AB}) = \text{Rank}(\mathbf{B}) - \text{Dim}\big(\text{Null}(\mathbf{A}) \cap \text{Range}(\mathbf{B})\big), \tag{A.5}$$

where $\mathbf{A}$ and $\mathbf{B}$ are $n \times p$ and $p \times q$ matrices, respectively. Since $\text{Rank}(\mathbf{\Omega}) = N$ and there is no intersection between the nullspace of $\mathbf{W}$ and the range of $\mathbf{\Omega}$, $\text{Dim}\big(\text{Null}(\mathbf{W}) \cap \text{Range}(\mathbf{\Omega})\big) = 0$, the matrix $\mathbf{W\Omega}$ has also rank of N. Similarly, $\text{Null}(\bar{\mathbf{T}}^{\text{T}}) \cap \text{Range}(\mathbf{W\Omega}) = \emptyset$ and the matrix $\bar{\mathbf{T}}^{\text{T}}\mathbf{W\Omega}$ is full rank.

Appendix B

Derivation of $\boldsymbol{\mathcal{F}}_b\mathbf{A}^{\mathrm{H}}$

The key idea in the derivation of $\boldsymbol{\mathcal{F}}_b\mathbf{A}^{\mathrm{H}}$ is based on the fact that inner product of two complex exponential signals with different frequencies is zero.

$$\sum_{\ell=0}^{N-1} e^{j\frac{2\pi\ell}{N}(i-k)} = N\delta_{ik}. \tag{B.1}$$

From the definitions of $\boldsymbol{\mathcal{F}}_b$ and $\mathbf{A}$, $\boldsymbol{\Gamma} = \boldsymbol{\mathcal{F}}_b\mathbf{A}^{\mathrm{H}}$ can be obtained as $\boldsymbol{\Gamma} = [\boldsymbol{\Gamma}_0^{\mathrm{T}}, \ldots, \boldsymbol{\Gamma}_{N-1}^{\mathrm{T}}]^{\mathrm{T}}$ where $\boldsymbol{\Gamma}_i$'s are $M \times MN$ block matrices that can be mathematically shown as

$$\boldsymbol{\Gamma}_i = \frac{1}{\sqrt{N}}\boldsymbol{\mathcal{G}}^{\mathrm{H}} \sum_{\ell=0}^{N-1} \mathcal{W}^{i\ell}\boldsymbol{\mathcal{E}}_\ell^{\mathrm{H}}, \tag{B.2}$$

where $\mathcal{W}^{i\ell} = e^{-j\frac{2\pi i\ell}{N}}$. Based on the definition of $\boldsymbol{\mathcal{E}}_\ell$ and (B.1) we have

$$\sum_{\ell=0}^{N-1} \mathcal{W}^{i\ell}\boldsymbol{\mathcal{E}}_\ell^{\mathrm{H}} = N\boldsymbol{\Psi}_\kappa, \tag{B.3}$$

where $\kappa = (N-i) \bmod N$, $\boldsymbol{\Psi}_\kappa = \mathrm{diag}\{[\underbrace{\boldsymbol{\psi}_\kappa^{\mathrm{T}}, \ldots, \boldsymbol{\psi}_\kappa^{\mathrm{T}}}_{M \text{ block vectors}}]^{\mathrm{T}}\}$,

$$\boldsymbol{\psi}_\kappa = [0, \ldots, 1, \ldots, 0]^{\mathrm{T}},$$
$$\uparrow$$
$$\kappa^{\mathrm{th}} \text{ position}$$

$\boldsymbol{\psi}_\kappa$'s are $N \times 1$ vectors and $\boldsymbol{\Psi}_\kappa$ is a diagonal matrix whose main diagonal elements are made up of M concatenated copies of the vector $\boldsymbol{\psi}_\kappa$. From (B.3) and (B.1), $\boldsymbol{\Gamma}_i$'s

can be obtained as

$$\mathbf{\Gamma}_i = \sqrt{N}\boldsymbol{\mathcal{G}}^{\mathrm{H}}\mathbf{\Psi}_{\kappa}. \tag{B.4}$$

Accordingly, it can be perceived that the block matrices $\mathbf{\Gamma}_i$'s and hence the matrix $\mathbf{\Gamma}$ are sparse. The matrix $\mathbf{\Gamma}_i$ has only M^2 non-zero elements which are located on the circularly equidistant columns $\kappa, \kappa + N, \ldots, \kappa + (M-1)N$. The elements of two consecutive non-zero columns of $\mathbf{\Gamma}_i$ are circularly shifted copies of each other. For instance, the second non-zero column of $\mathbf{\Gamma}_i$ is a circularly shifted version of the first non-zero one by one sample. From (B.4), the first non-zero column of $\mathbf{\Gamma}_i$ can be derived as $\sqrt{N}[g_{\kappa}, g_{\kappa+(M-1)N}, \ldots, g_{\kappa+N}]^{\mathrm{T}}$ which is the circularly folded version of the κ^{th} polyphase component of the prototype filter. One can further deduce that the matrix $\mathbf{\Gamma}$ is a real one consisted of the prototype filter coefficients.

Appendix C

Closed Form Derivation of $\boldsymbol{\mathcal{D}}$

The polyphase components of the prototype filter $\mathbf{g}$ can be defined as the vectors $\mathbf{g}_0, \mathbf{g}_1, \ldots, \mathbf{g}_{N-1}$ where $\mathbf{g}_i = [g_i, g_{i+N}, \ldots, g_{i+(M-1)N}]^{\mathrm{T}}$. As it is shown in Appendix B, $\boldsymbol{\Gamma} = \boldsymbol{\mathcal{F}}_b \mathbf{A}^{\mathrm{H}}$ is a sparse matrix with only M non-zero elements in each column. The elements of $\boldsymbol{\Gamma}$ can be mathematically represented as

$$[\boldsymbol{\Gamma}]_{ni} = \begin{cases} \sqrt{N}[\tilde{\mathbf{g}}_{n'}]_k, & n = \kappa M, \ldots, (\kappa+1)M - 1, \\ & n' = i \bmod N, \\ & k = (n + M - \lfloor \frac{i}{N} \rfloor) \bmod M, \\ 0, & \text{otherwise}, \end{cases} \tag{C.1}$$

where $\tilde{\mathbf{g}}_{n'}$ is circularly folded version of $\mathbf{g}_{n'}$ and $\kappa = (N - i) \bmod N$. From (C.1), it can be deduced that each group of M consecutive rows of $\boldsymbol{\Gamma}$, i.e., $\boldsymbol{\Gamma}_i$'s, whose non-zero elements are comprised of the elements of the vectors $\tilde{\mathbf{g}}_{n'}$'s, is mutually orthogonal to the other ones. This is due to the fact that the sets of column indices of $\boldsymbol{\Gamma}_i$'s with non-zero elements are mutually exclusive with respect to each other. The block-diagonal matrix $\boldsymbol{\mathcal{D}}$, as derived earlier in (5.8), can be calculated as $\boldsymbol{\mathcal{D}} = \boldsymbol{\mathcal{F}}_b(\mathbf{A}^{\mathrm{H}}\mathbf{A})\boldsymbol{\mathcal{F}}_b^{\mathrm{H}}$ which can be rearranged as $\boldsymbol{\mathcal{D}} = (\boldsymbol{\mathcal{F}}_b\mathbf{A}^{\mathrm{H}})(\boldsymbol{\mathcal{F}}_b\mathbf{A}^{\mathrm{H}})^{\mathrm{H}} = \boldsymbol{\Gamma}\boldsymbol{\Gamma}^{\mathrm{H}}$.

Due to orthogonality of $\boldsymbol{\Gamma}_i$'s with respect to each other, i.e., $\boldsymbol{\Gamma}_i\boldsymbol{\Gamma}_j^{\mathrm{H}} = \mathbf{0}_M$, $i \neq j$, it can be discerned that $\boldsymbol{\mathcal{D}}$ has a block-diagonal structure. Based on equation (C.1), only equidistant columns of $\boldsymbol{\Gamma}_i$'s with circular distance of N are non-zero and two consecutive and non-zero columns are circularly shifted copies of each other with one sample. As a case in point, consider $\boldsymbol{\Gamma}_0$ and (C.1). Therefore, the elements $[\boldsymbol{\Gamma}_0]_{00} = \sqrt{N}[\tilde{\mathbf{g}}_0]_0$, $[\boldsymbol{\Gamma}_0]_{(M-1)0} = \sqrt{N}[\tilde{\mathbf{g}}_0]_{(M-1)}$ and $[\boldsymbol{\Gamma}_0]_{0N} = \sqrt{N}[\tilde{\mathbf{g}}_0]_{(M-1)}$, $[\boldsymbol{\Gamma}_0]_{(M-1)N} = \sqrt{N}[\tilde{\mathbf{g}}_0]_{(M-2)}$

illustrate that the consecutive and non-zero columns of $\mathbf{\Gamma}_0$ are circularly shifted versions of each other. Using (C.1), one can conclude that the same property holds for the other non-zero columns of $\mathbf{\Gamma}_0$ and all the other $\mathbf{\Gamma}_i$'s.

The goal here is to derive a closed form for $\boldsymbol{\mathcal{D}}$.

$$\boldsymbol{\mathcal{D}} = \mathbf{\Gamma}\mathbf{\Gamma}^{\mathrm{H}} = \begin{bmatrix} \mathbf{\Gamma}_0 \\ \vdots \\ \mathbf{\Gamma}_{N-1} \end{bmatrix} \begin{bmatrix} \mathbf{\Gamma}_0^{\mathrm{H}} & \cdots & \mathbf{\Gamma}_{N-1}^{\mathrm{H}} \end{bmatrix}. \tag{C.2}$$

$\boldsymbol{\mathcal{D}}$ is an $MN \times MN$ matrix comprised of $M \times M$ submatrices which are all zero except the ones located on the main diagonal, i.e., $\boldsymbol{\mathcal{D}}_i = \mathbf{\Gamma}_i\mathbf{\Gamma}_i^{\mathrm{H}}$. From (C.1), it can be understood that the first non-zero columns of the matrices $\mathbf{\Gamma}_i$ and $\mathbf{\Gamma}_i^{\mathrm{H}}$ are equal to $\sqrt{N}\tilde{\mathbf{g}}_\kappa$ and $\sqrt{N}\mathbf{g}_\kappa$, respectively and the rest of their non-zero columns are circularly shifted version of their first non-zero column. Removing zero columns of $\mathbf{\Gamma}_i$'s

$$\boldsymbol{\mathcal{D}}_i = \mathbf{\Gamma}_i\mathbf{\Gamma}_i^{\mathrm{H}} = \tilde{\mathbf{\Gamma}}_i\tilde{\mathbf{\Gamma}}_i^{\mathrm{H}}, \tag{C.3}$$

where $\tilde{\mathbf{\Gamma}}_i$ and $\tilde{\mathbf{\Gamma}}_i^{\mathrm{H}}$ are circulant matrices with the first columns equal to $\sqrt{N}\tilde{\mathbf{g}}_\kappa$ and $\sqrt{N}\mathbf{g}_\kappa$, respectively. Since, $\tilde{\mathbf{\Gamma}}_i$ and $\tilde{\mathbf{\Gamma}}_i^{\mathrm{H}}$ are real and circulant, $\boldsymbol{\mathcal{D}}_i$ is also a real and circulant matrix which can be obtained as

$$\boldsymbol{\mathcal{D}}_i = N\mathrm{circ}\{\mathbf{g}_\kappa \textcircled{M} \tilde{\mathbf{g}}_\kappa\}. \tag{C.4}$$

References

[1] K. Raghunath and A. Chockalingam, "SIR analysis and interference cancellation in uplink OFDMA with large carrier frequency/timing offsets," *IEEE Trans. Wireless Commun.*, vol. 8, no.5, pp. 2202–2208, May 2009.

[2] M. Morelli, C. C. J. Kuo, and M. O. Pun, "Synchronization techniques for orthogonal frequency division multiple access (OFDMA): A tutorial review," *Proc. of the IEEE*, vol. 95, no.7, pp. 1394–1427, July 2007.

[3] Y. Na and H. Minn, "Line search based iterative joint estimation of channels and frequency offsets for uplink OFDM systems," *IEEE Trans. Wireless Commun.*, vol. 6, no. 12, pp. 4374–4382, 2007.

[4] X. N. Zeng and A. Ghrayeb, "Joint CFO and channel estimation for OFDMA uplink: an application of the variable projection method," *IEEE Trans. Wireless Commun.*, vol. 8, no. 5, pp. 2306–2311, 2009.

[5] T. Marzetta, "Noncooperative cellular wireless with unlimited numbers of base station antennas," *IEEE Transactions on Wireless Communications*, vol. 9, no. 11, pp. 3590–3600, 2010.

[6] J. Jose, A. Ashikhmin, T. Marzetta, and S. Vishwanath, "Pilot contamination problem in multi-cell TDD systems," in *IEEE International Symposium on Information Theory, ISIT 2009*, June 2009, pp. 2184–2188.

[7] F. Rusek, D. Persson, B. K. Lau, E. Larsson, T. Marzetta, O. Edfors, and F. Tufvesson, "Scaling up MIMO: Opportunities and challenges with very large arrays," *Signal Processing Magazine, IEEE*, vol. 30, no. 1, pp. 40–60, Jan 2013.

[8] H. Q. Ngo and E. Larsson, "EVD-based channel estimation in multicell multiuser MIMO systems with very large antenna arrays," in *IEEE International Conference on Acoustics, Speech and Signal Processing (ICASSP)*, March 2012, pp. 3249–3252.

[9] H. Yin, D. Gesbert, M. Filippou, and Y. Liu, "A coordinated approach to channel estimation in large-scale multiple-antenna systems," *IEEE Journal on Selected Areas in Communications*, vol. 31, no. 2, pp. 264–273, February 2013.

[10] R. Müller, L. Cottatellucci, and M. Vehkaperä, "Blind pilot decontamination," *arXiv: 1309.6806*, 2014.

[11] P. Banelli, S. Buzzi, G. Colavolpe, A. Modenini, F. Rusek, and A. Ugolini, "Modulation formats and waveforms for 5G networks: Who will be the heir of OFDM?: An overview of alternative modulation schemes for improved spectral efficiency," *IEEE Signal Processing Magazine*, vol. 31, no. 6, pp. 80–93, Nov 2014.

[12] G. Fettweis, M. Krondorf, and S. Bittner, "GFDM - generalized frequency division multiplexing," in *IEEE 69th Vehicular Technology Conference, 2009. VTC Spring 2009.*, 2009, pp. 1–4.

[13] A. Tonello and M. Girotto, "Cyclic block FMT modulation for broadband power line communications," in *IEEE International Symposium on Power Line Communications and Its Applications (ISPLC), 2013*, March 2013, pp. 247–251.

[14] H. Lin and P. Siohan, "An advanced multi-carrier modulation for future radio systems," in *IEEE International Conference on Acoustics, Speech and Signal Processing (ICASSP), 2014*, May 2014, pp. 8097–8101.

[15] B. Farhang-Boroujeny, "OFDM Versus Filter Bank Multicarrier," *Signal Processing Magazine, IEEE*, vol. 28, no. 3, pp. 92–112, 2011.

[16] R. Chang, "Synthesis of band-limited orthogonal signals for multipath channel data transmission," *Bell Sys. Tech. J.*, 1966.

[17] B. Saltzberg, "Performance of an efficient parallel data transmission system," *IEEE Transactions on Communication Technology*, vol. 15, no. 6, pp. 805–811, 1967.

[18] V. Vakilian, T. Wild, F. Schaich, S. Ten Brink, and J.-F. Frigon, "Universal-filtered multi-carrier technique for wireless systems beyond lte," in *IEEE Globecom Workshops (GC Wkshps)*, Dec 2013, pp. 223–228.

[19] I. S. Gaspar, L. L. Mendes, N. Michailow, and G. Fettweis, "A Synchronization Technique for Generalized Frequency Division Multiplexing," *EURASIP Journal on Advances in Signal Processing*, vol. 2014, no. 1, p. 67, 2014.

[20] A. Farhang, N. Marchetti, and L. Doyle, "Low Complexity LS and MMSE Based CFO Compensation Techniques for the Uplink of OFDMA Systems," *Proc. of the IEEE ICC '13*, June 2013.

[21] A. Farhang, A. Javaid Majid, N. Marchetti, L. E. Doyle, and B. Farhang-Boroujeny, "Interference localization for uplink OFDMA systems in presence of CFOs," in *Proc. of IEEE Wireless Communications and Networking Conference (WCNC)*, April 2014.

[22] A. Farhang, N. Marchetti, L. Doyle, and B. Farhang-Boroujeny, "Filter bank multicarrier for massive MIMO," in *Proc. of IEEE Vehicular Technology Conference (VTC Fall)*, 2014.

[23] A. Farhang, A. Aminjavaheri, N. Marchetti, L. Doyle, and B. Farhang-Boroujeny, "Pilot decontamination in CMT-based masive MIMO networks," in *Proc. of 11th International Symposium on Wireless Communications Systems (ISWCS)*, Aug. 2014.

[24] A. Farhang, N. Marchetti, F. Figueiredo, and J. Miranda, "Massive MIMO and waveform design for 5th generation wireless communication systems," in *1st International Conference on 5G for Ubiquitous Connectivity (5GU)*, Nov 2014, pp. 70–75.

[25] A. Farhang, N. Marchetti, and L. Doyle, "Low complexity GFDM receiver design: A new approach," in *IEEE International Conference on Communications (ICC)*, June 2015, pp. 4775–4780.

[26] A. Aminjavaheri, A. Farhang, N. Marchetti, L. E. Doyle, and B. Farhang-Boroujeny, "Frequency spreading equalization in multicarrier massive MIMO," in *IEEE International Conference on Communication Workshop (ICCW)*, June 2015, pp. 1292–1297.

[27] A. Farhang, N. Marchetti, L. Doyle, and B. Farhang-Boroujeny, "Low complexity CFO compensation in uplink OFDMA systems with receiver windowing," *IEEE Transactions on Signal Processing*, vol. 63, no. 10, pp. 2546–2558, May 2015.

[28] A. Selim, A. Farhang, and L. Doyle, "Towards easier compliance with out-of-band emissions regulations," in *International Conference on Computing, Networking and Communications (ICNC)*, Feb 2014.

[29] Z. Sharifian, M. J. Omidi, A. Farhang, and H. Saeedi-Sourck, "Polynomial based compressing and iterative expanding for PAPR reduction in GFDM," in *Proc. of 23rd Iranian Conference on Electrical Engineering (ICEE)*, 2015.

[30] J. G. Proakis and M. Salehi, *Digital Communications, 5th Edition.* McGraw Hill, 2007.

[31] B. Farhang-Boroujeny, *Signal Processing Techniques for Software Radios, 2nd edition.* Lulu publishing house, 2011.

[32] R. Chang, "High-speed multichannel data transmission with bandlimited orthogonal signals," *Bell Sys. Tech. J.*, vol. 45, pp. 1775–1796, Dec. 1966.

[33] M. Zimmerman and A. L. Kirsch, "The AN/GSC-10 (KATHRYN) variable rate data modem for HF radio," *IEEE Transactions on Communication Technology*, vol. 15, no. 2, pp. 197–204, April 1967.

[34] G. Porter, "Error distribution and diversity performance of a frequency-differential PSK HF modem," *IEEE Transactions on Communication Technology*, vol. 16, no. 4, pp. 567–575, August 1968.

[35] S. Weinstein and P. Ebert, "Data transmission by frequency-division multiplexing using the discrete fourier transform," *IEEE Transactions on Communication Technology*, vol. 19, no. 5, pp. 628–634, October 1971.

[36] A. Peled and A. Ruiz, "Frequency domain data transmission using reduced computational complexity algorithms," in *IEEE International Conference on Acoustics, Speech, and Signal Processing, ICASSP'80*, vol. 5, Apr 1980, pp. 964–967.

[37] J. Chow, J. Tu, and J. Cioffi, "A discrete multitone transceiver system for HDSL applications," *IEEE Journal on Selected Areas in Communications*, vol. 9, no. 6, pp. 895–908, Aug 1991.

[38] "IEEE standard for broadband over power line networks: Medium access control and physical layer specifications," *IEEE Std 1901-2010*, pp. 1–1586, Dec 2010.

[39] "Radio broadcasting systems ; digital audio broadcasting (DAB) to mobile, portable and fixed receivers," *ETSI std 300 401*, May 2001.

[40] "Digital video broadcasting (DVB); frame structure channel coding and modulation for a second generation digital terrestrial television broadcasting system (DVB-T2)," *ETSI std 302 755*, 2012.

[41] "IEEE 802.11 Task Group a, Part 11: Wireless LAN Medium Access Control (MAC) and Physical Layer (PHY) Specifications: High-speed Physical Layer in the 5 GHz Band," *IEEE*, 1999.

[42] "IEEE standard for local and metropolitan area networks, part 16: air interface for fixed and mobile broadband wireless access systems amendment 2: physical and medium access control layers for combined fixed and mobile operation in licensed bands and corrigendum 1," *IEEE 802.16e-2005*, Feb. 2006.

[43] "3GPP TS 36.211, Evolved Universal Terrestrial Radio Access (E-UTRA); Physical channels and modulation," *3GPP*, 2011.

[44] S. Hikmet and K. Georges, "Orthogonal frequency-division multiple access and its application to CATV networks," *European Transactions on Telecommunications, Volume 9, Issue 6, pages 507-516*, 1998.

[45] M. Bellanger and J. Daguet, "TDM-FDM transmultiplexer: Digital polyphase and FFT," *IEEE Transactions on Communications*, vol. 22, no. 9, pp. 1199–1205, Sep 1974.

[46] "Wideband air interface isotropic orthogonal transform algorithm-public safety wideband data standards project digital radio technical standards," *TIA Committee TR-8.5*, 2003.

[47] K. Lee, S.-R. Lee, S.-H. Moon, and I. Lee, "MMSE-based CFO compensation for uplink OFDMA systems with conjugate gradient," *IEEE Trans. Wireless Commun.*, vol. 11, no.8, pp. 2767–2775, Aug. 2012.

[48] H. Saeedi-Sourck, Y. Wu, J. Bergmans, S. Sadri, and B. Farhang-Boroujeny, "Complexity and performance comparison of filter bank multicarrier and OFDM in uplink of multicarrier multiple access networks," *Signal Processing, IEEE Transactions on*, vol. 59, no. 4, pp. 1907–1912, April 2011.

[49] J. Andrews, S. Buzzi, W. Choi, S. Hanly, A. Lozano, A. Soong, and J. Zhang, "What will 5G be?" *Selected Areas in Communications, IEEE Journal on*, vol. 32, no. 6, pp. 1065–1082, June 2014.

[50] M. Renfors, J. Yli-Kaakinen, and F. Harris, "Analysis and design of efficient and flexible fast-convolution based multirate filter banks," *Signal Processing, IEEE Transactions on*, vol. 62, no. 15, pp. 3768–3783, Aug 2014.

[51] M. Bellanger, "FBMC physical layer: a primer," Tech. Rep., 06/2010.

[52] M. Bellanger, "FS-FBMC: An alternative scheme for filter bank based multicarrier transmission," in *5th International Symposium on Communications Control and Signal Processing (ISCCSP)*, May 2012, pp. 1–4.

[53] M. Bellanger, "FS-FBMC: A flexible robust scheme for efficient multicarrier broadband wireless access," in *IEEE Globecom Workshops*, 2012.

[54] V. Berg, J.-B. Dore, and D. Noguet, "A flexible FS-FBMC receiver for dynamic access in the TVWS," in *9th International Conference on Cognitive Radio Oriented Wireless Networks and Communications (CROWNCOM)*, June 2014, pp. 285–290.

[55] G. Fettweis, M. Krondorf, and S. Bittner, "GFDM - Generalized Frequency Division Multiplexing," in *Vehicular Technology Conference, 2009. VTC Spring 2009. IEEE 69th*, April 2009, pp. 1–4.

[56] M. Schellmann, Z. Zhao, H. Lin, P. Siohan, N. Rajatheva, V. Luecken, and A. Ishaque, "FBMC-based air interface for 5G mobile: Challenges and proposed solutions," in *9th International Conference on Cognitive Radio Oriented Wireless Networks and Communications (CROWNCOM)*, June 2014, pp. 102–107.

[57] A. Tonello, "A novel multi-carrier scheme: Cyclic block filtered multitone modulation," in *IEEE International Conference on Communications (ICC)*, June 2013, pp. 5263–5267.

[58] J. Proakis and D. Manolakis, *Digital signal processing.* Pearson Prentice Hall, 2007.

[59] S. H. Song, G. L. Chen, and K. B. Letaief, "Localized or Interleaved? A tradeoff between diversity and CFO interference in multipath channels," *IEEE Trans. Wireless Commun.*, vol. 10, no.9, pp. 2829–2834, Sept. 2011.

[60] J.-J. van de Beek, M. Sandell, and P. Borjesson, "ML estimation of time and frequency offset in OFDM systems," *IEEE Transactions on Signal Processing*, vol. 45, no. 7, pp. 1800–1805, Jul 1997.

[61] J.-J. van de Beek, P. Borjesson, M.-L. Boucheret, D. Landstrom, J. Arenas, P. Odling, C. Ostberg, M. Wahlqvist, and S. Wilson, "A time and frequency synchronization scheme for multiuser OFDM," *Selected Areas in Communications, IEEE Journal on*, vol. 17, no. 11, pp. 1900–1914, Nov 1999.

[62] S. Barbarossa, M. Pompili, and G. Giannakis, "Channel-independent synchronization of orthogonal frequency division multiple access systems," *IEEE Journal on Selected Areas in Communications*, vol. 20, no. 2, pp. 474–486, Feb 2002.

[63] Z. Cao, U. Tureli, and Y.-D. Yao, "Deterministic multiuser carrier-frequency offset estimation for interleaved OFDMA uplink," *Communications, IEEE Transactions on*, vol. 52, no. 9, pp. 1585–1594, Sept 2004.

[64] R. Miao, J. Xiong, L. Gui, and J. Sun, "Iterative approach for multiuser carrier frequency offset estimation in interleaved OFDMA uplink," *IEEE Transactions on Consumer Electronics*, vol. 55, no. 3, pp. 1039–1044, August 2009.

[65] R. Schmidt, "Multiple emitter location and signal parameter estimation," *IEEE Transactions on Antennas and Propagation*, vol. 34, no. 3, pp. 276–280, Mar 1986.

[66] J. Lee, S. Lee, K.-J. Bang, S. Cha, and D. Hong, "Carrier frequency offset estimation using ESPRIT for interleaved OFDMA uplink systems," *IEEE Transactions on Vehicular Technology*, vol. 56, no. 5, pp. 3227–3231, Sept 2007.

[67] R. Roy and T. Kailath, "Esprit-estimation of signal parameters via rotational invariance techniques," *Acoustics, Speech and Signal Processing, IEEE Transactions on*, vol. 37, no. 7, pp. 984–995, Jul 1989.

[68] M. Morelli, "Timing and frequency synchronization for the uplink of an ofdma system," *IEEE Transactions on Communications*, vol. 52, no. 2, pp. 296–306, Feb 2004.

[69] M.-O. Pun, M. Morelli, and C.-C. Kuo, "Maximum-likelihood synchronization and channel estimation for OFDMA uplink transmissions," *IEEE Transactions on Communications*, vol. 54, no. 4, pp. 726–736, April 2006.

[70] Man On Pun, M. Morelli, and C.-C. Kuo, "Iterative detection and frequency synchronization for ofdma uplink transmissions," *IEEE Transactions on Wireless Communications*, vol. 6, no. 2, pp. 629–639, Feb 2007.

[71] P. Sun and L. Zhang, "Low complexity pilot aided frequency synchronization for OFDMA uplink transmission," *IEEE Transactions on Wireless Communications*, vol. 8, no. 7, pp. 3758–3769, July 2009.

[72] P. Sun, M. Morelli, and L. Zhang, "Carrier frequency offset tracking in the IEEE 802.16e OFDMA uplink," *Wireless Communications, IEEE Transactions on*, vol. 9, no. 12, pp. 3613–3619, December 2010.

[73] K. Lee, S.-H. Moon, and I. Lee, "A pilot-aided frequency offset estimation algorithm for OFDMA uplink systems," in *IEEE Vehicular Technology Conference (VTC Fall)*, 2012.

[74] J. Choi, C. Lee, H. W. Jung, and Y. H. Lee, "Carrier frequency offset compensation for uplink of OFDM-FDMA systems," *IEEE Communications Letters*, vol. 4, no. 12, pp. 414–416, Dec 2000.

[75] D. Huang and K. B. Letaief, "An interference-cancellation scheme for carrier frequency offsets correction in OFDMA systems," *IEEE Trans. Commun.*, vol. 53, no.7, pp. 1155–1165, July 2005.

[76] G. Chen, Y. Zhu, and K. B. Letaief, "Combined MMSE-FDE and interference cancellation for uplink SC-FDMA with carrier frequency offsets," *Proc. of the IEEE ICC '10*, pp. 1–5, May 2010.

[77] T. Yucek and H. Arslan, "Carrier frequency offset compensation with successive cancellation in Uplink OFDMA Systems," *IEEE Trans. Wireless Commun.*, vol. 6, no.10, pp. 3546–3551, Oct. 2007.

[78] S. Ahmed and L. Zhang, "Low complexity iterative detection for OFDMA uplink with frequency offsets," *IEEE Trans. Wireless Commun.*, vol. 8, no. 3, pp. 1199–1205, 2009.

[79] P. Schniter, "Low-complexity equalization of OFDM in doubly selective channels," *IEEE Trans. Signal Processing.*, vol. 52, no. 4, pp. 1002–1011, 2004.

[80] H. C. Nguyen, E. de Carvalho, and R. Prasad, "Multi-user interference cancellation scheme(s) for muliple carrier frequency offset compensation in uplink ofdma," in *IEEE Personal, Indoor and Mobile Radio Communications, 2006*, Sept 2006, pp. 1–5.

[81] Huan Cong Nguyen, E. de Carvalho, and R. Prasad, "Multi-user interference cancellation schemes for carrier frequency offset compensation in uplink OFDMA," *IEEE Transactions on Wireless Communications*, vol. 13, no. 3, pp. 1164–1171, March 2014.

[82] S. Manohar, D. Sreedhar, V. Tikiya, and A. Chockalingam, "Cancellation of multiuser interference due to carrier frequency offsets in uplink OFDMA," *IEEE Transactions on Wireless Communications*, vol. 6, no. 7, pp. 2560–2571, July 2007.

[83] Z. Cao, U. Tureli, and Y.-D. Yao, "Low-complexity orthogonal spectral signal construction for generalized OFDMA uplink with frequency synchronization errors," *IEEE Trans. Veh. Technol.*, vol. 56, no. 3, pp. 1143–1154, May 2007.

[84] M. Huang, X. Chen, S. Zhou, and J. Wang, "Iterative ICI cancellation algorithm for uplink OFDMA system with carrier-frequency offset," *IEEE 62nd Vehicular Technology Conference,*, vol. 3, pp. 1613–1617, Fall 2005.

[85] C. Y. Hsu and W. R. Wu, "A low-complexity zero-forcing CFO compensation scheme for OFDMA uplink systems," *IEEE Trans. Wireless Commun.*, vol. 7, no.10, pp. 3657–3661, Oct. 2008.

[86] K. Lee and I. Lee, "CFO compensation for uplink OFDMA systems with conjugated gradient," *Proc. of the IEEE ICC '11*, pp. 1–5, June 2011.

[87] B. Farhang-Boroujeny and C. (George) Yuen, "Cosine modulated and offset QAM filter bank multicarrier techniques: A continuous-time prospect," *EURASIP Journal on Applied Signal Processing, 2010, special issue on Filter Banks for Next Generation Multicarrier Wireless Communications*, vol. 2010, p. 16 pages, 2010.

[88] K. Martin, "Small side-lobe filter design for multitone data-communication applications," *IEEE Transactions on Circuits and Systems II: Analog and Digital Signal Processing*, vol. 45, no. 8, pp. 1155–1161, Aug 1998.

[89] S. Mirabbasi and K. Martin, "Overlapped complex-modulated transmultiplexer filters with simplified design and superior stopbands," *IEEE Transactions on Circuits and Systems II: Analog and Digital Signal Processing*, vol. 50, no. 8, pp. 456–469, Aug 2003.

[90] J. Hoydis, S. ten Brink, and M. Debbah, "Massive MIMO in the UL/DL of cellular networks: How many antennas do we need?" *IEEE Journal on Selected Areas in Communications*, vol. 31, no. 2, pp. 160–171, 2013.

[91] J. Hoydis, C. Hoek, T. Wild, and S. ten Brink, "Channel measurements for large antenna arrays," in *International Symposium on Wireless Communication Systems (ISWCS), 2012*, 2012, pp. 811–815.

[92] J. Jose, A. Ashikhmin, T. Marzetta, and S. Vishwanath, "Pilot contamination and precoding in multi-cell TDD systems," *IEEE Transactions on Wireless Communications*, vol. 10, no. 8, pp. 2640–2651, 2011.

[93] X. Gao, O. Edfors, F. Rusek, and F. Tufvesson, "Linear pre-coding performance in measured very-large MIMO channels," *IEEE Vehicular Technology Conference (VTC Fall), 2011*, pp. 1–5, 2011.

[94] S. Payami and F. Tufvesson, "Channel measurements and analysis for very large array systems at 2.6 Ghz," *Proc. 6th European Conference on Antennas and Propagation (EuCAP12)*, pp. 433–437, Mar. 2012.

[95] U. Madhow and M. Honig, "MMSE interference suppression for direct-sequence spread-spectrum CDMA," *IEEE Transactions on Communications*, vol. 42, no. 12, pp. 3178–3188, 1994.

[96] B. Farhang-Boroujeny, *Adaptive Filters: Theory and Applications*, 2nd ed. New York, NY, USA: John Wiley & Sons, Inc., 2013.

[97] T. Starr, J. M. Cioffi, and P. J. Silverman, *Understanding Digital Subscriber Line Technology*. Prentice Hall PTR, 1999.

[98] Y. G. Li and G. L. Stuber, *Orthogonal Frequency Division Multiplexing for Wireless Communications*. New York, NY: Springer, 2006.

[99] A. Farhang, M. Kakhki, and B. Farhang-Boroujeny, "Wavelet-OFDM versus filtered-OFDM in power line communication systems," *5th International Symposium on Telecommunications (IST), 2010*, pp. 691–694, 2010.

[100] R. Datta and G. Fettweis, "Improved ACLR by cancellation carrier insertion in GFDM based cognitive radios," in *IEEE Vehicular Technology Conference (VTC Spring)*, 2014.

[101] N. Michailow, M. Matthe, I. Gaspar, A. Caldevilla, L. Mendes, A. Festag, and G. Fettweis, "Generalized Frequency Division Multiplexing for 5th Generation Cellular Networks (Invited Paper)," *Communications, IEEE Transactions on*, vol. PP, no. 99, pp. 1–1, 2014.

[102] N. Michailow, S. Krone, M. Lentmaier, and G. Fettweis, "Bit error rate performance of generalized frequency division multiplexing," in *Vehicular Technology Conference (VTC Fall), 2012 IEEE*. IEEE, 2012, pp. 1–5.

[103] R. Datta, N. Michailow, M. Lentmaier, and G. Fettweis, "GFDM Interference Cancellation for Flexible Cognitive Radio PHY Design," in *Vehicular Technology Conference (VTC Fall), 2012 IEEE*, Sept 2012, pp. 1–5.

[104] I. Gaspar, N. Michailow, A. Navarro, E. Ohlmer, S. Krone, and G. Fettweis, "Low Complexity GFDM Receiver Based on Sparse Frequency Domain Processing," in *Vehicular Technology Conference (VTC Spring), 2013 IEEE 77th*, June 2013, pp. 1–6.

[105] M. Matthe, L. Mendes, and G. Fettweis, "Generalized frequency division multiplexing in a gabor transform setting," *IEEE Communications Letters,*, vol. 18, no. 8, pp. 1379–1382, Aug 2014.

[106] N. Michailow, I. Gaspar, S. Krone, M. Lentmaier, and G. Fettweis, "Generalized frequency division multiplexing: Analysis of an alternative multi-carrier technique for next generation cellular systems," in *Wireless Communication Systems (ISWCS), 2012 International Symposium on*. IEEE, 2012, pp. 171–175.

[107] T. De Mazancourt and D. Gerlic, "The inverse of a block-circulant matrix," *IEEE Trans. Antennas and Propag.*, vol. 31, no.5, pp. 808–810, Sept. 1983.

[108] D. Boswarthick, O. Hersent, and O. Elloumi, *M2M communications : a systems approach*. Wiley-Blackwell, 2012.

[109] F. Sjoberg, R. Nilsson, M. Isaksson, P. Odling, and P. Borjesson, "Asynchronous Zipper," *Proc. of the IEEE ICC '99*, pp. 231–235 vol.1, 1999.

[110] C. D. Meyer, *Matrix Analysis and Applied Linear Algebra*. SIAM, 2001.

[111] G. H. Golub and C. F. Van Loan, *Matrix computations (3rd Ed.)*. Johns Hopkins University Press, 1996.

[112] J. Markel, "FFT pruning," *IEEE Trans. Audio and Electroacoustics*, vol. 19, no. 4, pp. 305–311, 1971.

[113] The IEEE802.16 Broadband Wireless Access Working Group, Channel Models for Fixed Wireless Applications [Online]. Available: http://www.ieee802.org/16/tg3/contrib/802163c-01_29r4.pdf.

[114] B. Farhang-Boroujeny, "Multicarrier modulation with blind detection capability using cosine modulated filter banks," *IEEE Transactions on Communications*, vol. 51, no. 12, pp. 2057–2070, 2003.

[115] N. Krishnan, R. D. Yates, and N. B. Mandayam, "Uplink linear receivers for multi-cell multiuser MIMO with pilot contamination: Large system analysis," in *arXiv:1307.4388*.

[116] D. Godard, "Self-recovering equalization and carrier tracking in two-dimensional data communication systems," *IEEE Transactions on Communications*, vol. 28, p. 11, 1980.

[117] M. Renfors, F. Bader, L. Baltar, D. Le Ruyet, D. Roviras, P. Mege, M. Haardt, and T. Hidalgo Stitz, "On the use of filter bank based multicarrier modulation for professional mobile radio," in *IEEE 77th Vehicular Technology Conference (VTC Spring)*, June 2013, pp. 1–5.

[118] M. Park, K. Ko, H. Yoo, and D. Hong, "Performance analysis of OFDMA uplink systems with symbol timing misalignment," *IEEE Communications Letters*, vol. 7, no. 8, pp. 376–378, 2003.

[119] S. Hashemizadeh, M. Omidi, H. Saeedi-Sourck, and B. Farhang-Boroujeny, "Sensitivity analysis of OFDMA and SC-FDMA uplink systems to carrier frequency offset," *Wireless Personal Communications*, pp. 1–24, 2014.

[120] D. Mattera, M. Tanda, and M. Bellanger, "Analysis of an FBMC/OQAM scheme for asynchronous access in wireless communications," *EURASIP Journal on Advances in Signal Processing*, vol. 2015, no. 1, p. 23, 2015.

[121] T. Fusco, A. Petrella, and M. Tanda, "Sensitivity of multi-user filter-bank multicarrier systems to synchronization errors," in *3rd International Symposium on Communications, Control and Signal Processing (ISCCSP)*. IEEE, 2008, pp. 393–398.

[122] H. Saeedi-Sourck, S. Sadri, and B. Farhang-Boroujeny, "Sensitivity analysis of the multiuser offset QAM multicarrier systems to carrier frequency and timing offsets," in *5th International Symposium on Telecommunications (IST)*. IEEE, 2010, pp. 48–52.

[123] F. Schaich and T. Wild, "Relaxed synchronization support of universal filtered multi-carrier including autonomous timing advance," in *11th International Symposium on Wireless Communications Systems (ISWCS)*. IEEE, 2014, pp. 203–208.

[124] A. Sahin, I. Guvenc, and H. Arslan, "A survey on multicarrier communications: Prototype filters, lattice structures, and implementation aspects," *IEEE Communications Surveys Tutorials*, vol. 16, no. 3, pp. 1312–1338, Third 2014.

[125] M. Matthé, N. Michailow, I. Gaspar, and G. Fettweis, "Influence of pulse shaping on bit error rate performance and out of band radiation of generalized frequency division multiplexing," in *IEEE International Conference on Communications Workshops (ICC)*. IEEE, 2014, pp. 43–48.

[126] B. Farhang-Boroujeny and H. Moradi, "Derivation of GFDM based on OFDM principles," in *IEEE International Conference on Communications (ICC)*, June 2015, pp. 2680–2685.

[127] J. Anderson, F. Rusek, and V. Owall, "Faster-than-nyquist signaling," *Proceedings of the IEEE*, vol. 101, no. 8, pp. 1817–1830, Aug 2013.